

The DTIC Review

Optical and Infrared Detection and Countermeasures

19961009 001

Vol. 2, No. 3
October 1996

The DTIC Review is published quarterly by the Defense Technical Information Center (DTIC), DTIC-BRR, 8725 John J. Kingman Road, Suite 0944, Ft. Belvoir, VA 22060-6218
Telephone: (703) 767-8266, DSN 427-8266
FAX: (703) 767-9070, DSN 427-9070
Email: bibs@dtic.mil

Opinions expressed herein are those of the authors and do not necessarily reflect those of the Department of Defense or its elements.

Editorial Staff.

Editor: Christian M. Cupp

Compiler and Research Advisor: Phyllis Levine

Composition Editor: Charlotte Sisson

Composition Editor (Electronic): Pam Shepherd

Distribution. *The DTIC Review* is approved for public release.

DRAFT SF 298

| | | | | | |
|--|---------------------------|----------------------------|--|---|---|
| 1. Report Date (dd-mm-yy) October, 1996 | | 2. Report Type | | 3. Dates covered (from... to) | |
| 4. Title & subtitle The DTIC Review Optical and Infrared Detection and Countermeasures Volume. 2 No. 3 | | | | 5a. Contract or Grant # | |
| | | | | 5b. Program Element # | |
| 6. Author(s) Christian M. Cupp, Editor Phyllis Levine, Compiler | | | | 5c. Project # | |
| | | | | 5d. Task # | |
| | | | | 5e. Work Unit # | |
| 7. Performing Organization Name & Address Defense Technical Information Center (DTIC) DTIC-BRR 8725 John J. Kingman Rd., Suite 0944 Ft. Belvoir, VA 22060-6218 | | | | 8. Performing Organization Report # DTIC/TR-96/10 | |
| 9. Sponsoring/Monitoring Agency Name & Address Same as # 7 | | | | 10. Monitor Acronym | |
| | | | | 11. Monitor Report # | |
| 12. Distribution/Availability Statement Approved for Public Release; Distribution is unlimited | | | | | |
| 13. Supplementary Notes This publication is published irregularly by the Defense Technical Information Center | | | | | |
| 14. Abstract The military in all countries is paying serious attention to developments in infrared and laser technology. Increasingly, optical and advanced infrared (IR) countermeasures systems and technologies play a significant and important role in modern military engagements. Their application is essential to emerging reconnaissance, strike and targeting strategies and architectures and precision of weapons systems. This in turn is driving the need for more advanced, higher performance infrared countermeasure systems. This edition of The DTIC Review features the latest requirements, developments and technologies in advanced infrared countermeasures systems. This issue goes on further to examine current, evolving and | | | | | |
| 15. Subject Terms Advanced Technologies, Infrared Detector, Infrared Detection, Countermeasures, Wavelets, Sensors | | | | | |
| 16. Report U2 | 17. Abstract U2 | 18. This Page U2 | 19. Limitation of Abstract Unlimited | 20. # of Pages | 21. Responsible Person (Name and Telephone #) |

The DTIC Review

Optical and Infrared Detection and Countermeasures

AD-A314 689

TABLE OF CONTENTS

| | |
|--------------------------------|---|
| Introduction | 1 |
| Document 1 | |
| AD Number: | A311 078 |
| Corporate Author: | Arizona State University; Tempe, AZ |
| Unclassified Title: | Scale-Based Techniques in Secure and Jam-Resistant Communication System |
| Report Date: | July 1996 3 |
| Document 2 | |
| AD Number: | A309 670 |
| Corporate Author: | Arnold Engineering Development Center; Arnold Air Force Base, TN |
| Unclassified Title: | Direct Write Scene Generation Development Efforts for Closed-Loop Evaluation of Focal Plane Arrays |
| Report Date: | May 1996 5 |
| Document 3 | |
| AD Number: | A307 620 |
| Corporate Author: | Dahlgren Division; Naval Surface Warfare Center, VA |
| Unclassified Title: | Detection Range Performance-Horizon Infrared Surveillance Sensor (HISS) |
| Report Date: | January 1995 7 |
| Document 4 | |
| AD Number: | A292 784 |
| Corporate Author: | Quantum Magnetics, Inc.; San Diego, CA |
| Unclassified Title: | Inductively Coupled IR Staring Array Based on Photofluxonic Pixels |
| Report Date: | March 1995 9 |
| Electronic References | 11 |
| Additional References | 15 |
| DTIC Document Order Form | 45 |

FOREWORD

The editors have selected the topic: Optical and Infrared Detection and Countermeasures. *The DTIC Review* brings its readers the full text of selected technical reports as well as a bibliography of other references of interest under one cover. This format provides our readership with a sampling of documents from our collection on a particular topic of current interest. The editorial staff hopes that you find this effort of value and appreciates your comments.



Kurt N. Molholm
Administrator

INTRODUCTION

The military in all countries is paying serious attention to developments in infrared and laser technology. Increasingly, optical and advanced infrared (IR) countermeasures systems and technologies play a significant and important role in modern military engagements. Their application is essential to emerging reconnaissance, strike and targeting strategies and architectures and precision of weapons systems. This in turn is driving the need for more advanced, higher performance infrared countermeasure systems.

This edition of *The DTIC Review* features the latest requirements, developments and technologies in advanced infrared countermeasures systems. This issue goes on further to examine current, evolving and future threats associated with infrared countermeasures.

The selected documents and bibliography are a representation of the information available on emerging technologies and technology forecasting from DTIC's extensive collection on the subject. In-depth literature searches may be requested by contacting the Reference and Retrieval Branch at the Defense Technical Information Center on (703) 767-8274, DSN: 427-8274, FAX: (703) 767-9070, Email: bibs@dtic.mil.

DOCUMENT 1

Scale-Based Techniques in Secure and Jam-Resistant Communication System

AD-A311 078

July 1996

**Arizona State University
Tempe, AZ**

TRC Report No. TRC-DC-9602

SCALE-BASED TECHNIQUES IN SECURE AND JAM-RESISTANT COMMUNICATION SYSTEMS

Douglas Cochran
Department of Electrical Engineering
Arizona State University
Tempe, Arizona 85287-5706

1 July 1996

Final Technical Report

Prepared for:

AIR FORCE OFFICE OF SCIENTIFIC RESEARCH
AFOSR/NM
10 Duncan Avenue, Suite B115
Bolling AFB, DC 20332-6448

Under Grant No. F49620-93-1-0051

REPORT DOCUMENTATION PAGE

Form Approved
OMB No. 0704-0188

Public reporting burden for this collection of information is estimated to average 1 hour per response, including the time for reviewing instructions, searching existing data sources, gathering and maintaining the data needed, and completing and reviewing the collection of information. Send comments regarding this burden estimate or any other aspect of collection of information, including suggestions for reducing this burden, to Washington Headquarters Services, Directorate for Information Operations and Reports, 1215 Jefferson Davis Highway, Suite 1204, Arlington, VA 22202-4302, and to the Office of Management and Budget, Paperwork Reduction Project (0704-0188), Washington, DC 20503.

| | | | | |
|--|--|---|--|--|
| 1. AGENCY USE ONLY (Leave blank) | | 2. REPORT DATE 1 July 1996 | 3. REPORT TYPE AND DATES COVERED Final Technical Report, Nov. 1992-Jan. 1996 | |
| 4. TITLE AND SUBTITLE Scale-Based Techniques in Secure and Jam-Resistant Communication Systems | | | 5. FUNDING NUMBERS F49620-93-1-00 2304/ES 6112F | |
| 6. AUTHOR(S) Douglas Cochran | | | 7. PERFORMING ORGANIZATION NAME(S) AND ADDRESS(ES) Arizona State University; Tempe, AZ 85287-7206 | |
| 9. SPONSORING/MONITORING AGENCY NAME(S) AND ADDRESS(ES) Air Force Office of Scientific Research 110 Duncan Avenue, Suite B115 Bolling AFB, DC 20332 | | | 10. SPONSORING AGENCY REPORT NUMBER AFOSR-TR-96 0375 | |
| 11. SUPPLEMENTARY NOTES | | | | |
| 12a. DISTRIBUTION / AVAILABILITY STATEMENT Distribution Unlimited | | | 12b. DISTRIBUTION CODE | |
| 13. ABSTRACT (Maximum 200 words) This three-year project has focused on theoretical development and preliminary performance analysis of wavelet-based multiple access communication systems. Sets of orthonormal wavelet symbols suitable for asynchronous multiple access spread spectrum communications were developed. Investigation of possible countermeasures to wavelet-based communication systems led to development of a cyclostationary signal detector for which detection thresholds corresponding to desired false-alarm probabilities can be determined analytically. This detector was applied against both traditionally modulated and low probability of detection signals, including wavelet modulated signals. Some basic research on wavelet analysis performed in connection with this project led to a class of multidimensional generalizations of the wavelet transform. | | | | |
| 14. SUBJECT TERMS Spread Spectrum Communication Systems, Wavelets, Cyclostationary Signal Processing | | | 15. NUMBER OF PAGES 28 | |
| | | | 16. PRICE CODE | |
| 17. SECURITY CLASSIFICATION OF REPORT UNCLASSIFIED | 18. SECURITY CLASSIFICATION OF THIS PAGE UNCLASSIFIED | 19. SECURITY CLASSIFICATION OF ABSTRACT UNCLASSIFIED | 20. LIMITATION OF ABSTRACT UL | |

1 Introduction

This report summarizes the results obtained in a three-year investigation into the application of wavelet methods in modulation techniques for multi-user spread spectrum communication systems. The investigation was undertaken between November 1992 and January 1996.

2 Objectives

The objectives of this project remained essentially as outlined in the project proposal and previous status reports:

- **Task 1:** Development of and evaluation of wavelet symbols for multiple access spread spectrum communications.
- **Task 2:** Evaluation of communication system performance.
- **Task 3:** Investigation of possible countermeasures to wavelet-based spread spectrum.

In addition to addressing these objectives, some basic research on wavelet analysis was performed in connection with the project which led to a class of multidimensional generalizations of the wavelet transform.

3 Status of Effort

The project was completed in January, 1996 with the benefit of a two-month extension of the original three-year time line.

Task 1 led to development and analysis of a class of bandlimited orthonormal wavelet sets having properties well suited for use with the wavelet-based scale-division multiple access communication scheme around which much of this project was based.

Crosstalk effects in scale-division multiple access under asynchronous and distributed operation were studied under Task 2. Other performance questions originally planned to be addressed under this Task were de-emphasized in later stages of the project in view of published work on performance of wavelet-based communication protocols by other researchers.

Task 3 led to introduction and evaluation of an algorithm for detection of cyclostationary signals. This detector was used to evaluate the detectability of scale-division multiple access signals by cyclostationary methods.

4 Accomplishments / New Findings

At the inception of this project, only a handful of researchers had looked into the possibility of using wavelets [8, 44, 49, 50] or fractal signals [57, 58] in the modulation of communication signals. The research group at Arizona State University was the first to investigate multiple access issues in this context [8]. There are now over forty published papers in this area [2, 5, 9-13, 17-21, 24-30, 33-36, 38-45, 47, 49-50, 53, 55-59].

Work under this effort focused on wavelet-based multiple-access techniques in which digital communication signals are encoded on orthogonal wavelet sets, as was introduced in [8] and described in the original proposal. Highlights of the results obtained in this project are summarized below.

4.1 Orthonormal Wavelet Symbols

Scale-division multiple access (SDMA) refers to a multiple-access communication scheme in which the orthogonal symbols are obtained by dilation and time shifting of a single prototype wavelet. The various users' messages are separated into channels based on the scale of dilation of the wavelet symbol on which their messages are encoded – hence the term SDMA [8, 10, 52]. As shown in these references, the spectral structure of a transmitted SDMA signal depends on the choice of the prototype wavelet symbol in a straightforward way.

The goals in construction of wavelets for use as symbols in SDMA are different from those encountered in designing wavelets for other applications. For use in time-frequency analysis of signals, for example, it is generally desirable for wavelets to have their energy simultaneously concentrated in both the time and frequency domains in order to provide signal analysis that is localized in the phase plane. In spread spectrum applications, however, wavelets should be compactly supported or highly concentrated in the time domain while having broadband frequency structure.

In general, SDMA relies on exact synchronization of all transmitters in the network to maintain orthogonality of the signals and avoid channel crosstalk. Even if this is achieved, time delays introduced by propagation through the transmission medium will cause the received signals to be non-orthogonal. This issue may be addressed by requiring that the channels in the network use symbols with Fourier transforms having disjoint supports. In this project, orthonormal wavelet bases generated by mother wavelets whose frequency spectra are supported in several disjoint bands were constructed.

The simplest example of a dyadic orthonormal basis of bandlimited wavelets is generated by the

mother wavelet defined in the frequency domain by

$$\hat{h}(\omega) = \begin{cases} 1 & \pi \leq |\omega| < 2\pi \\ 0 & \text{otherwise} \end{cases} \quad (1)$$

with $a_0 = 2$ and $b_0 = 1$. A related, but more complicated, example of an orthonormal basis of bandlimited wavelets was described by Mallat using the mother wavelet defined by

$$\hat{h}(\omega) = \begin{cases} 1 & |\omega| \in [\frac{4}{7}\pi, \pi) \cup [4\pi, \frac{32}{7}\pi) \\ 0 & \text{otherwise} \end{cases} \quad (2)$$

Examination of the relationship between these two wavelet bases gives insight about how to construct other bandlimited wavelet bases in which the dilations of the mother wavelet h do not overlap in the frequency domain.

In what follows, the connected components of the support of a mother wavelet's Fourier transform \hat{h} will be called "slots." Throughout this section h will be a real-valued wavelet, which implies that $\hat{h}(-\omega) = \hat{h}^*(\omega)$ and hence the slots are symmetric about $\omega = 0$. Accordingly, when the values or support of \hat{h} are specified on the positive frequency axis, they will be assumed to be given on the negative frequency axis by symmetry. The class of wavelets to be constructed will be categorized according to the number of slots they have in the positive frequency axis. The wavelet defined by (1) is thus a "one-slot" wavelet while the one defined by (2) is a "two-slot" wavelet. The following sections describe the construction of " n -slot" orthonormal wavelet bases.

Suppose the support S_0 of \hat{h} is the union of n disjoint intervals

$$S_0 = [s_0, s_1] \cup [s_2, s_3] \cup \cdots \cup [s_{n-1}, s_n] \quad (3)$$

Then the support of \hat{h}_m^k is

$$S_m = [s_0 2^{-m}, s_1 2^{-m}] \cup [s_2 2^{-m}, s_3 2^{-m}] \cup \cdots \cup [s_{n-1} 2^{-m}, s_n 2^{-m}]$$

If the measure of $S_m \cap S_{m'}$ is zero for all non-equal integers m and m' , S_0 will be called an *orthogonal support*. In particular, an orthogonal support consisting of n disjoint intervals will be called an *n -slot orthogonal support*.

If $\|h\| = 1$ and the support of \hat{h} is orthogonal,

$$\langle h_m^n, h_{m'}^{n'} \rangle = \frac{1}{2\pi} \langle \hat{h}_m^n, \hat{h}_{m'}^{n'} \rangle = 0$$

for all $m \neq m'$. In this case, for the time-shifted and dilated replicates h_m^n of h to form an orthonormal set in L^2 , it remains only to ensure that h_m^n and $h_{m'}^{n'}$ are orthonormal for $n \neq n'$ and all m .

This is simplified by the observation that

$$\langle h_m^n, h_m^{n'} \rangle = \langle h_0^n, h_0^{n'} \rangle$$

Thus, one must only verify that all of the time-shifted replicates of h are orthonormal at a single level of dilation.

4.1.1 Construction of Orthogonal Supports

Consider real numbers $0 < c_0 < \dots < c_n = 2c_0$. Then

$$[c_0, 2c_0] = [c_0, c_1] \cup [c_1, c_2] \cup [c_2, c_3] \cup \dots \cup [c_{n-1}, 2c_0]$$

Let p_1, \dots, p_n be distinct integers and dilate each sub-interval $[c_j, c_{j+1}]$ by 2^{p_j+1} to form a set

$$\begin{aligned} S_0 &= [c_0 2^{p_1}, c_1 2^{p_1}] \cup [c_1 2^{p_2}, c_2 2^{p_2}] \cup \dots \cup [c_{n-1} 2^{p_n}, 2c_0 2^{p_n}] \\ &= [s_0, s_1] \cup [s_2, s_3] \cup \dots \cup [s_{2n}, s_{2n-1}] \end{aligned}$$

Then S_0 is clearly an n -slot orthogonal support. Conversely, suppose S_0 is an n -slot orthogonal support of the form (3). Then it is straightforward to show that S_0 can be generated by the method just described with possibly some subintervals deleted.

4.1.2 Orthonormality of the Wavelets

Suppose $\|h\| = 1$ and the support of \hat{h} is orthogonal. Then $\{h_m^n\}$ is an orthonormal wavelet set if and only if $\langle h_0^n, h_0^{n'} \rangle = 0$ for all integers n and n' with $n \neq n'$. This is equivalent to

$$\begin{aligned} 0 &= \langle h_0^n, h_0^{n'} \rangle = \int_{\mathbb{R}} h(t-n) h^*(t-n') dt \\ &= \frac{1}{2\pi} \int_{\mathbb{R}} e^{-in\omega} \hat{h}(\omega) e^{in'\omega} \hat{h}^*(\omega) d\omega = \frac{1}{2\pi} \int_{\mathbb{R}} e^{i(n'-n)\omega} |\hat{h}(\omega)|^2 d\omega \end{aligned}$$

for all $n \neq n'$. With $k \triangleq n - n' \neq 0$, this expression becomes

$$\int_{\mathbb{R}} e^{ik\omega} |\hat{h}(\omega)|^2 d\omega = 0 \quad (4)$$

for any non-zero integer k . The following section presents some orthonormal wavelet sets corresponding to certain solutions of this equation.

4.1.3 Flat n -Slot Orthonormal Wavelets

The first n -slot orthonormal wavelets constructed were similar to the wavelets defined by (1) and (2) in that their Fourier transforms are constant on the n slots and zero elsewhere. These will be called *flat* n -slot wavelets. Construction of "non-flat" n -slot orthonormal wavelets is undertaken in the next section of this report.

Let

$$V = [c_0 2^{p_1}, c_1 2^{p_1}] \cup [c_1 2^{p_2}, c_2 2^{p_2}] \cup \dots \cup [c_{n-1} 2^{p_n}, c_n 2^{p_n}]$$

where $0 < c_0 < \dots < c_n = 2c_0$ and p_1, p_2, \dots, p_n are integers and define

$$\alpha = \left(\frac{1}{\pi} \sum_{j=1}^n 2^{p_j} (c_j - c_{j-1}) \right)^{-1/2}$$

Then if $\hat{h}(\omega) = \alpha$ for $\omega \in V$ and $\hat{h}(\omega) = 0$ otherwise, $\|h\| = 1$ and equation (4) reduces to

$$\begin{aligned} & \int_{\mathbb{R}} e^{ik\omega} |\hat{h}(\omega)|^2 d\omega \\ &= \alpha^2 \left(\int_{-c_0 2^{p_1}}^{-c_1 2^{p_1}} + \int_{c_0 2^{p_1}}^{c_1 2^{p_1}} + \int_{-c_1 2^{p_2}}^{-c_2 2^{p_2}} + \int_{c_1 2^{p_2}}^{c_2 2^{p_2}} + \dots + \int_{-c_{n-1} 2^{p_n}}^{-c_n 2^{p_n}} + \int_{c_{n-1} 2^{p_n}}^{c_n 2^{p_n}} \right) e^{ik\omega} d\omega \\ &= 2\alpha^2 \left(\int_{c_0 2^{p_1}}^{c_1 2^{p_1}} + \int_{c_1 2^{p_2}}^{c_2 2^{p_2}} + \dots + \int_{c_{n-1} 2^{p_n}}^{c_n 2^{p_n}} \right) \cos(k\omega) d\omega \\ &= \frac{2\alpha^2}{k} \{ -\sin(c_0 2^{p_1} k) + \sin(c_1 2^{p_1} k) - \sin(c_1 2^{p_2} k) + \sin(c_2 2^{p_2} k) - \\ & \quad \dots - \sin(c_{n-1} 2^{p_n} k) + \sin(c_n 2^{p_n} k) \} = 0 \end{aligned}$$

for all $k \neq 0$. This is equivalent to

$$-\sin(c_0 2^{p_1} k) + \sin(c_1 2^{p_1} k) - \sin(c_1 2^{p_2} k) + \sin(c_2 2^{p_2} k) - \dots - \sin(c_{n-1} 2^{p_n} k) + \sin(c_n 2^{p_n} k) = 0 \quad (5)$$

for all $k \neq 0$. If $c_0 2^{p_1}, c_1 2^{p_1}, c_1 2^{p_2}, c_2 2^{p_2}, \dots, c_{n-1} 2^{p_n}$, and $c_n 2^{p_n}$ satisfy equation (5), then so will $M c_0 2^{p_1}, M c_1 2^{p_1}, M c_1 2^{p_2}, M c_2 2^{p_2}, \dots, M c_{n-1} 2^{p_n}$, and $M c_n 2^{p_n}$ for any natural number M . Thus, there exists a support of lowest dilation level which will be called the *mother support*. In other words, if the end points of the support

$$V = [c_0 2^{p_1}, c_1 2^{p_1}] \cup [c_1 2^{p_2}, c_2 2^{p_2}] \cup \dots \cup [c_{n-1} 2^{p_n}, c_n 2^{p_n}]$$

satisfy (5) and the end points of the dilated support

$$[c_0 2^{p_1}/M, c_1 2^{p_1}/M] \cup [c_1 2^{p_2}/M, c_2 2^{p_2}/M] \cup \dots \cup [c_{n-1} 2^{p_n}/M, c_n 2^{p_n}/M]$$

do not satisfy (5) for any $M \in \mathbb{N}$, then V is the mother support. •

Example 1 In the one-slot case, the support consists of only one interval $[c_0 2^{p_1}, 2c_0 2^{p_1}]$ with $c_0 > 0$. Denoting $a = c_0 2^{p_1}$, equation (5) becomes $-\sin(ak) + \sin(2ak) = 0$, or

$$\sin(ak)[2\cos(ak) - 1] = 0$$

The only non-trivial solution of this equation that holds for any non-zero integer k is $a = m\pi$ with $m \in \mathbb{N}$. Hence, the support is $[m\pi, 2m\pi]$, the mother support is $[\pi, 2\pi]$, and an orthonormal wavelet basis obtained having the mother wavelet defined in equation (1).

Example 2 In the two-slot case, the cut points c_0 and c_1 and the dilation p should satisfy

$$-\sin(c_0 k) + \sin(c_1 k) - \sin(c_1 2^p k) + \sin(2c_0 2^p k) = 0$$

This equation can be decomposed into two equations (with loss of some solutions)

$$\begin{cases} \sin(2c_0 2^p k) - \sin(c_0 k) = 0 \\ \sin(c_1 2^p k) - \sin(c_1 k) = 0 \end{cases}$$

which can be solved simultaneously under the additional conditions $\|h\| = 1$ and $\alpha = 1$ to yield

$$\begin{cases} c_0 = \frac{2^p}{2^{p+1}-1} \pi \\ c_1 = \pi \end{cases}$$

With $p = 0$ and $c_0 = \pi$, the wavelet obtained is the one defined in equation (1); $p = 2$ and $c_0 = \frac{4}{3}\pi$ yields the wavelet of equation (2). For $p = 1$ and $c_0 = \frac{2}{3}\pi$, a new bandlimited orthonormal mother wavelet defined by

$$\hat{h}(\omega) = \begin{cases} 1 & |\omega| \in [\frac{2}{3}\pi, \pi) \cup [2\pi, \frac{8}{3}\pi) \\ 0 & \text{otherwise} \end{cases}$$

is obtained.

4.1.4 Non-Flat n -Slot Orthonormal Wavelets

Denoting $\hat{\psi} = |\hat{h}|^2$, equation (4) becomes

$$\int_{\mathbb{R}} e^{ik\omega} |\hat{h}(\omega)|^2 d\omega = \int_{\mathbb{R}} \hat{\psi}(\omega) e^{ik\omega} d\omega = 2\pi \psi(k) = 0. \quad (6)$$

for all non-zero integers k . This formulation leads to the following:

Theorem 1 Let $\hat{\psi}$ be a real-valued and non-negative function with orthogonal support. Further suppose $\int_{\mathbb{R}} \hat{\psi}(\omega) d\omega = 2\pi$ and $\psi(k) = 0$ for all non-zero integers k . Then with $|\hat{h}| = \sqrt{\hat{\psi}}$ and the phase of \hat{h} chosen arbitrarily (except for conjugate symmetry), h is an orthonormal mother wavelet.

In view of this result, construction of the desired non-flat wavelets hinges on finding functions ψ having the properties specified. Such functions may be constructed as follows.

Denote $\text{sinc}(t) \triangleq \frac{\sin(\pi t)}{\pi t}$ and observe that $\text{sinc}(k) = 0$ for all non-zero integers k . Its Fourier transform has values

$$\widehat{\text{sinc}}(\omega) = \begin{cases} 1 & |\omega| < \pi \\ 0 & \text{otherwise} \end{cases}$$

Suppose $S = [c_0 2^{p_1}, c_1 2^{p_1}] \cup \dots \cup [c_{n-1} 2^{p_n}, c_n 2^{p_n}]$ is an n -slot orthogonal support in which each slot has measure larger than 2π . Let \hat{f} be any non-trivial L^2 function supported in $[c_0 2^{p_1} + \pi, c_1 2^{p_1} - \pi] \cup \dots \cup [c_{n-1} 2^{p_n} + \pi, c_n 2^{p_n} - \pi]$ (figure 1) and whose convolution with $\widehat{\text{sinc}}$ is non-negative. Then $\psi(t) \triangleq f(t) \text{sinc}(t)$ is zero for all non-zero integer values of t , $\hat{\psi} = [\widehat{\text{sinc}} * \hat{f}]$ is non-negative, and the support of $\hat{\psi}$ is orthogonal. Hence, an orthonormal mother wavelet h can be obtained by letting

$$|\hat{h}|^2 = \frac{2\pi \hat{\psi}}{\int_{\mathbb{R}} \hat{\psi}(\omega) d\omega}$$

and setting the phase of \hat{h} arbitrarily.

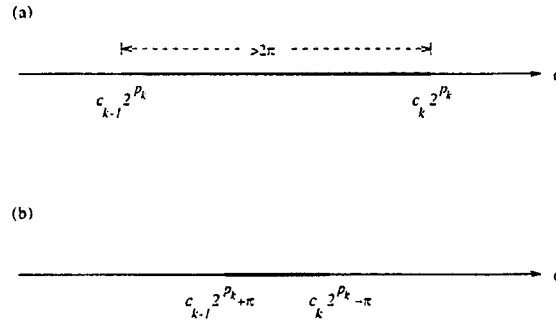


Figure 1: (a) Each interval in the original n -band orthogonal support S has length larger than 2π . (b) The support of \hat{f} is formed by shrinking each interval in S by π on its left and right ends.

Note that h may be a dilated version of another orthonormal mother wavelet. If after rescaling, there exists some $N \in \mathbb{N}$, such that $h(2^{-N}t)$ satisfies equation (4), i.e.,

$$\int_{\mathbb{R}} e^{i\omega k} |\hat{h}(2^N \omega)|^2 d\omega = 0$$

for all nonzero integers k , and

$$\int_{\mathbb{R}} e^{i\omega k} |h(2^{N+1} \omega)|^2 dt \neq 0$$

for some nonzero integer k , then h' defined by $h'(t) = 2^{-N/2} h(2^{-N}t)$ is also an orthonormal mother wavelet.

The first part of the following result is a consequence of the above construction; the converse portion is proven in [10].

Theorem 2 *For any n -slot orthogonal support S_0 , there exist orthonormal mother wavelets having support S_0 . Conversely, any n -slot orthonormal mother wavelet can be constructed in the way discussed above.*

Example 3 Let $c_0 = \pi$, $p_1 = 1$, $c_1 = 7\pi/4$, and $c_2 = 2$. Then the support of \hat{h} is $[\pi, 7\pi/4] \cup [7\pi, 8\pi]$. Expand this support by a factor of 4 to $[4\pi, 7\pi] \cup [28\pi, 32\pi]$ to make the length of each interval larger than 2π . Choose the support of \hat{f} to be $[5\pi, 6\pi] \cup [29\pi, 31\pi]$ and generate \hat{f} subject to the condition that $\hat{f} * \widehat{\text{sinc}}$ must be real and nonnegative; here define \hat{f} by

$$\hat{f}(\omega) = \begin{cases} 1 & 5\pi < |\omega| \leq 6\pi \text{ and } 29\pi < |\omega| \leq 31\pi \\ 0 & \text{elsewhere} \end{cases}$$

Then

$$\hat{\psi}(\omega) = [\hat{f} * \widehat{\text{sinc}}](\omega)$$

and $\hat{\psi}$ is as shown in figure 2. Taking the square root of $\hat{\psi}$ as the absolute value of \hat{h} and imposing zero phase, the orthonormal mother wavelet with Fourier transform depicted in figure 3 is obtained.

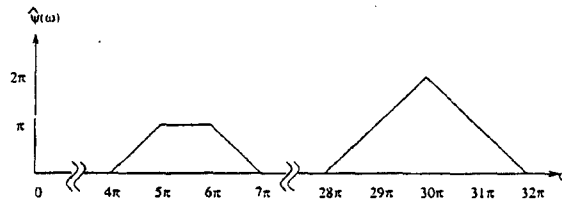


Figure 2: Convolution of \hat{f} with the Fourier transform of a sinc function ensures $\psi(k) = 0$ for all non-zero integers k .

4.2 Orthonormal Wavelet Symbols with Frequency Overlap

If bandlimited wavelets are to be used as orthogonal symbols in a low-probability of exploitation (LPE) communication system, it may be desirable to have the bands overlap to avoid the possibility of an unintended receiver separating the channels using a relatively simple bank of bandpass filters. Following a technique developed by Suter and Oxley [46], bandlimited wavelet symbols have been

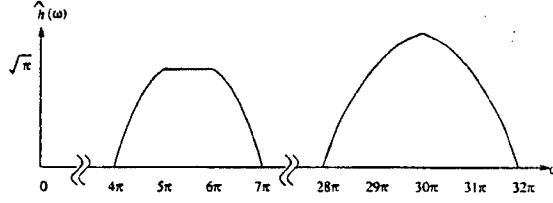


Figure 3: An orthogonal mother wavelet h is obtained as the inverse Fourier transform of the square root of $\hat{\psi}$.

developed which (i) generate orthonormal sets and (ii) whose replicates at different scales overlap in the frequency domain. The approach is summarized below.

The construction given in [46] assumes that the real line has been partitioned into disjoint intervals I_j , $j \in \mathbb{Z}$. If $\{f_{j,k} | k \in \mathbb{Z}\}$ is an orthonormal basis for $L^2(I_j)$, then $\{f_{j,k} | j, k \in \mathbb{Z}\}$ is an orthonormal basis for $L^2(\mathbb{R})$. A new orthonormal basis is constructed by extension of the functions $f_{j,k}$ off the interval I_j in a specific way, resulting in a basis in which the elements “overlap.”

This construction is modified to the wavelet case to construct “overlapped” bandlimited orthonormal wavelet symbols as follows. Let h be a bandlimited wavelet having the properties:

1. The Fourier transform \hat{h} of h is real-valued and even. The steps in the construction described below apply to the portion of \hat{h} on the positive frequency axis and are assumed to also be applied to the portion of \hat{h} on the negative frequency axis to maintain even symmetry.
2. The support of \hat{h} is orthogonal in the sense introduced above; i.e., the portion on the positive frequency axis is of the form

$$[2^{d_1}\pi, 2^{d_1}a_1] \cup \dots \cup [2^{d_n}a_{n-1}, 2^{d_n}2\pi]$$

where $n \geq 1$, $\pi < a_1 < \dots < a_{n-1} < 2\pi$, and d_1, \dots, d_n are integers. The construction given here also assumes $d_1 \neq 2d_n$.

For integers j and k , define

$$h_{j,k}(t) = 2^{-\frac{j}{2}} h\left(\frac{t - 2^j k}{2^j}\right) \quad (7)$$

and denote by $\hat{h}_{j,k}$ the Fourier transform of $h_{j,k}$.

Suppose $\{h_{j,k} | j, k \in \mathbb{Z}\}$ is an orthonormal basis of $L^2(\mathbb{R})$ (some examples of such bases are constructed above and others are described in [6]). With $\epsilon < \min\{(a_1 - \pi)/2, (2\pi - a_{n-1})/2\}$, define an extension $\tilde{\hat{h}}$ of \hat{h} by

1. Constructing the odd extension of \hat{h} about the point $2^{d_1}\pi$ into the interval $[2^{d_1}(\pi - \epsilon), 2^{d_1}\pi]$;
2. Constructing the even extension of \hat{h} about the point $2^{d_n}2\pi$ into the interval $[2^{d_n}2\pi, 2^{d_n}(2\pi + \epsilon)]$;
- and
3. Repeating these steps on the negative frequency axis to preserve even symmetry.

An example is shown in figure 4 using Mallat's wavelet defined in equation (1).

Denote the extended wavelet just constructed by $\tilde{\hat{h}}$ and let \hat{w} denote an frequency domain window function with support identical to that of $\tilde{\hat{h}}$ and with the amplitude normalization properties described in [46]. An example of \hat{w} is depicted in figure 4. With u defined by

$$\hat{u}(\omega) = \hat{w}(\omega)\tilde{\hat{h}}(\omega) \quad (8)$$

the set $\{u_{j,k}|j,k \in \mathbb{Z}\}$ is shown to be an orthonormal wavelet basis of $L^2(\mathbb{R})$. Also, by construction, the dilated replicates of \hat{u} have non-trivial overlap. Figure 5 shows a particular overlapped bandlimited orthonormal wavelet symbol $\hat{u}(\omega)$ constructed in the above example.

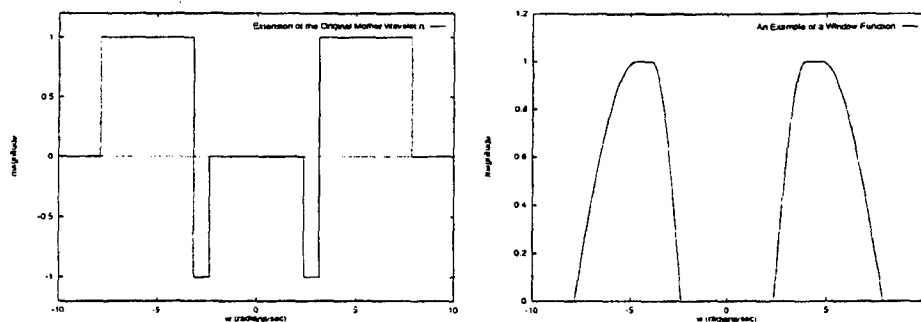


Figure 4: Initial frequency extension $\tilde{\hat{h}}(\omega)$ of the wavelet h (left) and the window function $\hat{w}(\omega)$ applied to it (right).

4.3 Countermeasures

A detector for cyclostationary signals was developed during this effort. This detector (depicted in figure 6) uses magnitude-squared coherence (MSC) estimation as a measure of the spectral correlation in a signal. The use of MSC estimation allows the statistical behavior of the detector in a noise-only environment to be determined analytically and threshold values corresponding to desired false alarm probabilities to be computed [15, 16]. These capabilities represent a substantial improvement over similar cyclostationary detectors described in the research literature.

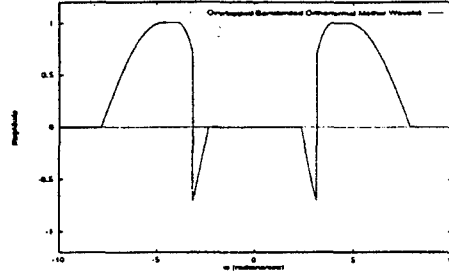


Figure 5: Example of an overlapped bandlimited orthonormal wavelet symbol $\hat{u}(\omega)$.

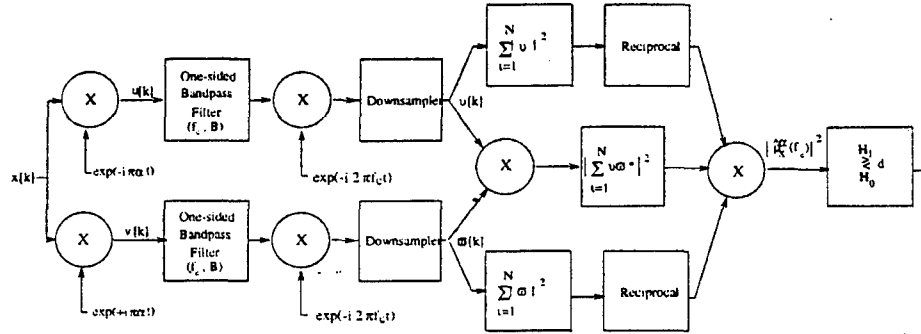


Figure 6: Discrete-time version of cyclostationary feature detector.

Receiver operating characteristic (ROC) curves for this detector against various types of cyclostationary communication signals have been determined by (i) using the analytical results to set detection a threshold for a particular false alarm probability, and then (ii) running computer simulations with signal present to estimate the corresponding detection probability. Performance results were obtained by applying the detector against standard communication signals (e.g., polar BPSK) and against some LPE-type communication signals, including direct sequence spread spectrum, transmitted reference spread spectrum, and SDMA signals. The case of SDMA signals was of particular interest in this project, and is discussed further below.

Consider an M -channel SDMA signal r described by

$$r(t) = \sum_{m=0}^{M-1} \sum_{k=-\infty}^{\infty} b_{m,k} \psi_k^m(t) \quad (9)$$

where $b_{m,k}$ represents the k^{th} bit on the m^{th} channel and ψ_k^m is k^{th} time-shifted replicate of the wavelet symbol ψ at dilation level m . The spectral correlation density (SCD) of such a SDMA signal

was found to be

$$S_x^\alpha(f) = \begin{cases} \frac{1}{T_0} \sum_{m=0}^{M-1} \sum_{k=-\infty}^{\infty} \hat{\psi}\left(\frac{f+\alpha/2}{2^m}\right) \hat{\psi}^*\left(\frac{f-\alpha/2}{2^m}\right) \delta\left(\alpha - \frac{n 2^m}{T_0}\right) & \alpha = \frac{p}{T_0} \\ 0 & \alpha \neq \frac{p}{T_0} \end{cases} \quad (10)$$

where $\hat{\psi}$ is the Fourier transform of ψ , f is the spectral frequency, α is the cyclic frequency, and T_0 is the fundamental bit period (i.e., the time shift required for orthonormality of the wavelet symbols at the lowest scale of dilation). This expression shows that the SCD of a SDMA signals will be non-zero only at cyclic frequencies that are integer multiples of $1/T_0$. This behavior, which has also been verified empirically, indicates that SDMA signals exhibit cyclostationary characteristics that can possibly be exploited for the purpose of signal detection.

The cyclostationary feature detector was applied to detect the presence of a SDMA signal in noise. A six-channel SDMA signal was used as the input signal for the single-cycle detector. The wavelet symbol used in the SDMA signal was the Daubechies-4 wavelet. An initial analysis was performed to determine at which values of α the spectral correlation density would be nonzero. It was found that the SCD had a strong component at $\alpha = 2^6/T_0$ and $f = 0$. The single-cycle detector was set to operate at these values of f and α . The number N of independent samples used in the correlations performed by the single-cycle detector was set to 32. The bandwidth of the single-sided bandpass filters was set to $1.28/T_0$. Simulations were run at three different SNR's: 0dB, 3dB and 9dB. One thousand outputs were used in obtaining the empirical cumulative distribution for each SNR setting. The ROC curves obtained by this procedure are shown in figure 7. These results suggest that SDMA signals are vulnerable, at least to some extent, to detection by cyclostationary methods.

Another detector for polycyclic signals based on generalized coherence estimation [7] has been defined and its application against various types of communications waveforms, including SDMA, is currently under investigation.

4.4 Generalized Wavelet Transforms

Work in connection with this project has led to consideration of how the continuous wavelet transform can be generalized to higher dimensions. Some mathematical results arising from this work and a connection with image analysis are summarized in this section.

Several multidimensional generalizations of the one-dimensional wavelet transform are currently. In the most widely known (and obvious) generalization, one-dimensional transforms are applied

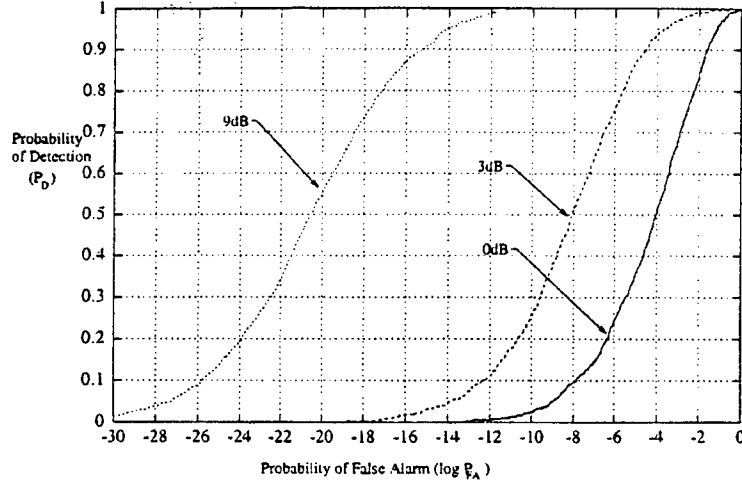


Figure 7: ROC curves for the single-cycle detector with a six-channel SDMA signal at its input.

separately in each orthogonal direction. In what follows, this will be referred to as the rectilinear wavelet transform; it is the method used by most wavelet-based image compression techniques. Another wavelet generalization is the two dimensional transform by Murenzi[37], literature on which can be more easily found in the paper by Antoine *et al.* [1]. Here, it will be called the circular wavelet transform, since it generalizes the dilations of the wavelet transform to the set of dilations and rotations on \mathbb{R}^2 . Neither of these generalizations encompasses the other. Thus, a question of interest is whether there is a stronger generalization that encompasses both. The remainder of this section describes a generalized wavelet transform that includes as special cases the one-dimensional, rectilinear, and circular wavelet transforms. Among the multidimensional wavelet transforms that arise from this approach are several that appear to be unknown in engineering applications. The circular wavelet transform is shown to arise as a result of the relationship between \mathbb{R}^2 and \mathbb{C} in the context of this generalization and is further shown to be strongly related to the cortex transform of Watson [54]. An implementation of the cortex transform from the circular wavelet transform is developed as an example of this relationship.

4.4.1 Theoretical development

Recall first the essentials of one-dimensional wavelet analysis, details of which can be found in [14]. With $a, b, x \in \mathbb{R}$, $h \in L^2(\mathbb{R})$, and \hat{h} the Fourier transform of h , define

$$[\Delta^{(a,b)}h](x) = \frac{1}{\sqrt{a}} h\left(\frac{x-b}{a}\right)$$

and

$$C_h = \int_{\mathbb{R}} \frac{|\hat{h}(x)|^2}{|x|} dx.$$

If C_h is finite, h is admissible. In this case, the reconstruction theorem states that any $f \in L^2(\mathbb{R})$ can be reconstructed from its wavelet coefficients $\langle f, \Delta^{(a,b)} h \rangle$ by the formula

$$f = \frac{1}{C_h} \int_{\mathbb{R}} \int_{\mathbb{R}} \frac{1}{a^2} \langle f, \Delta^{(a,b)} h \rangle \Delta^{(a,b)} h \, db \, da.$$

The rectilinear wavelet transform generalizes the one-dimensional transform to a separable multidimensional transform by letting $a, b, x \in \mathbb{R}^n$, i.e.,

$$a = \begin{bmatrix} a_1 \\ \vdots \\ a_n \end{bmatrix} \quad b = \begin{bmatrix} b_1 \\ \vdots \\ b_n \end{bmatrix} \quad x = \begin{bmatrix} x_1 \\ \vdots \\ x_n \end{bmatrix},$$

with the following alterations in the definitions and theorem:

$$[\Delta^{(a,b)} h](x) = \frac{1}{\sqrt{a_1 \cdots a_n}} h \left(\begin{bmatrix} \frac{x_1 - b_1}{a_1} \\ \vdots \\ \frac{x_n - b_n}{a_n} \end{bmatrix} \right)$$

$$C_h = \int_{\mathbb{R}^n} \frac{|\hat{h}(x)|^2}{|x_1 \cdots x_n|} dx$$

$$f = \frac{1}{C_h} \int_{\mathbb{R}^n} \int_{\mathbb{R}^n} \frac{1}{a_1^2 \cdots a_n^2} \langle f, \Delta^{(a,b)} h \rangle \Delta^{(a,b)} h \, db \, da.$$

This generalization is equivalent to taking the one-dimensional wavelet transform successively in each orthogonal direction of the multidimensional space. For $n = 1$, the rectilinear wavelet transform reduces to the one-dimensional wavelet transform.

An alternative generalization of the one-dimensional wavelet transform to \mathbb{R}^2 is the circular wavelet transform [1, 37], for which $a \in \mathbb{R}$ is replaced with the pair $(a, \theta) \in \mathbb{R} \times [0, 2\pi)$ and $b \in \mathbb{R}$ is replaced by $b = [b_1, b_2]^T \in \mathbb{R}^2$. Let r_θ denote the matrix which performs rotation in \mathbb{R}^2 by θ degrees. Then the definitions and theorem for circular wavelet analysis are

$$[\Delta^{(a,\theta,b)} h](x) = \frac{1}{a} h \left(a^{-1} r_{-\theta}(x - b) \right)$$

$$C_h = \int_{\mathbb{R}^2} \frac{|\hat{h}(x)|^2}{\|x\|^2} dx$$

$$f = \frac{1}{C_h} \int_{\mathbb{R}} \int_0^{2\pi} \int_{\mathbb{R}^2} \frac{1}{a^4} \langle f, \Delta^{(a,\theta,b)} h \rangle \Delta^{(a,\theta,b)} h \, a \, db \, d\theta \, da.$$

Clearly, the circular wavelet transform has a different character than the rectilinear wavelet transform on \mathbb{R}^2 . In particular, it allows non-separable wavelets in two dimensions and replaces independent dilation in each dimension by rotation and dilation simultaneously in both dimensions. Despite their distinct characters, both the rectilinear and circular wavelet transforms arise as special cases of a more general multidimensional wavelet transform, the formulation of which is based on ring multiplications on \mathbb{R}^2 .

Consider \mathbb{R}^n as a vector space over the field \mathbb{R} . If a ring multiplication "o" is introduced to \mathbb{R}^n so that \mathbb{R}^n becomes an algebra under the multiplication then there is, for each $a \in \mathbb{R}^n$, a left regular representation $L_a : \mathbb{R}^n \rightarrow \mathbb{R}^n$ defined by $L_a x = a \circ x$. There is also an associated linear operator $S_x : \mathbb{R}^n \rightarrow \mathbb{R}^n$ defined by $S_x a = L_a^T x$. Suppose the ring multiplication has the property that the set of elements with ring inverses are dense in \mathbb{R}^n . Then, with $h \in L^2(\mathbb{R}^n)$ and $a, b, x \in \mathbb{R}^n$, the following definitions and theorem form the mathematical foundation of a generalized multidimensional wavelet analysis:

$$\begin{aligned} \left[\Delta^{(a,b)} h \right] (x) &= \frac{1}{\sqrt{|\det L_a|}} h(L_a^{-1}(x - b)), \\ C_h &= \int_{\mathbb{R}^n} \frac{|\hat{h}(x)|^2}{|\det S_x|} dx, \\ f &= \frac{1}{C_h} \int_{\mathbb{R}^n} \int_{\mathbb{R}^n} \frac{1}{|\det L_a|^2} \langle f, \Delta^{(a,b)} h \rangle \Delta^{(a,b)} h \, db \, da. \end{aligned}$$

As examples of this, suppose the ring multiplication on \mathbb{R}^n is defined by

$$\begin{bmatrix} a_1 \\ \vdots \\ a_n \end{bmatrix} \circ \begin{bmatrix} b_1 \\ \vdots \\ b_n \end{bmatrix} = \begin{bmatrix} a_1 b_1 \\ \vdots \\ a_n b_n \end{bmatrix}$$

then L_a and S_a are the diagonal matrices defined by $L_a = S_a = \text{diag}(a_1, a_2, \dots, a_n)$. This makes the generalized definitions and theorem equivalent to the definitions and theorem of rectilinear wavelet analysis. Since rectilinear wavelet analysis with $n = 1$ is the same as one-dimensional wavelet analysis, both one-dimensional wavelet analysis and rectilinear wavelet analysis arise as special cases of this formulation.

Similarly, circular wavelet analysis comes from the ring multiplication "o" on \mathbb{R}^2 defined by

$$\begin{bmatrix} a_1 \\ a_2 \end{bmatrix} \circ \begin{bmatrix} b_1 \\ b_2 \end{bmatrix} = \begin{bmatrix} a_1 b_1 - a_2 b_2 \\ a_1 b_2 + a_2 b_1 \end{bmatrix}.$$

This ring multiplication is same as the multiplication of the complex numbers. In this case

$$L_a = \begin{bmatrix} a_1 & -a_2 \\ a_2 & a_1 \end{bmatrix} = |a| r_{L_a},$$

$$S_x = \begin{bmatrix} x_1 & x_2 \\ x_2 & -x_1 \end{bmatrix},$$

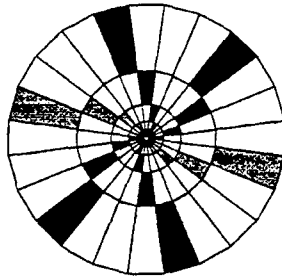
and the generalized definitions and reconstruction theorem become equivalent to the definitions and reconstruction theorem of circular wavelet analysis.

4.4.2 Connection to the cortex transform

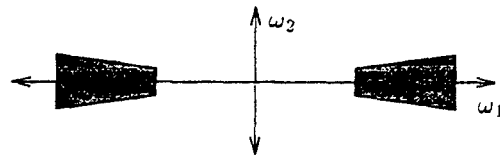
Circular wavelet analysis has fundamental variables of scale (which corresponds to logarithmic frequency), rotation, and two-dimensional positional shift. These correspond to the basic organization of Watson's cortex transform[54], which was devised as a means to process images in a similar way to the processing in the human visual cortex. Hence there is a relationship between the circular wavelet transform, the cortex transform, and image processing in the human visual cortex. It is shown here that this relationship can be strengthened by actually deriving the cortex transform from the circular wavelet transform.

The cortex transform was implemented by Watson by partitioning the frequency domain into separate angularly oriented regions at logarithmically spaced frequency steps, bandlimiting the image to each region, and sampling the bandlimited pieces as efficiently as possible using available techniques from sampling theory.

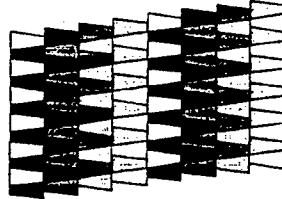
Following a similar procedure, the frequency domain can be divided according to the figure below, where zero frequency is in the center:



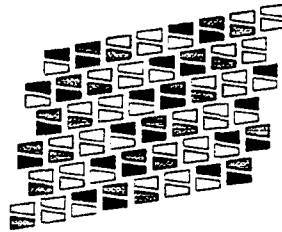
This division corresponds to a discrete sampling of the frequency and rotation variables of the circular wavelet transform. In order to bandlimit the image to a given region, the "mother wavelet" h is chosen so that its Fourier transform \hat{h} is the characteristic function a *bin*, which consists of two opposing frequency regions as shown below:



Once the image is bandlimited to a bin, positional samples are used to represent the bandlimited function. These positional samples produce frequency replications. Aliasing is avoided by preventing these frequency replications from overlapping. An example of an optimal sampling for a bin is shown below.



This frequency replication pattern is according to theory the optimally efficient replication that avoids aliasing, but in practice aliasing is not avoided due to filter imperfections. Thus, it is often desirable to introduce a controlled amount of inefficiency in order to reduce aliasing. In this case, the frequency replication pattern looks more like this:



The efficiency of this sampling is controlled, so it is easy to make it more efficient than the fixed efficiency sampling proposed by Watson.

Preliminary results show that the transform adequately represents an image and reconstructs it from its representation (figure 8). In order to obtain these results, special consideration must be paid to preserving frequencies near zero, since the transform has a singularity there. It is also crucial that the image be of relatively large size (at least 256×256 pixels), since the processing assumes an image is continuous, and the violation of this assumption by a coarsely sampled image introduces significant artifacts.

5 Personnel Supported

Personnel contributing to this research effort were:

- D. Cochran, Principal Investigator
- S. Enserink, Research Assistant



Figure 8: The Leena image (left) and the result after it has been decomposed and reconstructed by the transform (right).

- S. Han, research Assistant
- R. Martin, Research Associate
- D. Sinno, Research Assistant
- C. Wei, Research Assistant

The research component of the following graduate degrees were sponsored or partially sponsored under this project:

1. C. Wei, Master of Science in Electrical Engineering, May 1993. Thesis: *Scale-Division Multiple Access*
2. S. Enserink, Master of Science in Electrical Engineering, May 1994. Thesis: *A Cyclostationary Feature Detector*
3. R. Martin, Doctor of Philosophy in Electrical Engineering, December 1994. Dissertation: *Multidimensional Wavelet Transforms and an Application to Image Processing.*

6 Related Publications

6a. Papers published

[6a-1] C. Wei and D. Cochran, "Construction of Discrete Orthogonal Wavelet Bases," *Record of the IEEE International Symposium on Information Theory*, San Antonio, January 1993.

[6a-2] C. Wei and D. Cochran, "Bandlimited Orthogonal Wavelet Symbols" (Invited paper), *Proceedings of the 27th Annual Asilomar Conference on Signals, Systems, and Computers*, Pacific Grove, California, November 1993.

[6a-3] C. Wei and D. Cochran, "A Wavelet-Based Multiple Access Spread Spectrum Modulation Scheme," *Proceedings of the IEEE International Phoenix Conference on Computers and Communications*, April 1994.

[6a-4] D. Cochran and C. Wei, "Wavelet-based spread spectrum communications," (Invited paper) *Proceedings of the IEEE Dual-Use Technologies and Applications Conference*, vol. II, pp. 392-401, Utica NY, May 1994.

[6a-5] S. Enserink and D. Cochran, "A Cyclostationary Feature Detector," *Proceedings of the 28th Annual Asilomar Conference on Signals, Systems, and Computers*, Pacific Grove, California, October 1994.

[6a-6] R. Martin and D. Cochran, "Generalized Wavelet Transforms and Cortical Filtering," *Proceedings of the 28th Annual Asilomar Conference on Signals, Systems, and Computers*, Pacific Grove, California, October 1994.

[6a-7] D. Cochran, "Review of Cyclostationarity in Communications and Signal Processing," (Invited book review) *Proceedings of the IEEE*, vol. 82, no. 10, October 1994.

[6a-8] S. Han and D. Cochran, "Orthonormal Bases of Bandlimited Wavelets with Frequency Overlap," *Proceedings of the IEEE International Conference on Acoustics, Speech, and Signal Processing*, vol. 3, pp. 1541-1543, Detroit, May 1995.

[6a-9] S. Enserink and D. Cochran, "On Detection of Cyclostationary Signals," *Proceedings of the IEEE International Conference on Acoustics, Speech, and Signal Processing*, vol. 3, pp. 2004-2007, Detroit, May 1995.

[6a-10] D. Cochran, H. Gish, and D. Sinno, "A Geometric Approach to Multiple-Channel Signal Detection," *IEEE Transactions on Signal Processing*, vol. SP-43(9), September 1995.

6b. Papers accepted for publication

[6b-1] D. Cochran and J.J. Clark, "Time-Warped Bandlimited Functions: Sampling, Bandlimit-ness, and Uniqueness of Representation," To appear in: *SIAM Journal on Applied Mathematics*.

[6b-2] A. Clausen and D. Cochran, "An Invariance Property of the Generalized Coherence Estimate," To appear in: *IEEE Transactions on Signal Processing*.

6c. Recent submissions

[6c-1] A. Clausen and D. Cochran, "Generalized Coherence: Invariance of Estimate to Distribution of One Channel," Submitted to the 30th Asilomar Conference on Signals, Systems, and Computers, November 1996.

[6c-2] L.L. Scharf and D. Cochran, "On the Distribution of Linear Prediction Error," Submitted to the 30th Asilomar Conference on Signals, Systems, and Computers, November 1996.

[6c-3] J.Q. Trelewicz and D. Cochran, "A Sampling Approach to Bandlimited Instantaneously Companded Signals," Submitted to the 30th Asilomar Conference on Signals, Systems, and Computers, November 1996.

6d. Other related publications

[6d-1] D. Cochran, "Review of *Cyclostationarity in Communications and Signal Processing*," (Invited review) in *IEEE Communications Magazine*, vol. 32, no. 4, April 1994. Also in *Proceedings of the IEEE*, October 1994.

7 Interactions/Transitions

7a. Meetings, Conferences, and Seminars

Numerous university and industrial colloquium presentations have been presented on the research performed in this project. These include:

- D. Cochran presented a talk entitled "Wavelet-Based Multiple-Access Spread Spectrum" in the Motorola Government Systems and Technologies Group Signal Processing Series [16 attendees] in March 1993.
- D. Cochran presented a talk entitled "Detection of Cyclostationary and Polycyclostationary Signals" at the DSP group meeting at MIT [17 attendees] in October 1994. During the same visit, he met with A. Willsky, C. Karl, and R. Learned to exchange ideas on wavelet and wavelet-packet methods in spread spectrum.
- D. Cochran presented a talk entitled "Multidimensional Wavelet Generalizations and Watson's Cortex Transform" in the Vision Seminar at Harvard [25 attendees] in September 1994.
- D. Cochran presented a talk entitled "Wavelet Applications in Communications" in a seminar

sponsored jointly by the DSP and Communications groups at Georgia Tech [45 attendees] in October 1994.

In addition, D. Cochran participated in the following conference activities related to the topic of this project:

- He organized and chaired an invited session entitled "Applications of Wavelets and Chaotic Signals in Communications" at the Asilomar Conference on Signals, Systems, and Computers in November 1993. Participants included R. Orr (Atlantic Aerospace), S. Isabelle (MIT), M. Motamed and A. Zakhor (UC Berkeley), C. Wei (Arizona State University), and J.S. Goldstein (USAF and Georgia Tech).
- He was a keynote speaker (with J.J. Benedetto, M.V. Wickerhauser, and W. Sweldens) at a wavelet applications workshop in Melbourne, Australia in February 1995. The topic of this presentation was wavelet applications in communication systems.
- He is scheduled to be plenary speaker (with L. Cohen) at the ANZIS-96 Conference in November 1996.

7b. Consultive and Advisory Functions

During this project, D. Cochran consulted informally with J. Stephens at Wright Laboratory and with Capt. J.S. Goldstein and Dr. A. Lindsey of Rome Laboratory on applications of wavelets and cyclostationary signal processing in covert communications and countermeasures. He has also been collaborating with the Centre for Signal and Information Processing Research (CSSIP) and the Defence Science and Technology Organization (DSTO) in Australia on wavelet applications in communications and other topics.

7c. Transitions

None.

8 New Discoveries

No inventions or patent disclosures have resulted from this research program.

9 Honors/Awards

None.

References

- [1] R.M.J.P. Antoine, P. Carrette and B. Piette, "Image analysis with two-dimensional continuous wavelet transform," *Signal Processing*, vol. 31, pp. 241-272, 1993.
- [2] F. Argenti, H. Benelli, and A. Mecocci, "Source coding and transmission of HDTV images with the wavelet transform," *IEEE Journal on Selected Areas in Communications*, vol. 11(1), January 1993.
- [3] R.G. Baraniuk and D.L. Jones, "Warped wavelet bases: Unitary equivalence and signal processing," *Proceedings of the IEEE International Conference on Acoustics, Speech, and Signal Processing*, vol. 3, pp. 320-323, 1993.
- [4] R.G. Baraniuk and D.L. Jones, "Shear madness: New orthonormal bases and frames using chirp functions," *IEEE Transactions on Signal Processing*, vol. 41, no. 12, pp. 3543-3549, December 1993.
- [5] S.A. Benno and J.M.F. Moura, "Shiftable representations and multipath processing," *Proceedings of the IEEE-SP International Symposium on Time-Frequency and Time-Scale Analysis*, October 1994.
- [6] A. Bonami, F. Soria, and G. Weiss, "Band-limited wavelets," *Journal of Geometric Analysis*, vol. 3, pp. 543-577, 1993.
- [7] D. Cochran, H. Gish, and D. Sinno, "A geometric approach to multiple-channel signal detection," *IEEE Transactions on Signal Processing*, to appear.
- [8] D. Cochran and C. Wei, "Scale based coding of digital communication signals," *Proceedings of the IEEE-SP International Symposium on Time-Frequency and Time-Scale Analysis*, October 1992.
- [9] D. Cochran and C. Wei, "Wavelet-based spread spectrum communications," *Proceedings of the IEEE Dual-Use Technologies and Applications Conference*, vol. II, pp. 392-401, Utica NY, May 1994.

- [10] D. Cochran and C. Wei, "Wavelet-based spread spectrum communications," *Proceedings of the IEEE Dual-Use Technologies and Applications Conference*, vol. II, pp. 392-401, Utica NY, May 1994.
- [11] F. Daneshgaran and M. Mondin, "Coded modulation and frequency-hopped CDMA with wavelets," *Proceedings of the IEEE Military Communications Conference (MILCOM-95)*, pp. 896-900, San Diego, 1995.
- [12] F. Daneshgaran and M. Mondin, "Synchronous frequency-hopped CDMA using wavelets," *Record of the IEEE International Symposium on Information Theory*, Whistler BC, 1995.
- [13] F. Daneshgaran and M. Mondin, "Wavelets and scaling functions as envelope waveforms for modulation," *Proceedings of the IEEE-SP International Symposium on Time-Frequency and Time-Scale Analysis*, pp. 397-400, October 1994.
- [14] I. Daubechies, *Ten Lectures on Wavelets*. SIAM Press, 1992.
- [15] S. Enserink and D. Cochran, "A Cyclostationary Feature Detector," *Proceedings of the 38th Annual Asilomar Conference on Signals, Systems, and Computers*, Pacific Grove, California, November 1994.
- [16] S. Enserink and D. Cochran, "On Detection of Cyclostationary Signals," To appear in: *Proceedings of the IEEE International Conference on Acoustics, Speech, and Signal Processing*, Detroit, April 1995.
- [17] N. Erdol and F. Basbug, "Use of the wavelet transform in optimal receiver design," *Applied Optics*, vol. 33(23), August 1994.
- [18] N. Erdol, F. Bao, and Z. Chen, "Wavelet modulation: A prototype for digital communication systems," *Proceedings of the 1995 Southcon Conference*, pp. 168-171, Fort Lauderdale, 1995.
- [19] N. Erdol and F. Bao, "Wavelet transform based optimal receivers," *Proceedings of the 27th Asilomar Conference on Signals, Systems and Computers*, vol. 2, pp. 916-919, November 1993.
- [20] P.P. Gandhi, S.S. Rao and R.S. Pappu, "On waveform coding using wavelets," *Proceedings of the 27th Asilomar Conference on Signals, Systems and Computers*, vol. 2, pp. 901-905, November 1993.

- [21] P.P. Gandhi, S.S. Rao and R.S. Pappu, "Wavelets for baseband coding of waveforms," *Proceedings of the Global Communications Conference (GLOBECOM-94)*, San Francisco, November 1994.
- [22] H. Gish and D. Cochran, "Invariance of magnitude-squared coherence estimate with respect to second-channel statistics," *IEEE Transactions on Acoustics, Speech, and Signal Processing*, vol. ASSP-35, no. 12, pp. 1774-1776, December 1987.
- [23] S. Han and D. Cochran, "Orthonormal Bases of Bandlimited Wavelets with Frequency Overlap," To appear in: *Proceedings of the IEEE International Conference on Acoustics, Speech, and Signal Processing*, Detroit, April 1995.
- [24] K. Hetling, M. Medley, G. Saulnier, and P. Das, "A PR-QMF (wavelet) based spread spectrum communications system," *Proceedings of the IEEE Military Communications Conference (MILCOM-94)*, Long Branch NJ, October 1994.
- [25] W.W. Jones, "Multi-scale wavelet modulation," *Proceedings of the 26th Southeastern Symposium on System Theory*, pp. 576-580, Athens Ohio, March 1994.
- [26] R.E. Learned, H. Krim, B. Claus, A.S. Willsky, and W.C. Karl, "Wavelet-packet-based multiple access communication," *Proceedings of the SPIE International Symposium on Optics, Imaging, and Instrumentation - Mathematical Imaging: Wavelet Applications in Signal and Image Processing*, pp. 2303-2320, July 1994.
- [27] R.E. Learned, H. Krim, B. Claus, A.S. Willsky, and W.C. Karl, "Wavelet-packet-based multiple access communication," *Proceedings of the SPIE International Symposium on Optics, Imaging, and Instrumentation - Mathematical Imaging: Wavelet Applications in Signal and Image Processing*, pp. 2303-2320, July 1994.
- [28] R.E. Learned, S. Mallat, B. Claus, and A.S. Willsky, "Geometric interpretation of multiaccess joint detection and the alternating projection algorithm," To appear in *Proceedings of the IEEE International Conference on Acoustics, Speech, and Signal Processing*, Detroit, April 1995.
- [29] Y.-C. Lin and C.-C.J. Kuo, "Modulation classification using wavelet transform," *SPIE Proceedings No. 2303: Wavelet Applications*, pp. 260-271, July 1994.
- [30] M.J. Lyall, S.S. Rao, and P.P. Gandhi, "Wavelets and waveform coding: Extensions and new results," *SPIE Proceedings — Wavelet Applications*, vol. 2303, pp. 177-188, July 1994.

- [31] H. Maeda, T. Kitagawa, and S. Kodama, "Identification of Impulse Responses by Wavelet Transform," *Electronics and communications in Japan*, Part 3, vol. 77, no. 4, p. 81, April 1994.
- [32] R. Martin and D. Cochran, "Generalized Wavelet Transforms and Cortical Filtering," *Proceedings of the 28th Annual Asilomar Conference on Signals, Systems, and Computers*, Pacific Grove, California, November 1994.
- [33] M. Medley, G. Saulnier, and P. Das, "Applications of the wavelet transform in spread spectrum communications systems," *SPIE Proceedings — Wavelet Applications*, vol. 2242, pp. 54-68, April 1994.
- [34] M.J. Medley, P.K. Das, and G.J. Saulnier, "Applications of discrete wavelet transform excision to spread spectrum signals," *Proceedings of the NJIT Symposium on Applications of Subbands and Wavelets*, March 1994.
- [35] M. Medley, G.J. Saulnier, and P. Das, "Radiometric detection of direct-sequence spread spectrum signals with interference excision using the wavelet transform" *Proceedings of the IEEE International Conference on Communications (ICC-94)*, New Orleans, May 1994.
- [36] M. Mettke, M.J. Medley, G.J. Saulnier, and P. Das, "Wavelet transform excision using IIR filters in spread spectrum communication systems," *Proceedings of the Global Telecommunications Conference (GLOBECOM-94)*, vol. 3, pp. 1627-1631, San Francisco, November 1994.
- [37] R. Murenzi, *Ondelettes multidimensionnelles et applications à l'analyse d'images*. Ph.D. Thesis, IPT Louvain La Neuve, Belgium, 1990.
- [38] R.S. Orr, C. Pike, M. Bates, "Multiple access communications using wavelet technology," *SPIE Proceedings No. 2491 — Wavelet Applications for Dual Use*, April 1995.
- [39] R.S. Orr, C. Pike, and M.J. Lyall, "Wavelet transform domain communications," *SPIE Proceedings No. 2491 — Wavelet Applications for Dual Use*, April 1995.
- [40] R.S. Orr, C. Pike, M. Tzannes, S. Sandberg, and M. Bates, "Covert communications employing wavelet technology," *Proceedings of the 27th Asilomar Conference on Signals, Systems, and Computers*, vol. 1, pp. 523-527, November 1993.
- [41] H.S. Ptasinski and R.D. Fellman, "Implementation and simulation of a fractal modulation communication system," *Proceedings of the IEEE International Conference on Communications*, pp. 1551-1555, 1994.

- [42] H.S. Ptasinski and R.D. Fellman, "Performance analysis of a fractal communication system," *SPIE Proceedings — Wavelet Applications*, vol. 2242, April 1994.
- [43] S.S. Rao, M.J. Lyall, and P.P. Gandhi, Biorthogonal wavelets for waveform coding in BPSK and QPSK systems, *Proceedings of the 26th Southeastern Symposium on System Theory*, pp. 590-594, Athens Ohio, March 1994.
- [44] H. Resnikoff *et al.*, "Novel spread spectrum CODEC apparatus and method," U.S. Patent No. 5081645, January 1992.
- [45] S.D. Sandberg, M.A. Tzannes, P.N. Heller, R.S. Orr, C.M. Pike, and M.L. Bates, "A family of wavelet-related sequences as a basis for an LPI/D communications system prototype," *Proceedings of the IEEE Military Communications Conference (MILCOM-93)*, vol. 2, pp. 537-542, October 1993.
- [46] B.W. Suter and M.E. Oxley, "On variable overlapped windows and weighted orthonormal bases," *IEEE Transactions on Signal Processing*, vol. 42, no. 8, pp. 1973-1982, August 1994.
- [47] M.V. Tazebay, A.N. Akansu, and M. Sherman, "A novel adaptive time-frequency technique for direct-sequence spread spectrum communications," *Proceedings of the IEEE-SP International Symposium on Time-Frequency and Time-Scale Analysis*, October 1994.
- [48] M.K. Tsatsanis and G.B. Giannakis, "Time-varying system identification and model validation using wavelets," *IEEE Transactions on Signal Processing*, vol. ASSP-41(12), pp. 3512-3523, December 1993.
- [49] M.A. Tzannes and M.C. Tzannes, "Bit-by-bit channel coding using wavelets," *Proceedings of the Global Telecommunications Conference (GLOBECOM-92)*, vol. 2, pp. 684-688, Orlando FL, December 1992.
- [50] M.A. Tzannes and M.C. Tzannes, "Block biorthogonal channel coding using wavelets," *Proceedings of the IEEE Military Communications Conference (MILCOM-92)*, October 1992.
- [51] A.B. Watson, "Efficiency of a Model Human Image Code," *Journal of the Optical Society of America A*, vol. 4, no. 12, pp. 2401-2417, December 1987.
- [52] C. Wei, *Scale-Division Multiple Access*. M.S. Thesis, Arizona State University, May 1993.
- [53] C. Wei and D. Cochran, "Bandlimited orthogonal wavelet symbols," *Proceedings of the 27th Asilomar Conference on Signals, Systems, and Computers*, vol. 1, pp. 528-532, November 1993.

- [54] A.B. Watson, "Efficiency of a model human image code," *Journal of the Optical Society of America A*, vol. 4, pp. 2401-2417, December 1987.
- [55] G.W. Wornell, "Communication over fractal channels," *Proceedings of the IEEE International Conference on Acoustics, Speech, and Signal Processing*, vol. 3, pp. 1945-1948, May 1991.
- [56] G.W. Wornell, "Emerging applications of multirate signal processing and wavelets in digital communications," *Proceedings of the IEEE*, vol. 84(4), pp. 586-603, April 1996.
- [57] G.W. Wornell, *Synthesis, Analysis, and Processing of Fractal Signals*. Ph.D. Thesis, Massachusetts Institute of Technology, October 1991.
- [58] G.W. Wornell and A.V. Oppenheim, "Wavelet-based representations for a class of self-similar signals with application to fractal modulation," *IEEE Transactions on Information Theory*, vol. IT-38(2), pp. 785-800, March 1992.
- [59] C.J. Zarowski, "Spectral characteristics and computation of wavelets for fractal modulation," *Proceedings of the Pacific Rim Conference on Communications, Computation, and Signal Processing*, Victoria BC, 1993.

DOCUMENT 2

Direct Write Scene Generation Development Efforts for Closed-Loop Evaluation of Focal Plane Arrays

AD-A309 670

May 1996

**Arnold Engineering Development Center
Arnold Air Force Base, TN**

AEDC-TR-95-34



Direct Write Scene Generation Development Efforts for Closed-Loop Evaluation of Focal Plane Arrays

S. L. Steely, R. H. Fugerer, H. S. Lowry, III, and L. L. Holt
Sverdrup Technology, Inc., AEDC Group

May 1996

Final Report for Period 1 October 1994 - 30 September 1995

Approved for public release; distribution is unlimited.

**ARNOLD ENGINEERING DEVELOPMENT CENTER
ARNOLD AIR FORCE BASE, TENNESSEE
AIR FORCE MATERIEL COMMAND
UNITED STATES AIR FORCE**

NOTICES

When U. S. Government drawings, specifications, or other data are used for any purpose other than a definitely related Government procurement operation, the Government thereby incurs no responsibility nor any obligation whatsoever, and the fact that the Government may have formulated, furnished, or in any way supplied the said drawings, specifications, or other data, is not to be regarded by implication or otherwise, or in any manner licensing the holder or any other person or corporation, or conveying any rights or permission to manufacture, use, or sell any patented invention that may in any way be related thereto.

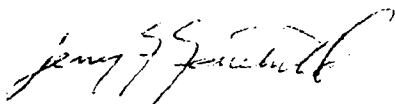
Qualified users may obtain copies of this report from the Defense Technical Information Center.

References to named commercial products in this report are not to be considered in any sense as an endorsement of the product by the United States Air Force or the Government.

This report has been reviewed by the Office of Public Affairs (PA) and is releasable to the National Technical Information Service (NTIS). At NTIS, it will be available to the general public, including foreign nations.

APPROVAL STATEMENT

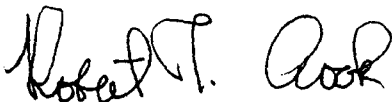
This report has been reviewed and approved.



JERRY F. FAIRCHILD, Capt. USAF
Facility and Instrumentation Technology
Applied Technology Division
Test Operations Directorate

Approved for publication:

FOR THE COMMANDER



ROBERT T. CROOK
Deputy Director of Technology
Deputy of Operations

| REPORT DOCUMENTATION PAGE | | | Form Approved OMB No. 0704-0188 | |
|--|---|---|--|--|
| Public reporting burden for this collection of information is estimated to average 1 hour per response, including the time for reviewing instructions, searching existing data sources, gathering and maintaining the data needed, and completing and reviewing the collection of information. Send comments regarding this burden estimate or any other aspect of this collection of information, including suggestions for reducing this burden, to Washington Headquarters Services, Directorate for Information Operations and Reports, 1215 Jefferson Davis Highway, Suite 1204, Arlington, VA 22202-4302, and to the Office of Management and Budget, Paperwork Reduction Project (0704-0188), Washington, DC 20503. | | | | |
| 1. AGENCY USE ONLY (Leave blank) | 2. REPORT DATE May 1996 | 3. REPORT TYPE AND DATES COVERED Final Report for Period October 1994 - September 1995 | | |
| 4. TITLE AND SUBTITLE Direct Write Scene Generation Development Efforts for Closed-Loop Evaluation of Focal Plane Arrays | | 5. FUNDING NUMBERS PE - 65807F PN - 0103 | | |
| 6. AUTHOR(S) Steely, S. L., Fugerer, R. H., Lowry, H. S. III, and Holt, L. L., Sverdrup Technology, Inc., AEDC Group | | | | |
| 7. PERFORMING ORGANIZATION NAME(S) AND ADDRESS(ES) Arnold Engineering Development Center/DOT Air Force Materiel Command Arnold Air Force Base, TN 37389-9011 | | 8. PERFORMING ORGANIZATION (REPORT NUMBER) AEDC-TR-95-34 | | |
| 9. SPONSORING/MONITORING AGENCY NAME(S) AND ADDRESS(ES) Arnold Engineering Development Center/DOT Air Force Materiel Command Arnold Air Force Base, TN 37389-9011 | | 10. SPONSORING/MONITORING AGENCY REPORT NUMBER | | |
| 11. SUPPLEMENTARY NOTES Available in Defense Technical Information Center (DTIC). | | | | |
| 12A. DISTRIBUTION/AVAILABILITY STATEMENT Approved for public release; distribution is unlimited. | | | 12B. DISTRIBUTION CODE | |
| 13. ABSTRACT (Maximum 200 words) Laser-based closed-loop Direct Write Scene Generation (DWSG) methods are being developed at AEDC to simulate dynamic sensor operations and complex infrared scenes. New photonic image-synthesis methods are being developed to employ image-to-object Whittaker-Shannon sampling, anisoplanatic optical convolution by quasi-isoplanatic spatial decomposition, and high-speed digital electronics for acousto-optic modulation. Because of the large terabyte volume of data to be processed, the increased bandwidth requirements, and the increased simulation fidelity required for DT&E and OT&E of focal plane array sensors, the laser-based DWSG methodology is being extended to accommodate optical and computational decomposition methods to better exploit highly and massively parallel real-time image-processing schemes. Optical and computational decomposition will not only provide high-fidelity optical simulation for anisoplanatic optical sensors and complex infrared scenes, but will also facilitate high-speed parallel-processing schemes for real-time closed-loop DWSG and sensor operations. A computer simulation has been constructed and is being used to develop and evaluate the high-speed computational algorithms required for scene extraction and convolutions. A Proof-of-Principle demonstration using existing DWSG hardware also illustrated the feasibility of the concept. This technology effort helps to establish and provide new focal plane array optical diagnostics for cost-effective and systematic DT&E and OT&E of large FPA sensors using parametric and statistical methods not amenable to costly field or flight testing methods. | | | | |
| 14. SUBJECT TERMS sensors, test and evaluation, closed-loop, real-time, surveillance, seeker, simulations, focal plane array, DWSG, laser testing, noise | | | 15. NUMBER OF PAGES 50 | |
| | | | 16. PRICE CODE | |
| 17. SECURITY CLASSIFICATION OF REPORT UNCLASSIFIED | 18. SECURITY CLASSIFICATION OF THIS PAGE UNCLASSIFIED | 19. SECURITY CLASSIFICATION OF ABSTRACT UNCLASSIFIED | 20. LIMITATION OF ABSTRACT SAME AS REPORT | |

COMPUTER GENERATED

Standard Form 298 (Rev. 2/89)
Prescribed by ANSI Std. Z39.18

PREFACE

The work reported herein was conducted by the Arnold Engineering Development Center (AEDC), Air Force Materiel Command (AFMC), under Program Element 65807F. The results were obtained by Micro Craft Technology, technical services contractor at AEDC, Arnold Air Force Base, TN 37389-4300 under AEDC Job Number 0103. The Air Force Project Manager was Capt. Frank Fairchild, AEDC/DOT. Although the project comprises several work phases described in different technical reports, this technical report describes and primarily focuses on the Closed-Loop Direct Write Scene Generation (CLDWSG) project efforts initiated on October 1, 1994 and completed on September 30, 1995. This manuscript was approved for publication on March 1, 1996.

CONTENTS

| | <u>Page</u> |
|--|-------------|
| 1.0 INTRODUCTION | 7 |
| 2.0 SENSOR MISSION AND SOURCE RADIATION ISSUES | 8 |
| 3.0 DWSG OPERATIONAL DESCRIPTION | 9 |
| 4.0 BACKGROUNDS, TARGETS, AND SENSOR SIMULATION CONCEPTS | 10 |
| 4.1 Radiation Sources | 10 |
| 4.2 Sensor Viewing Considerations | 11 |
| 4.3 Optical Effects and Imaging | 11 |
| 4.4 Anisoplanatic Optical Systems | 13 |
| 5.0 CLDWSG CONFIGURATION SELECTION METHODOLOGY | 14 |
| 6.0 INITIAL CLDWSG IMPLEMENTATION EFFORTS | 16 |
| 7.0 PROOF-OF-PRINCIPLE CLDWSG DEMONSTRATION EFFORTS | 18 |
| 8.0 CONCLUDING REMARKS | 19 |
| REFERENCES | 19 |

ILLUSTRATIONS

| <u>Figure</u> | <u>Page</u> |
|---|-------------|
| 1. Sensor Testing and Evaluation Diagram Illustrating Closed-Loop DWSG Development | 21 |
| 2. Illustration of the Laser-Based Direct-Write Scene Generation Methodology for Focal Plane Array Diagnostics and Scene-Generation Schemes | 22 |
| 3. Laser-Based Direct-Write Scene Generation Methods for Photocharacterization and Evaluation of Focal Plane Array Sensor Systems | 22 |
| 4. DWSG Operation for Laser-Based Photonics Illustrating the Resolvable Spots for Sub-pixel Irradiation at Twice the Rayleigh Resolution | 23 |
| 5. Potential Noise Sources for DWSG Photonics and FPA Operation | 23 |
| 6. Normal Airy Pattern for $T = 0.0$ | 24 |
| 7. FPA DWSG Laser-Beam Irradiance Pattern for Truncation Ratios $T = 0, 1.0$, and 1.5 ... | 24 |
| 8. FPA DWSG Laser-Beam Irradiance Pattern for Truncation Ratios $T = 0, 2.0, 2.5$, and 3.5 | 24 |
| 9. Percent Encircled Energy for a Radius Set at the $1/e^2$ Irradiance Level | 24 |
| 10. FPA Laser-Beam Irradiance Spot Size for Various Encircled Energies | 24 |
| 11. Sensor View of Earth for Above- and Below-the-Horizon Perspectives Require Quite Different Databases for Simulation of Real-World Background and Target Engagements and Related Phenomena Exploited for Efficient Detection, Discrimination, and Tracking | 25 |
| 12. Multisensor Perspective and Simulation will Depend on Mission as Well as on Environmental and Operational Characteristics | 26 |
| 13. Illustration of Methodology to View Backgrounds and Targets for Relative Coordinate Systems from a Space-Based Sensor in an Earth Orbit | 27 |
| 14. Illustration of a 3D-to-2D Spatial Mapping of Space-Based Backgrounds and Targets onto the FPA for DWSG Optical Simulation Efforts | 28 |

| <u>Figure</u> | <u>Page</u> |
|--|-------------|
| 15. Concept Illustration of the Scene being Mapped onto the FPA, Which Could also be Usefully Viewed as the FPA Field of View being Mapped onto the 2-D Projection of the Background and Target Scene | 29 |
| 16. Illustration of the Object Plane being Transformed to the Image Plane for FPA Irradiation via the Optical System for a Simple Background and Target Map | 30 |
| 17. Different Concepts and Methods for Computing the PSF or the OTF for either Direct Convolution Methods or OTF Methods of Determining and Simulating a Sensor's Imaging Properties | 31 |
| 18. Optical Convolution can be Accomplished by either Direct Methods or by Indirect FFT Methods Using the Convolution Theorem and the OTF of the Sensor System (The Method Chosen Depends on Computational/Photonic Speed as well as Fidelity Issues/Trades) | 31 |
| 19. Background, Target, and FPA Sampling Provide Efficient and Flexible Computational Schemes for Scene Extraction and Image Convolution by Employing Whittaker-Shannon Sampling Ideas. | 32 |
| 20. Illustration of a Spatial Decomposition Method to Support Anisoplanatic Optical Simulation that Could also Support Parallel and Massively Parallel Processing Schemes for the Laser-Based DWSG Photonics | 32 |
| 21. Illustration of a 4 x 4 Optical Decomposition to Support Parallel Processing Schemes and Anisoplanatic Optical Simulation without any Regard for Diffraction Effects/Loss, Spectral Leakage, etc. | 33 |
| 22. Illustration of Potential Simulation Artifacts that can Result from Decomposition Methods that Fail to Account for Diffraction Effects, Spectral Leakage, etc. | 33 |
| 23. Methodology for Using Extended Computational Regions to not only Support Anisoplanatic Decomposition for Better Fidelity and Simulation, but to also Support Real-Time Closed-Loop Parallel Processing Schemes | 34 |
| 24. Illustration of a Decomposition Method to Arrive at the Composite Field of View for an Anisoplanatic Optical System being Simulated in the Laser-Based DWSG Scene Generation Methodology | 34 |
| 25. Illustration of Methodology to Derive the Integrated Photoflux from a Double Convolution Process that can be Accomplished from a More Efficient System Transfer Function Operation and Application of the Convolution Theorem. | 35 |
| 26. Illustration of the Effects of Wavelength-Dependent Variation of the PSF and Optical Cutoff Frequency as Seen in the Magnitude of the Optical Transfer Functions (Modulation Transfer Function, MTF). | 36 |
| 27. Illustration of the Concept of an Effective PSF Resulting from a Number of Contributing Sources such as Broadband Radiation, Optical Diffraction, Deterministic and Stochastic Jitter and Resulting Blur, or Other Sources. | 37 |
| 28. Example of the Screen of the Closed-Loop Simulator for Algorithm Development, Diagnostic Efforts, and Demonstrations | 37 |
| 29. Dependence of DWSG Parameters Determining a Test Configuration. | 38 |
| 30. Modular Flexibility of the DWSG Test Configuration | 38 |
| 31. FPATC Configuration Options for Various FPA Testing Methods. | 39 |

| <u>Figure</u> | <u>Page</u> |
|--|-------------|
| 32. Page One of the DWSG Configuration Spreadsheet (Optical Parameters) | 40 |
| 33. Page Two of DWSG Configuration Spreadsheet (Electronic Parameters) | 41 |
| 34. Example DWSG Laser Irradiance Calculation Spreadsheet | 42 |
| 35. DWSG Configuration Visualization Program Sample Output | 43 |
| 36. Open-Loop FPATC Concept | 44 |
| 37. Closed-Loop FPATC Concept | 44 |
| 38. Computational Steps Required for FPATC Closed-Loop Simulation | 45 |
| 39. Closed-Loop Computational Steps using Direct Convolution | 45 |
| 40. Comparison of Direct Convolution and FFT Computational Methods | 46 |
| 41. DWSG RF Control Electronics Module | 46 |
| 42. Theoretical Determination and Comparison of the FPATC RF Control Electronics Capabilities | 47 |

1.0 INTRODUCTION

This report describes efforts to develop a closed-loop Direct Write Scene Generation (DWSG) Focal Plane Array Test Capability (FPATC) at Arnold Engineering Development Center (AEDC) (Refs. 1-8). The Closed-Loop DWSG (CLDWSG) development efforts support current and future space-sensor test efforts. Recent strategic and tactical programs such as Alert and Report Missiles (ALARM), Brilliant Eyes (BE), Exo-atmospheric Kill Vehicle (EKV), Follow-on Early Warning System (FEWS), Space-Based Infrared System (SBIRS), and Theater High-Altitude Area Defense (THAAD) help establish the need for test capabilities that range from chip-level Focal Plane Array (FPA) characterization to complete sensor subsystem calibration and mission simulation.

DWSG high-speed photonics processing is required for closed-loop operation and simulation of dynamic and interactive sensor commands that reposition the sensor's field of view within the field of regard, and for high-fidelity simulation of optical blurring and temporal effects such as jitter. The real-time CLDWSG method requires performance of a number of operations within the framing rate of the focal plane array of the sensor. These operations include:

- Selection and transfer of the scene background field of regard,
- Calculation and inclusion of target intensities and positions,
- Rotation and translation of the composite background and target scenes to simulate interactive sensor pointing commands,
- Simulation of sensor and satellite jitter,
- Simulation of optical blurring resulting from aberrations and diffraction for broadband spectral radiation,
- Integration of the photon flux over each FPA pixel element,
- FPA pixel responsivity calibration,
- and compensation for acousto-optic (AO) cell optical modulation and other system (RF generation, power amplifiers, etc.) inefficiencies.

AEDC is developing laser-based CLDWSG methods to simulate dynamic sensor operations and complex infrared scenes. New photonic image-synthesis methods are being developed to employ image-to-object Whittaker-Shannon sampling, anisoplanatic optical convolution by quasi-isoplanatic spatial decomposition, and high-speed digital electronics for acousto-optic modulation. Because of the large terabyte volume of data to be processed, the increased bandwidth requirements, and the increased simulation fidelity required for DT&E and OT&E of FPA sensors, the laser-based DWSG methodology is being extended to accommodate optical and computational decomposition methods to better exploit highly and massively parallel real-time image processing schemes.

Section 2.0 describes the process used to derive and establish testing methodologies and requirements from sensor system missions, background/target radiation and corresponding scientific phenomena, sensor parameters, and evaluation and testing objectives. Section 3.0 provides a brief explanation and overview of the DWSG methodology, and Section 4.0 explains the methodology used for deriving and simulating sensor optical properties and image synthesis methods to include the effects of aberrations and diffraction. The CLDWSG configuration selection methodology is described in Section 5.0, along with a program developed to help support test configuration decisions. The initial efforts to implement a CLDWSG configuration using existing FPATC hardware is described in Section 6.0. A Proof-of-Principle demonstration using the existing FPATC hardware is then described in Section 7.0.

2.0 SENSOR MISSION AND SOURCE RADIATION ISSUES

Testing and evaluation (T&E) and modeling and simulation (M&S) of electro-optical sensor systems to assess their operational characteristics, performance limits, and to support engagement scenario simulations can be accomplished and understood using a top-down approach for establishing comparative models and corresponding testing criteria. Figure 1 illustrates a mission-driven approach to establish CLDWSG requirements using a sensor's mission and characteristics and related sensor T&E objectives.

As illustrated in Fig. 1, identification of the mission objectives and profiles and the expected functional requirements are primary steps in designing, developing, and testing electro-optical systems. This is true whether an optical system is designed and developed for detection, discrimination, search and track, ranging, warning, or enhanced imaging, as is done with traditional FLIR-type electro-optical systems. Depending on its function and mission, a sensor will generally have a particular set of important design and test parameters that characterize its operation, function, and performance. Not all parameters will be used universally for all optical systems. Also, some parameters will vary in importance, depending on the mission and the function of the electro-optic sensor system. For example, the signal-to-noise ratio in a detection or warning system is important to increase the probability of detection and decrease the probability of false alarms with little concern devoted to reproducing the exact target-signal waveforms. In contrast, imaging systems emphasize the reproduction of scene imagery with little distortion of the original object scene. The signal-to-noise ratio sometimes receives very little emphasis in some imaging systems, as compared to detection- or warning-type optical systems.

Another important step is identification of the radiation sources and related phenomenologies that will be exploited to accomplish the sensor's mission, i.e., the target and background spectral radiances, shapes, sizes, spatial extents/distributions, Wiener spectrums (spatial power spectral densities), temporal variations, etc. A target's velocity and trajectory are also critical in establishing a sensor's operation (scan, step-stare, staring), field of view, and data processing schemes employed, as well as the sensor testing methods chosen for accurate and adequate measurement programs and mission simulations.

3.0 DWSG OPERATIONAL DESCRIPTION

The DWSG methodology illustrated in Fig. 2 provides high-speed photonics for visible and infrared FPA diagnostics using lasers for real-time evaluation and scene simulation. The DWSG Focal Plane Array Test Capability (FPATC) includes lasers operating at 0.514, 1.06, 5.4, and/or 10.6 μm , and acousto-optic (AO) modulators for laser beam control (Ref. 2). High-speed RF electronics use Direct Digital Synthesis (DDS) to drive the AO modulators with multifrequency input for multibeam output. DDS frequency modulation provides extremely accurate and independent deflection of the multibeam laser "rake"; DDS amplitude modulation similarly provides accurate and independent multibeam intensity control. Laser beam scan optics focus the laser beams onto subpixel regions for pixel-to-pixel photoflux deposition with minimal stray radiation from diffraction. The laser beam rake is then step-scanned across the FPA during each integration period, as illustrated in Figs. 2 and 3.

Subpixel irradiation (illustrated in Fig. 4) is also used to minimize DWSG optically induced cross-talk signals and related signal perturbations. Modular and multiple laser beam systems and acousto-optic photonics also help to ensure that most of the photons designated for specific subpixel regions during a given FPA frame are delivered to the desired pixel for high-fidelity scene simulation having similar signal and noise properties as those with normal thermal-source FPA modes of operation. The DWSG resolution (laser beam spot size and separation) is designed to be approximately twice the normal Rayleigh resolution criteria of most acousto-optic modulators.

DWSG acousto-optic noise sources (Fig. 5) are also minimized to mitigate undesirable photonic fluctuations. One should note that the equivalence of using lasers instead of thermal sources for photodetection evaluation depends not only on generating the same mean number of detectable photoevents, but also on generating the same photonic noise. Effective signal-to-noise ratios and detection equivalence also depend on the absence of signal artifacts or photonic perturbations resulting from using lasers instead of thermal sources. The useful domain and relevance for using lasers instead of thermal sources for photodetector evaluation have been investigated to ascertain differences and similarities regarding spectral distributions, coherence domains and integration volumes, degree/states of polarization, and aspects of photon packets (Refs. 3-6). Lasers and thermal sources are known to have inherently different optical properties and different photon statistics that can be observed with special photon counting and coherence experiments. However, in theoretical and experimental DWSG domains of visible and infrared wavelengths and thermal sources with moderate temperatures, lasers and thermal sources are practically indistinguishable, exhibiting near-Poisson photon statistics with similar FPA signals and photonic fluctuations (Refs. 4-6). Experimental investigations indicate that DWSG methods are suitable for optical diagnostics and evaluation of a variety of FPAs (Ref. 3).

The DWSG laser beam is directed through a 2-D acousto-optic scanner to direct the beam through the scan optics, and focused onto the FPA subpixel region. The acousto-optic modulator actually clips or truncates the laser beam, producing an intensity pattern that is neither Gaussian nor Bessel-function distributed. For a laser beam waist ω and circular aperture of radius a , a truncation ratio is defined as $T = a/\omega$ (Ref. 7). For uniform irradiance onto the AO-cell aperture, the intensity pattern at the focal plane is represented by the traditional Bessel-function distributed

Airy irradiance pattern as illustrated in Fig. 6. As the truncation ratio increases, the irradiance pattern transitions from an Airy pattern to a Gaussian beam pattern, as illustrated in Figs. 7 and 8.

There are numerous definitions for the spot size of an irradiance pattern, and for a $1/e^2$ radius, the encircled energy for increasing truncation ratios exhibits a maximum near $T = 1.4$ (illustrated in Fig. 9). One could also define and use an 84-percent encircled-energy spot size or some other value such as 90- or 95-percent encircled energy. Figure 10 illustrates the radius of the laser-beam spot as a function of the truncation ratio. The current design criterion for the DWSG is to provide approximately 90 percent of the energy or photons into the desired pixel region. For $T > 1.0$, the irradiance patterns are very similar for either a circular or a square aperture which may be desirable to further increase the relative flux onto the desired pixel (Ref. 6).

4.0 BACKGROUNDS, TARGETS, AND SENSOR SIMULATION CONCEPTS

New CLDWSG photonic image synthesis methods are being incorporated to provide more realistic optical simulations with either real or synthetic scenes. These photonic image synthesis methods can more accurately generate and represent temporal power spectral densities and spatial Wiener spectrums for complex background and target scene simulations that are more representative of scenes and convolved FPA images anticipated in and typical of real-world FPA sensor operation.

4.1 RADIATION SOURCES

FPA sensor evaluation, modeling, and simulation ultimately depend on the mission and objectives of the electro-optical FPA sensor system and a sensor's modes of operation. Some emphasis has been devoted to understanding the mission, background, and target phenomenologies; object-to-image mappings; scene distortions resulting from 3-D to 2-D radiance mappings from space to sensor FPA coordinates; and temporal variations. The "reality" or "truth" of any validation and verification effort has to be cast in context of the intended purpose and use of the sensor being evaluated and tested.

Furthermore, no absolute truth table or matrix exists to determine or provide "absolute" scenes for testing and simulation. In source generation, detection, and simulation, there are and will be natural photonic fluctuations and spatial/temporal variations that are necessary to provide the inherent fluctuations anticipated in real-world engagements. There are many stochastic and quasi-periodic fluctuations that cannot be simulated absolutely/exactly. Scene simulation and detection validation should be based on a statistical ensemble instead of any concept of absolute scene "truth" data. Any potential object scene is then considered as one sample from an ensemble of possible scenes that represent the stochastic statistical population. Scene "truth" is then a relative measure of the ensemble mean, variance, and higher-order moments that ultimately describe the population's probability distribution. Accurate signal-to-noise simulations are often needed to judge the success or failure, not of any single event or single test case, but of an ensemble of detection events that can be described by the normal laws of stochastic processes and related detection criteria such as probability of detection, probability of false alarms, etc.

4.2 SENSOR VIEWING CONSIDERATIONS

To help better understand potential methodologies being considered for closed-loop DWSG operation, a number of concepts are briefly discussed to provide an overview of some basic principles being considered and evaluated. A sensor's geometry for above-the-horizon or below-the-horizon viewing is illustrated in Figs. 11 and 12. The background and targets detected by a sensor will generally depend on the sensor's field of regard and field of view, both of which can be time-dependent, semi-deterministic processes or stochastic processes. Typical orbital positions will vary the field of regard that is viewed from space-based sensor systems, and corresponding background-to-FPA and target-to-FPA mappings have to be considered. In addition, differences resulting from using different wavebands for normal sensor operations in atmospheric absorption bands or transmission windows of interest must also be accommodated. The background and target radiance levels reaching the sensor depend not only on the emission or scattering properties of the sources, but also on the transmission of the intervening medium such as the atmosphere and clouds.

A sensor's spatial location and relative orientation help to determine the field of regard as illustrated in Figs. 13 and 14. A 3-D geometry of space can be viewed as being either functionally or optically mapped onto a sensor's FPA, as illustrated in Figs. 14 and 15. One can either think of the background and targets within the field of regard as being projected onto the FPA, or as the FPA being projected into the 3-D space, as illustrated in Fig. 15. A set of radiance field-of-regard mappings for selected orbital parameters can then be viewed as two-dimensional mappings onto an extended FPA and could, in principle, be precomputed or preselected for typical orbital parameters. The individual sensor FPA image frames could then be processed to include optical effects for time-dependent pointing vectors within the field of regard.

4.3 OPTICAL EFFECTS AND IMAGING

Sensor imaging of quasi-monochromatic, thermal, or blackbody sources generally depends on the theory of partial coherence. In many cases this generalization can be simplified to one of the two extreme cases of partial coherence, either totally coherent or totally incoherent, with the understanding that it is an approximation with known errors acceptable for the intended purpose of modeling and simulation. Neither of these two extremes (coherent or incoherent radiation) exists completely for real sources which are always partially coherent to some degree and partially polarized, also. Thermal or blackbody sources are normally modeled using the simple, incoherent superposition assumptions for adding or integrating the statistically independent object sources to obtain the integrated images with very good approximations to the "real world" for many cases. Each case is normally evaluated on an individual basis to ensure that the assumptions and simplifications are indeed representative of real-world engagement "reality."

Imaging and photodetection, as illustrated in Fig. 16, follow the laws of optical diffraction, and optical components are not perfect. The images of "point" sources are not "point" sources because of the inherent wave-nature of photons and resulting diffraction and aberration effects. As a "point" source is moved within the field of view of a sensor, the corresponding image of the "point" source may vary noticeably, depending on the wavelength and the degree of aberrations

present. For practical purposes, many optical systems can be considered spatially invariant and the image blur or point-spread function does not vary as measured, and, for a given wavelength range, the optical system can be considered diffraction limited. In other cases, there may be considerable distortions and variations in the point-spread function resulting from optical aberrations which need to be taken into consideration. The optical components effectively map the object plane onto the image plane with potential aberrations, blurring, distortions, magnification, or minification that transform the object into the image. If one can compute this transformation function, then the image can be accurately determined and properly simulated. Simulations should also consider the nature of the sensor system mission, any integrated detector effects, and the corresponding data processing algorithms used. Verification and validation methods should be applied to demonstrate and further ensure that the evaluation methods and corresponding simulations are relevant for the intended purpose.

There are a number of concepts and methods for determining a sensor's point-spread function (PSF) or its optical transfer function (OTF) as illustrated in Fig. 17. A sensor's image and the FPA's integrated photoflux can then be determined by basic integration methods or, for near spatially invariant FOV regions, by convolution methods or by way of the convolution theorem using OTF frequency-domain methods, as illustrated in Fig. 18. The method chosen depends on the desired fidelity as well as the computational performance desired. As with any computational/scientific model, these methods have inherent assumptions and simplifications. These have to be understood to provide a quantitative method to account for and potentially accommodate any resulting errors.

A geometrical point source is imaged into a diffraction pattern. Only as the geometrical image size increases relative to the PSF dimension do we see any structure or effects of the shape/size of the "point" source. Only after the geometrical image dimension increases to on the order of magnitude of the Airy radius do we even see the effects of its shape and size. Even square sources or arbitrary source shapes appear to be "point" sources when their maximum geometrical image dimension is small compared to the PSF dimension. The spatial and structural features are not observed until the geometrical image dimension is on the order of magnitude of the optical system's PSF dimension. In the frequency domain, one says the high-frequency content is stripped off and the image does not have sharp edges or discontinuous spatial features. If a small square's diffracted image has the same PSF as that produced by a small circular source, they can be indistinguishable. Under some circumstances we can then conceivably simulate images with sources that are distinctly different, yet yield the same effective image as detected by the FPA. Using the Whittaker-Shannon sampling theory, we can even use an array of sources that generate the same irradiance pattern if intensities are properly selected for OTF-filtered, bandwidth-limited optical images.

One distinct feature of the process of convolution is that when the point-spread function is "small," the image and object can be very similar. The image is also said to be of high fidelity when there are few or no aberrations present. In the limit of aberrationless, linear, shift-invariant, delta-function PSFs, the image will be an "exact" duplicate of the object scene (an idealism). As the point-spread function increases in relative dimension, the image will lose much of its clarity and fidelity; considerable differences between the object and the image can result. In the limit of

very large PSFs, the image will blur into a uniform irradiance pattern with near-zero information content or modulation (maximum entropy), especially when the PSF's dimension is large compared with the largest geometrical image features present.

In the realm of Fourier optics, the object and PSF convolution can be viewed as a filtering process. With this perspective, the object is viewed in the frequency domain and the OTF filters or attenuates the high-frequency components (amplitude and phase) of the object scene resulting in a low-frequency image. For incoherent imaging and when the geometrical image's spatial frequency is on the order of magnitude of the reciprocal of half the PSF dimension, the contrast or modulation reduces to zero and the image details or information is lost. Any spatial frequency beyond the cut-off frequency of the optical system will be attenuated in the image plane. The high-frequency details are essentially filtered out by the optical sensor's low-pass, spatial frequency OTF.

4.4 ANISOPLANATIC OPTICAL SYSTEMS

For our applications, the scene and FPA are quantized into small grid-sampled regions (as illustrated in Fig. 19) to perform the integrated image and detector photoflux computations. The degree or level of sampling needed for a scene and FPA combination depends on the desired DWSG simulation fidelity.

For optical scene simulations requiring real-time closed-loop operation, the satellite/sensor interactively updates the line-of-sight pointing vector relative to the sensor's position in space and to the background field of regard. To incorporate and support interactive CLDWSG operation and to accommodate simulation of nonuniform anisoplanatic optical systems, the scene is decomposed into quasi-isoplanatic regions for narrow spectral bands, as illustrated in Fig. 20. For this method, the scene is decomposed into segments that allow for an application of direct convolutions or OTF methods via the convolution theorem for regions of quasi-isoplanatic patches. The spatial decomposition not only provides for improved optical fidelity in simulating anisoplanatic sensor optics, but also provides a method to decompose and compute the scene segments in parallel. When these methods are used, it is important to examine the effects of spatial decomposition and to mitigate edge effects, and diffraction losses, while at the same time providing anisoplanatic optical simulation.

With the scene decomposed into quasi-isoplanatic regions, one can use either direct methods or the convolution theorem for image computation and synthesis. For broadband radiation, effective PSFs can be used when sample points have the same relative spectral distribution. When there are regions in the scene that have considerable variation in spectral content (from region to region), then one could employ complete spectral decomposition and image synthesis for effective photon flux.

Spatial FOV decomposition, computation, and synthesis of the object/image scene provides a useful method that facilitates multiple PSFs to be used to determine and directly simulate an anisoplanatic optical system. Figures 21 and 22 illustrate that the spatial decomposition and computational methods may lead to anomalous computational artifacts resulting from simulated

diffraction/PSFs, sampling, and other windowing effects. Various methods to improve the optical simulation and to mitigate computational artifacts have been investigated and illustrated in Fig. 23. In these examples, extended domains help to improve the simulation fidelity and subsequently improve experimental testing results. Figure 24 illustrates the improvement obtained from using extended computational domains to simulate anisoplanatic optical aberrations with a reduction in computational artifacts and related errors.

For direct computation methods, the image is integrated over each FPA pixel element to determine the number of photoevents for each frame. However, the integrated detector photoflux can be viewed more generally as a convolution of the image irradiance with a detector, as illustrated in Fig. 25. The detector convolution can then be computed directly, and integrated photoflux values can be obtained from the respective grid point locations as desired, or arbitrary detector repositioning can be introduced to simulate perturbations in the detector's position, row offsets, and alignment errors.

For many applications and missions, a sensor will be detecting broadband radiation, and one needs to account for the spectral distribution of radiation as well as the spectral response of the sensor system. The PSF and OTF can vary considerably due to broad spectral distributions (see Figs. 26 and 27). There are also other blurring effects such as jitter which vary the image considerably in real systems. When we introduce aberrations and polychromatic or broadband radiation, the total detectable irradiance on the FPA will deviate from the simple deterministic one-case PSF/OTF normally used for simulation. However, in practice, a composite PSF from a polychromatic point source imaged with optical aberrations and vibrational blur can be approximated with a two-dimensional Gaussian-distributed PSF, as illustrated in Fig. 27.

To help diagnose, investigate, and simulate the effects of potential real-time closed-loop DWSG operation that includes optical diffraction and aberration effects, a PC-based program has been developed. An example of the program's output using the OTF method for simulation is illustrated in Fig. 28.

5.0 CLDWSG CONFIGURATION SELECTION METHODOLOGY

The determination of the optimum DWSG configuration for testing a FPA is not necessarily simple and straightforward. FPAs are developed with various sizes, aspect ratios, pitches, speeds, and spectral bandpasses, and typically the SGTC AODs must be specifically arranged to meet the needs of the test article. In light of frequent inquiries from FPA vendors as to the test potential of the SGTC, an Excel[®] spreadsheet has been created to enable a DWSG engineer to develop the test configuration in a systematic and timely manner, so that even while the prospective user is watching, his questions can be answered. An executable program written in Visual Basic has also been created to provide a visual perspective of the projection footprints of each individual AOD onto the surface of the FPA under test.

Two operational constraints of the DWSG hardware play a role in determining the test configuration:

- Acousto-optic deflector access time
- Acousto-optic deflector aperture (this with (1) and the RF frequency bandwidth determine the time-bandwidth product, or resolution of the deflector)

There are several key parameters associated with the test article which also influence the DWSG test configuration:

- Number of pixels in each axis of the FPA
- FPA pixel pitch (this with (1) determines total spatial extent of FPA)
- FPA integration time
- Spatial offsets, if any, between groups of rows or columns

The interaction of these parameters is shown in Fig. 29. The highly flexible modular nature of the DWSG layout can accommodate a wide variety of test configurations. Three basic approaches to these configurations are shown in Fig. 30.

The main configuration options for the FPATC are shown in Fig. 31. The TDWSG configuration is similar to option B, except that it has only 12 modules which cover 75 percent of the 512×512 area. Option C illustrates the case when there is a half-pixel offset between regions of an FPA. There is also a limited capability to perform continuous projection as in option D, where each AOD limits the scan to one column.

The object in using the Excel spreadsheet is to be able to respond very quickly to a potential user's request to test their FPA, and to diagnose difficult testing situations so that the possible options can be determined. It considers a number of items:

- Projection extent of the test article (pixel extent in each axis, presence of individual sub-module FPAs, if the projection is in sections, or to the complete FPA, if spatial averaging is used),
- Metrics and operational parameters of the FPA (pixel pitch, active area, spectral response, mission bandpass, fill factor, integration time, and type of reset),
- Projection hardware (wavelength, number of AODs at operational wavelengths, optics, aperture, and facility), and
- Drive electronics (multiple DRES components, multiplexing, and data throughput).

The number of AODs and the manner of their projection (coincident or adjacent) through each scan lens and the number of scan lenses needed are also considered. As the data are input and decisions are made concerning the best means of projection, various messages (special configuration information in blue, warnings in red, and suggestions in green) are produced. The user can also add notes. The Excel spreadsheet can be printed out in a convenient two-page format that describes the optical and electronic configurations (see examples in Figs. 32 and 33).

Once the configuration is determined, the derived optical dwell time must be consistent with test article compatibility measurements. The optical power needed to fully illuminate the projection must be available with the facility hardware. Another Excel spreadsheet (illustrated in Fig. 34) has been developed to aid in this determination.

The configuration conceptualization program illustrates the footprints of the AOD projections and the relation to the surface of the FPA. An example of its output is shown in Fig. 35. Some additional concept layout may need to be performed to ensure that the derived configuration is physically possible.

6.0 INITIAL CLDWSG IMPLEMENTATION EFFORTS

This section describes the current status of recent AEDC technology efforts tasked with the implementation of real-time, closed-loop scene manipulation methods using AEDC's FPATC mission simulation test capability. Figure 36 shows the current FPATC open-loop capability/concept using the Direct Write Scene Generation method to test sensors at the component or subsystem level. In this configuration, test scenarios are played into the sensor under test and then captured at the sensor's output. Also, there is no feedback between the radio frequency (RF) electronics that control the projection and data acquisition electronics that capture the sensor output.

Figure 37 illustrates a concept for a closed-loop FPATC capability. The test article is a sensor subsystem including FPA operational hardware and flight navigation hardware. Under closed-loop conditions, flight hardware tracking algorithms output new line-of-sight coordinates that are accepted by FPATC hardware and used to create the next sequential frame to be projected. Because the DWSG does not project through a sensor's optics, real-time digital simulation of sensor optical effects is a critical part of realistic simulations.

The initial closed-loop proof-of-principle (PoP1) demonstration focuses on using the FPATC first to interactively manipulate or construct scenario frames by responding to changes in line-of-sight or pointing-vector coordinates, and second, to demonstrate computational capabilities for simulating optical effects in the constructed image scene. The pointing-vector information can be computer generated, input by a user who is interactively viewing the scenario, or both. Before a PoP1 demonstration capability could be designed and integrated into the FPATC, it was necessary to understand some of the computational requirements for closed-loop operation in general, and the PoP1 demonstration specifically.

Figure 38 outlines the steps required to interactively compute a 2-D infrared-rendered scenario frame based on a pointing-vector input. These steps include rotation, translation, and extraction of the scene image; application of the optical transfer function using a 2-D FFT then inverse FFT approach; detector integration for greater than 1:1 image sampling; radiometric, laser, and RF calibration; and projection buffer loading before outputting the frame. An equation was then derived by predicting the number of compute cycles required for the whole process and summing the total. The equation is written as a function of test parameters such as oversampling ratio, number of FPA rows and columns, and point-spread function size. To be conservative, no

optimization was done on the calculation of compute cycles per step. A compute cycle is assumed to be the time required to perform an add, subtract, multiply, divide, or memory move.

There are some optimizations that could be done to combine steps in the process and speed up the calculations. Figure 39 shows the equation that would result if the FFT approach were substituted with direct convolution using a restricted kernel. Direct convolution is not always, however, the most optimal method to choose. Issues concerning kernel size relative to sampling ratio can cause fidelity problems in the simulation and create excessive computational loading. However, for applications that permit the fidelity levels associated with a smaller point-spread function kernel, direct convolution is simpler and efficient to implement. Figure 40 tabulates direct convolution versus FFT methods and indicates a crossover point between FFT and direct convolution performance near a 9×9 kernel size.

After considering worst-case computational requirements for closed-loop, a three-fold implementation strategy was adopted: (1) capabilities of existing FPATC hardware designs were examined for PoP1 demonstrations; (2) off-the-shelf hardware and software subsystems that could be integrated into the FPATC were investigated; and (3) integration of off-the-shelf subsystems and components with in-house developments that could meet closed-loop requirements were investigated.

Figure 41 illustrates an in-house-designed DWSG RF control module. The module uses a TMS320C30 (C30) Digital Signal Processor (DSP) to control 16 RF channels (or FPA scan lines) during a mission simulation. In open-loop simulation, the system uses the DSP as a data pump to produce new frames rapidly during simulation. However, in closed-loop simulation, the DSP's computational capabilities could be tapped to execute the required closed-loop processing steps on scene data stored in each processor's memory. Thirty-two C30's work together in a Single Instruction Multi-Data (SIMD) architecture in the FPATC DWSG electronics. Because the SIMD architecture is very compatible with image processing and the decomposition methods required for anisoplanatic optical simulation, the PoP1 demo was implemented using existing FPATC designs and hardware. Reference 8 documents the hardware architectures developed for the DWSG control electronics.

Figure 42 illustrates the anticipated computational capabilities using all of the DWSG RF control electronics. For example, the chart predicts that a 128×128 FPA could be operated at 13 frames per sec with full 5x oversampled fidelity. This frame rate is considered more than adequate for proof-of-principle demonstration. However, many 128×128 FPAs operate at frame rates in excess of 1,000 frames per sec. Such a frame rate would require a computational capability of better than 50 GFLOPs for high-fidelity simulation. These computational loads reinforce the need for advanced hardware development beyond the PoP1 demonstration capability and continued investigation of smart fidelity trade-offs and advanced algorithm developments that will reduce the hardware's computational requirement.

Using the FPATC hardware and software for the PoP1 demonstration is cost effective because it delays, by at least one year, large material procurements for more advanced subsystems. This approach recognizes that using an opportunity to wait for new electronic

capabilities and cost decreases while demonstrating the principles of closed-loop operation is an optimal path to take in a time of rapidly changing electronics developments.

Based on results from the PoP1 demonstration, a more detailed development plan will be completed for advanced hardware and software designs. During and after developing the PoP1 demonstration with existing hardware designs, it is also important to investigate other potential vendors for signal processing hardware and software.

7.0 PROOF-OF-PRINCIPLE CLDWSG DEMONSTRATION EFFORTS

The first closed-loop Direct Write Scene Generation Proof of Principle (PoP1) Demonstration helped to evaluate the capacity and functionality of the current FPATC configuration to interactively manipulate a dynamic scene projection by responding to changing pointing vectors. For this PoP1 demonstration, the dynamic scene consists of a static background scene and a multiple frame target database overlaid onto the background scene. The PoP1 interactive interface is mouse-driven, which allows the user to select the pointing vector coordinates via the mouse with a real-time display depicting the current frame being projected.

The CLDWSG PoP1 Demo consisted of three major software components operating in conjunction with the other. The first software component is the CLDWSG Scene Projection software executing in the DRES. This software component computes the new frame information based upon the target file database and the new pointing vector. This software component is distributed over multiple C30 processors operating in parallel. Each processor performs the computations for a portion of the scene to be projected. A number of steps are required in the computation:

- Clear targets out of background scene from previous frame
- Overlay new targets onto background scene
- Retrieve new pointing vector from SCRAMNET shared memory
- Using the new pointing vector, translate, rotate, and extract the new scene image using nearest-neighbor method
- Perform Optical Sensor PSF diffraction effects using Direct Convolution with a 3×3 kernel
- Integrate photoflux over FPA pixel elements
- Convert from FPA output levels to RF dB levels using a 5th-order polynomial
- Convert from RF dB levels to attenuator commands using a lookup table
- Load RF electronics with attenuator commands

The second software component in the CLDWSG PoP1 demonstration is the closed-loop control program which was executed on a 66-MHz 486 PC. This program interactively creates new pointing vectors consisting of 2D axial and angular parameters. The angular values are created from interactively clicking the mouse button. A left-mouse button click increments delta

theta in a positive angular direction, whereas a right-mouse button click will increment delta theta in a negative angular direction. Once the pointing vector has been created, it is transferred to the CLDWSG Scene Projection software operating on the DRES via SCRAMNET-shared memory. The pointing vector is transferred to the CLDWSG real-time display software operating on a DIPIX frame grabber interface.

The third CLDWSG PoP1 demonstration software component is the CLDWSG real-time display. This software component operates on a C30-based DIPIX frame grabber. This display assists the user in creating the desired pointing vector. The entire background scene with overlaid targets is displayed in real time synchronously with the scene projection. For visual comparison, the translated, rotated, and extracted image to be projected is also displayed to the side of the background scene. Using these two displays in conjunction with the mouse, the user can select the desired portion of the background scene to be projected.

8.0 CONCLUDING REMARKS

In order to provide more optimized optical simulation fidelity and to reduce computational burdens, closed-loop DWSG image synthesis methods are being developed which employ image-to-object Whittaker-Shannon sampling, anisoplanatic optical convolution by quasi-isoplanatic spatial decomposition, and high-speed digital electronics for acousto-optic modulation. Optical and computational decomposition will not only provide high-fidelity optical simulation for anisoplanatic optical sensors and complex infrared scenes, but will also facilitate high-speed parallel-processing schemes for real-time CLDWSG and sensor operations.

The current trend in FPA development is to develop devices that operate at very short integration times. Thus, to keep up with FPA technology, there must be corresponding increases in acousto-optic cell and other scanner technologies (Ref. 9). A Phase I SBIR program (AF 95-005) was funded by AEDC to develop new techniques for acousto-optic deflectors with higher access times (5 μ sec or less for 256×256 resolvable spots; 50- to 100-MHz driving frequencies) than are currently possible with standard designs. One contract was awarded to Physical Optics Corporation based on a multisectional concept which uses available acousto-optic materials. Prototype hardware for this effort will be delivered to AEDC. An additional contract was awarded to Aurora Associates, who is currently procuring acousto-optic materials for further study.

A computer testbed has been constructed and is being used to develop and evaluate the high-speed computational algorithms required for scene extraction and convolutions. The proof-of-principle demonstration provides assurance that the computation and photonics methods used are not only feasible, but the concept is scaleable. This technology effort helps to provide new optical diagnostics for cost-effective and systematic DT&E and OT&E of large FPA sensors using parametric and statistical methods not amenable to costly field or flight testing methods.

REFERENCES

1. Lowry, H. S., Tripp, D. M., and Elrod, P. D. "Current Status of Direct Write Scene Generation at AEDC." *SPIE Orlando Conference Proceedings*, SPIE, Vol. 2223, April 1994.
2. Lowry, H. S. and Elrod, P. D. "Completion of the Scene Generation Test Capability (SGTC) at AEDC." *SPIE Orlando Conference Proceedings '95*, SPIE, Vol. 2469, April 1995.
3. Lowry, H. S., Tripp, D. M., and Elrod, P. D. "Equivalence of FPA Response to Continuous and Pulsed Laser Radiation." *SPIE Orlando Conference Proceedings*, SPIE, Vol. 2225, April 1994.
4. Steely, S. L. "Laser versus blackbody photostochastic fluctuations." *Annual OSA Conference Proceedings*, Vol. 16, October 1993.
5. Steely, S. L. "Aspects of laser versus blackbody photodetection: coherent versus thermal-source photonic fluctuations." *CLEO Conference Proceedings*, May 1994.
6. Steely, S. L., Lowry, H. S., and Tripp, D. M. "Aspects of Laser Versus Blackbody Photodetection: Laser-Based Photonics for Focal-Plane-Array Diagnostics." *SPIE AeroSense Orlando '95 Conference on Target and Backgrounds: Characterization and Representation*, Paper No. 2469-35, April 1995.
7. Steely, S. L., Lowry, H. S., Fugerer, R. H., and Elrod, P. D. "Real-Time Anisoplanatic Convolution Methods for Laser-Based Scene Generation: Closed-Loop Focal-Plane-Array Test and Evaluation Methods." *SPIE AeroSense Orlando '95 Conference on Target and Backgrounds: Characterization and Representation*, Paper No. 2469-05, April 1995.
8. Fugerer, R. H., Lowry, H. S., Hervig, D. J., and Holt, L. L. "Signal Processing Hardware and Software Applied to the Development of a Real-Time Infrared Mission Simulation Test Capability." *SPIE AeroSense Orlando '95 Conference on Target and Backgrounds: Characterization and Representation*, April 1995.
9. Lowry, H. S., Tripp, D. M., Nicholson, R. A., Fugerer, R. H., Steely, S. L., and Holt, L. L. "Initial Test Efforts Using AEDC's Focal Plane Array Test Chamber." *SPIE Orlando Conference 2742*, April 1996.

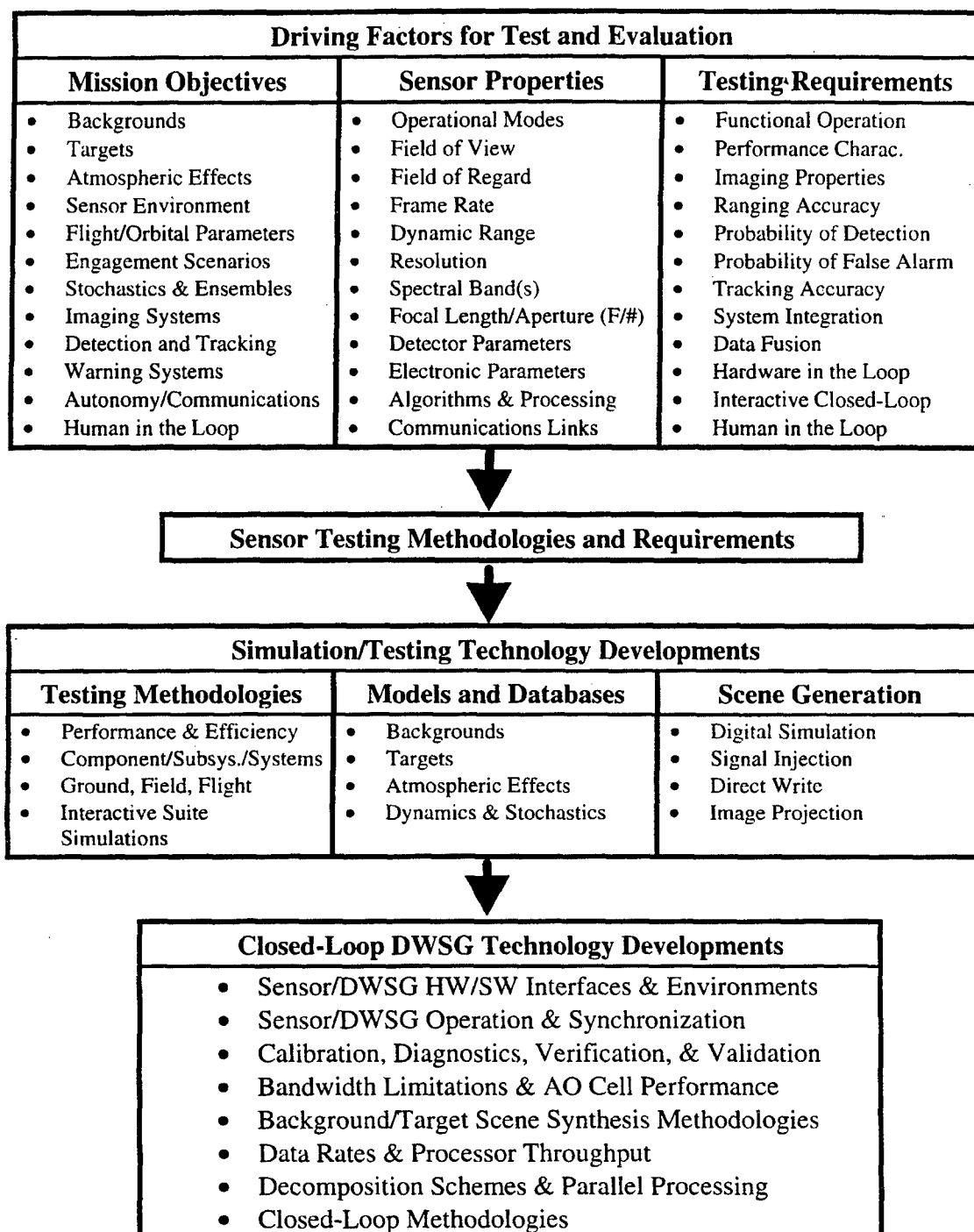


Figure 1. Sensor testing and evaluation diagram illustrating closed-loop DWSG development.

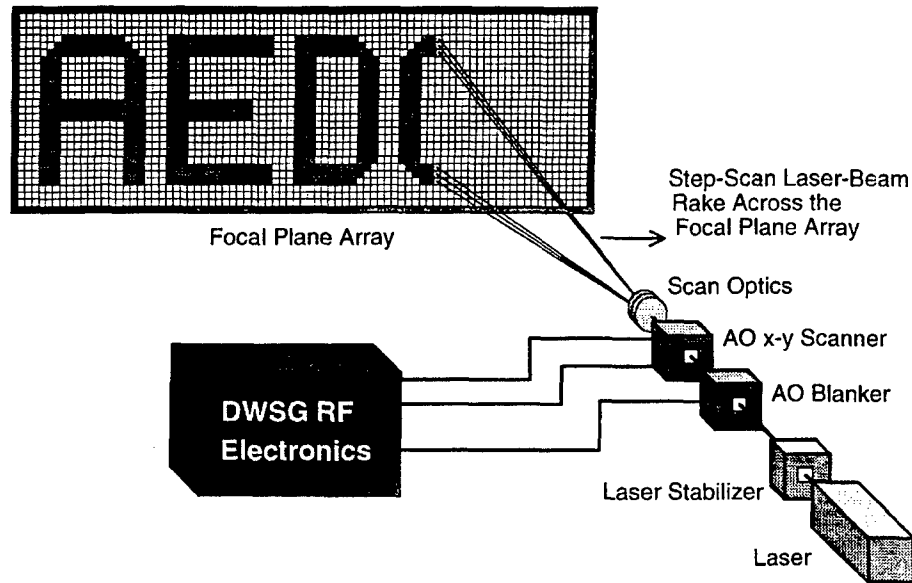


Figure 2. Illustration of the laser-based Direct-Write Scene Generation methodology for focal-plane-array diagnostics and scene-generation schemes.

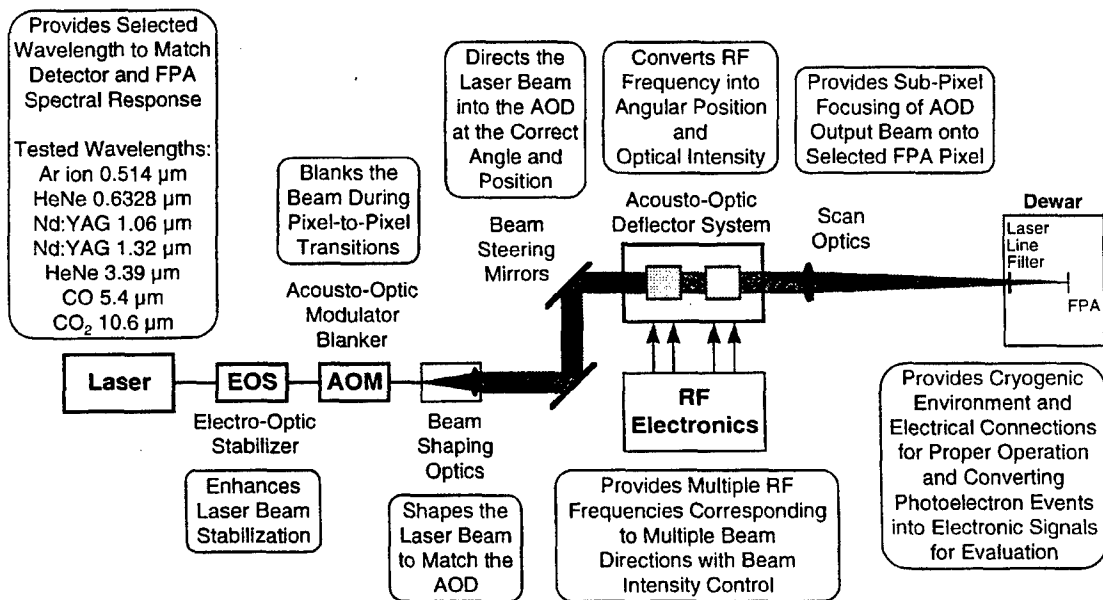


Figure 3. Laser-based Direct-Write Scene Generation methods for photo- characterization and evaluation of focal-plane-array sensor systems.

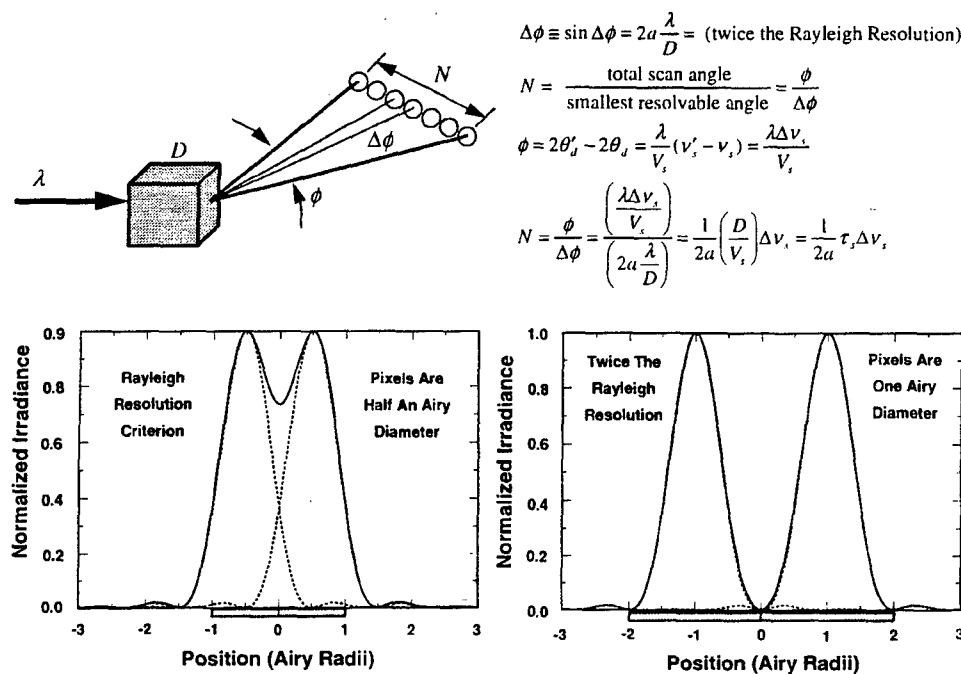


Figure 4. DWSG operation for laser-based photonics illustrating the resolvable spots for sub-pixel irradiation at twice the Rayleigh resolution.

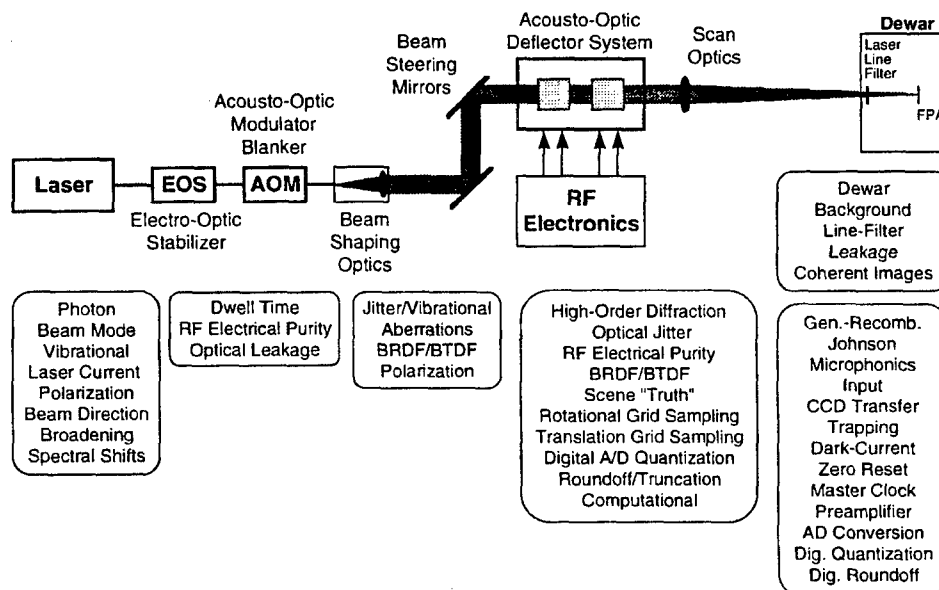


Figure 5. Potential noise sources for DWSG photonics and FPA operation.

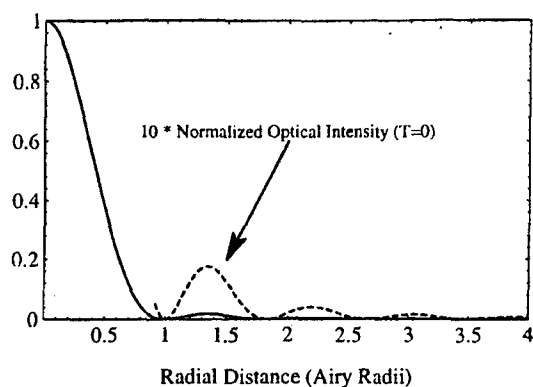


Figure 6. Normal Airy pattern for $T = 0.0$.

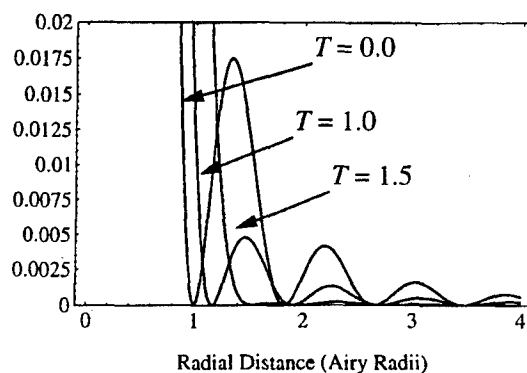


Figure 7. FPA DWSG laser beam irradiance pattern for small truncation ratios $T = 0, 1.0$, and 1.5 .

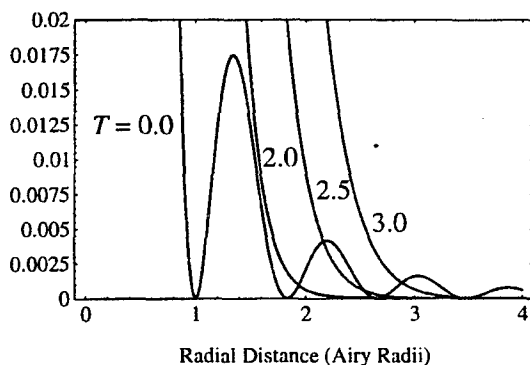


Figure 8. FPA DWSG laser beam irradiance pattern for small truncation ratios $T = 0, 2.0, 2.5$, and 3.5 .

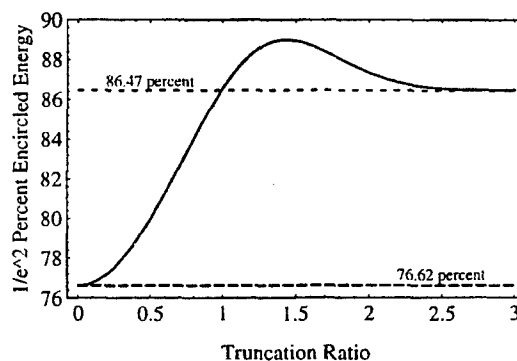


Figure 9. Percent Encircled energy for a radius set at the $1/e^2$ irradiance level.

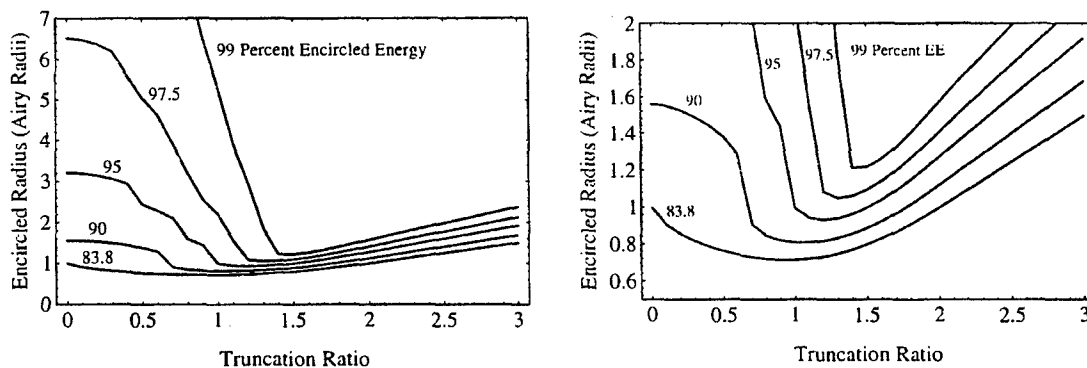


Figure 10. FPA laser-beam irradiance spot size for various encircled energies.

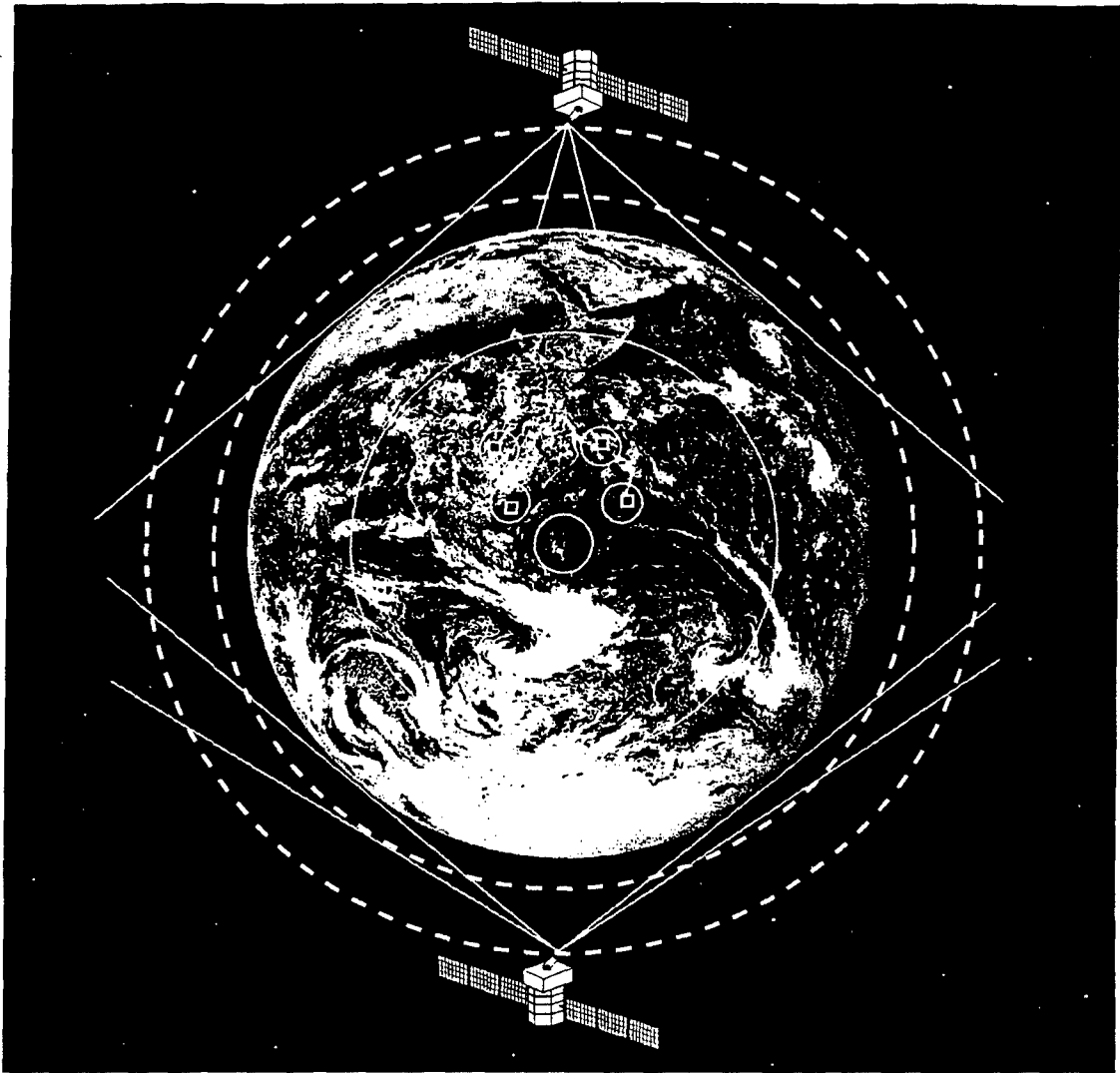


Figure 11. Sensor view of earth for above- and below-the-horizon perspectives require quite different data bases for simulation of real-world background and target engagements and related phenomena exploited for efficient detection, discrimination, and tracking.

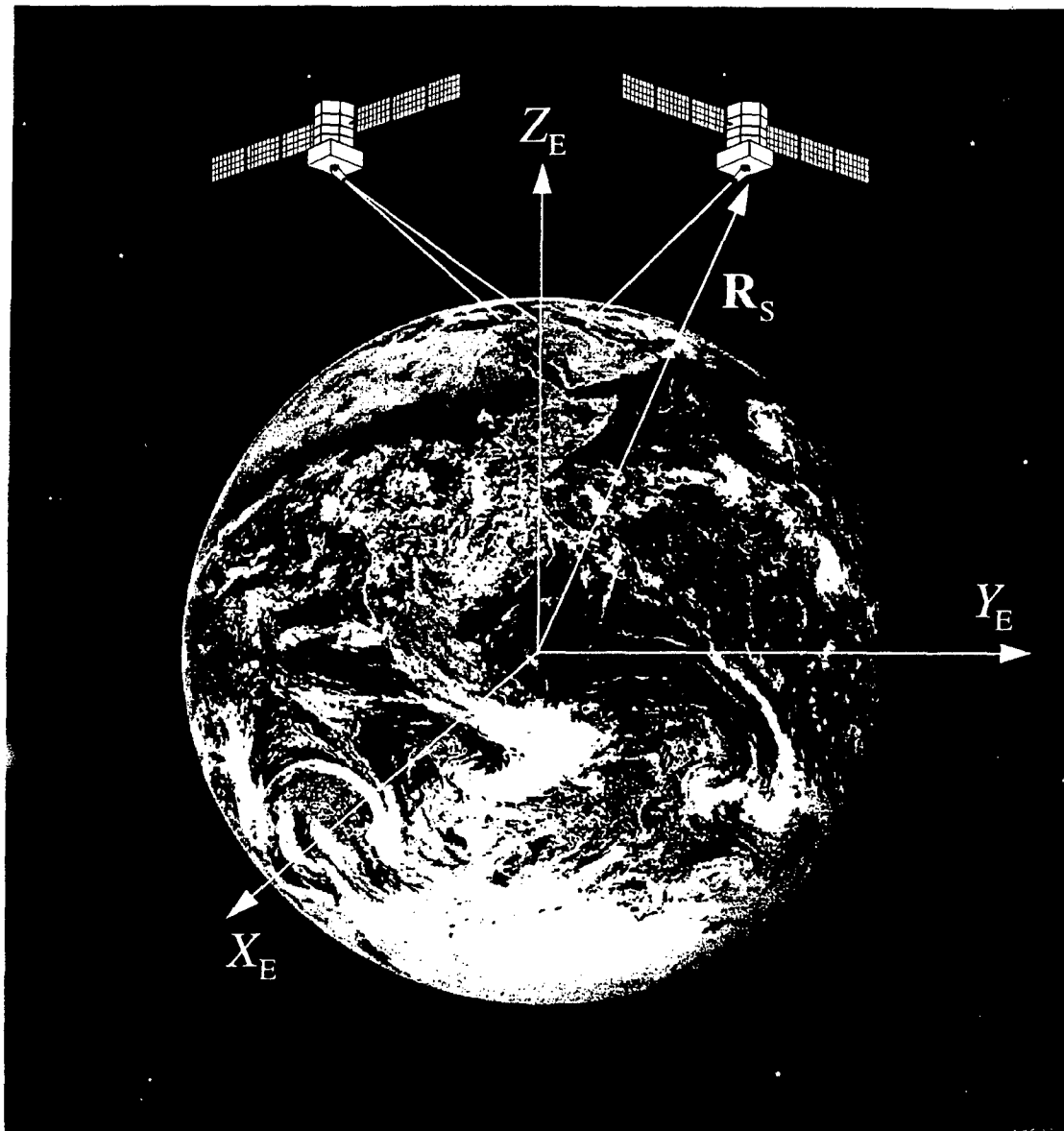


Figure 12. Multisensor perspective and simulation will depend on mission as well as on environmental and operational characteristics.

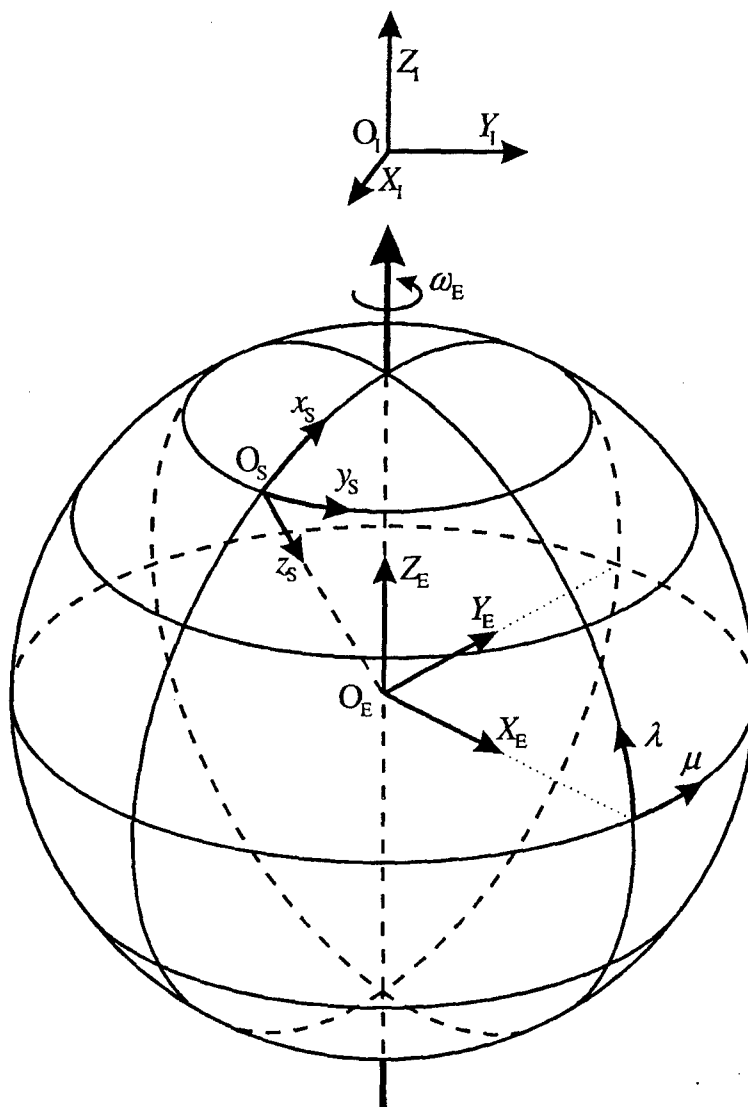


Figure 13. Illustration of methodology to view backgrounds and targets for relative coordinate systems from a space-based sensor in an earth orbit.

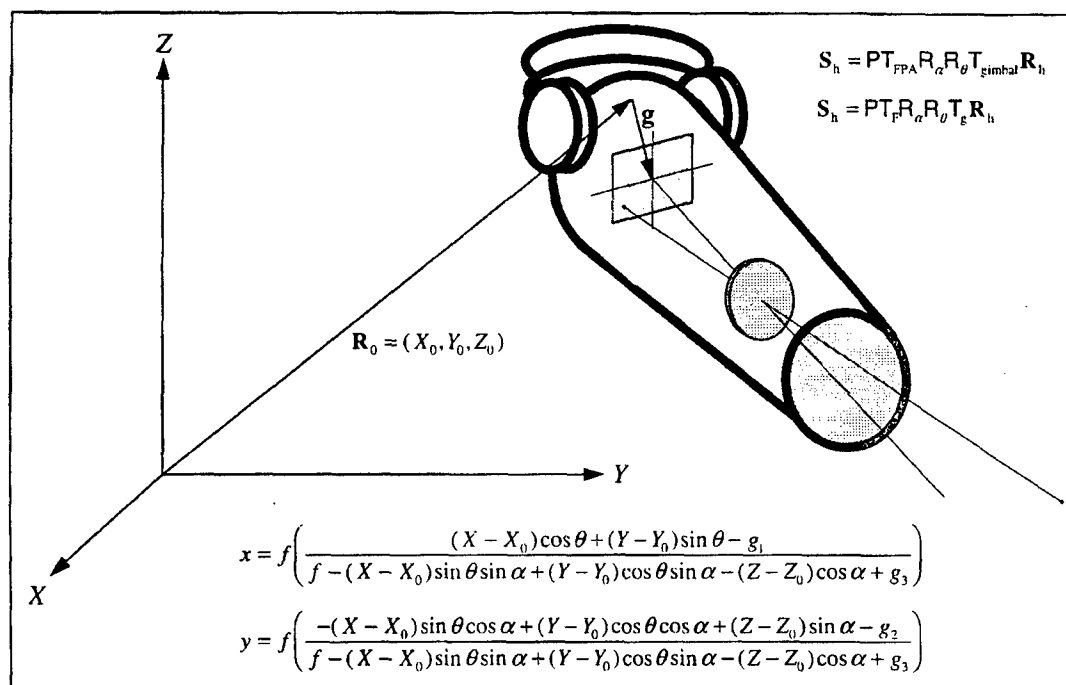
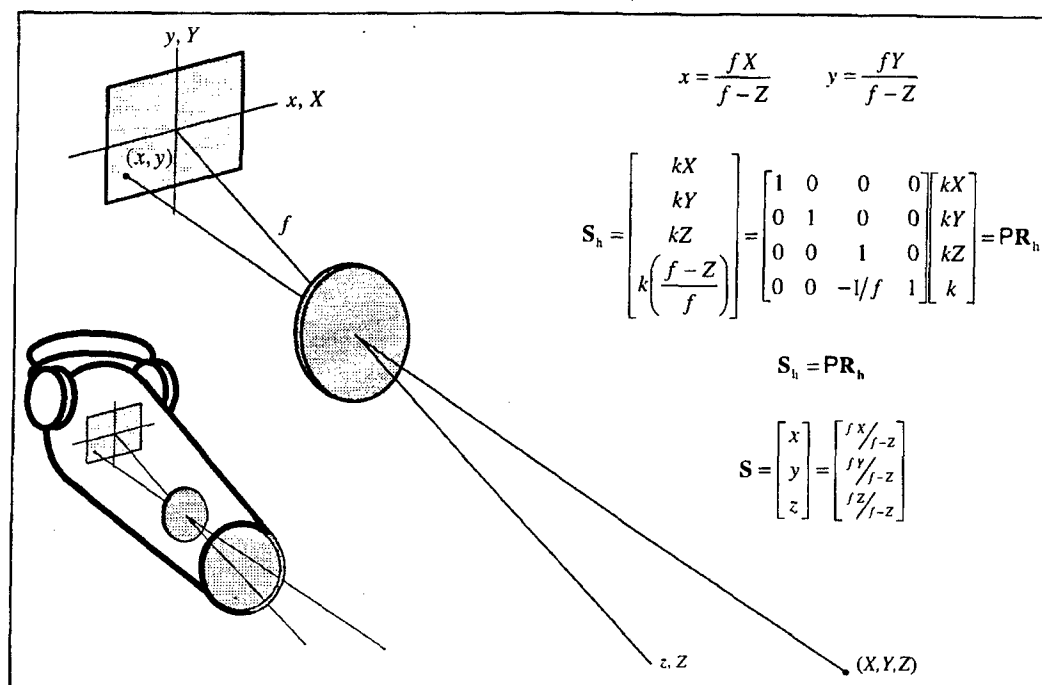


Figure 14. Illustration of a 3D-to-2D spatial mapping of space-based backgrounds and targets onto the FPA for DWSG optical simulation efforts.

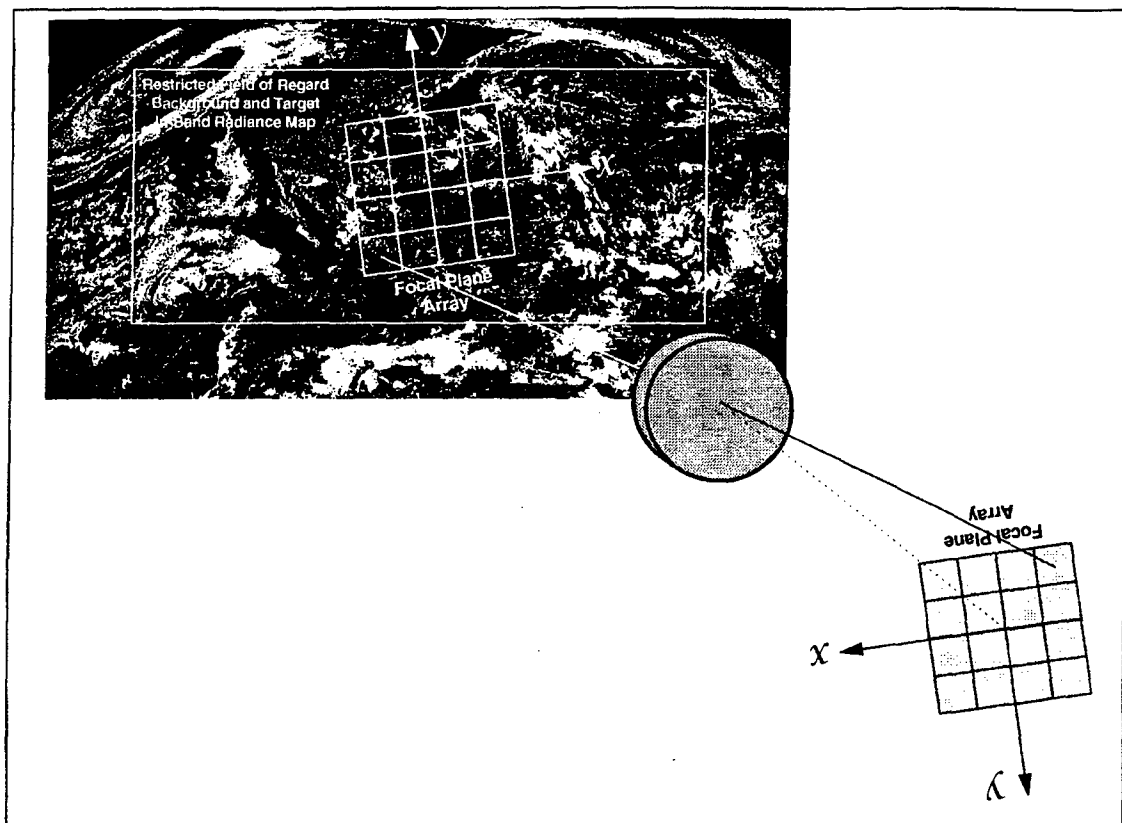


Figure 15. Concept illustration of the scene being mapped onto the FPA, which could also be usefully viewed as the FPA field of view being mapped onto the 2-D projection of the background and target scene.

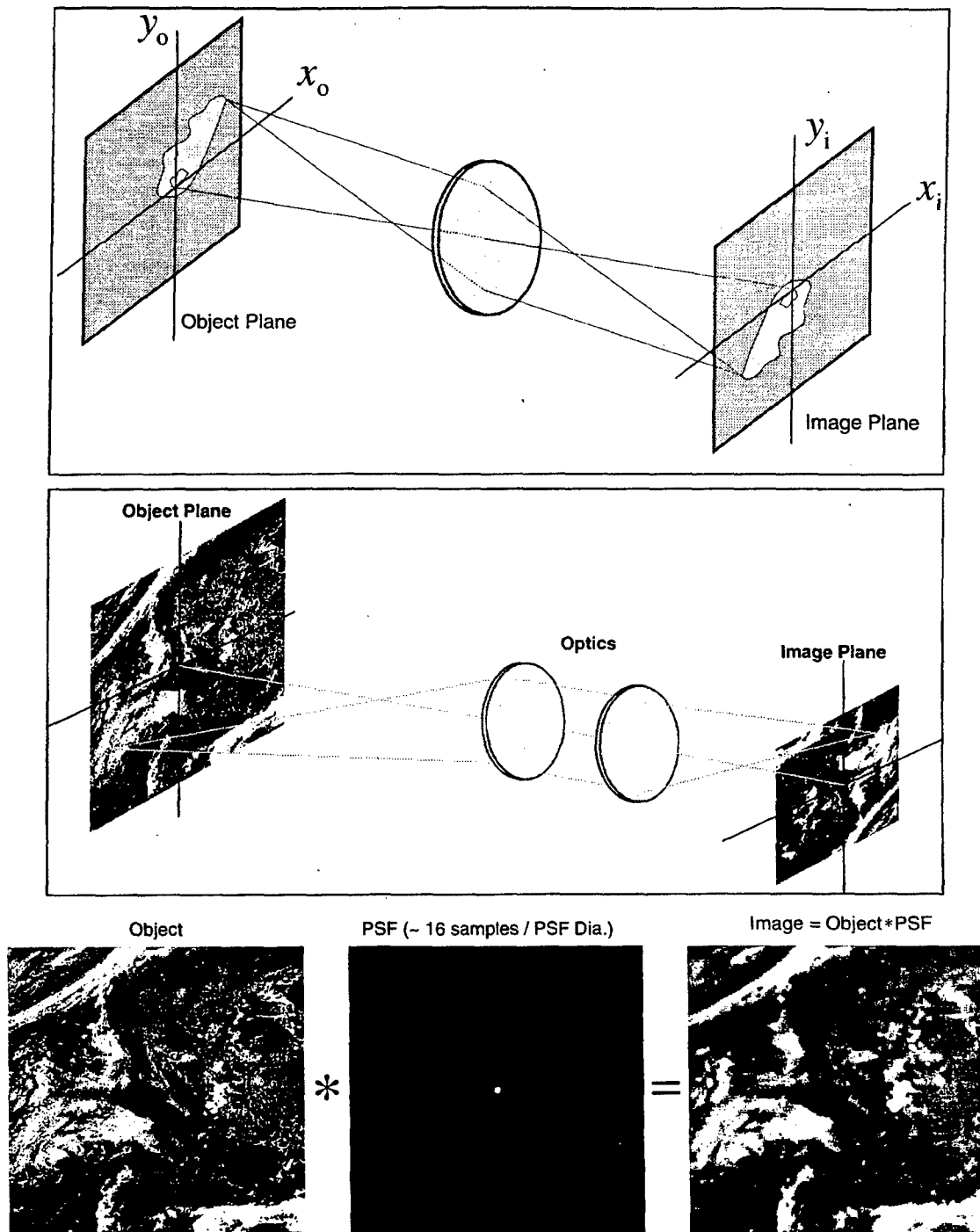


Figure 16. Illustration of the object plane being transformed to the image plane for FPA irradiation via the optical system for a simple background and target map.

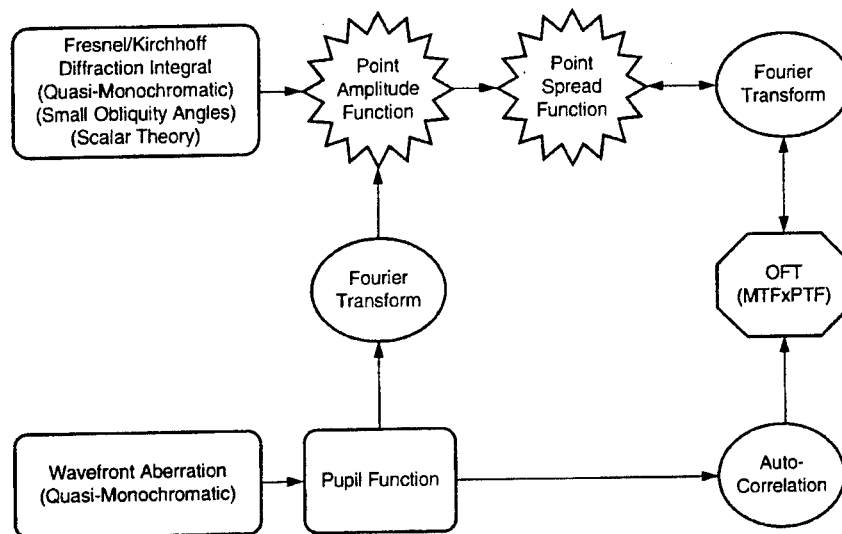


Figure 17. Different concepts and methods for computing the PSF or the OTF for either direct convolution methods or OTF methods of determining and simulating a sensor's imaging properties.

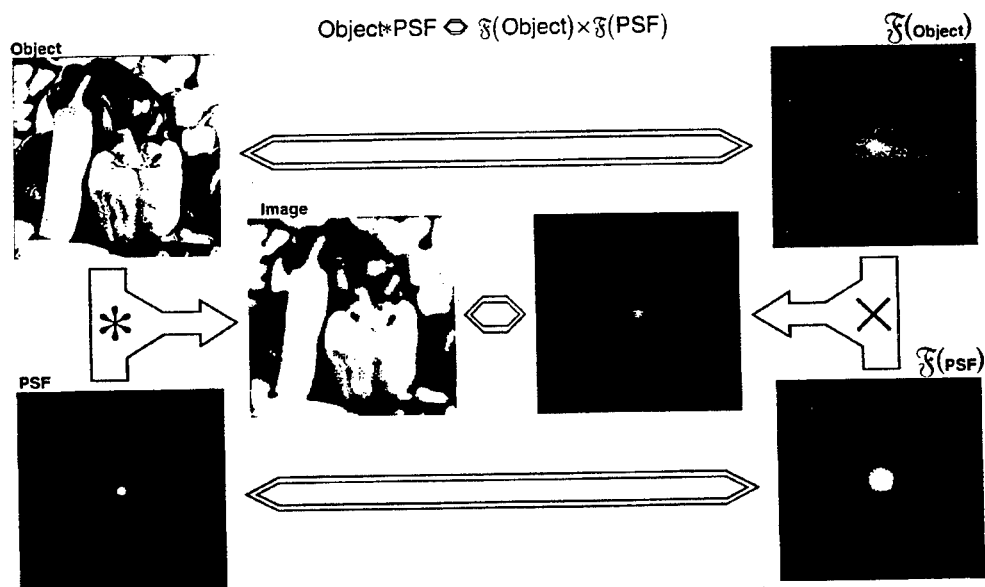


Figure 18. Optical convolution can be accomplished by either direct methods or by indirect FFT methods using the convolution theorem and the OTF of the sensor system (the method chosen depends on computational/photonic speed as well as fidelity issues/trades).

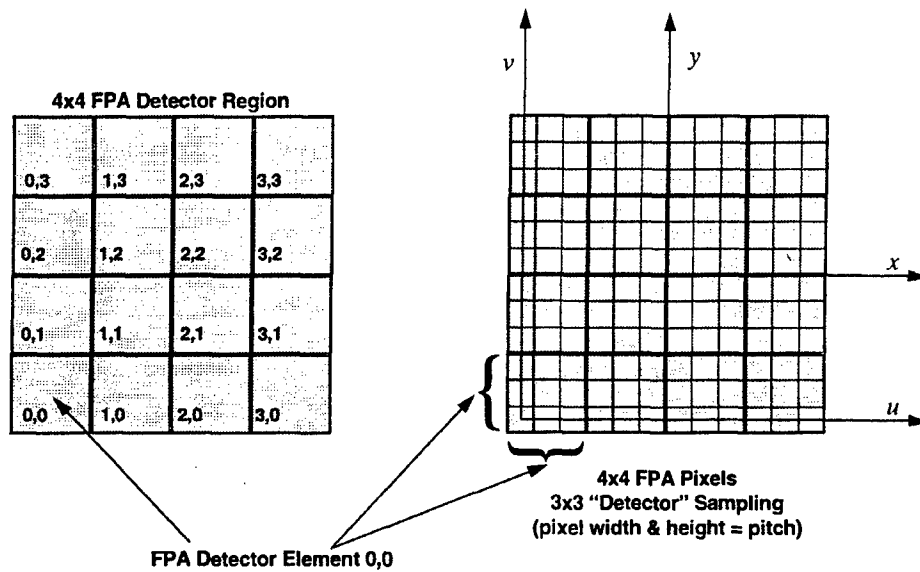


Figure 19. Background, target, and FPA sampling provide efficient and flexible computational schemes for scene extraction and image convolution by employing Whittaker-Shannon sampling ideas.

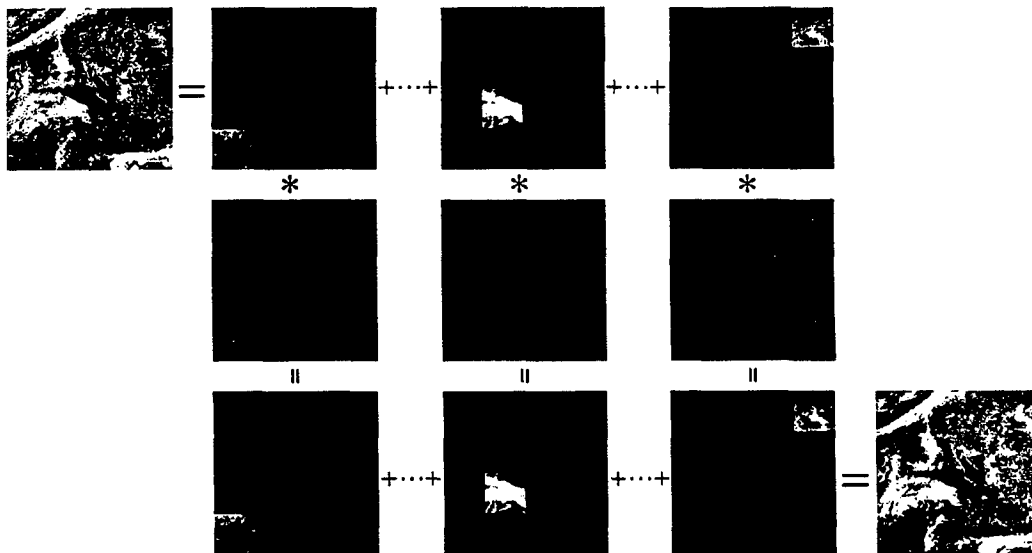


Figure 20. Illustration of a spatial decomposition method to support anisoplanatic optical simulation that could also support parallel and massively parallel processing schemes for the laser-based DWSG photonics.

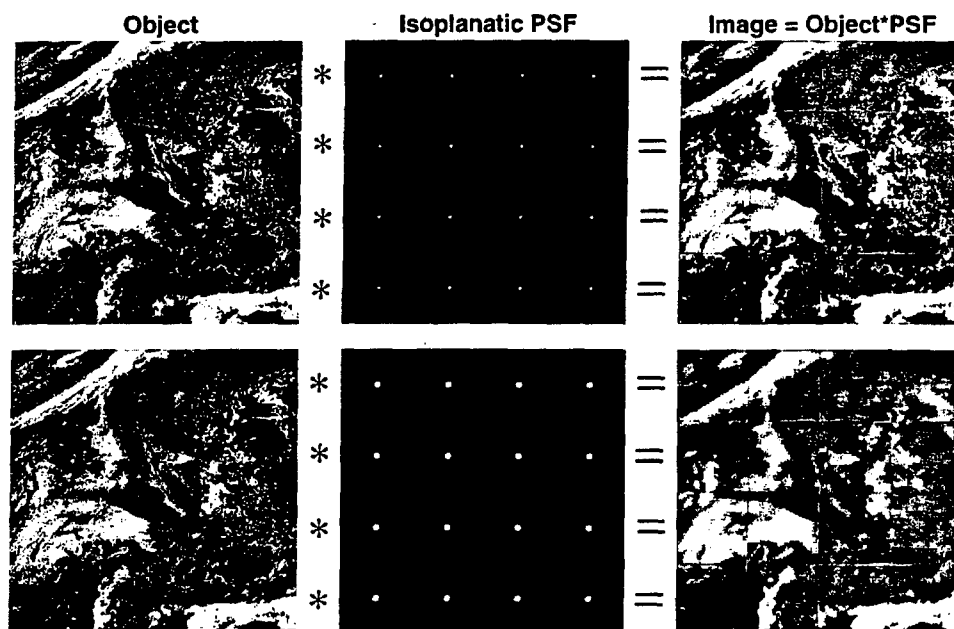


Figure 21. Illustration of a 4x4 optical decomposition to support parallel processing schemes and anisoplanatic optical simulation without any regard for diffraction effects/loss or spectral leakage.

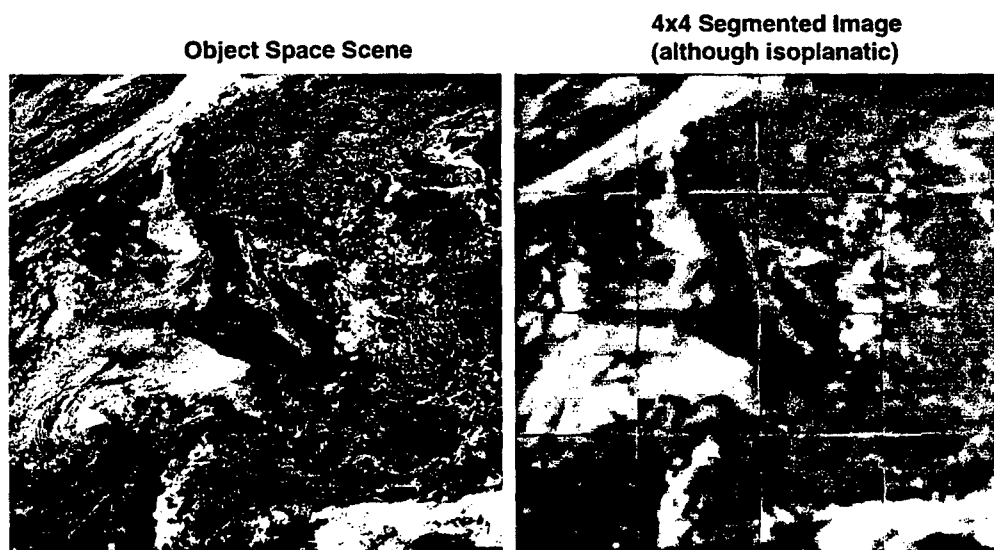


Figure 22. Illustration of potential simulation artifacts that can result from decomposition methods that fail to account for diffraction effects and spectral leakage.

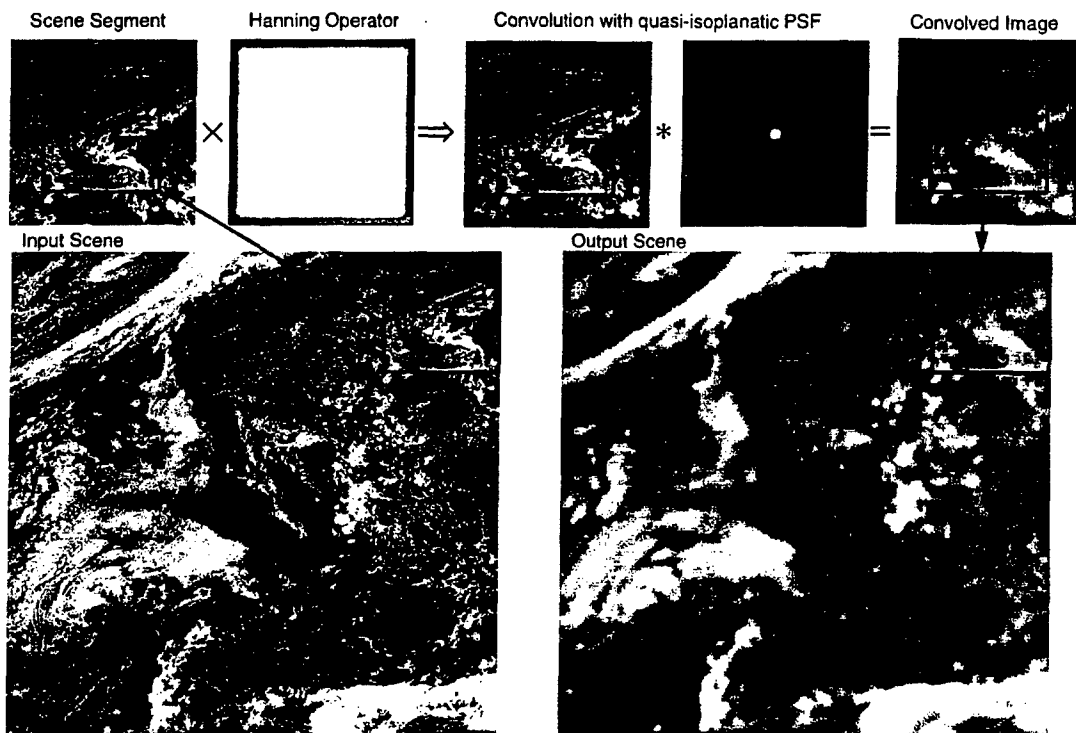


Figure 23. Methodology for using extended computational regions to not only support anisoplanatic decomposition for better fidelity and simulation but to also support real-time closed-loop parallel processing schemes.

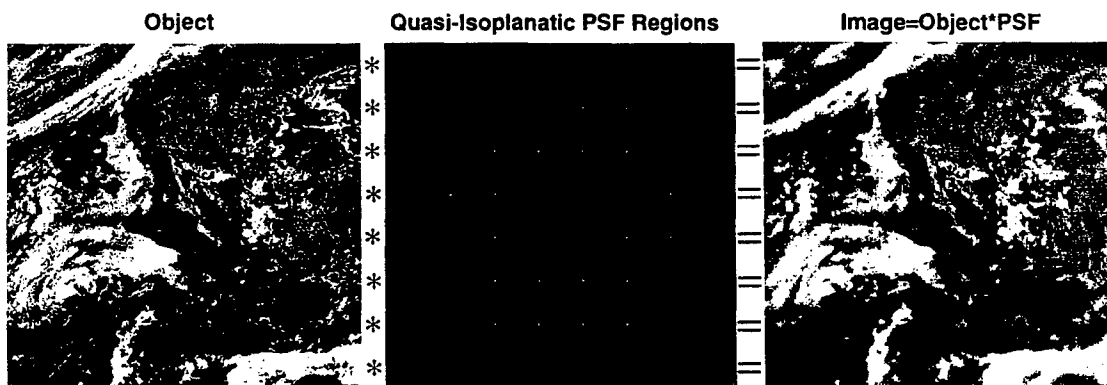


Figure 24. Illustration of a decomposition method to arrive at the composite field of view for an anisoplanatic optical system being simulated in the laser-based DWSG scene generation methodology.

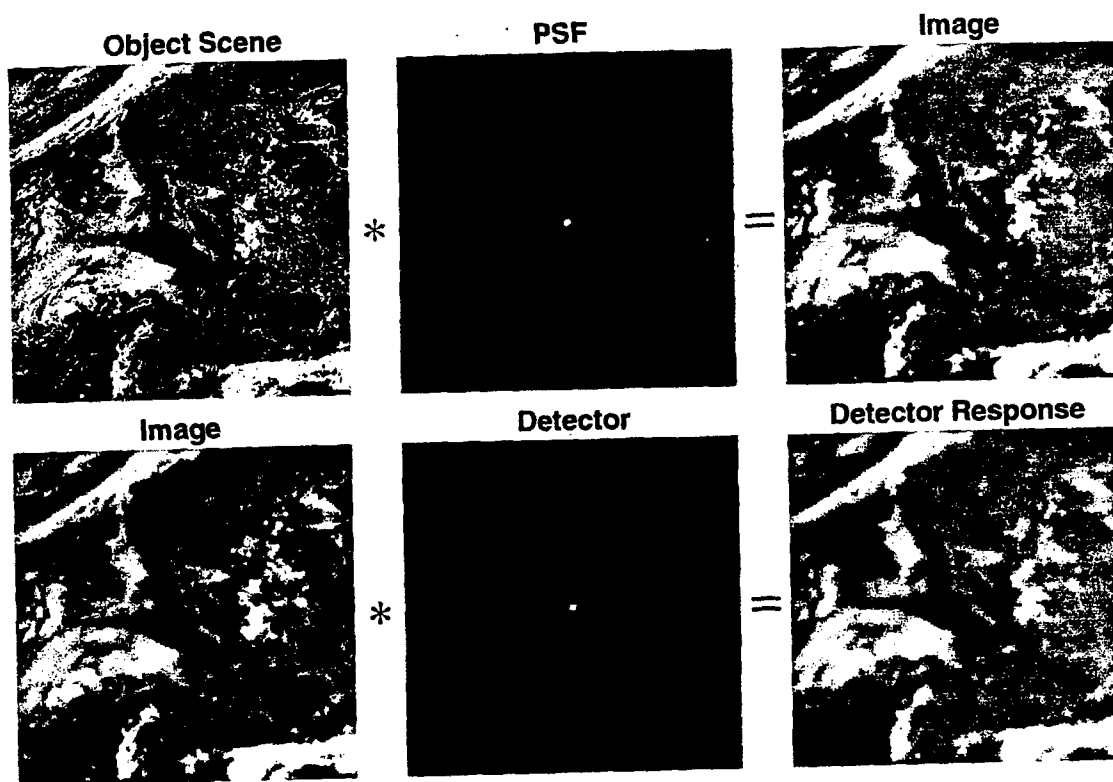


Figure 25. Illustration of methodology to derive the integrated photoflux from a double convolution process that can be accomplished from a more efficient system transfer function operation and application of the convolution theorem.

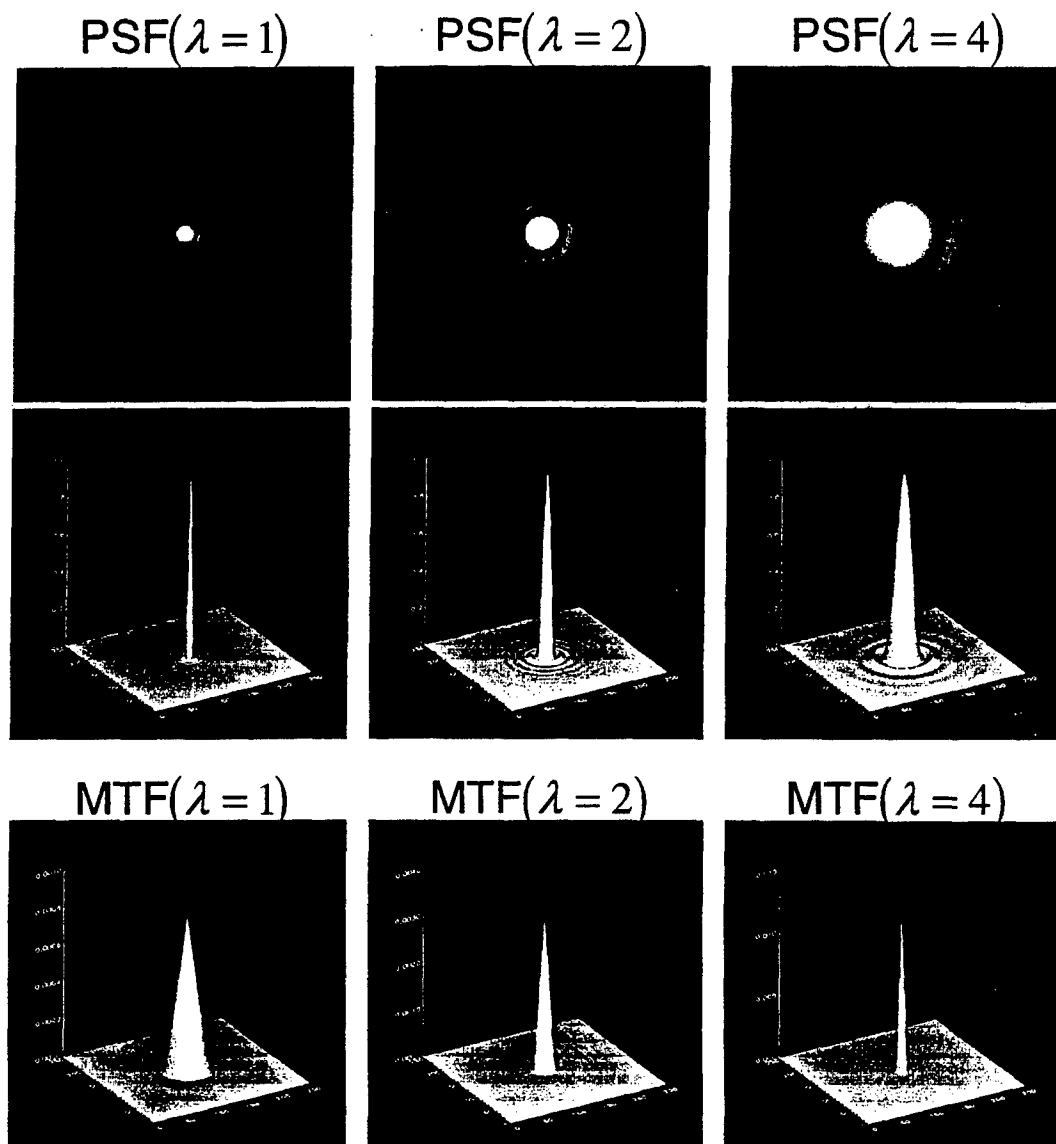


Figure 26. Illustration of the effects of wavelength dependent variation of the PSF and optical cutoff frequency as seen in the magnitude of the optical transfer functions (modulation transfer function, MTF).

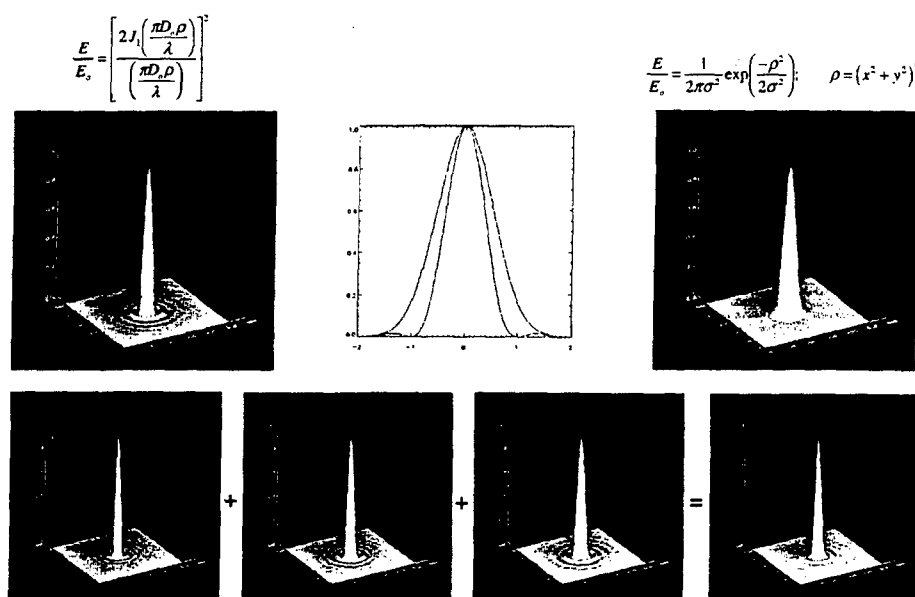


Figure 27. Illustration of the concept of an effective PSF resulting from a number of contributing sources such as broadband radiation, optical diffraction, deterministic and stochastic jitter and resulting blur, or other sources.

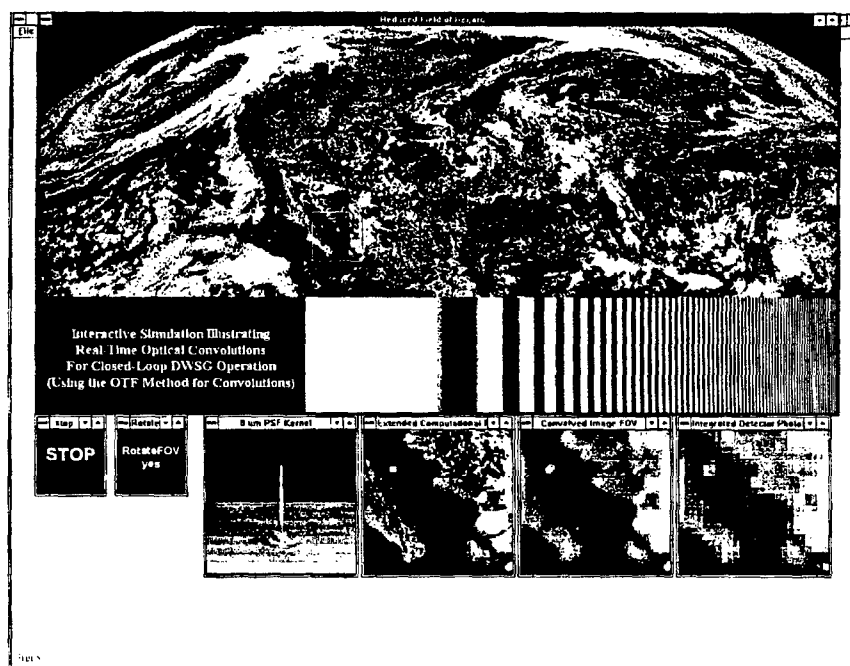


Figure 28. Example of the screen of the closed-loop simulator for algorithm development, diagnostic efforts, and demonstrations.

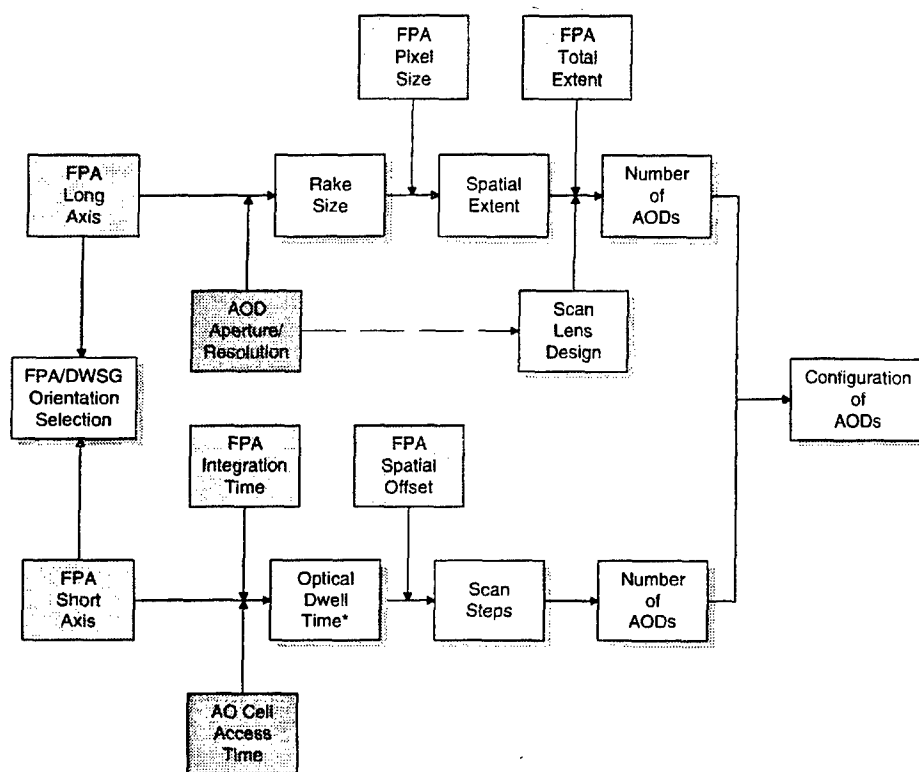


Figure 29. Dependence of DWSG parameters determining a test configuration.

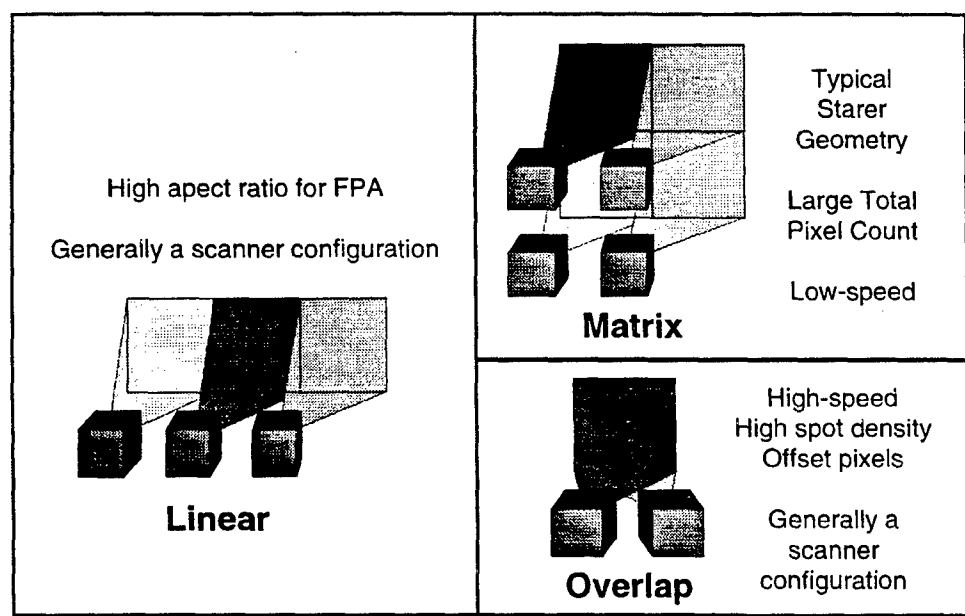


Figure 30. Modular flexibility of the DWSG test configuration.

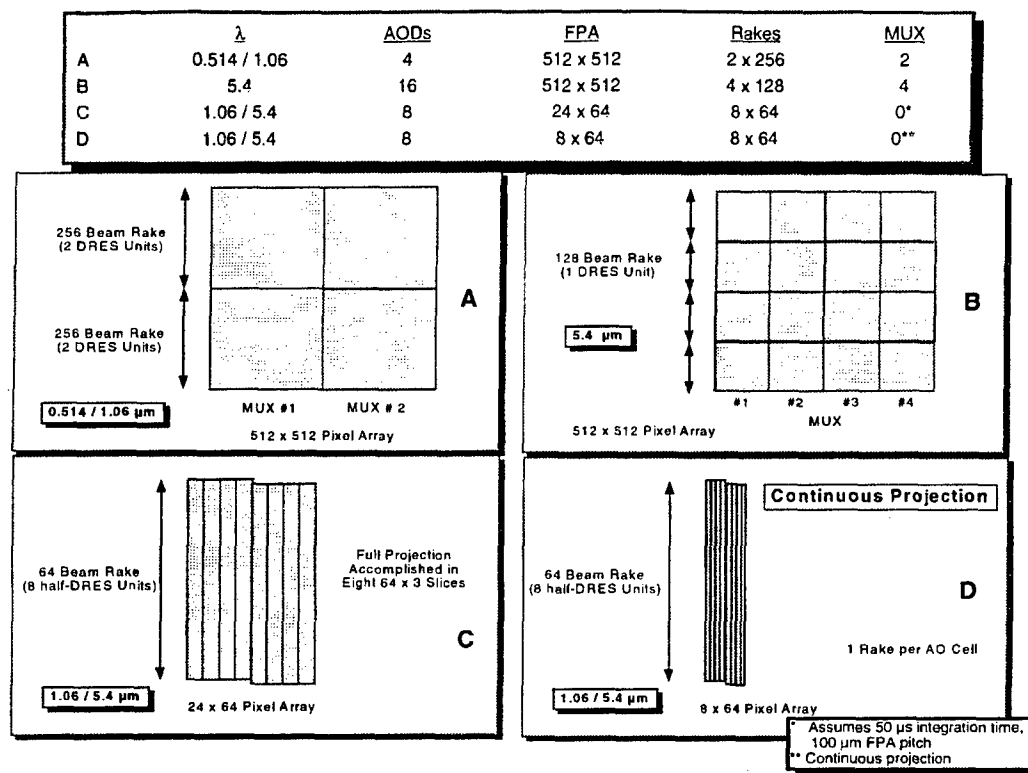


Figure 31. FPATC configuration options for various FPA testing methods.

| DWSG Configuration Calculations | | | | | | | | | | Reset Nominal Configuration | # | Example |
|---|------------------|-------------------------------------|------------------------|------------------------------|----------------------|-------------------|--|--|--|-----------------------------|---|---------|
| FPA Material | Si:As | 128 | Vendor | XXX | Program | Internal Research | | | | | | |
| # Horizontal Pixels: | 128 | # Vertical Pixels (rel): | C | Total # Pixels: | 16384 | | | | | | | |
| Section or complete FPA described (SIC)? | | Active Pixel Dimension (µm): | 100 | Square Pitch (Y/N)? | Y | | | | | | | |
| Ver. Pixel Pitch (µm): | 100 | Horizontal axis extent (nm): | 128 | Fill Factor (%) | 100.0 | | | | | | | |
| Avg. Pixel Pitch (µm): | 100 | Mission wavelength range (µm): | 3 to 12 | Integration time (ms): | 5 | | | | | | | |
| Wavelength range (µm): | | Optical Dwell Minimum (µs): | 2 | Multiplex factor | 1 | | | | | | | |
| Traveling Reset (Y/N): | N | Compatibility measurements at (µm): | 1.06 | | | | | | | | | |
| Number of independent sub-module FPAs: | 1 | | | | | | | | | | | |
| COMPATIBILITY MEASUREMENTS AT 1.06 µm | | | | | | | | | | | | |
| Projection Wavelength (µm): | 1.06 | TDWSG or FPATC? | FPATC | Small Pixel Optics? | N | | | | | | | |
| AOD Material | TeO2 | AOD Module size: | 256 | Scan lens design pitch (µm): | 128:128 | | | | | | | |
| Spatial Averaging | Hor pix: Ver pix | 1:1 | Test article coverage: | 1.31 | Composite pixel (µm) | 100 | | | | | | |
| 90 % encircled energy diameter (µm) | 96.0 | Gaussian % EOAD: | 9.3 | Half time-bandwidth of AOD: | 256 | | | | | | | |
| Percent aperture fill: | 100 | Aperture size (nm): | | | | | | | | | | |
| # Pixels in long dimension: | 128 | AOD's in long dimension: | 1 | Total AODs: | 4 | | | | | | | |
| # Pixels in short dimension: | 128 | AOD's in short dimension: | 4 | | | | | | | | | |
| Scan Steps Covered | 128 | | | | | | | | | | | |
| Access time (µs): | 15 | Step time (µs): | 156.3 | Optical Dwell time (µs): | 141.3 | | | | | | | |
| Percent of module used in step direction: | 12.5 | Steps per module: | 32 | | | | | | | | | |
| REDUCED STEP COVERAGE: OPTIMIZE COVERED PIX | | | | | | | | | | | | |
| SCAN LENS DESIGNED FOR AOD OVERLAP? | | | | | | | | | | | | |
| SUMMARY: | | | | | | | | | | | | |
| Store Data for Mathematics or VB Graphics Program | | | | | | | | | | | | |
| Projection Wavelength (µm): 1.06 | | | | | | | | | | | | |
| Facility: FPATC | | | | | | | | | | | | |
| Number of AODs Needed per Section: 4 (1x4) | | | | | | | | | | | | |
| Optical Dwell Time (µs): 141.3 | | | | | | | | | | | | |
| 90 % enc energy dia (µm): 96.0 | | | | | | | | | | | | |
| Total Number of AODs Needed: 4 | | | | | | | | | | | | |
| Small Pixel Optics? N | | | | | | | | | | | | |
| Spatial Averaging: 1:1 | | | | | | | | | | | | |
| Percent aperture fill: 100 | | | | | | | | | | | | |
| Steps per module: 32 | | | | | | | | | | | | |
| Double Projection Pass? N | | | | | | | | | | | | |
| Number of sections: 1 | | | | | | | | | | | | |

Figure 32. Page one of the DWSG configuration spreadsheet (optical parameters).

| | | | | | | |
|-------------------------------------|--|---|--|-------|------------------------------------|-------|
| DRES: | | Number of channels required per rake: | | 128 | Number of pixels per AOD: | 16384 |
| Number of rakes: | | RF Center Frequency (MHz): | | 1 | Total number of RF channels: | 128 |
| Lower Limit of RF Frequency (MHz): | | RF Bandpass (MHz): | | 70 | Upper Limit of RF Frequency (MHz): | 40 |
| RF Frequency Shift per Pixel (MHz): | | Deflection rate ($\mu\text{m}/\text{MHz}$): | | 50 | Frequency range for scan (MHz): | 90 |
| Frequency range for rake (MHz): | | Aggregate Data rate (Mpix/sec): | | 0.156 | Aggregate Data rate (Mbyte/sec): | 2.5 |
| Data rate per rake (Mpix/sec): | | Optical Dwell Time (μs): | | 20.0 | | 20.0 |
| Data rate per rake (Mbyte/sec): | | | | 3.3 | | 3.3 |
| | | | | 6.6 | | 6.6 |
| | | | | 39.1 | | 24.1 |

Figure 33. Page two of DWSG configuration spreadsheet (electronic parameters).

Laser Irradiance from TDWSG SPA for 128 x 128 Module

Nd:Yag diode-pumped

Amoco 1064EH 350

| | |
|--|----------------------------|
| 100 micron pixel size | 1.06 microns |
| 80 micron 90 % encircled energy spot | 0.45 mm beam diameter |
| 128 step by 128 rake spots | 0.35 W laser output |
| 1 AOD(s) per scan lens | 9.3 mm AOD aperture |
| 1 AOD(s) per laser | 25 % total diffraction eff |
| 100.00 ms integration time (estimated) | 3 dB bandwidth rolloff |
| 98.08 dwell/step percentage | 15 μ s access time |
| 1.00E+11 radiometric background | warm std bandpass filter |

| Conditions at exit of: | condition | % capacity | transmission | photon rate (ph/sec) | beam dia (mm) | irradiance ph/(cm ² sec) |
|----------------------------|-----------|------------|--------------|-------------------------|------------------|--|
| Laser | 0.35 W | 100.00 | 1 | 1.87E+18 | 0.45 | 1.17E+21 |
| stabilization | | 100.00 | 1.00 | 1.87E+18 | 0.45 | 1.17E+21 |
| modulator/blanker | | 67.00 | 0.9 | 1.13E+18 | 0.45 | 7.08E+20 |
| correction wedge | | | 0.95 | 1.07E+18 | 0.45 | 6.72E+20 |
| aperture | | | 0.95 | 1.02E+18 | 0.45 | 6.39E+20 |
| collimator + (diverger) | | | 0.95 | 9.65E+17 | 9.3 | 1.42E+18 |
| neutral density filter | | | 1 | 9.65E+17 | 9.3 | 1.42E+18 |
| initial beamsplitters | | | 1.00 | 9.65E+17 | 9.3 | 1.42E+18 |
| input turning mirrors | | | 0.96 | 9.27E+17 | 9.3 | 1.36E+18 |
| AO deflector X | | 100.00 | 0.50 | 4.63E+17 | 9.3 | 6.82E+17 |
| scan dwell time fraction | | 0.70 | 1 | 3.23E+15 | 9.3 | 4.75E+15 |
| bandwidth rolloff | | | 0.50 | 1.62E+15 | 9.3 | 2.38E+15 |
| AO deflector Y | | 10.00 | 0.50 | 8.09E+13 | 9.3 | 1.19E+14 |
| number of beams in rake | 128 | 0.71 | 1 | 5.75E+11 | 9.3 | 8.46E+11 |
| bandwidth rolloff | | | 0.50 | 2.88E+11 | 9.3 | 4.24E+11 |
| AO turning mirrors | | | 0.97 | 2.79E+11 | 9.3 | 4.11E+11 |
| Main beamsplitter/combiner | | | 1 | 2.79E+11 | 9.3 | 4.11E+11 |
| Scan lens system | | | 0.9 | 2.51E+11 | 9.3 | 3.70E+11 |
| Dewar window | | | 0.95 | 2.39E+11 | 1 | 3.04E+13 |
| Laser line filter | | | 0.7 | 1.67E+11 | 0.5 | 8.52E+13 |
| FPA (single pixel) | | 96.11 | 1 | 1.67E+11 | 0.1 | 2.05E+15 |

Throughput

8.96E-08

Dynamic Range for one pixel (above background level: 1 E+04 is essential)

2.05E+04

Assumes all pixels full on

Consider Additional Safety Factor:

~ 2 if two spectral bandwidths are to be illuminated

Figure 34. Example DWSG laser irradiance calculation spreadsheet.

| | | |
|---|--|---|
| Draw DWSG Configuration | Switch ADD's between Linear and Matrix | Switch Sections between Linear and Matrix |
| Switch between linear and matrix configurations until proper coverage is achieved | | |
| Solid regions are FPA; Outlines are ADD footprints | | |
| Internal Research XXX Si:As 128 x 128 DWSG configuration # Example | | |

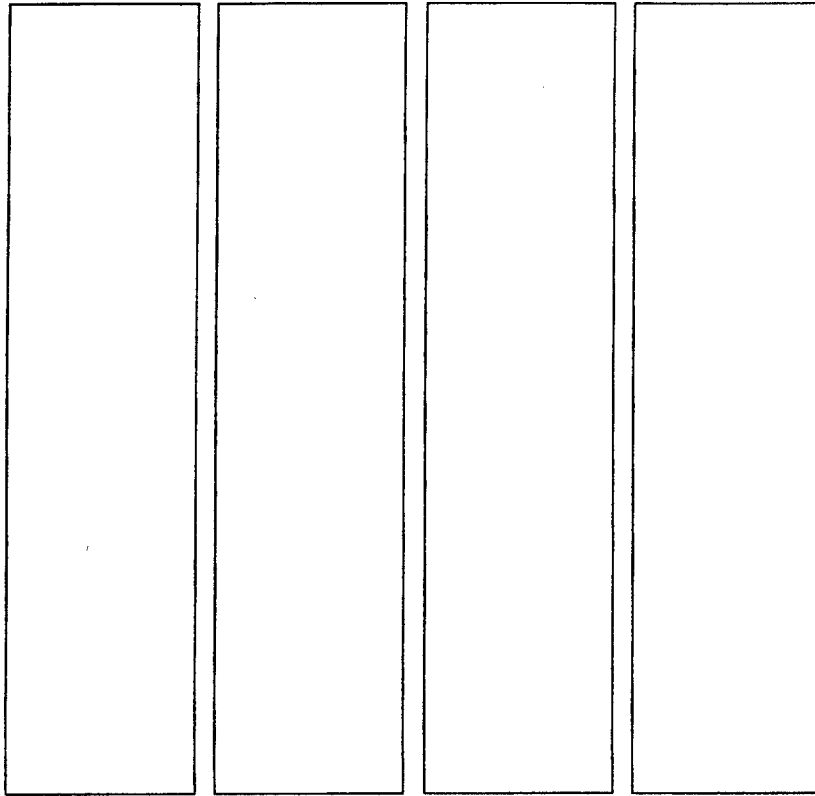


Figure 35. DWSG configuration conceptualization program sample output.

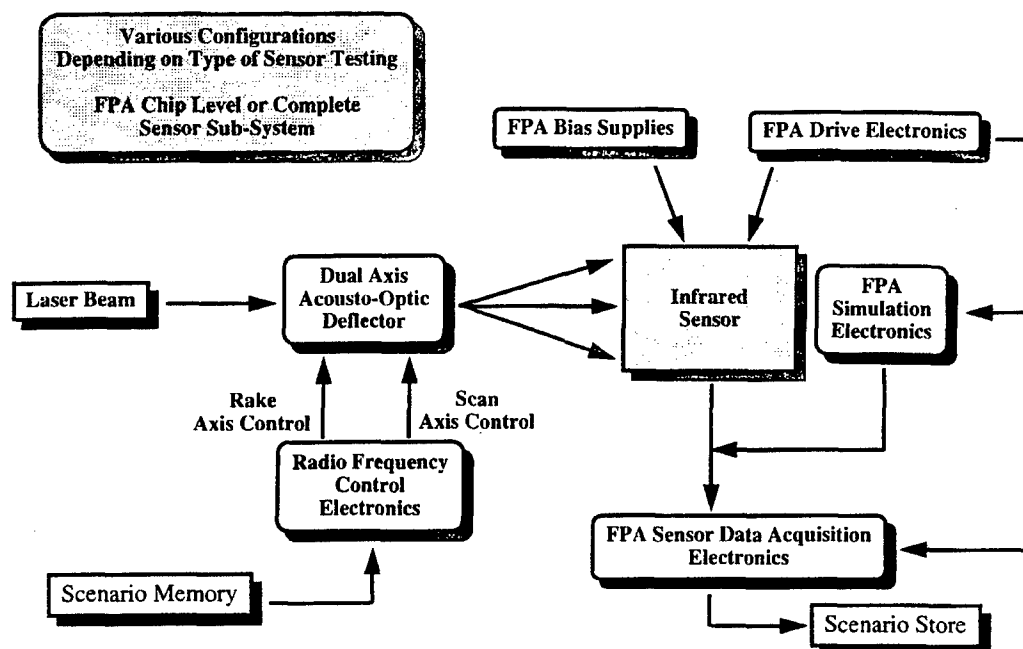


Figure 36. Open-loop FPATC concept.

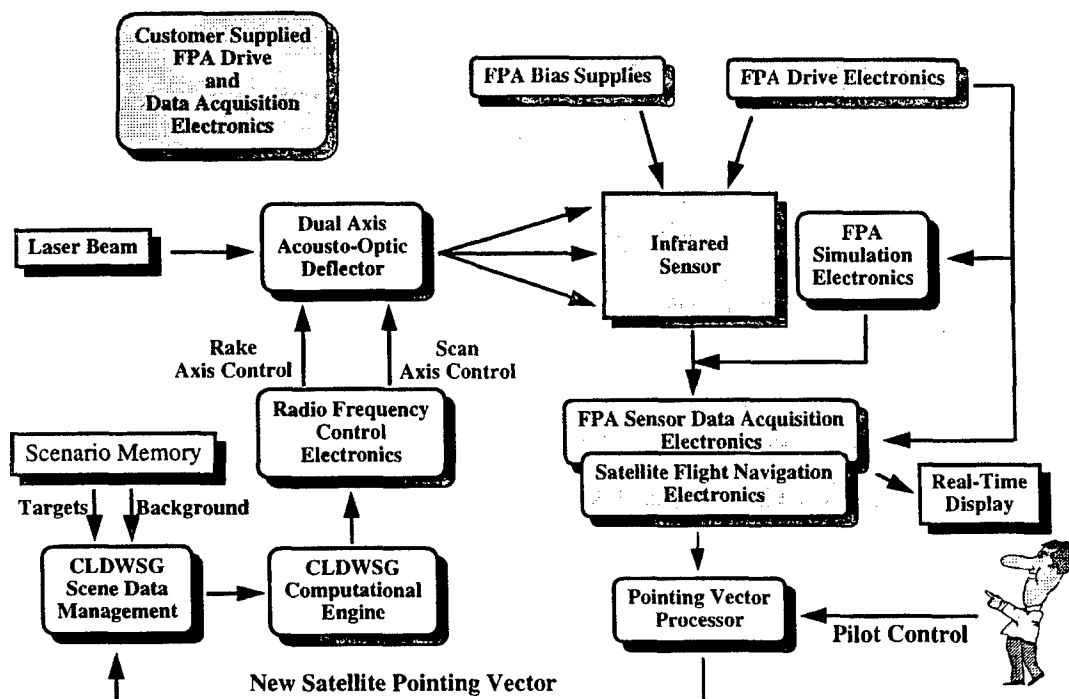


Figure 37. Closed-loop FPATC concept.

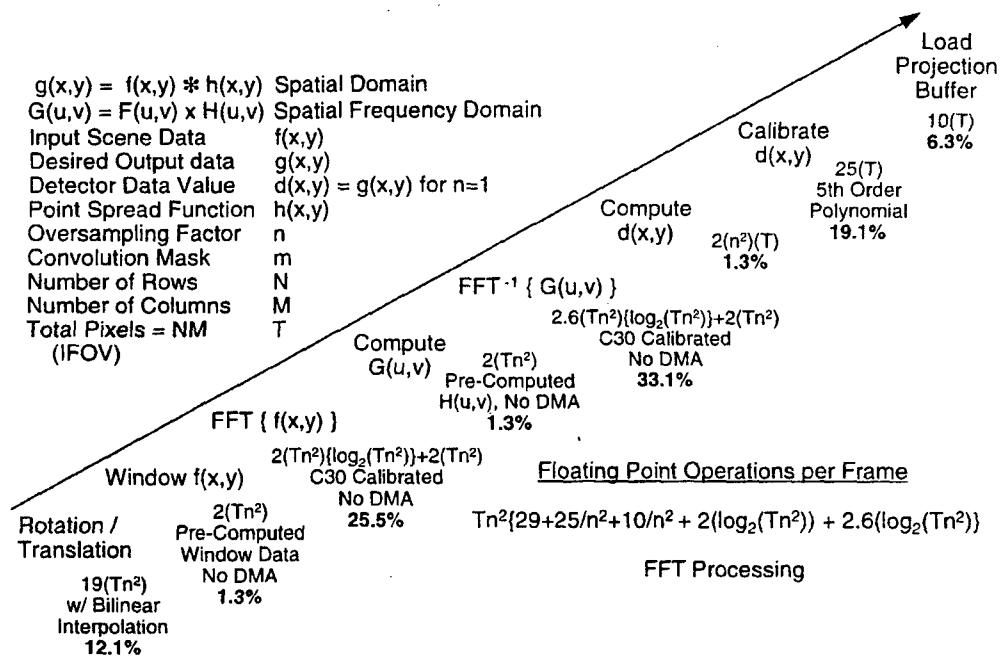


Figure 38. Computational steps required for FPATC closed-loop simulation.

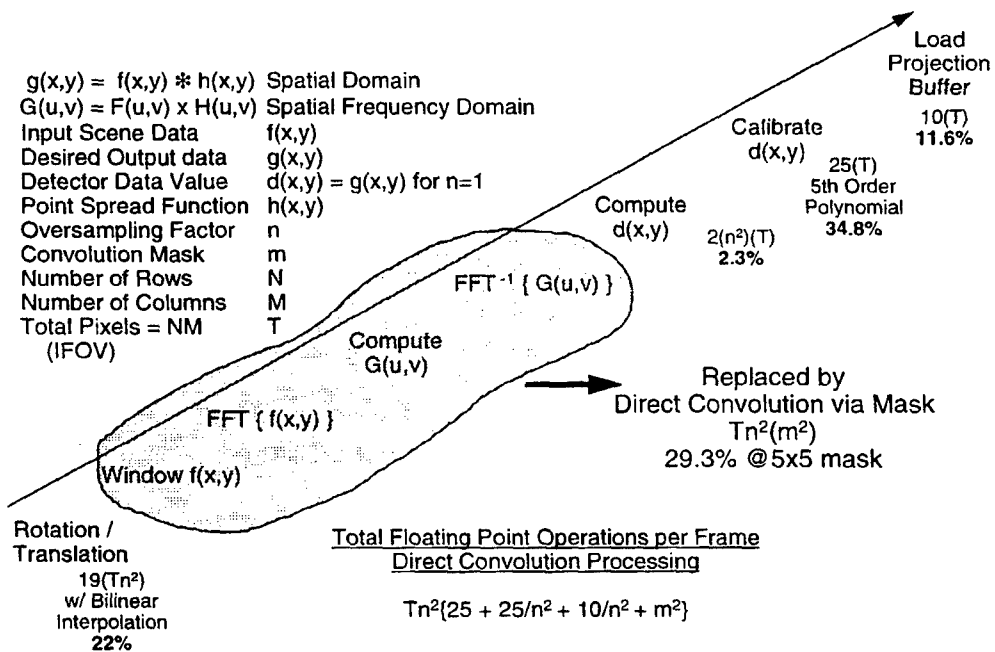


Figure 39. Closed-loop computational steps using direct convolution.

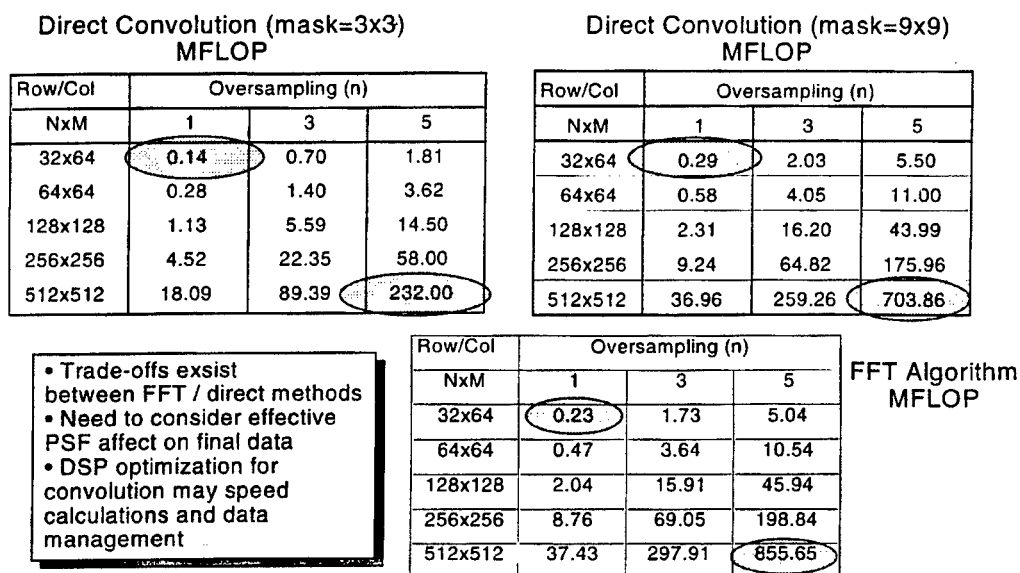


Figure 40. Comparison of direct convolution and FFT computational methods.

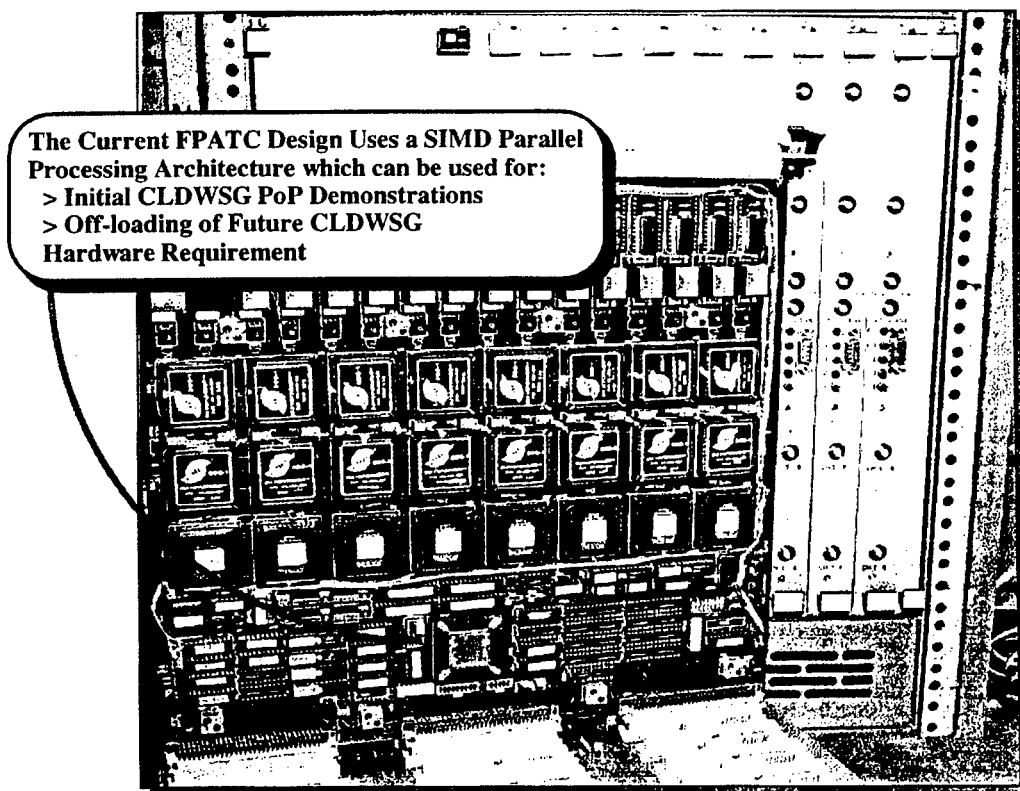
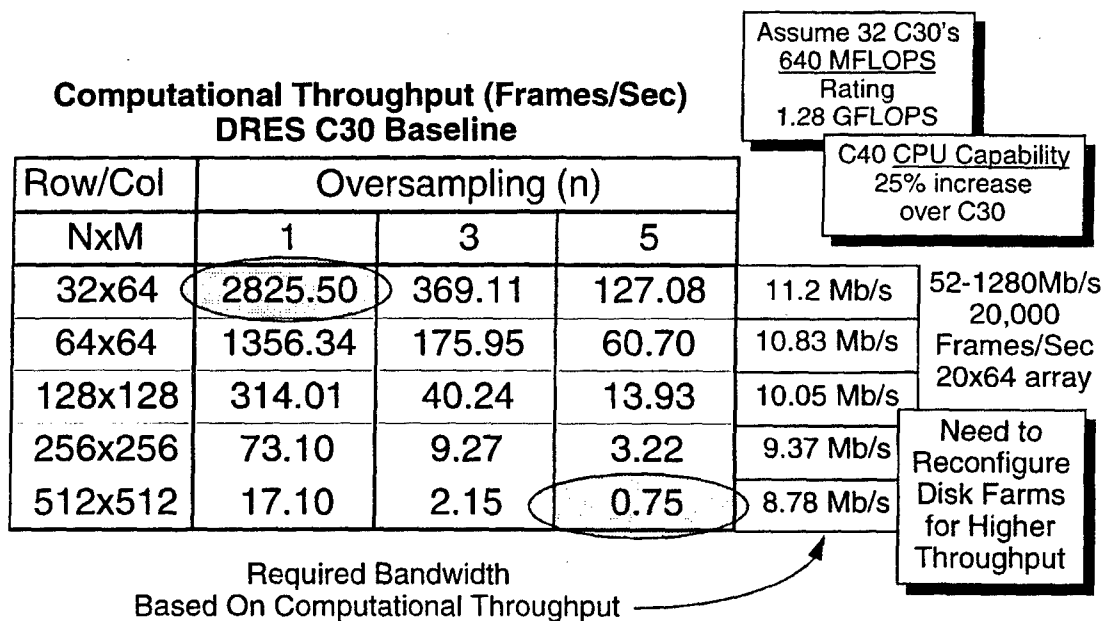


Figure 41. DWSG RF control electronics module.



**Figure 42. Theoretical determination and comparison of the FPATC
RF control-electronics capabilities.**

DOCUMENT 3

Detection Range Performance-Horizon Infrared Surveillance Sensor (HISS)

AD-A307 620

January 1995

**Dahlgren Division
Naval Surface Warfare Center, VA**

**DAHLGREN DIVISION
NAVAL SURFACE WARFARE CENTER**

Dahlgren, Virginia 22448-5100



NSWCDD/MP-94/363

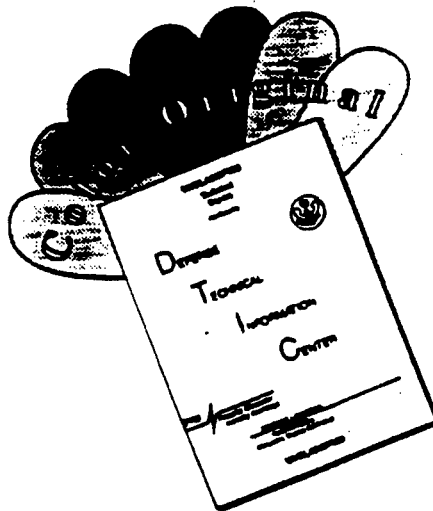
**DETECTION RANGE PERFORMANCE-HORIZON INFRARED
SURVEILLANCE SENSOR (HISS)**

**BY PATRICK A. DEZEEUW
SHIP DEFENSE SYSTEMS DEPARTMENT**

JANUARY 1995

Approved for public release; distribution is unlimited.

DISCLAIMER NOTICE



THIS DOCUMENT IS BEST QUALITY AVAILABLE. THE COPY FURNISHED TO DTIC CONTAINED A SIGNIFICANT NUMBER OF COLOR PAGES WHICH DO NOT REPRODUCE LEGIBLY ON BLACK AND WHITE MICROFICHE.

REPORT DOCUMENTATION PAGE

Form Approved
OBM No. 0704-0188

Public reporting burden for this collection of information is estimated to average 1 hour per response, including the time for reviewing instructions, searching existing data sources, gathering and maintaining the data needed, and completing and reviewing the collection of information. Send comments regarding this burden or any other aspect of this collection of information, including suggestions for reducing this burden, to Washington Headquarters Services, Directorate for Information Operations and Reports, 1215 Jefferson Davis Highway, Suite 1204, Arlington, VA 22202-4302, and to the Office of Management and Budget, Paperwork Reduction Project (0704-0188), Washington, DC 20503.

| | | | | | |
|--|---|--|-----------------------------------|---|--|
| 1. AGENCY USE ONLY (Leave blank) | | 2. REPORT DATE January 1995 | | 3. REPORT TYPE AND DATES COVERED | |
| 4. TITLE AND SUBTITLE DETECTION RANGE PERFORMANCE-HORIZON INFRARED SURVEILLANCE SENSOR (HISS) | | | | 5. FUNDING NUMBERS | |
| 6. AUTHOR(s) Patrick A. Dezeeuw | | | | | |
| 7. PERFORMING ORGANIZATION NAME(S) AND ADDRESS(ES) Commander Naval Surface Warfare Center, Dahlgren Division (Code F44) 17320 Dahlgren Road Dahlgren, VA 22448-5100 | | | | 8. PERFORMING ORGANIZATION REPORT NUMBER NSWCDD/MP-94/363 | |
| 9. SPONSORING/MONITORING AGENCY NAME(S) AND ADDRESS(ES) | | | | 10. SPONSORING/MONITORING AGENCY REPORT NUMBER | |
| 11. SUPPLEMENTARY NOTES | | | | | |
| 12a. DISTRIBUTION/AVAILABILITY STATEMENT Approved for public release; distribution is unlimited. | | | | 12b. DISTRIBUTION CODE | |
| 13. ABSTRACT (Maximum 200 words) The Horizon Infrared Surveillance Sensor (HISS) Phase 2 system was involved in field testing at Wallops Island, Virginia from November 1993 through April 1994. This report discusses the HISS project and presents results from the analysis of system detection range performance. The HISS Phase 2 detection range performance has been used to demonstrate IR contributions to an integrated sensor system and to verify detection range predictions and improve the fidelity of current detection range performance models. | | | | | |
| 14. SUBJECT TERMS horizon infrared surveillance sensor, infrared, detection range | | | | 15. NUMBER OF PAGES | |
| | | | | 16. PRICE CODE | |
| 17. SECURITY CLASSIFICATION OF REPORT UNCLASSIFIED | 18. SECURITY CLASSIFICATION OF THIS PAGE UNCLASSIFIED | 19. SECURITY CLASSIFICATION OF ABSTRACT UNCLASSIFIED | 20. LIMITATION OF ABSTRACT SAR | | |

NSN 7540-01-280-5500

Standard Form 298 (Rev 2-89)
Prescribed by ANSI std. Z39-18
298-102

FOREWORD

The Horizon Infrared Surveillance Sensor (HISS) Phase 2 system was involved in field testing at Wallops Island, Virginia from November 1993 through April 1994. This report discusses the HISS project and presents results from the analysis of system detection range performance. The HISS Phase 2 detection range performance has been used to demonstrate IR contributions to an integrated sensor system and to verify detection range predictions and improve the fidelity of current detection range performance models.

I wish to acknowledge the following members of the HISS test team for the operation of the HISS system during the data collection period: Everett Bryant, Connie Huffman, Keith Merranko, Sheldon Zimmerman, Ken Hepfer and Robert Headley.

This report has been reviewed by Roger Carr, Head, Photonic Systems Branch and Stuart Koch, Head, Search and Track Division.

Approved by:

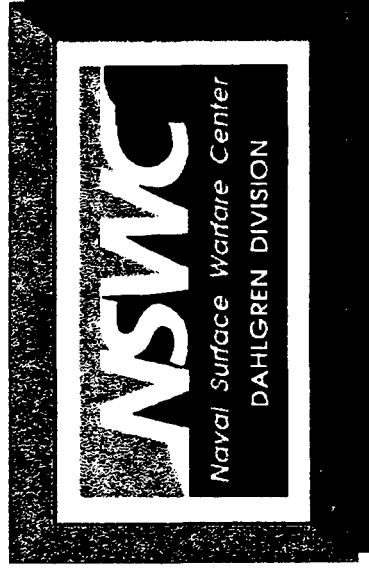


T. C. PENDERGAST, Head
Ship Defense Systems Department

NSWCDD/MP-94/363

This report presents preliminary results from our recent field tests of the Horizon Infrared Surveillance Sensor (HISS) Phase 2 system performed by the Photonic Systems Branch at the Naval Surface Warfare Center, Dahlgren Division (NSWCDD).

Detection Range Performance Horizon Infrared Surveillance Sensor



**Analysis of Test Data Collected
at NSWCDD / Wallops Island Detachment,
November 1993 through April 1994**

**Patrick A. Dezeuw
Photonic Systems Branch, Code F44
Naval Surface Warfare Center, Dahlgren Division**

A background of the HISS system and a description of the Wallops Island test setup are provided. The variation in the intensity of a towed, height-keeping target known as the TLX-1 and an explanation of this variation are also provided.

The detection range performance data for 25 TLX target runs is presented, and an analysis of this data in a number of different formats is provided. The performance prediction analysis that was done is described and compared with the Wallops Island test results.

Finally, data results are summarized and conclusions provided.



Outline

- HISS Introduction / System Description
- Wallops Island Test Description
- Description of TLX Target
- Detection Range Performance Data
- Comparison with Predicted Performance
- Summary

NSWCDD/MP-94/363

The primary goal of the HISS project is to provide risk reduction to the surface Navy'sIRST engineering and manufacturing development by demonstrating basic horizonIRST hardware.

This includes the development at NSWCDD of special target detection-discrimination algorithms which were implemented in real-time hardware.

The HISS project was developed to support on-going experiments in the area of multi-sensor integration (MSI).

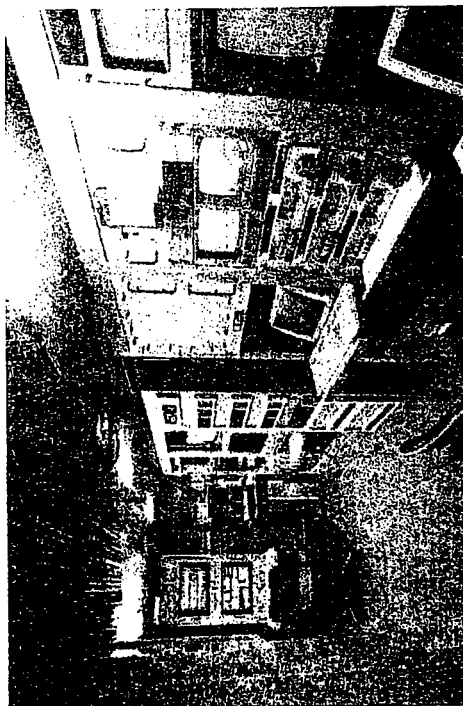
Another important goal is to use the data gathered to compare predicted detection range performance against achieved performance to validate currentIRST performance models.

Also from these tests, we have collected a large database of high resolution, high sensitivity digital video imagery which includes target, background and clutter data. The data gathered and lessons learned will be passed to follow-on efforts.



Goals of the HISS Project

- Demonstrate basic horizon IRST hardware
- Develop / Implement real-time target detection processing
- Demonstrate IR contributions to an integrated sensor system
- Verify detection range predictions
- Provide data and experience for follow-on efforts
 - high resolution / high sensitivity images
 - land background data
 - solar clutter data
 - etc.



The HISS project follows a phased approach to reduce risk and provide interim capability. Each phase focuses on a certain part of the Infrared Search and Track (IRST) detection problem. Lessons learned from each phase are applied to the next phase.

- In Phase 1, data was recorded using a high resolution, high sensitivity, 3-to 5- μ m staring sensor at the Wallops Island facility. In the follow-on data analysis effort, target detection algorithms were developed which provided suitable target detection performance in terms of detection range in non-real time.
- In Phase 2, previously developed signal processing algorithms in a real time signal processor were implemented. The team also participated in real-time multisensor integration (MSI) testing.
- In Phase 3, both sensor and processing aspects of the system are upgraded to demonstrate a full performance horizon IRST. The Phase 3 system is also designed to gather data to evaluate the merit of dual subband operation as an additional discrimination tool.



Three Phase Approach

- **Phase 1**
 - prototype a sensor of requisite sensitivity and resolution
 - develop target detection algorithms (non-real time)
- **Phase 2**
 - prototype real time signal processor which implements the algorithms developed under phase 1
 - develop interface to MSI processor
- **Phase 3**
 - prototype mirror stabilized scanner configuration
 - upgrade signal processor capacity

The HISS system is designed to address the most stressing threat to the ship's combat system under a wide variety of weather conditions.

The system must have the resolution to discriminate targets from clutter near the horizon. This equipment is designed to be a component of multi-sensor integration system and must have a false alarm rate (FAR) consistent with MSI operation.

The system is designed for land-based and shipboard field testing.

The system must process infrared (IR) imagery, develop detections and provide those detections to an MSI processor with minimal latency. (Typically, the detection report will leave the system less than 100 msec after the IR radiation first impinges on the sensor.)



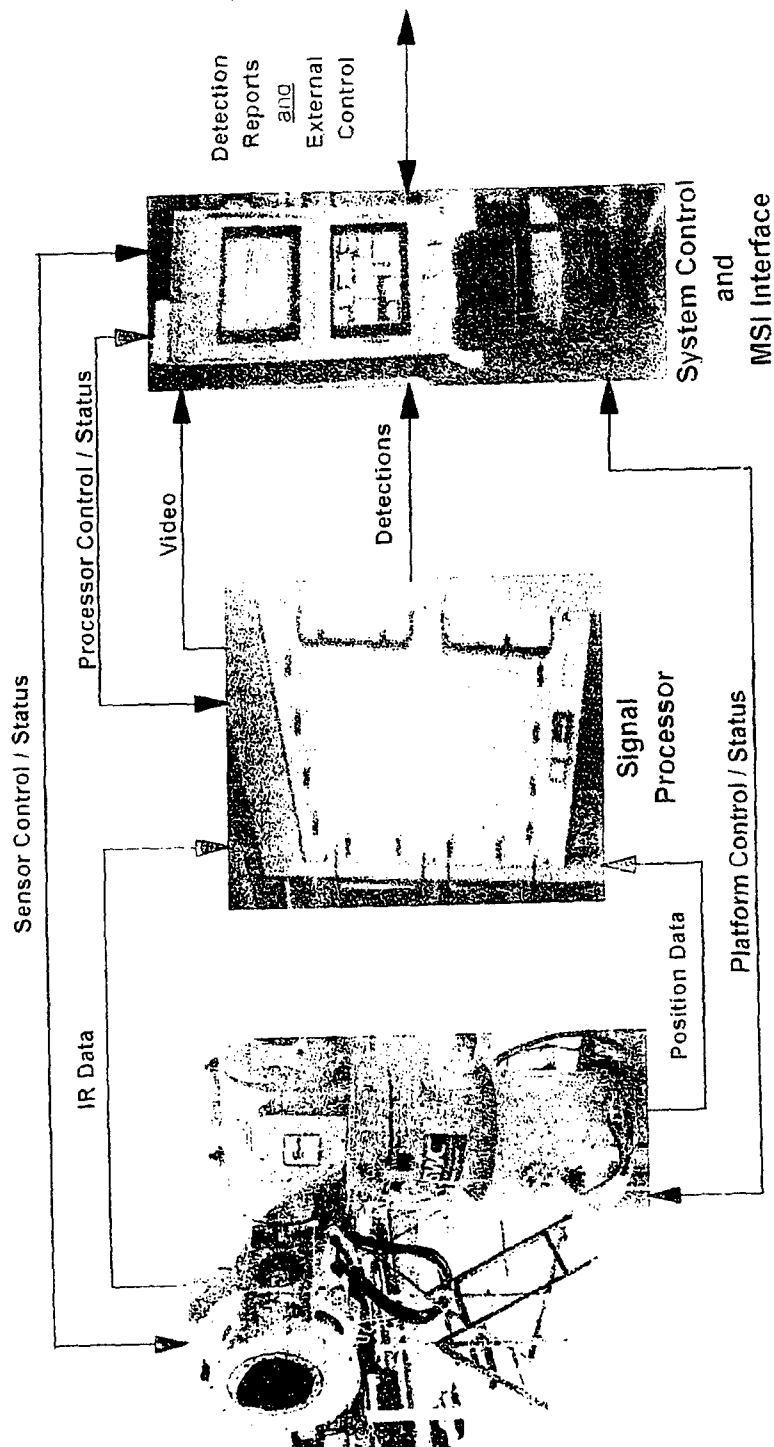
Level of Performance Required

- Detect supersonic (M2+), low flying targets at the horizon limit under most weather conditions
- Discriminate targets from near horizon clutter with a FAR consistent with MSI operation
- Operate in both land-based and shipboard test environments
- Provide target information in real-time to an external interface

NSWCDD/MP-94/363

This figure shows how the sensor and pedestal data are processed into detection reports that are sent to the system control center for transmittal to the MSI interface.

HISS Phase 2 System Block Diagram



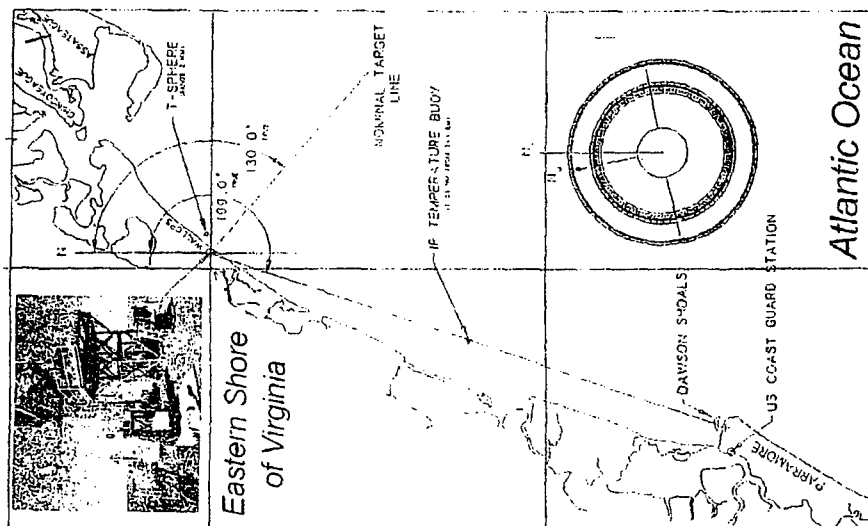
Field testing of the HISS Phase 2 system took place at Wallops Island Detachment, NSWCDD from November 1993 through April 1994.

This test location is a fully instrumented test range on the eastern shore of Virginia that allows for presentation of targets in a littoral environment.

This map shows the location of the test site with respect to the line-of-site of the targets.



Map of the Wallops Island Test Area



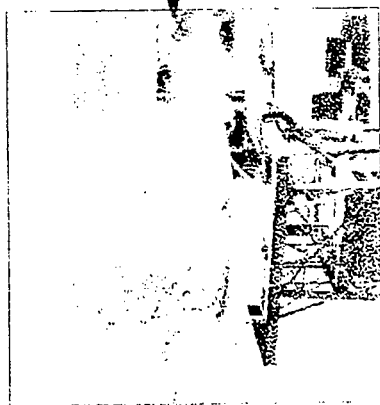
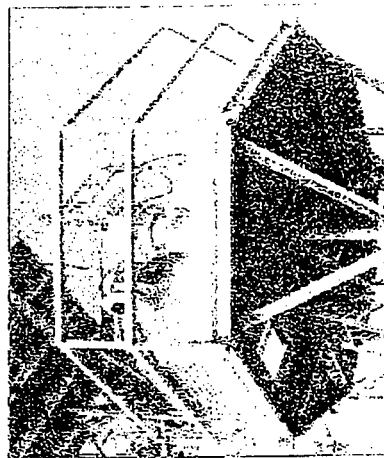
- Tests were performed at the Wallops Island Detachment of the Naval Surface Warfare Center / Dahlgren Division
- This is an instrumented test range on the Atlantic Ocean
- The nominal target line for aircraft, towed targets, and boat targets was 130 to 140° True.
- Variable height targets were also located at Parramore Island on 199° True.

This is the suite of equipment that participated in MSI testing at Wallops Island. The sensor and scanner for the HISS Phase 2 system is shown in the upper right.

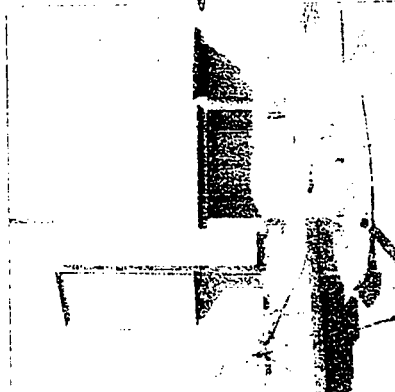
The equipment used in this test operated in real time to provide information to an MSI processor, which could then selectively cue the sensors. For instance, the HISS search zone could be cued based upon a radar contact.

The experiment also included a suite of IR and radio frequency (RF) propagation measurement equipment and meteorological data collection equipment.

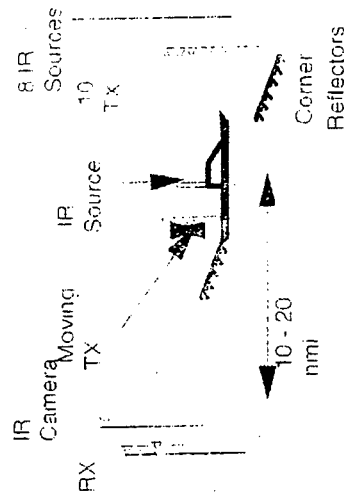
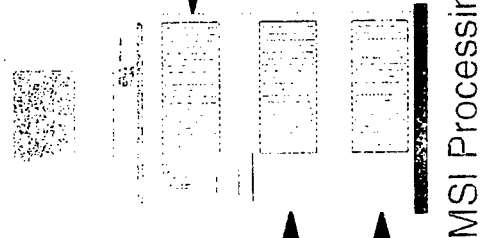
Wallops Island Experiment Equipment



Radar



Electronic Support Measures



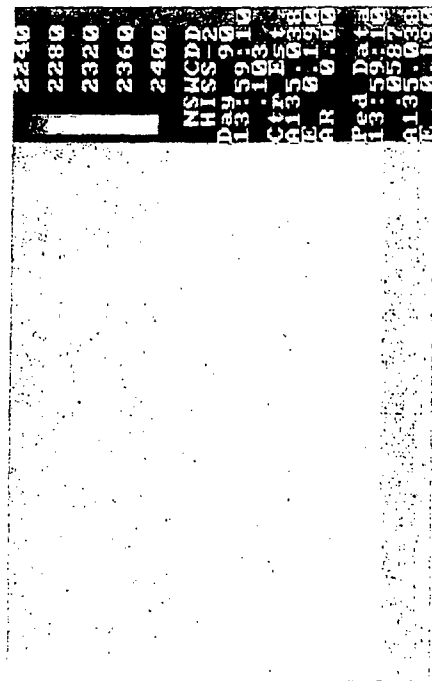
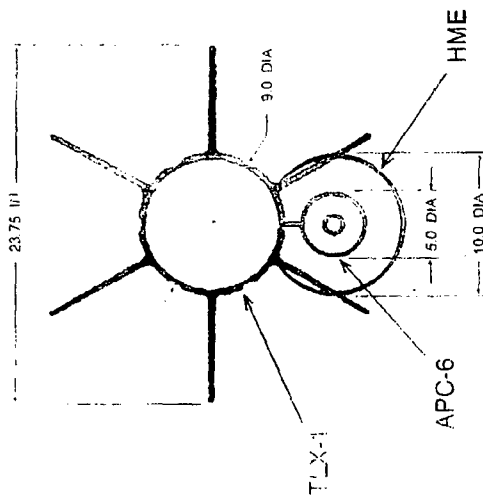
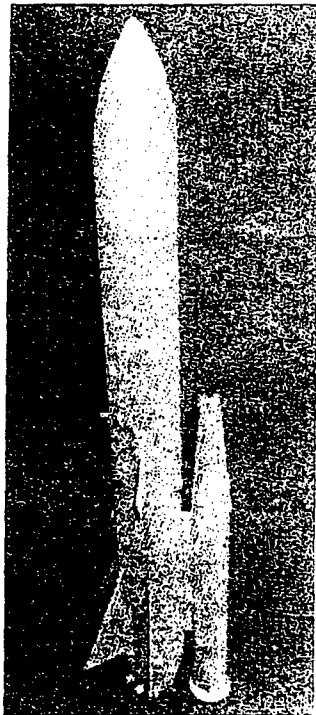
PROPAGATION MEASUREMENT

The subject of this report is the detection range performance of the HISS Phase 2 system against the TLX-1 towed, height-keeping target configured with an APC-6 plumer and hot metal emitter (HME). The APC-6 has an HME to produce IR radiation with spectral content more characteristic of the body radiation from a supersonic (Mach 2+) cruise missile.

Originally the HME had a diameter of 6.54 in. and a measured IR signature of 6 W/sr in-band. For the purpose of this test, it was replaced with a new configuration that has a 10-in. HME. The IR signature for the 10-in. HME was calculated to be about 20 to 40 W/sr. Unfortunately, the 10-in. HME had an unforeseen consequence on the drag of the TLX target that will be discussed latter.

This figure shows a side-aspect picture of the TLX with the 6.5-in. HME and a front-aspect diagram of the TLX with the 10-in. HME. It also shows some sample imagery of the TLX at a range of 15.7 nmi and an altitude of 30 ft.

TLX - Towed, Height-Keeping Target with Plumer and Hot Metal Emitter



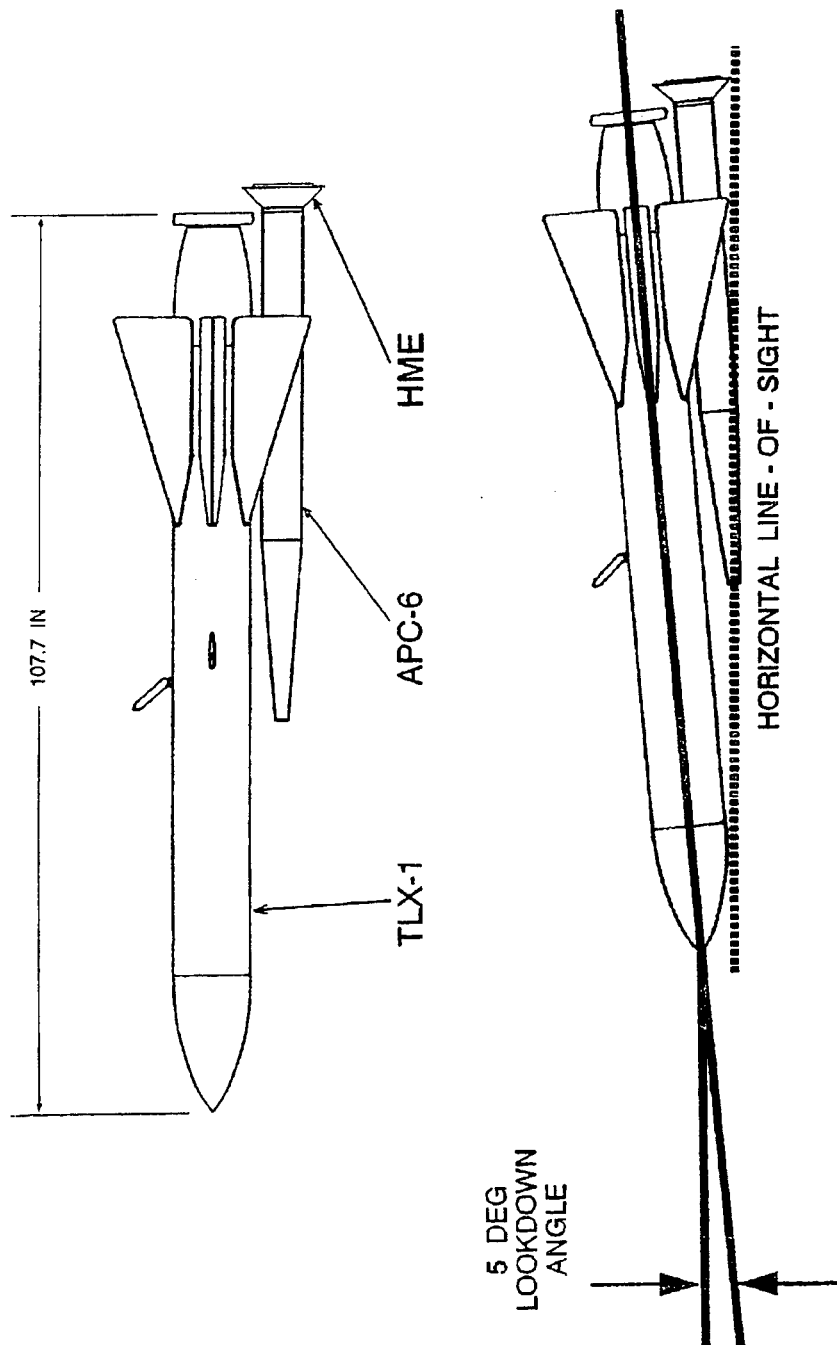
HISS Phase 2 Recorded Image
TLX, altitude: 30 feet, Range: 15.7 Nmiles

Adding the 10-in. HME resulted in increased drag on the lower rear of the TLX, which caused it to fly with the nose tilted down. Review of video taken with a Wallops Island surveillance video camera shows the TLX tilt-down angle to be approximately 5 deg.

As shown in this illustration, it is clear that when the line-of-sight to the target is exactly nose-on, there will be major obstruction of the HME. The HME is visible only when looking at the target from a side-aspect angle.

Further confirmation of this effect is shown next.

Effect of Drag on TLX Obscuration of HME



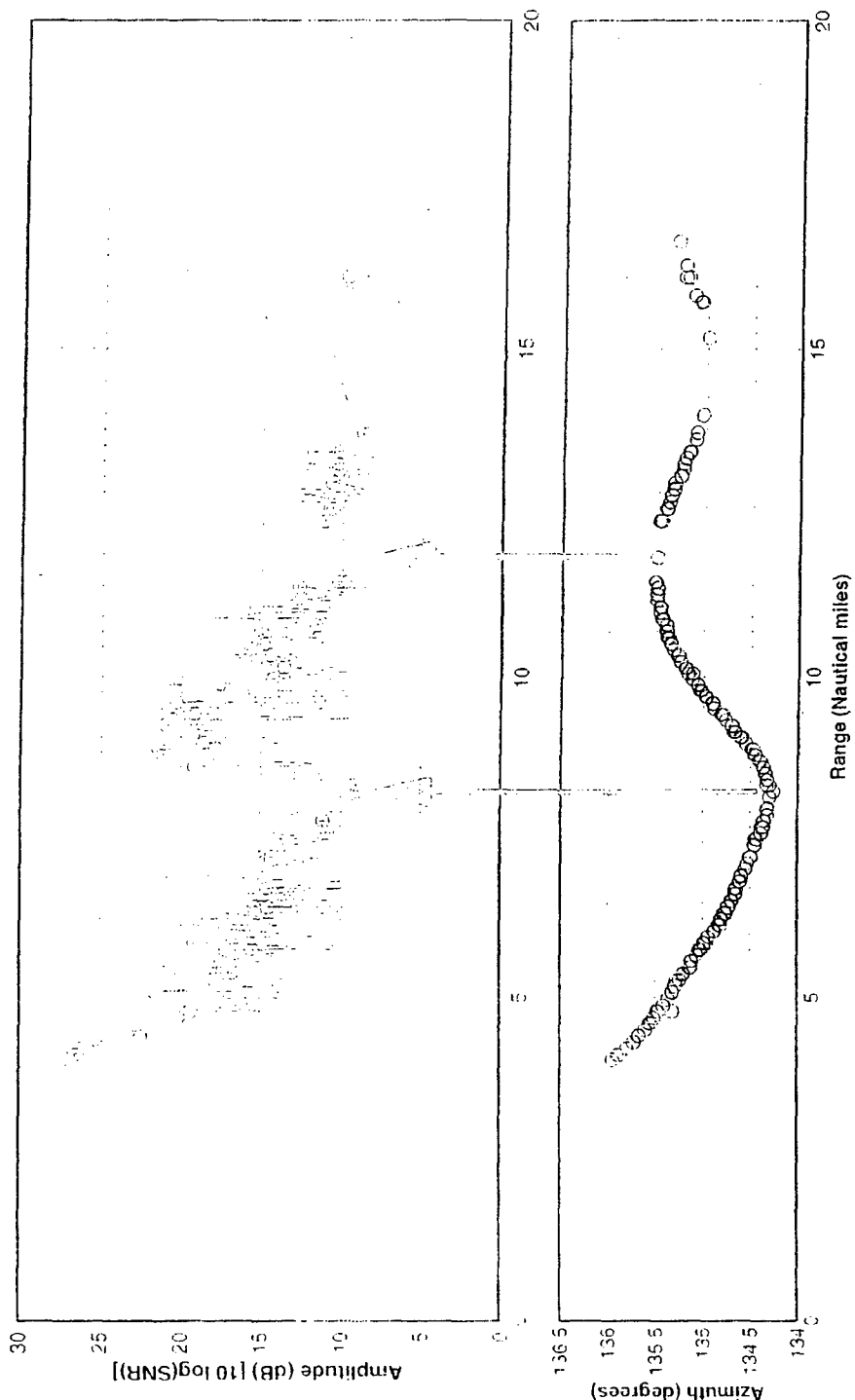
This is a sample of HISS detection data for event MSI-1, run 6, on March 22, 1994, which shows the target amplitude versus range compared with the target azimuth versus range.

From this comparison, it is clear that the maximum amplitude occurs when the target is at a side-aspect angle and that the minimum amplitude occurs when the target is at a front-aspect angle. This data sample is representative of all the TLX runs.

This data sample is further confirmation that the TLX was flying nose down and obscuring the HME when at a front-aspect angle.

Although this obstruction resulted in large variations in the apparent intensity of the TLX, the HISS performed extremely well at detecting the target.

Amplitude Variation Amplitude Nulls and Target Motion



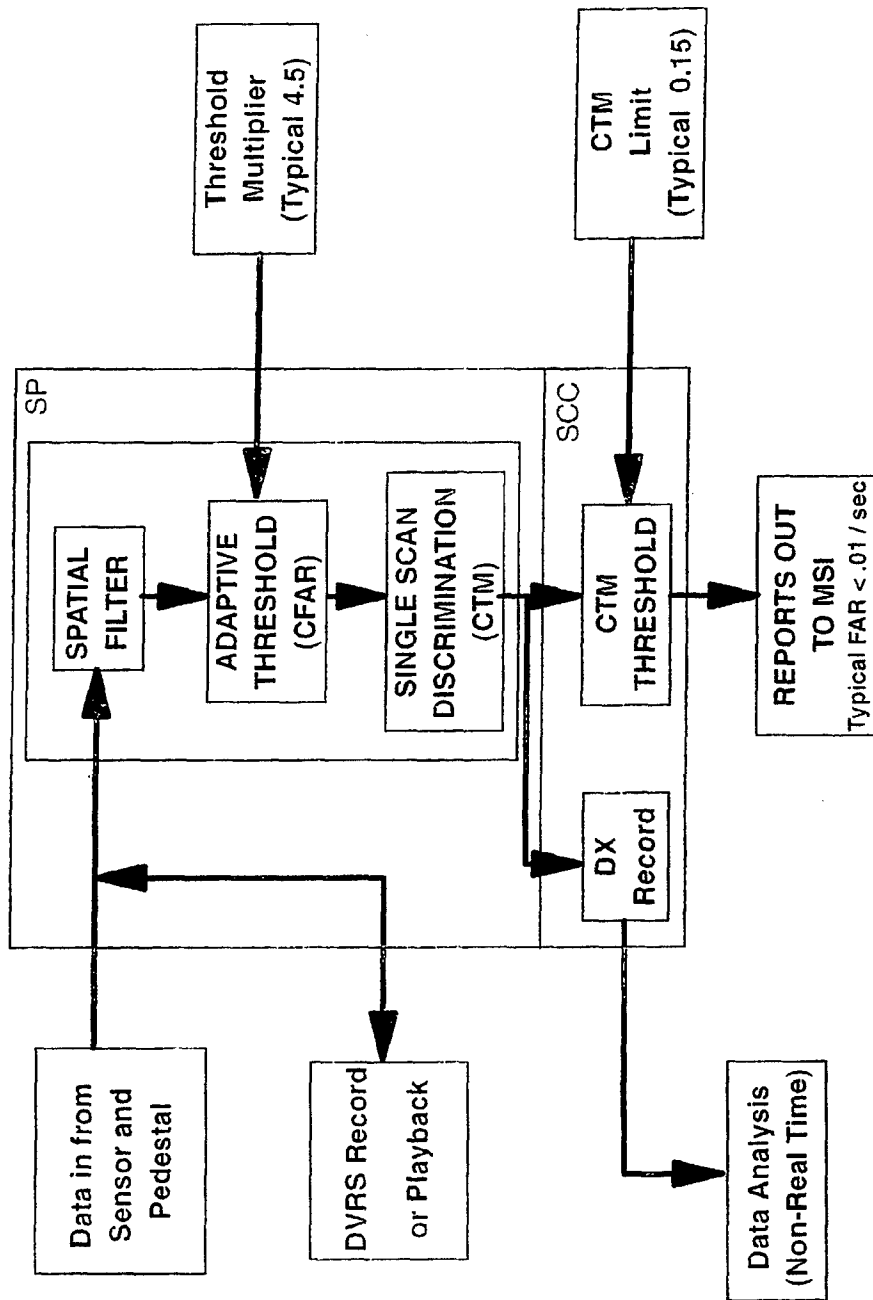
Before presenting the detection range results, some of the signal processor functions need to be described. The major steps in the signal processor are: the spacial filter to suppress extended objects the adaptive threshold to achieve an approximate constant FAR over the field of view and the single-scan discrimination function to rate each detection as to how *target like* it is. Comprehensive target metric (CTM) is the numerical value used to rate detections.

Although the signal processor is capable of producing up to 1000 detection reports per second, the threshold multiplier within the signal processor was usually set to produce something on the order of 100 reports per second or less.

Within the system control center (SCC), there is a CTM threshold function to further limit the detection reports sent out of the system to the multisensor integration program (MSIP). During MSI testing, the CTM threshold was typically set at 0.15 but was often raised to as much as 0.25 in cases of extreme clutter. The FAR out of the system to the MSIP was typically less than 0.01/sec.

Note that within the SCC, the data extraction function records all of the detection reports and this is the source for the detection range analysis.

Data Flow Block Diagram **Horizon Infrared Surveillance Sensor**



The following data results are based on an analysis of 25 tests events where the target was an inbound TLX towed target and the HISS was operated in a normal scan mode. Test events where there was evidence that the TLX plumer did not burn properly or the HME did not get up to the required temperature were eliminated from this data analysis.

Also, the TLX data does not include runs with extremely bad weather. Due to safety constraints, the aircraft towing the target was required to operate under visual flight rules (VFR) and could not be operated in extremely bad visibility conditions.

The detection data was processed using a detection merging algorithm to cluster groups of detections from a frame into a single detection. This detection merge algorithm is part of the current HISS Phase 3 processing.

This algorithm was useful because it reduces the amount of data to analyze and provides a correct *count* of detections. It does not affect the overall detection ranges associated with detection reports.



Overview of Data Analysis

- 25 Data Runs
 - Inbound TLX towed target runs
 - HISS scan mode only
 - Good HME burns only
 - Weather conditions above VFR minimums
- Detection Merging Algorithm
 - Clusters groups of detections from a frame
 - Part of current HISS phase 3 processing
 - Provides a correct count of detections
 - Does not effect overall detections ranges

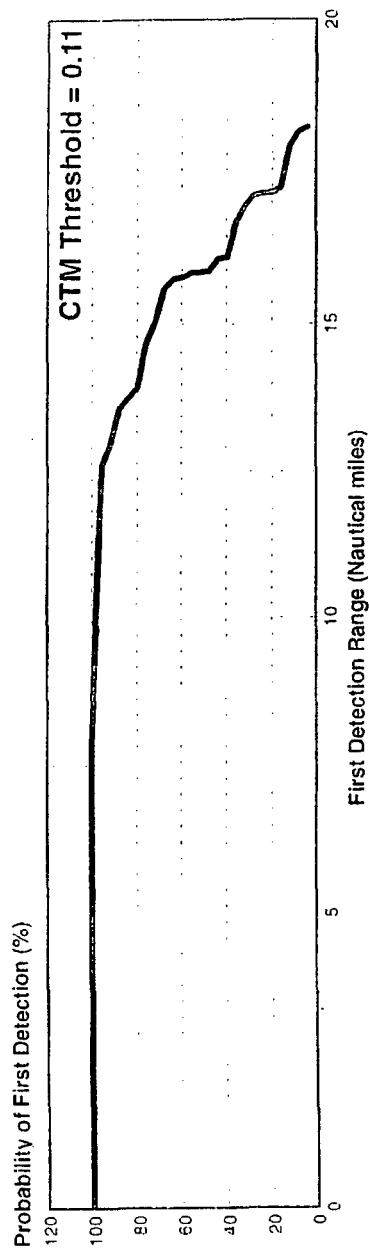
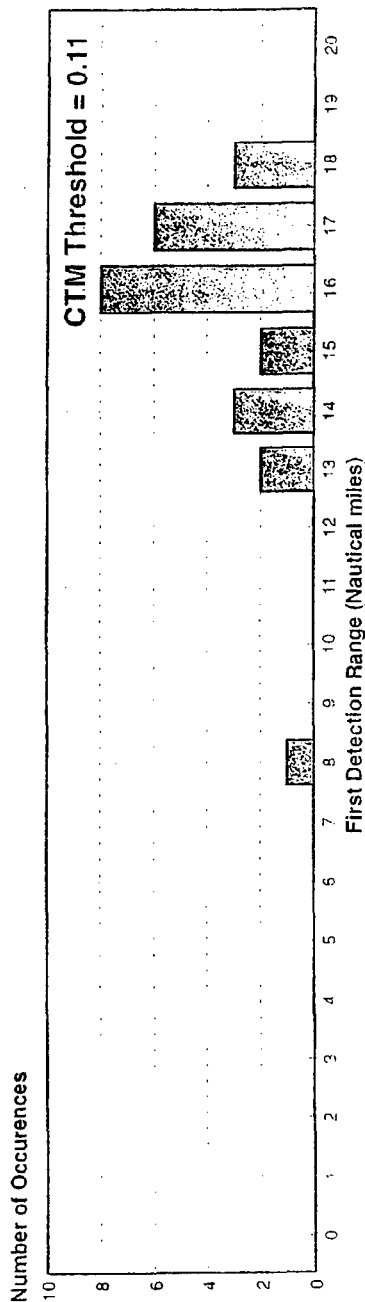
This figure shows the first detection range and the probability of detection for the 25 runs. For presentation purposes, the detection ranges were rounded to the nearest nautical mile.

Note that only detections above a CTM of 0.11 are included. Early FAR analysis indicated that a CTM limit of 0.11 would produce a FAR of about 1/sec under typical clutter conditions. This is the threshold that is used throughout this data analysis.

However, this was not the CTM limit that was used during testing to threshold detection reports to the MSI interface. The CTM threshold to the MSI interface was typically 0.15 or higher. This will be discussed in more detail later.

From this data distribution, one can see that the maximum first detection range was about 18 nmi, the minimum first detection range was about 8 nmi, and the median first detection range was about 16 nmi.

Probability of Detection TLX Towed Target - 25 sorties

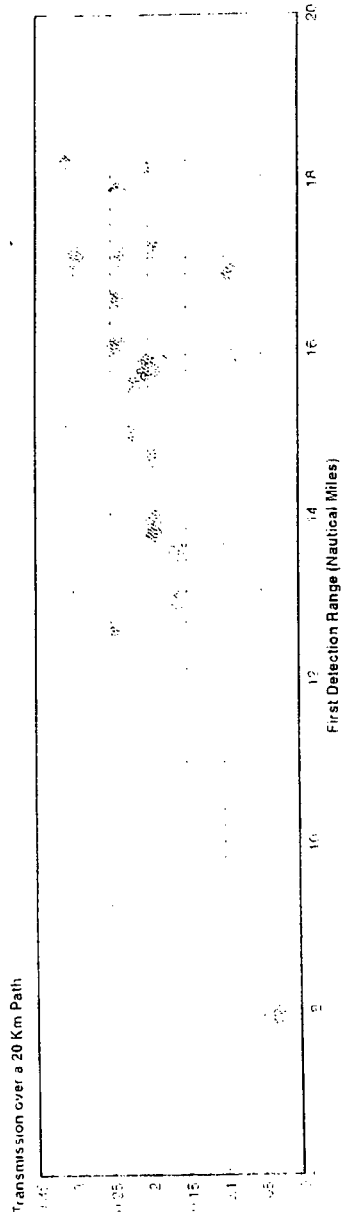
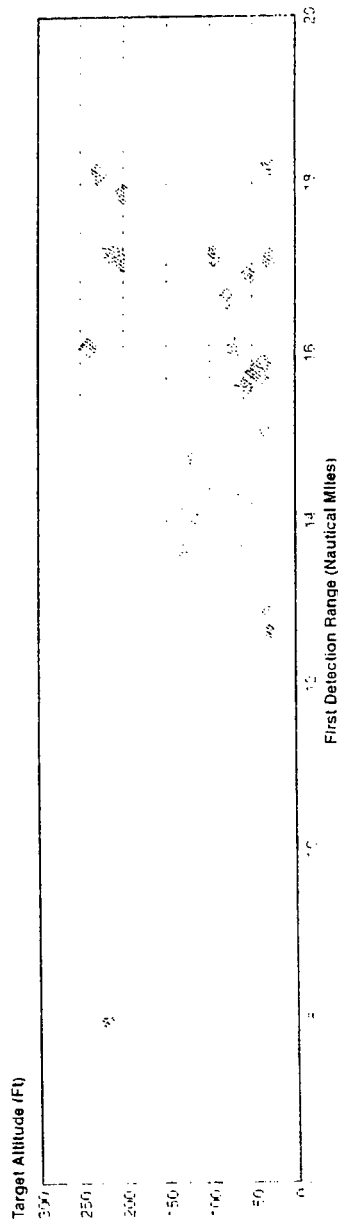


The test events using the TLX towed targets were typically conducted in a sequence of four inbound *burn* runs per day. The first run was usually around 200-ft altitude, and the next three runs were each at lower altitudes, approaching the intended altitude of 30 ft.

This figure shows the effects of target altitude as compared with the effects of atmospheric transmission in-band over a 20 Km path on first detection range. In the top chart, there is no apparent correlation between altitude and detection range. The longest detection range was at a high altitude. In the bottom of the figure, however, there does appear to be a correlation between atmospheric transmission on detection range. The longest detection range occurred during the time of the highest IR transmission. The shortest detection range occurred during the time of the lowest IR transmission.

On the previous figure, it was apparent that on a single day you could see the effect of altitude on reducing detection range. But if you look at all of the runs, it appears that the TLX altitude was not the most significant factor on reducing detection range, rather the overwhelming factor is the change in atmospheric transmission from day to day.

Target Detection Range Altitude vs Transmission



This figure shows a stacked bar graph that distributes the 25 maximum detection ranges by test day. From this distribution, some daily trends in the data can be seen. As expected, there are some days when the HISS performed better than others. For example, on day 089, the HISS had three long detection ranges; and, on day 083, the HISS had the shortest detection range.

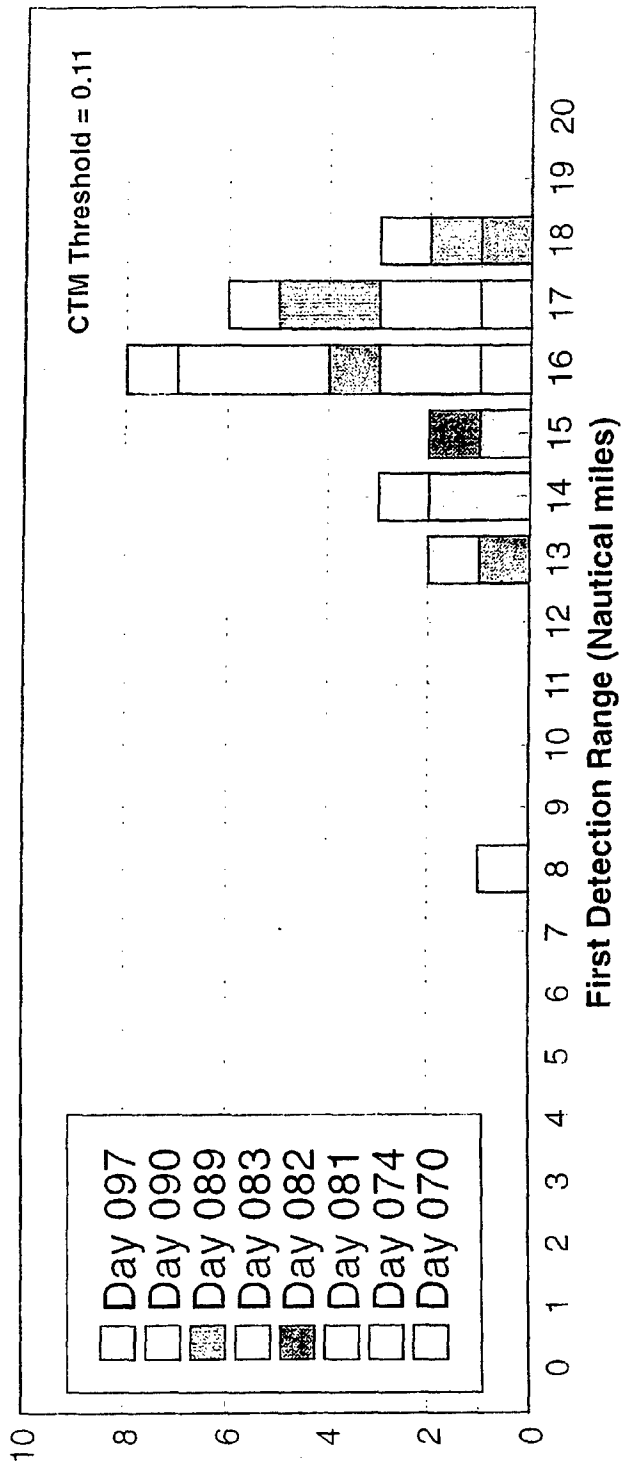
On other days, the ranges were more evenly distributed for a single day. For example, on day 082, the dominate factor on detection range appears to be the change in altitude of each of the four runs. The first run was at 200-ft altitude and had the longest detection range, the fourth run was at 30-ft altitude and had the shortest detection range.

Also day 082 had an anomalous refraction condition due to a strong positive temperature gradient extending up to about 100-ft altitude. This resulted in the lower altitude runs appearing against a sea clutter background that contributed to the shorter detection ranges.



Target Detection Range TLX Towed Target- by test day

Number of Occurences



During the MSI tests, the CTM limit was varied between 0.15 and 0.25 to maintain a low FAR (approximately 0.01/sec).

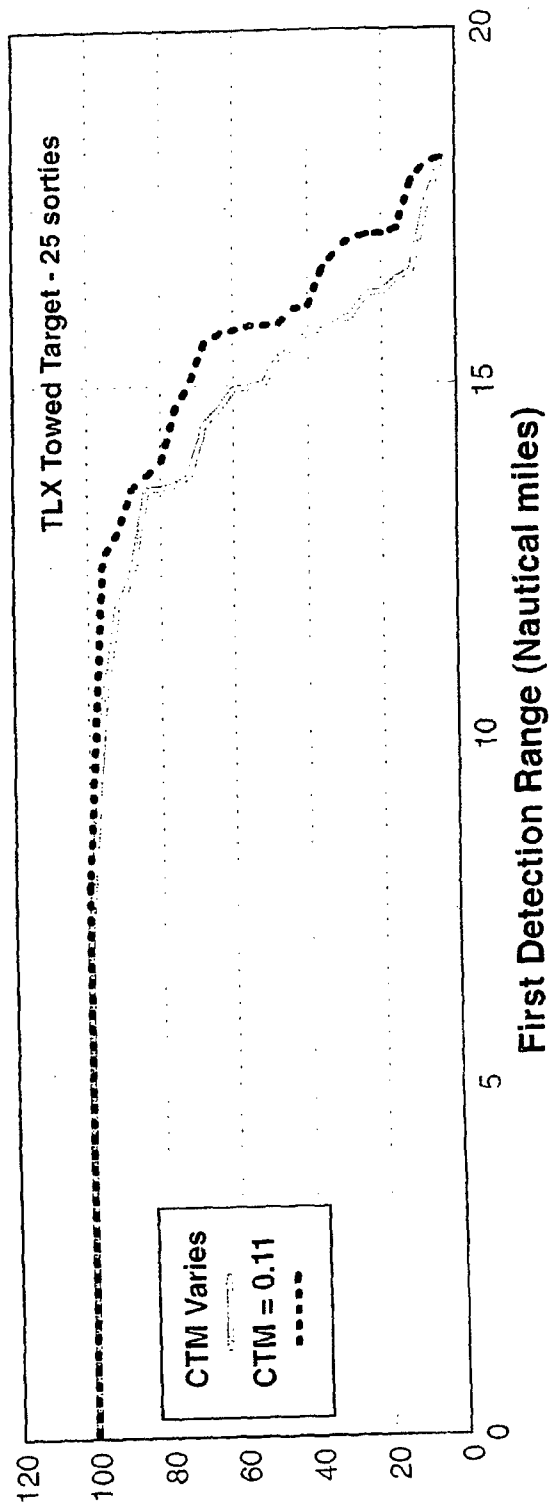
This figure compares the detection ranges between the CTM threshold used at the time of testing and a CTM threshold of 0.11, which results in a FAR of about 1/sec under typical clutter conditions.

This shows that the average probability of first detection range is about 1 nmi further when using the lower CTM threshold.

TLX Detection Ranges At Actual Reporting Thresholds



Probability of First Detection (%)



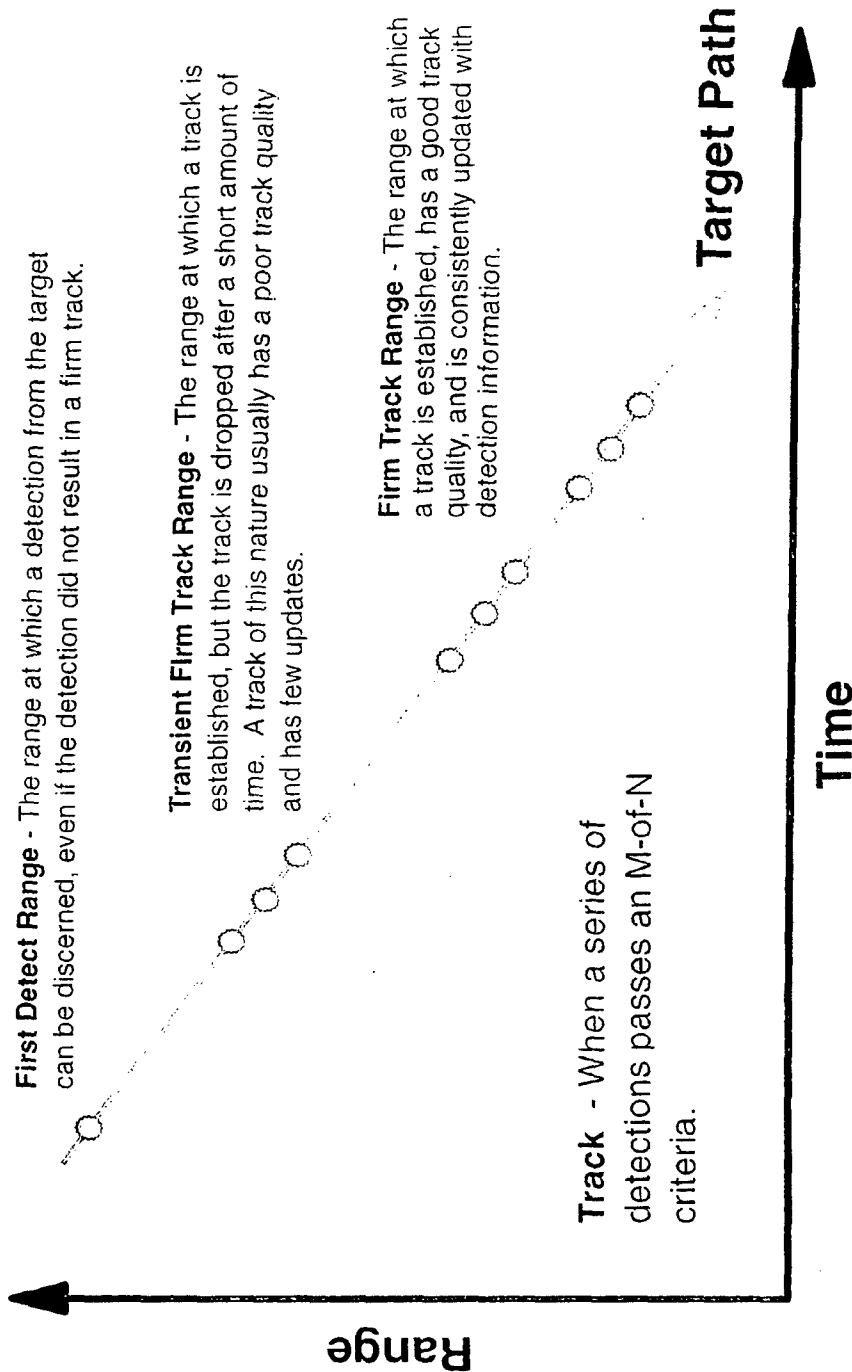
In support of the MSI data analysis effort, the first detection ranges were compared with the first track ranges for the 25 data runs. Since the HISS Phase 2 system does not have a track function, the following definitions were used to analyze the data: first detection, transient firm track, and firm track.

For a series of detections, the criteria for a track is when there were detections on two of three scans. The criteria for a *drop track* is when there are not detections for five scans in a row.

Therefore, if a series of detections develops a track but then drops track, it is considered to be a transient firm track, and if a series of detections does not drop track it is considered to be a firm track.



Definitions for MSI Data Analysis



Using the definitions detailed previously, this figure compares the first detection, transient firm track, and firm track ranges.

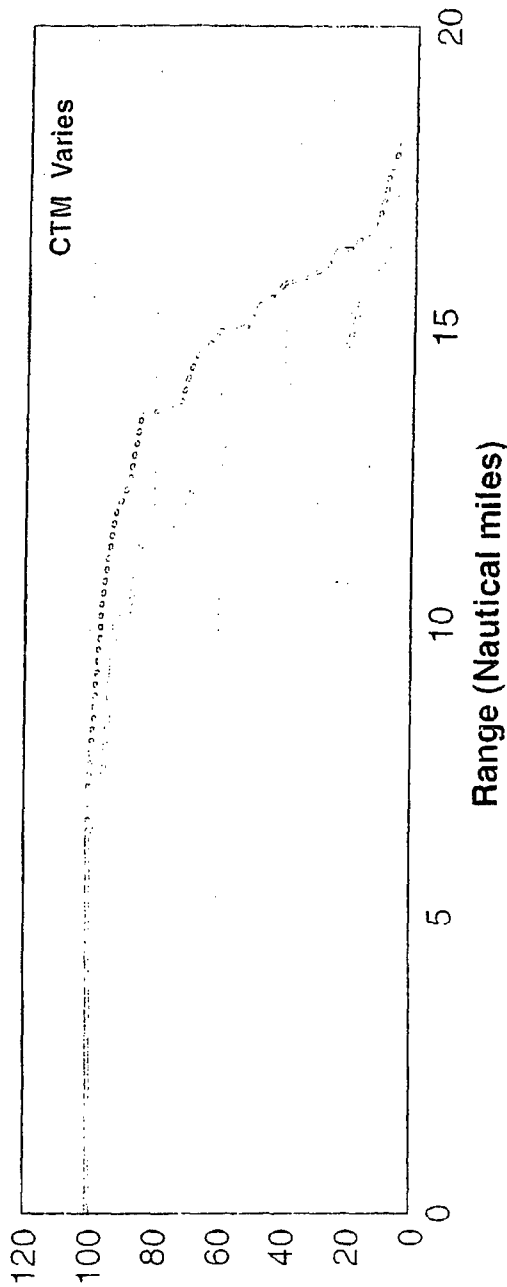
For this comparison, use the various CTM thresholds used at the time of testing to report detections to the MSI interface.

This figure shows that at the 50-percent probability of detection point, the firm track range is about 2 nmi less than the first detection range and the transient firm track range is about 1 nmi less than the first detection range. At least some of this reduction in track range is due to the variation in the TLX amplitude that was discussed earlier.

Detection and "Track" Ranges TLX Towed Target - 25 sorties



Probability of Detection (%)



First Detection "Transient Firm Track" "Firm Track"

Finally, the measured detection range performance from the Wallops Island tests is compared against predicted detection range performance. This shows the methodology developed at NSWCDD to predict detection range performance based on sensor modelling weather observation data.

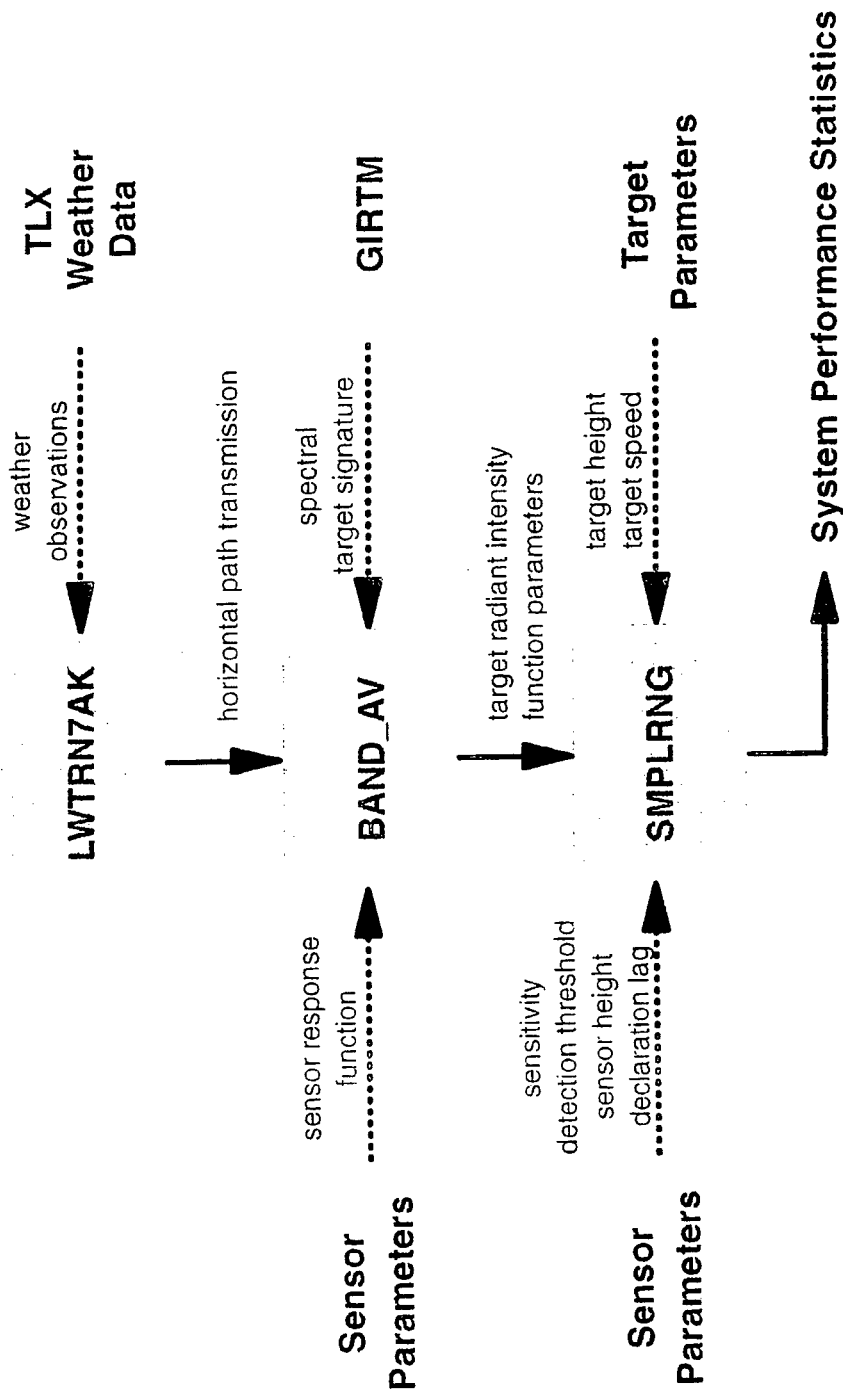
Program LWTRN7AK reads in a series a weather observations from a weather database, run LOWTRAN7 multiple times, and outputs path transmission files for each weather observation.

Program BAND_AV uses these output files to calculate the band averaged transmitted contrast irradiance based on a specified sensor response function and spectral target signature. For these calculations, the spectral target signature is obtained from general IR target model.

Program SMPLRNG calculates detection range based on BAND_AV output along with specified sensor parameters such as mounting height, sensitivity, detection threshold, etc. SMPLRNG also limits maximum detection range based on horizon obscuration under variable refraction conditions.



Statistical Performance Analysis



Using Wallops Island meteorological data as input, LOWTRAN was used to calculate transmission versus range factors for each of the 25 TLX runs. This data was then used to calculate the radiant intensity at the target source, also known as the target zero-range radiant intensity, J_0 . A J_0 value was calculated for every detection in the 25 runs.

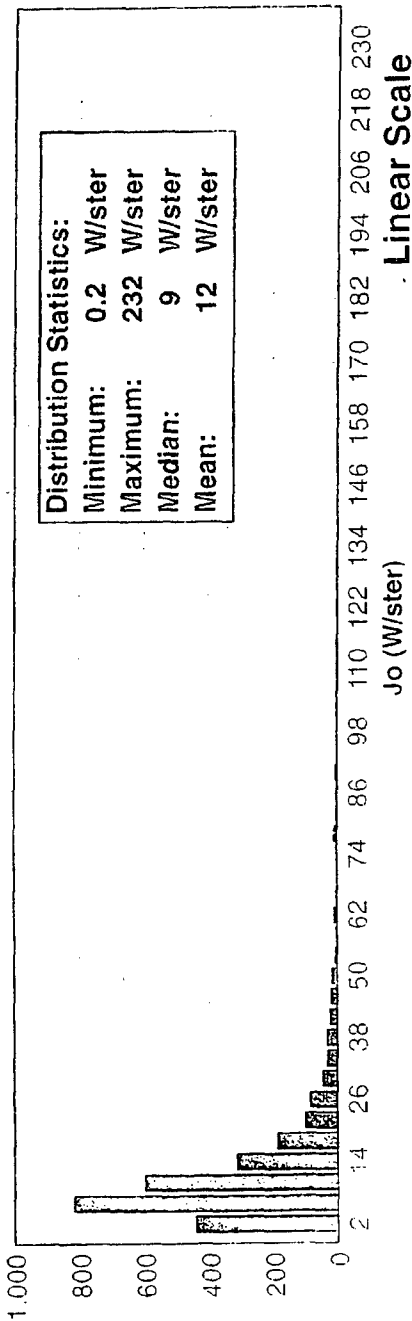
This resulted in a wide distribution of calculated target intensity values. This wide distribution is due to a number of error sources: inaccuracy in the LOWTRAN atmospheric calculations, variations in the sensor response for a given day (a fixed value of $NEI = 2 \text{ E-}14$ was used throughout this analysis), variation in the apparent target intensity due to atmospheric refraction effects, and attenuation to the target intensity due to obscuration of the target discussed earlier.

The top figure shows a histogram of the calculated J_0 values on a linear scale. The bottom figure shows the same distribution presented on a logarithmic scale. (Note that the bin widths are not of equal size on this figure.) On this scale, the distribution has a uniform bell-shape centered on about 10 W/sr , which is consistent with the calculated values for median and mean.

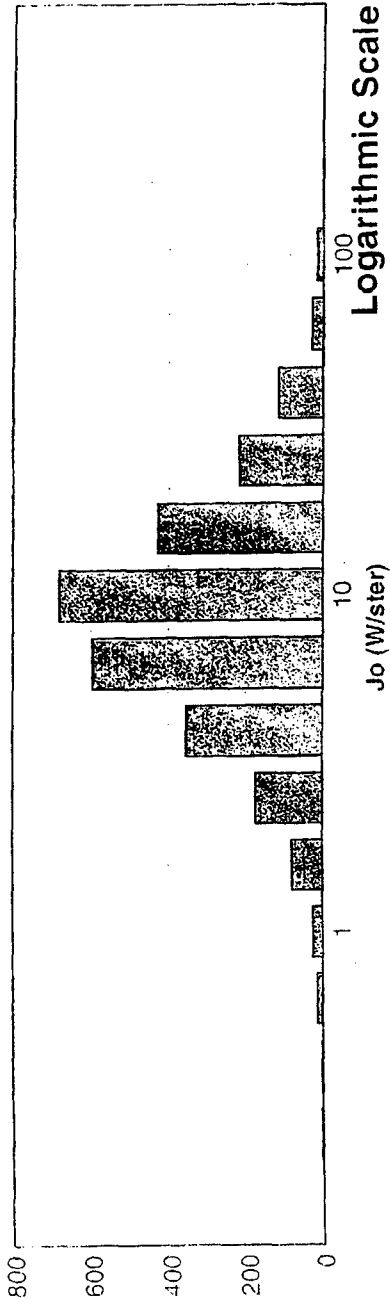
Calculated Target Intensity Wallops Island Met Data



Number of Occurrences



Number of Occurrences



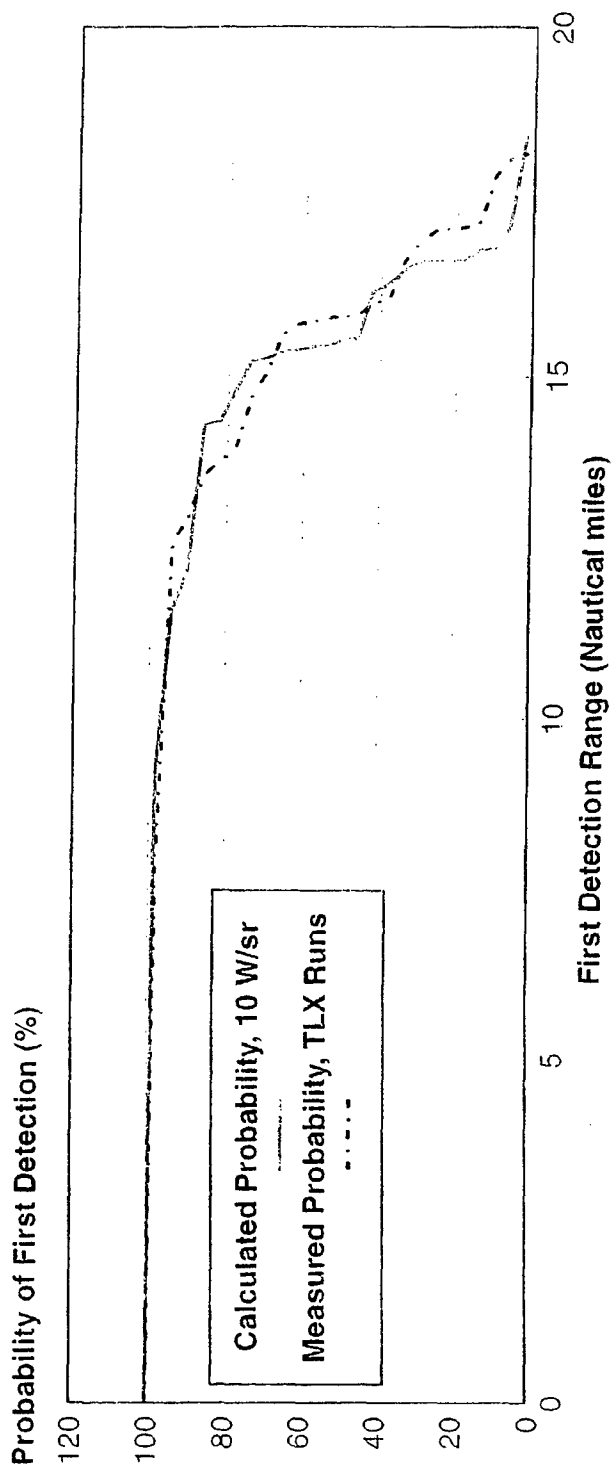
The statistical performance analysis model was used to predict the probability of first detection based upon sensor modelling, the weather conditions for each run, and a target intensity of 10 W/sr.

This figure shows that there is close agreement between the results of the 10-W/sr target prediction and the Wallops Island test results. Although the IR signature of the TLX target with the 10-in. HME was originally calculated to be at least 20 W/sr due to the significant obscuration of the target when facing at front-aspect angle it is presumed that the average target signature was something less than 20 W/sr.

Therefore, it is reasonable that the HISS detection range performance is consistent with the result of a 10 W/sr target under these weather conditions.



Comparison 10 W Target Prediction and Wallops Island Test Results



Although there were large fluctuations in the apparent intensity of the TLX, the HISS performed extremely well at detecting the target. The 50-percent probability of first detection range was about 16 nmi.

On a single day you could see the effect of the TLX altitude on reducing detection range. But when you look at all of the runs the most significant effect on detection range is from atmospheric transmission.

The probability of first detection was improved by about 1 nmi when using a detection threshold that resulted in a FAR of about 1/sec rather than a FAR of about 0.01/sec.

Using the definitions detailed earlier, at the 50-percent probability of detection point, the first firm track range is about 2 nmi less than the first detection range.

Based upon a comparison with a statistical model, the TLX target ranges obtained were consistent with an IR signature of about 10 W/sr.



Summary

- Although there were fluctuations in the apparent intensity of the TLX, the HISS performed extremely well at detecting the target.
- The most significant factor on reducing detection range was transmission rather than TLX altitude
- The probability of first detection improved by 1 nmi when using the lower detection threshold
- At the 50% probability of detection point, the first detection range is about 2 nmi farther than the first firm track range
- The performance we achieved was consistent with predicted results

The performance of the system can be predicted for other operating areas through the use of statistical weather databases.

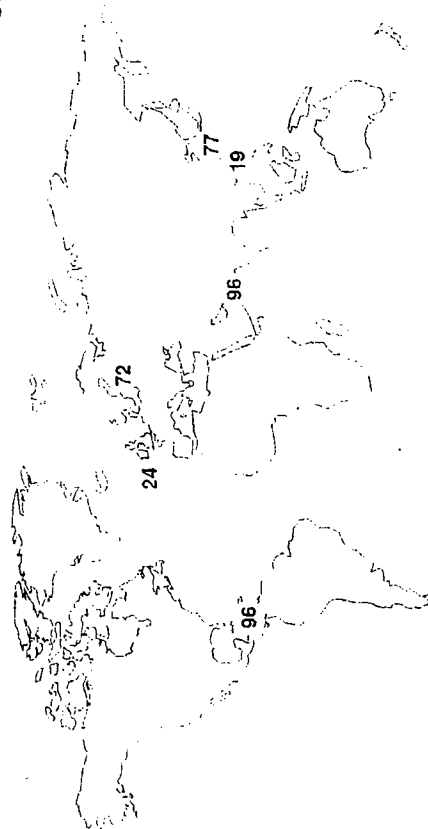
One commonly used weather database is the *Random 384* or *R384*. The sample was intended to represent the four following geographic areas with equal weight: Baltic Sea, Yellow Sea (Korea), Gulf of Oman (Persian Gulf), and Caribbean Sea. Each area is represented by 8 randomly selected weather sample per month for a total of $8 \times 12 \times 4 = 384$ samples.

For the Gulf of Oman and Caribbean Sea, it was possible to sample eight observations per month from these actual locations. For the Baltic Sea and the Yellow Sea, however, the samples were made up from available weather samples from the nearby area. For the Baltic Sea, samples were comprised from observations from the Gulf of Finland and from open ocean measurements at the same latitude as the Baltic Sea. For the Yellow Sea, samples were comprised from observations from the region between the Yellow Sea and East China Sea and from measurements from the central portion of the East China Sea.

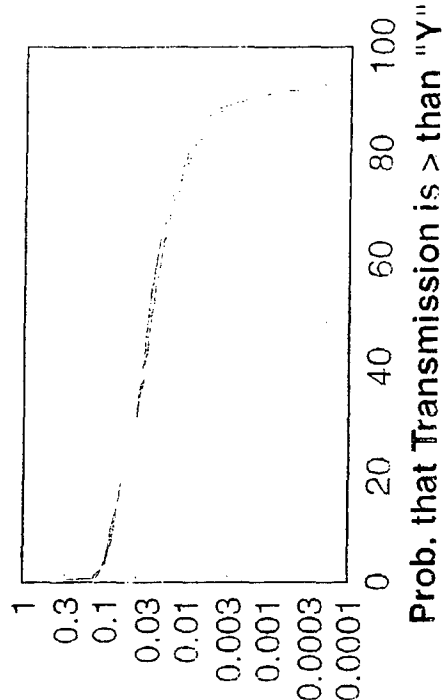


R384 Weather Sample

- 96 samples from each of the following general locations
 - Baltic Sea
 - Yellow Sea
 - Gulf of Oman
 - Caribbean Sea



"Y"



| | |
|--------|--------|
| "R384" | "R384" |
| MIR | FIR |
| "R400" | "R400" |
| MIR | FIR |

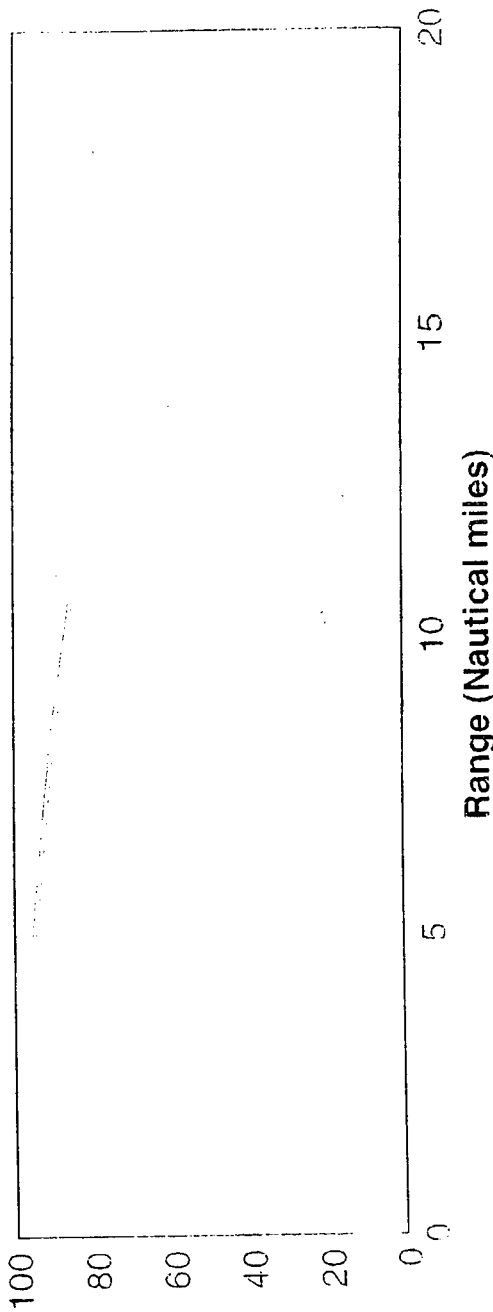
This figure shows the HISS Phase 2 system performance which can be expected against four notional targets whose signatures are 2.5, 5, 10 and 20 W/sr in the R384 weather environments. These targets are all assumed to be flying at an altitude of 15 meters and CTM reporting threshold is fixed at CTM - 0.11.

Predicted Performance Using R384 Weather Sample



HISS Phase 2
 Sensor Height = 25 meters
 Target Height = 15 meters
 CTM = 0.11

Probability of First Detection (%)



2.5 W 5 W 10 W 20 W

DISTRIBUTION

| | Copies | | Copies |
|--|--------|---------------------------------|--------|
| DOD ACTIVITIES (CONUS) | | ATTN CAPT WILSON USAF | 1 |
| ATTN CODE 723 (OSTROWSKI) | 1 | OFFICER IN CHARGE | |
| COMMANDER | | JOINT ELECTRONIC WARFARE CENTER | |
| CARDEROCK DIVISION | | 2 HALL BLVD STE 217 | |
| NAVAL SURFACE WARFARE CENTER | | SAN ANTONIO TX 78243-7008 | |
| SHIP IR SIGNATURES AND COUNTERMEASURES | | | |
| BETHESDA MD 20084-5000 | | ATTN CODE 501B (CAMPANA) | 1 |
| | | NAVAL AIR DEVELOPMENT CENTER | |
| | | WARMINSTER PA 18974-5000 | |
| ATTN OPNAV N865D (CDR JENKINS) | 1 | | |
| OPNAV N865D1 (CDR MACY) | 1 | ATTN CONWAY | 1 |
| CHIEF OF NAVAL OPERATIONS | | JONES | 1 |
| WASHINGTON DC 20350-2000 | | SMITH | 1 |
| | | COMMANDING OFFICER | |
| ATTN CODE 805 (BENNETT) | 1 | NAVAL AIR WARFARE CENTER | |
| COMMANDER | | AIRCRAFT DIVISION LAKEHURST | |
| CRANE DIVISION | | LAKEHURST NJ 08733-5000 | |
| NAVAL SURFACE WARFARE CENTER | | | |
| 300 HIGHWAY 361 | | ATTN COLBY | 1 |
| CRANE IN 47522-5001 | | COMMANDER | |
| | | NAVAL AIR WARFARE CENTER | |
| ATTN CODE E29L (TECHNICAL LIBRARY) | 1 | AIRCRAFT DIVISION | |
| COMMANDING OFFICER | | BLDG 304 | |
| CSSDD NSWC | | PATUXENT RIVER MD 20670-5304 | |
| 6703 W HIGHWAY 98 | | | |
| PANAMA CITY FL 32407-7001 | | ATTN ADAMYCK | 1 |
| | | COMMANDER | |
| DEFENSE TECHNICAL INFORMATION CENTER | | NAVAL AIR WARFARE CENTER | |
| 8725 JOHN J KINGMAN RD | 2 | WEAPONS DIVISION | |
| FT BELVOIR VA 22060-6218 | | 521 9TH ST | |
| | | POINT MUGU CA 93042-5001 | |

DISTRIBUTION (Continued)

| | Copies | | Copies |
|-------------------------------------|--------|--------------------------------------|--------|
| ATTN CODE 5622 (PRIEST) | 1 | ATTN ONR 31 (BUSS) | 1 |
| CODE 5622 (SHETTLE) | 1 | ONR 31 (HALL) | 1 |
| CODE 5622 (TAKKEN) | 1 | COMMANDER | |
| COMMANDING OFFICER | | OFFICE OF NAVAL RESEARCH | |
| NAVAL RESEARCH LABORATORY | | 800 N QUINCY STREET | |
| 4555 OVERLOOK AVENUE SW | | ARLINGTON VA 22217-5660 | |
| WASHINGTON DC 20375-5320 | | | |
| ATTN PMS 400B30A (CDR WILSON) | 1 | ATTN CODE P2333 (SHELTON) | 1 |
| SEA 62Y | 1 | PACIFIC MISSILE TEST CENTER | |
| SEA 91W21 (READING) | 1 | POINT MUGU CA 93042-5000 | |
| COMMANDER | | ATTN ANDERSON | 1 |
| NAVAL SEA SYSTEMS COMMAND | | KNEIZYS | 1 |
| 2531 JEFFERSON DAVIS HWY | | PHILLIPS LABORATORY AFSC OPS | |
| ARLINGTON VA 22242-5160 | | HANSCOM AIR FORCE BASE MA 01731-5000 | |
| ATTN CODE 764 (FORBES) | 1 | ATTN PEO TAD D2 (CAPT WILLIAMSON) | 1 |
| CODE 764 (METCALF) | 1 | PEO TAD D233 (LAM) | 1 |
| COMMANDING OFFICER | | PEO TAD D233 (MISANIN) | 1 |
| NCCOSC RDTE DIV 754 | | PROGRAM EXECUTIVE OFFICER | |
| 49336 DIGITAL ROAD | | THEATER AIR DEFENSE | |
| SAN DIEGO CVA 92152-7620 | | 2531 JEFFERSON DAVIS HIGHWAY | |
| | | ARLINGTON VA 22242-5170 | |
| ATTN BUSER | 1 | | |
| SELF | 1 | ATTN CODE 4Y21 (ECK) | 1 |
| NIGHT VISION AND ELECTRONIC SENSORS | | COMMANDER | |
| DIRECTORATE | | PORT HUENEME DIVISION | |
| 10221 BURBECK ROAD | | NAVAL SURFACE WARFARE CENTER | |
| FORT BELVOIR VA 22060 | | 4373 MISSILE WAY | |
| | | PORT HUENEME CA 93043-4307 | |

DISTRIBUTION (Continued)

| | Copies | | Copies |
|--|--------|--|--------|
| ATTN SPAWAR 332 (GIRATA) COMMANDER SPACE AND NAVAL WARFARE SYSTEMS COMMAND 2451 CRYSTAL RD ARLINGTON VA 22445-5200 | 1 | ATTN SMITH DIBIASIO AMBER 5756 THORNWOOD DRIVE GOLETA CA 93117-3802 | 1 |
| ATTN LT SLOOP COMMANDING OFFICER SURFACE WARFARE DEVELOPMENT GROUP NAVAL AMPHIBIOUS BASE LITTLE CREEK NORFOLK VA 23521-5160 | 1 | ATTN DAVIS LUBARD ARETE P O BOX 6024 SHERMAN OAKS CA 91413 | 1 |
| ATTN LANICH WRIGHT PATTERSON AIR FORCE BASE WRDC AARI 1 WRIGHT PATTERSON AIR FORCE BASE OH 45433-6543 | 1 | ATTN HAMM BALL AEROSPACE SYSTEM DIVISION P O BOX 1062 BOULDER CO 80306 | 1 |
| NON-DOD ACTIVITIES (CONUS) | | | |
| ATTN WHITE ABA ELECTROMECHANICAL SYSTEMS INC P O BOX 500 PINELLAS PARK FL 34290-0500 | 1 | ATTN AX BDM FEDERAL INC 4001 NORTH FAIRFAX DRIVE SUITE 750 ARLINGTON VA 22203 | 1 |
| ATTN DR SCOTT AERODYNE RESEARCH INC 45 MANNING ROAD BILLERICA MA 01821-3976 | 1 | ATTN ROY BOEING DEFENSE AND SPACE GROUP 1700 NORTH MOORE STREET ROSSLYN VA 22209-1989 | 1 |
| | | ATTN GRIMM THE CNA CORPORATION P O BOX 16268 ALEXANDRIA VA 22302-0268 | 1 |

DISTRIBUTION (Continued)

| | Copies | | Copies |
|--------------------------------|--------|-------------------------------|--------|
| ATTN ARMINTROUT MALONE | 1 | ATTN MILLER | 1 |
| CONTRAVES | 1 | IN DEF SERVICES INTERNATIONAL | |
| 615 EPSILON DRIVE | | 2735 HARTLAND ROAD SUITE 300 | |
| PITTSBURGH PA 15238-2880 | | FALLS CHURCH VA 22043 | |
| ATTN MCNALLY | 1 | ATTN BIBERMAN | 1 |
| DBA SYSTEMS INC | | DALCHER | 1 |
| BELTWAY BUILDING SUITE 200 | | FRIDLING | 1 |
| 9301 ANNAPOLIS ROAD | | NICHOLL | 1 |
| LANHAM SEABROOK MD 20706 | | INSTITUTE OF DEFENSE ANALYSIS | |
| ATTN ZIMMERMAN | 1 | 1801 N BEAUREGARD | |
| HONEYWELL | | ALEXANDRIA VA 22311 | |
| AEROSPACE AND DEFENSE GROUP | | ATTN FIGURSKI | 1 |
| 7900 WESTPARK DRIVE | | THE IRIA CENTER | |
| McLEAN VA 22102 | | ERIM | |
| ATTN BAUR | 1 | P O BOX 134001 | |
| PINES | 1 | ANN ARBOR MI 48113-4001 | |
| REY | 1 | ATTN DOCKERY | 1 |
| HUGHES | | LEWIS | 1 |
| ELECTRO OPTICAL SYSTEMS | | PERI | 1 |
| LOC EO BLDG E1 MS A151 | | PRENGAMAN | 1 |
| 2000 EAST EL SEGUNDO BOULEVARD | | REILLY | 1 |
| P O BOX 902 | | JOHNS HOPKINS UNIVERSITY | |
| EL SEGUNDO CA 90245 | | APPLIED PHYSICS LABORATORY | |
| | | JOHNS HOPKINS ROAD | |
| | | LAUREL MD 20723-6099 | |

DISTRIBUTION (Continued)

| | Copies | | Copies |
|--|-------------|--|--------|
| ATTN JONES KOLLMORGEN CORPORATION ELECTO OPTICAL DIVISION 347 KING STREET NORTHAMPTON MA 01060-2390 | 1 | ATTN CANTELLA OTAZO MASSACHUSETTS INSTITUTE OF TECHNOLOGY LINCOLN LABS 244 WOOD STREET LEXINGTON MA 02173 | 1 1 |
| ATTN GIFT AND EXCHANGE DIVISION LIBRARY OF CONGRESS WASHINGTON DC 20540 | 4 | ATTN DARREN MITRE CORPORATION 5254 POTOMAC DRIVE SUITE 5 DAHLGREN VA 22448 | 1 |
| ATTN MOORE LOCKHEED SANDERS INC MER15 1204 P O BOX 868 NASHUA NH 03061-0868 | 1 | ATTN SCHROEDER ONTAR CORPORATION 9 VILLAGE WAY NORTH ANDOVER MA 01845 | 1 |
| ATTN CARR KOLP MORRISON LORAL DEFENSE SYSTEMS AKRON 1210 MASSILLON ROAD AKRON OH 44315-0001 | 1 1 1 | ATTN SCHAFER PILKINGTON OPTRONICS INC 7550 CHAPMAN AVENUE GARDEN GROVE CA 92641 | 1 |
| ATTN DUGANNE MCDONNELL DOUGLAS ELECTRONIC SYSTEMS 700 ROYAL OAKS DRIVE P O BOX 5005 MONROVIA CA 91017-7105 | 1 | ATTN LAFFAN QUESTECH INC 7600 A LEESBURG PIKE FALLS CHURCH VA 22043 | 1 |
| ATTN B MURTHA MARTIN MARIETTA ELECTRONICS AND MISSILES P O BOX 555837 MP 718 ORLANDO FL 32855-5837 | 1 | ATTN LAMBERT RAYTHEON COMPANY MISSILE SYSTEMS DIVISION 50 APPLE HILL DRIVE TEWKSBURY MA 01876-0901 | 1 |

DISTRIBUTION (Continued)

| | Copies | | Copies |
|---------------------------------------|--------|--|--------|
| ATTN FOWKS | 1 | ATTN ARKIN | 1 |
| KWOK | 1 | WESTINGHOUSE ELECTRO OPTICAL SYSTEMS ORLANDO | |
| ROCKWELL INTERNATIONAL CORPORATION | | 9820 SATELLITE BOULEVARD | |
| TACTICAL SYSTEMS DIVISION | | ORLANDO FL 32821 | |
| 3370 MIRALOMA AVENUE | | | |
| P O BOX 4921 | | NON-DOD ACTIVITIES (NON-CONUS) | |
| ANAHEIM CA 92803-4921 | | | |
| ATTN VAN DER SCHOEFF | 1 | ATTN CHEVRETTE | 1 |
| STRATEGIC INSIGHT | | SMITHSON | 1 |
| 2011 CRYSTAL DRIVE SUITE 101 | | DEFENCE RESEARCH ESTABLISHMENT VALCARTIER | |
| ARLINGTON VA 22202 | | ELECTRO OPTICS DIVISION | |
| | | P O BOX 8800 | |
| | | COURCELETTE PQ G0A 1R0 CANADA | |
| ATTN SIMMONS | 1 | | |
| TEXAS INSTRUMENTS | | ATTN DR WOODRUFF | 1 |
| DEFENSE SYSTEMS AND ELECTRONICS GROUP | | DEFENCE SCIENCE AND TECHNOLOGY OFFICE | |
| 8505 FOREST LANE | | LAND SPACE AND OPTOELECTRONICS DIVISION | |
| P O BOX 660246 MS 3150 | | P O BOX 1500 | |
| DALLAS TX 75246 | | SALISBURY SOUTH AUSTRALIA 5108 | |
| | | | |
| ATTN KIM | 1 | ATTN FAO (LCDR LOVELOCK) | 1 |
| TRW DEFENSE SYSTEMS GROUP | | DGSW(N) | |
| 7600 COLSHIRE DRIVE | | DRA PORTSDOWN | |
| McLEAN VA 22102 | | PORTSMOUTH ENGLAND | |
| | | | |
| ATTN WEYGANDT | 1 | ATTN HUTCHINGS | 1 |
| WESTINGHOUSE ELECTRIC CORPORATION | | KNEPPER | 1 |
| ELECTRONIC SYSTEMS GROUP | | HOLLANDSE SIGNAALAPPARATEN | |
| P O BOX 746 MS G8 | | P O BOX 42 | |
| BALTIMORE MD 21203 | | 7550 GD HENGELO THE NETHERLANDS | |

DISTRIBUTION (Continued)

| | Copies | | Copies |
|--------------------------------------|--------|--|--------|
| ATTN HUMMEL | 1 | ATTN VAN KEMENADE | 1 |
| MINISTRY OF DEFENCE | | SPAR AEROSPACE LTD | |
| DMKM WCS | | ADVANCED TECHNOLOGY SYSTEMS GROUP | |
| HEMDC | | ELECTRO OPTICAL SYSTEMS DIVISION | |
| VD BURCHLAAN 31 | | 9445 AIRPORT ROAD | |
| POSTBUS 20702 | | BRAMPTON ON L6S 4J3 CANADA | |
| 2500 ES DEN HAGG THE NETHERLANDS | | | |
| ATTN DMCS 4 (MULLER) | 1 | ATTN DE JONG | 1 |
| NATIONAL DEFENCE HEADQUARTERS | | SCHWERING | 1 |
| MARITIME COMBAT SYSTEMS DEPARTMENT | | TNO PHYSICS AND ELECTRONICS LABORATORY | |
| 101 COLONEL BY DRIVE | | OUDE WAALSDORPERWEG 63 | |
| OTTAWA ON K1A 0K2 CANADA | | P O BOX 96864 | |
| | | 2509 JG THE HAGUE THE NETHERLANDS | |
| ATTN MAI | 1 | INTERNAL | |
| NAVAL ENGINEERING TEST ESTABLISHMENT | | B42 (BARNETT) | 1 |
| 161 RUE WANKLYN STREET | | B42 (BILLARD) | 1 |
| LASALLE PQ H8R 1Z2 CANADA | | B42 (CROWDER) | 1 |
| ATTN EDWARDS | 1 | B42 (LEE) | 1 |
| PARADIGM PATHWAYS GROUP | | B42 (PETROPOULOS) | 1 |
| 26 BEATTY CRESCENT | | E231 | 3 |
| AURORA ON L4G 5V1 CANADA | | E272 (BURRELL) | 1 |
| | | F07 | 1 |
| ATTN SAMUELSSON | 1 | F107 | 1 |
| SAAB MISSILES AB | | F11 | 1 |
| P O BOX 13045 | | F21 | 1 |
| S 402 51 GOTEBOG SWEDEN | | F31 (MANGLEBURG) | 1 |
| | | F32 (KEEL) | 1 |
| | | F32 (PORTER) | 1 |
| | | F406 | 1 |

DISTRIBUTION (Continued)

Copies

| | | |
|------|-------------|---|
| F41 | (FONTANA) | 1 |
| F41 | (LARSEN) | 1 |
| F41 | (MISCH) | 1 |
| F41 | (RIVERA) | 1 |
| F41 | (STAPLETON) | 1 |
| F44 | (AUSTIN) | 1 |
| F44 | (DEZEEUW) | 1 |
| F44 | (HEADLEY) | 5 |
| F44 | (HEPFER) | 1 |
| F44 | (HERRON) | 1 |
| F44 | (JOHNSON) | 1 |
| F44 | (OLDENBURG) | 1 |
| F44 | (PILLOW) | 1 |
| F44 | (RUDZINSKY) | 1 |
| F44 | (TRAHAN) | 1 |
| F44 | (WARDLAW) | 1 |
| F44 | (WILSON) | 1 |
| F44 | (ZURASKY) | 1 |
| G21 | (TROYER) | 1 |
| G33 | (DORAN) | 1 |
| G42 | | 1 |
| G531 | (FERSTL) | 1 |
| G63 | (LOW) | 1 |
| J31 | | 1 |
| N74 | (GIDEP) | 1 |

DOCUMENT 4

Inductively Coupled IR Staring Array Based on Photofluxonic Pixels

AD-A292 784

March 1995

**Quantum Magnetix, Inc.
San Diego, CA**

**Inductively Coupled IR Staring Array
Based on Photofluxonic Pixels**

Final Report

**Contract Number
F49620-94-C-0058**

Prepared by:

Dr. Andrew D. Hibbs

Dr. Alan L. Singsaas

Douglas A. Taussig

**Quantum Magnetics
11578 Sorrento Valley Road
San Diego, CA 92121
(619) 481-4015**

March 14, 1995

| REPORT DOCUMENTATION PAGE | | | Form Approved OMB No. 0704-0188 | |
|--|----------------------------------|---|------------------------------------|----------------------------------|
| <small>Public reporting burden for this collection of information is estimated to average 1 hour per response, including the time for reviewing instructions, searching existing data sources, gathering and maintaining the data needed, and completing and reviewing the collection of information. Send comments regarding this burden estimate or any other aspect of this collection of information, including suggestions for reducing this burden, to Washington Headquarters Services, Directorate for Information Operations and Reports, 1215 Jefferson Davis Highway, Suite 1204, Arlington, VA 22202-4302, and to the Office of Management and Budget, Paperwork Reduction Project (0704-0188), Washington, DC 20503.</small> | | | | |
| 1. AGENCY USE ONLY (Leave blank) | 2. REPORT DATE March 14, 1995 | 3. REPORT TYPE AND DATES COVERED Final: 15 Jul 94- 14 Jan 95 | | |
| 4. TITLE AND SUBTITLE Inductively Coupled IR Staring Array Based on Photofluxonic Pixels | | 5. FUNDING NUMBERS C F49620-94-C-0058 1662/01 63218C | | |
| 6. AUTHOR(S) Dr. Andrew D. Hibbs, Dr. Alan L. Singsaas, Douglas A. Taussig | | 7. PERFORMING ORGANIZATION NAME(S) AND Quantum Magnetix, Inc. 11578 Sorrento Valley Road San Diego, CA 92121 | | |
| 9. SPONSORING/MONITORING AGENCY NAME(S) AND U.S.A.F., A.F.M.C Air Force Office of Scientific Research 110 Duncan Ave., Suite B115 Bolling AFB DC 20332-0001 | | 8. PERFORMING ORGANIZATION REPORT NUMBER Final CM1198F AFOSR-TR-95-0241 | | |
| 10. SPONSORING/MONITORING AGENCY REPORT NUMBER F49620-94-C-0058 | | 11. SUPPLEMENTARY NOTES | | |
| 12a. DISTRIBUTION / AVAILABILITY STATEMENT 13. ABSTRACT (Maximum 200 words) The goal of this study was to investigate the feasibility of fabricating a new type of monolithic focal plane multipixel staring array for infrared (IR) radiation detection. This sensor works by the recently postulated process of photofluxonic conversion in which an infrared photon creates a vortex-antivortex pair in a superconducting material. The novelty of the new sensor lies in the detection mechanism itself, and in the way the vortex (or antivortex) is trapped in the device allowing individual sensing pixels to be readout without direct electrical connections. The overall objective of Phase I was to determine the feasibility of building an inductively coupled, non-contact staring array based on the new photofluxonic detection elements. To this end, we have performed a series of experiments on a single array element, a 2 mm diameter loop of YBa ₂ Cu ₃ O ₇ , and considered pixel requirements for constructing an array. The new system offers tremendous potential for improvement over current infrared detection devices via both the enhanced detection sensitivity and the greatly reduced system complexity | | 12b. DISTRIBUTION CODE | | |
| 14. SUBJECT TERMS Infared Detector, Photofluxonic Effect, Staring Focal Point Array, High Temperature Superconductivity | | 15. NUMBER OF PAGES 26 | | |
| 16. PRICE CODE | | 17. SECURITY CLASSIFICATION OF REPORT UNCLASSIFIED | | |
| 18. SECURITY CLASSIFICATION OF THIS PAGE UNCLASSIFIED | | 19. SECURITY CLASSIFICATION OF ABSTRACT UNCLASSIFIED | | 20. LIMITATION OF ABSTRACT UL |

Table of Contents

| | |
|---|----|
| 1 Executive Summary | 1 |
| 2 Introduction..... | 2 |
| 3 Task 1: Determine Pixel Requirements. | 5 |
| 3.1 Superconducting System..... | 5 |
| 3.2 Experimental Apparatus | 5 |
| 3.3 Biasing the Superconducting System..... | 8 |
| 3.4 Calculation of the coupling factors | 11 |
| 4 Task 2: Analyze Array Detection Issues | 13 |
| 4.1 Experimental Parameters | 13 |
| 4.2 Experimental Results | 13 |
| 4.2.1 Observation of the Photofluxonic Effect | 13 |
| 4.2.2 Flux Creep | 17 |
| 4.2.3 Comparison with Recent Research by Others | 18 |
| 4.3 Pixel Configuration..... | 19 |
| 5 Task 3: Analyze Pixel Bias Issues | 23 |
| 5.1 Refreshing the Pixels | 23 |
| 6 Task 4: Analyze Array Readout Issues | 23 |
| 6.1 The Array Configuration..... | 23 |
| 6.2 The Pixel Readout Scheme | 24 |
| 7 References..... | 26 |

1 Executive Summary

The goal of this study was to investigate the feasibility of fabricating a new type of monolithic focal plane multipixel staring array for infrared (IR) radiation detection. This sensor works by the recently postulated process of photofluxonic conversion in which an infrared photon creates a vortex-antivortex pair in a superconducting material. The novelty of the new sensor lies in the detection mechanism itself, and in the way the vortex (or antivortex) is trapped in the device allowing individual sensing pixels to be readout without direct electrical connections. The new system offers tremendous potential for improvement over current infrared detection devices via both the enhanced detection sensitivity and the greatly reduced system complexity.

Technical Objectives. The overall objective of Phase I was to determine the feasibility of building an inductively coupled, non-contact staring array based on the new photofluxonic detection elements. To this end, we have performed a series of experiments on a single array element, and considered pixel requirements for constructing an array, as summarized below.

1. **Investigate the photofluxonic effect.** We have experimentally investigated reproducibility of the photofluxonic effect in a 2 mm diameter loop of $\text{YBa}_2\text{Cu}_3\text{O}_7$. We have investigated the effect as a function of light intensity, temperature, and frequency of chopping the IR light source.
2. **Consider the physics of the pixel.** We consider the optimum coupling of the photodetection effect to the flux state of a pixel element, and consider the effect of a vortex pair on the supercurrent producing the Lorentz force. We compare various geometries for the superconducting array.
3. **Consider array readout methods.** We compare various methods for reading the magnetic flux signal out using SQUIDs or magneto-optic effects. We consider cooling requirements, and ways of refreshing the array.
4. **Compare recent literature.** We correlate experimental results and design considerations with recent published scientific results for both high and low T_c superconductors, and estimate the sensitivity of the prototype to be built in Phase II.

Work Performed. We have observed the conversion of quanta of light into quanta of magnetic flux via vortex-antivortex pair creation. In addition we have performed ancillary experiments which rule out thermally activated flux creep as a possible explanation of the phenomenon observed. The principal technical successes resulting from this study are as follows.

1. We have observed a reproducible change in the flux trapped in a high T_c superconducting loop on illuminating a small part of that loop with light.
2. We have observed distinct steps in the photoresponse of high T_c thin film loops of $\text{YBa}_2\text{Cu}_3\text{O}_7$. The magnitude of these steps is quantized in units which closely correspond with the predicted value for a single flux quantum.
3. The time dependent behavior of the response rules out flux creep as a possible explanation.

Potential Applications. The new sensor has applications in all situations in which existing cooler IR detectors are currently used. In addition, it has the potential to greatly exceed the sensitivity, bandwidth and spectral range capabilities of existing devices. Given the basic simplicity of the individual pixels and the promise of reading them out inductively (i.e., without making electrical connections) there is tremendous promise for constructing large area, low cost, arrays. Current applications for infrared imaging include: thermography, infrared spectroscopy, astronomy, and night vision devices for the police and military forces.

2 Introduction

Infrared detectors have traditionally been semiconductor devices, with both extrinsic and intrinsic detectors being used. In intrinsic detectors, the incident photons cause transitions between the valence and conduction bands. Intrinsic materials are more suited to production line processing using standard photolithographic techniques. In extrinsic detectors, the incident photons cause transitions between impurity levels in the bandgap and an adjacent band. Extrinsic device materials have a smaller absorption coefficient and hence need detector thicknesses of the order of a millimeter at meaningful impurity concentrations. In addition extrinsic materials are more noisy and require more cooling.

Superconductors have a lower energy gap compared to semiconductors (1 meV as compared to 1 eV). This makes the superconductors more sensitive to radiation, especially at relatively longer wavelengths (at which the energy per photon is relatively small). Additionally, superconducting devices have low power dissipation; when one is dealing with large array sizes (which would otherwise require a lot of cooling power) this makes superconducting arrays very attractive. A variety of detection mechanisms have been explored ranging from devices based on the temperature dependence of the superconducting energy gap [1] to bolometric resistive transition edge thermometers [2].

The new sensor investigated in this program represents a revolution in photodetection technology; both in the physics of the detection itself and in the simplicity of the pixel design, particularly for large arrays.

- The detection mechanism is based on a process in which the photon is transformed into one (or possibly several) flux quanta. These quanta are stored and read magnetically. The detection speed is of order 100 ps (10^{-10} s). Once trapped, the quanta may be stored indefinitely.
- The pixel design is such that the array may be read out and refreshed inductively via magnetic fields; No Electrical Connections are required to the array. In addition, the pixels have No Power Dissipation. This reduces the heat load onto the array simply to that of the radiation field being surveyed.

In the recently postulated process of photofluxonic conversion, an incident photon creates a vortex-antivortex pair by local depression of the superconducting energy gap in a current carrying superconductor. The supercurrent is diverted around a spot of scale of the coherence length, which is topologically equivalent to a closely spaced vortex-antivortex pair superimposed on an

otherwise uniform current flow as shown in Figure 1. Previously, photofluxonic processes have only been inferred from anomalous resistance measurements on very long detector strips. In this report we present direct observation of the creation of magnetic flux via the absorption of incident optical photons.

Each pixel of our device will be simply a loop of superconducting material of order 10 - 50 μm in diameter. A large circulating supercurrent is trapped in the superconducting ring by applying and then removing a small dc magnetic field. The vortex pair is pulled apart by the Lorentz force created by the circulating current as shown in Figure 2. One vortex (or antivortex - no absolute sign convention is possible) experiences force to the right and the other a force to the left. The vortices migrate under these forces with the net result being a transfer of one flux quantum (or "anti-quantum") from the left to the right of the current flow; i.e., into the superconducting ring. The change in flux is maintained by a small change in the circulating supercurrent in the ring. The arrival of vortices (or antivortices) at the inner edge of the ring reduces the flux stored in the ring by an easily measurable, quantized amount. In short, the device is a photon to fluxon converter.

Arrays based on our device will be much simpler to fabricate than any existing photodetector. The important difference is that the pixel elements (the superconducting loops) are electrically isolated from each other, i.e., there is no electrical interconnects between the elements or the rest of the system. This considerably simplifies the array fabrication process. In addition, even though pixel uniformity is desirable, it is not absolutely essential for the array to function well. As long as the loops are reasonably similar, the critical currents will be nearly the same. Since vortex-antivortex creation is not a strong function of the current within the loop, there is room for some variation in the loop parameters from pixel to pixel. This is a further help to the fabrication process.

The proposed device is actually the magnetic analogue of a photodiode, and the proposed device array is the counterpart of a CCD used in optical imaging. The photofluxonic model is analogous to photoconductivity through the formal duality between electric charge and magnetic flux in two dimensions [3]. A photon incident on the junction region of the sensor creates an excited vortex-antivortex pair (c.f. electron-hole pair) which is pulled apart by a current flowing through the junction (c.f. voltage for photoconductive sensors). The quantized magnetic flux created (c.f. electric charge) is stored in the superconducting ring (c.f. the capacitors in a CCD array) before being read. The fundamental advantage over CCD photosensors is that the greatly reduced energy gap for vortex pair creation in the superconductor based sensor opens up the opportunity for new regimes of IR detection.

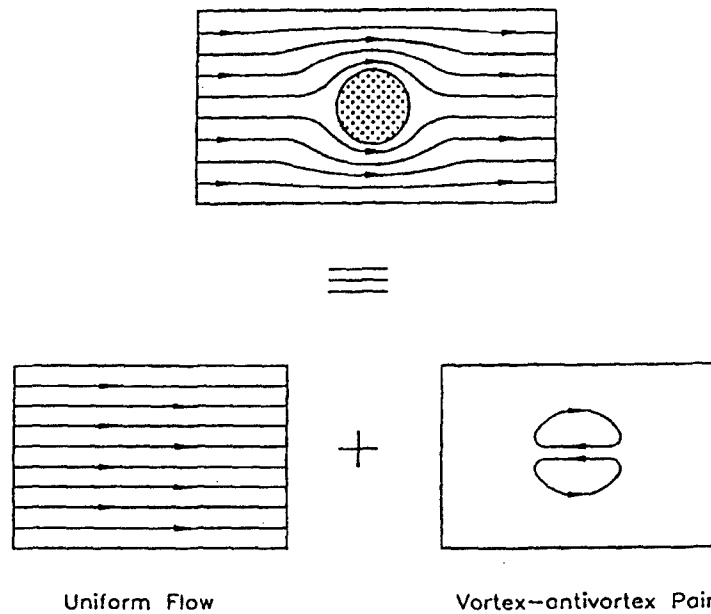


Figure 1. Creation of a Vortex-Antivortex Pair From a Non Superconducting Region.

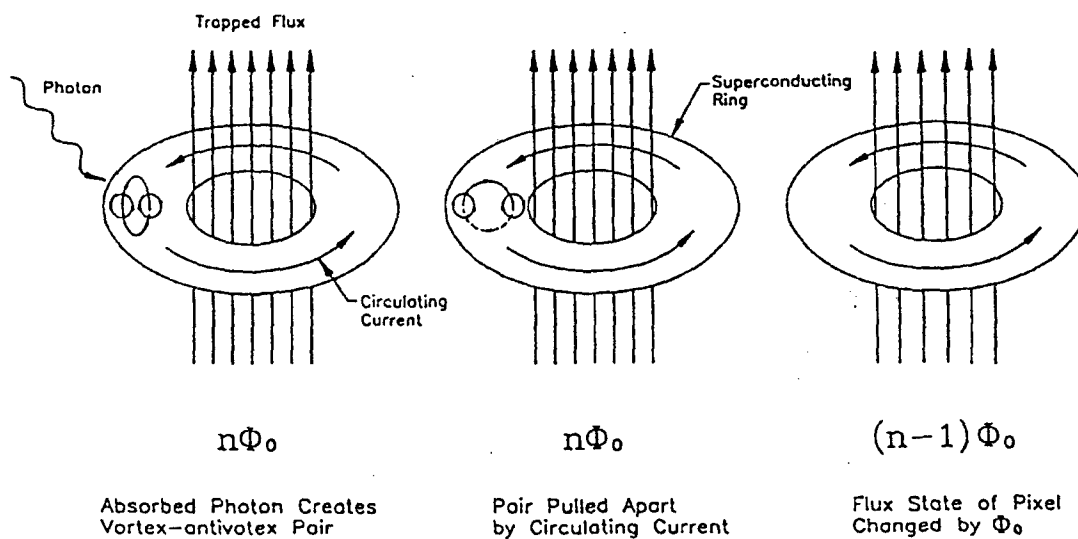


Figure 2. Separation and Trapping of Vortex-Antivortex Pair.

3 Task 1: Determine Pixel Requirements.

The major part of the project was to experimentally observe vortex-antivortex pair creation in a superconductor to determine requirements for an array of pixels. By a new method of detecting the created vortex (or antivortex) we hoped to circumvent many of the problems previously encountered by other researchers. The optical characteristics of potential HTS materials will dictate if arrays can be fabricated with dimensions and pixel sizes within usable limits.

3.1 Superconducting System

Although the photofluxonic model was first proposed to explain the infrared response of granular low T_c superconducting materials [4,5] it has also been applied to the so called nonbolometric response of high T_c superconductors. Since cooling to 80 K is considerably more convenient than cooling to 5 K, there is a significant advantage in fabricating the new sensor from high T_c materials. In order to better characterize the interaction of the pixels with the incident light, we made measurements at different temperatures.

Two high T_c films of passivated $\text{YBa}_2\text{Cu}_3\text{O}_7$ (YBCO) were obtained from IBM, one consisting of loops of 3 mm diameter and the other 2 mm diameter loops. The HTS chips are composed of a YSZ substrate with the HTS superconductor thin film loops, 40 microns wide, and 0.2 microns thick. The substrate is nearly transparent to visible and near IR; therefore, most of the light that doesn't hit the HTS film will pass through instead of being thermally absorbed by the substrate.

3.2 Experimental Apparatus

During the course of the experiment, a probe was built to evaluate experimentally the effects discussed in the Phase I work plan. The instrument is illustrated in Figure 3. The instrument is installed in an aluminum liquid helium dewar. The upper portion of the instrument is composed mostly of "nonmagnetic" type 304 stainless steel. The lower assembly, Figure 3b, is the crux of the experiment. The bottom of the probe are free of all magnetic alloys, being composed of brass and G10, and a few other materials (lead, niobium, etc.) named below.

The entire experiment is enclosed in a superconducting lead shield. This shield is completely closed at the bottom, and mostly closed at the top; it has some holes to accommodate screws and structure. Inside of the shield is a G10 vacuum cell. The cell is mounted to a brass flange with brass screws and utilizes an indium vacuum seal. The G10 cell has 6 mm thick side walls and a 1.5 mm thick "window" at the bottom. The machined surfaces of the G10 are further protected against vacuum leaks and permeability by a thin coat of epoxy.

Wound around the outer diameter of cell are 100 turns of multifilament Cu/NbTi wire. This single layer bias solenoid is centered with respect to the gradiometer. This solenoid supplies about 45 Oe/amp at the center and is used to induce a current in the HTS superconducting film.

Inserted into bottom of the G10 cell on the helium bath side is a first order gradiometer with 6 turn, 9 mm diam windings on a baseline of 6 mm. This gradiometer is made of #40 NbTi wire. The top of the gradiometer is butted up against the G10 cell's "window". This gradiometer is attached to a Quantum Design dc SQUID. The SQUID is controlled and data is acquired by a

Quantum Design dc5000 digital controller linked to a 486 computer via GPIB interface. An analog output on the dc5000 was utilized by a spectrum analyzer and an oscilloscope.

Inside of the cell (vacuum space) is the HTS chip platform. The platform is mounted such that the HTS chip will be 3 mm from the upper pickup loop of the gradiometer, centered in the lead shield. The platform is thermally isolated from the rest of the instrument by three small thin-walled G10 tubes. The platform is also shielded from thermal radiation by two layers of superinsulation. With this isolation about 8 mW of power is required to raise and sustain the platform temperature from the 4.2 K ambient temperature to 80 K.

Mounted on the platform are a germanium resistance thermometer, a heater winding, and the end of a fiber optic. The fiber optic is 0.4 mm in diameter and is held in a Teflon tube. The fiber is locked into position by a #0-80 brass set screw that gently squeezes the Teflon tube. The fiber is positioned such that the end is almost flush with the bottom of the platform. The chip is mounted centered on the bottom with the fiber emitting light on a portion of the superconducting loop.

The heater winding is composed of #40 twisted pair phosphor-bronze wire. The twisted pair was soldered at one end and wound around (50 turns, two layers) the platform. This corresponds to a heater resistance of 212 Ω . Under the heater wire is a aluminum split ring to ensure uniform heating of the platform. This split ring is heat sunk to the platform using GE7031 heat conducting varnish, as is the germanium thermometer leads. The thermometer itself is inserted into a slip fit hole with vacuum grease filling any gap.

The top of the dewar is composed of two sets of feedthrus: one for the vacuum space and another for the helium vapor space. A NW vacuum flange system was employed for the vacuum feedthrus, allowing versatility in changing the setup. The system is composed simply of a NW flange pipe cross (4 ports) bulkhead mounted to the top plate. One side port consists of a flange mounted circular multipin Deteronics vacuum feedthru that carries the 4 thermometer leads (#36 phosphor-bronze) and the two heater leads (#36 phosphor-bronze). The other side port has a vacuum valve to facilitate pump down and venting. The top port has an epoxy vacuum feedthru flange for the fiber optic. All the vacuum space wire pairs and the fiber optic were run down in #24 Teflon tubing. The vapor feedthrus consist of the following: the dc SQUID flex probe multipin connector, a 4 pin connector for the helium level meter, and a BNC feedthru for the bias solenoid.

Custom electronics were manufactured to ensure minimal noise and ground loop problems. Each circuit had a unique battery power source. The following circuits were made: a selectable low noise current source (10 μ A, 100 μ A, or 1 mA) for the thermometer; a low noise current source for the bias coil; and a voltage source for the heater windings. The thermometer was read out using a battery powered digital multimeter. All external cables were coaxial, with the exception of the He level meter and the SQUID cables.

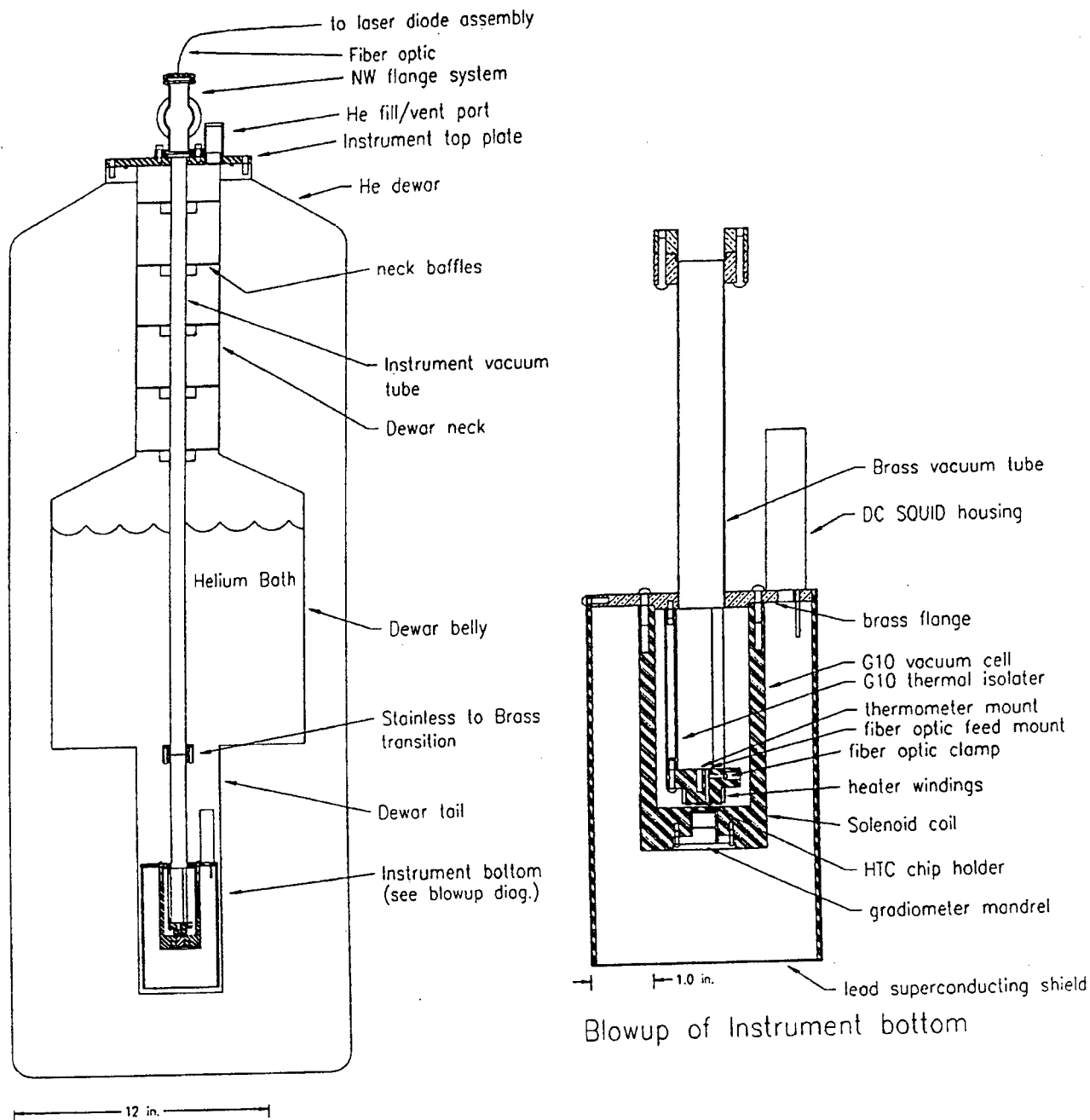


Figure 3. Experimental Apparatus Used for Optical Measurements.

The pickup coil detects quantized changes in flux from photons striking the loop surface and transmits this information to the SQUID coupled with the SQUID electronics, a Quantum Design Model 5000 dcSQUID Controller. The final output was plotted on an XY chart recorder, and/or collected digitally by a simple computer program written in C which reads the output of the dc5000 via a IEEE 488 card.

An optical isolation bench was configured with a laser source directed through a variable density filter and a neutral density filter of one percent transmission for intensity control. A fiber coupler with a 10X microscope objective was used to align this reduced intensity beam with the single mode fiber optic. The fiber feeds through a potted epoxy joint at the top of the probe with the lowest 3-5 cm terminating in the fixture at the bottom of the probe. This end of the fiber was positioned approximately 0.5 mm above the high T_c superconducting loop to be illuminated.

3.3 Biasing the Superconducting System

The Current Required to Bias the System. A large electrical current flowing normal to the vortex-antivortex pair is required to overcome the attractive force between the vortices. Kadin has postulated that the electrical current density, J , required to pull apart the vortex-antivortex pair should be of order the critical current density, J_c [6]. The maximum deviation below the critical current for which a pair will be separated depends on the frequency f of the radiation involved, and the characteristic size of the vortices. Kadin gives the following expression, in which J_0 is the mean field critical current density and d the film thickness:

$$J_0 - J = \frac{hf}{\phi_0 da}$$

The characteristic size a depends strongly on the nature of the superconducting state; for a homogeneous film it is of order the Ginzberg Landau coherence length ξ , for an intergranular array of Josephson junctions it is of order the grain size. Unfortunately, high T_c films exhibit varying degrees of granularity in their conduction properties depending on their quality. For photons of wavelength 600 nm, equation 1 gives an acceptable deviation from the critical current density of order 10^{11} A/m² for a homogeneous film and 10^8 A/m² for a granular film. Since typical values of J_0 are of order 10^{11} A/m² we see that, provided that the bias current density is close to the transport critical current density of 10^{11} A/m², there should be sufficient force to separate the pairs.

Establishing the Current. The simplest way to establish current densities of this magnitude in a closed superconducting loop is to trap a magnetic field within the loop. There are two ways to do this:

- a) Cool the loop through its superconducting transition in the presence of a magnetic field. Then remove the field. The density of magnetic flux, B , produced by this procedure is shown schematically in Figure 4a.
- b) Apply a magnetic field of magnitude twice that required to just penetrate the film. Then remove the field. As shown in Figure 4b this results in the same distribution of magnetic flux.

In the above analysis we have used the critical state model in which pinning sites within the superconducting material create a gradient in the magnetic flux density within the sample [7]. This gradient is formally equivalent to a constant current density equal to J_c flowing throughout the sample cross-section. The magnitude of the applied field required to trap the current is a factor of two greater when the flux is pushed into the film over when the film is cooled in the applied field.

There are several potential complications possible with this simple model. Firstly it assumes a homogeneous material. Secondly, it requires the flux to uniformly flow out of the sample on removal of the field and not leave by catastrophic flux jumps. In addition, for approach a), it is necessary for the sample to uniformly expel the flux within it on cooling. The major experimental complication arises if an insufficient magnetic field is applied in the flux trapping step. If the applied field is less than that at which flux just penetrates across the body of the loop to reach the center, then upon removal one will trap a complex flux and current distribution. A vortex-antivortex pair created in a region of uniform current will be pulled apart as required. However, on reaching the boundary between two regions of oppositely circulating current, a vortex will become trapped. The magnitude of the flux change in the ring will not be ϕ_0 , but some small fraction of it.

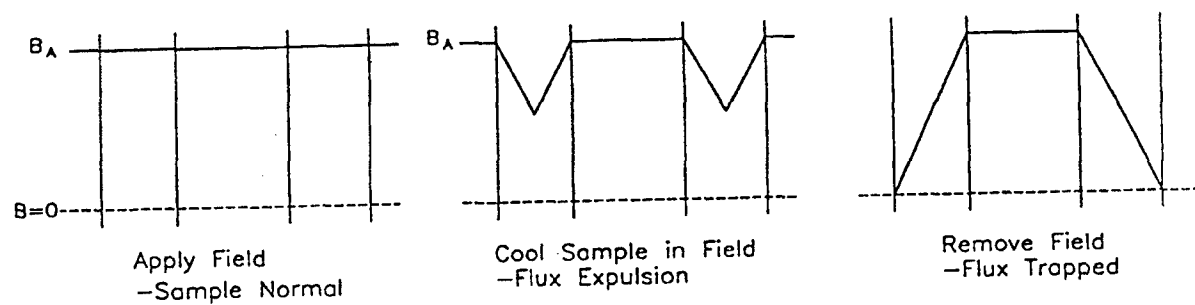
Experimental Verification. To verify that the high T_c loops could indeed support a bulk supercurrent, and to investigate the reproducibility of trapping such a current, a series of measurements was performed in a commercial SQUID magnetometer.

Initially, a simple sequence of measurements was performed at 0 gauss, with measurements taken at 5 Kelvin increments starting at 100 K down to 50 K. This verified a transition temperature at just above 80 K for the YBCO. Subsequent sequences were created to study various effects in the ring, including persistence and flux creep. The 5 mm square wafers were mounted such that the magnetic field was perpendicular to the plane of the loop.

We investigated both methods of trapping a circulating current. In the first the sample was warmed to 110 K, i.e., above the superconducting transition temperature, the desired field applied and the sample cooled to 5 K. The sample's magnetic moment was measured and then the applied field reduced to zero while maintaining a temperature of 5 K and a second measurement made. In the second test run the sample was held at a constant 5 K and measurements were taken as follows: apply a field, measure the susceptibility, apply the next higher field, etc., until a field of 300 gauss was reached. The field is then reduced in steps to 0 G, to look for a permanent diamagnetic moment.

The results of the second type of measurement on the YBCO loop are shown in Figure 5. We see that, as expected, the diamagnetic moment of the loop increases as the applied field is increased. We see that upon removal of the applied field the sample retains a permanent magnetic moment. This is due to a trapped supercurrent flowing around the loop. As the field was lowered, at an applied field of approximately 100 G the high T_c loop is no longer stable in the applied field. The pinning potential is unable to support the flux gradient, flux "jumps" into the center of the loop, and a supercurrent flows in the opposite direction around the inside circumference of the loop to maintain the flux within it. The magnetic moment is thereby reduced. As the external

a) Temperature Cycling



b) Constant Sample Temperature

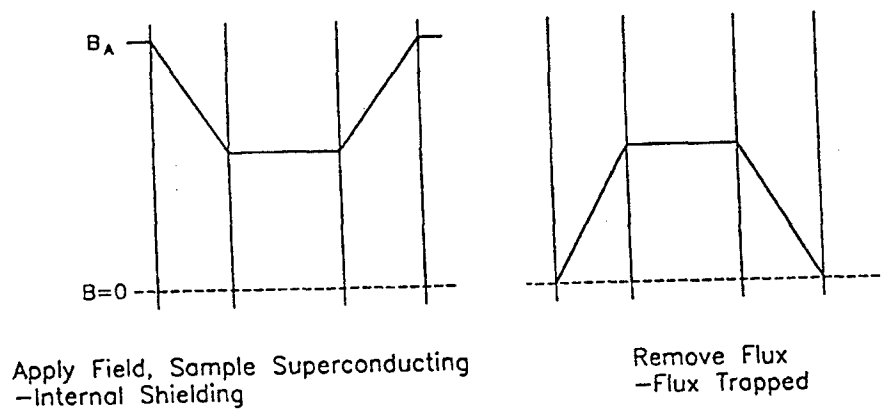


Figure 4. Two Methods of establishing uniform circulating current densities.

field is increased further the sample undergoes additional flux jumps but its maximum magnetic moment always remains of the same order.

It is clear that the preferred method of trapping flux is the method of applying a field to the already cold superconductor. This is because the method of cooling in an applied field involves waiting for thermal equilibrium in the pixel array, which in general would result in a much longer dead time for the detector. One scenario under which one could imagine a heating method would be feasible is in the case of pixels of small mass that are well-coupled to a relatively massive substrate. If the pixels were small enough, one could heat them with a short laser pulse to instigate the normal state at the same time the applied field is raised to a value where the trapped current is a maximum. This method of "charging" the detector will be considered further in Phase II work.

Calculation of the Circulating Current Trapped in the HTS Loop. One may calculate the induced circulating current from the measured magnetic moment. In Figure 5 the maximum screening current in the sample occurs at an applied field of 150 G. The measured moment at this field is equal to 8×10^{-5} emu = 8×10^{-8} Am². The area of the loop is 3.1×10^{-6} m² implying a circulating current I of $m_m/A = 0.025$ A. By using the relation $I_{max} = t \cdot b \cdot J_c$, with the thickness of the film $t = 0.2$ μm and the width $b = 0.004$ cm, the critical current of the film $J_c = 3 \times 10^6$ A/cm². From Figure 5 we see that the residual moment of 7×10^{-8} Am² upon removing the applied field implies a current flowing of 0.038 A, or a current density of 4.5×10^6 A/cm². This compares favorably with the vendor-supplied value.

It is instructive to calculate the magnetic field trapped in the loop on removal of the applied field. The inductance of the loop is given by [8] $L = 0.004\pi a [\log_e (8a/b) - 1/2]$. This equation was used to describe the YBCO loop where the radius $a = 0.1$ cm and the width $b = 0.004$ cm. $L = 0.012$ μH was the resulting value of the inductance. We can estimate the magnetic field created by a current flowing in the loop from $B = L I_{max} / A$, where B is the magnetic field in gauss, L and I_{max} are the inductance and maximum current of the loop as described above, and A is the area of the loop. Using these expressions we find that a trapped current of 0.02 A creates a magnetic field of about 1 G at the center of the loop. For reference it should be noted that a maximum of approximately 2×10^5 flux quanta may be trapped in the high T_c loops used in this study.

3.4 Calculation of the coupling factors

It is important to calculate the flux coupled in to the SQUID for a $1 \phi_0$ change in the flux state of the high T_c loop in order to compare the experimental results with theory. Simple circuit analysis leads to the following expression for the flux coupled into the SQUID:

$$\phi_{sq} = \frac{M_{sq} M_P}{L (L_{sq} + L_P)} \phi_0$$

The self-inductance and mutual inductance of the SQUID were $L_{sq} = 1.85$ μH and $M_{sq} = 0.01$ μH, respectively. The self inductance of the 2 mm diam YBCO loop is 0.006 μH and the self inductance of the NbTi pickup coil was 2 μH. ($\phi_0 = 2 \times 10^{-15}$ Wb, the numerical value of one flux quanta.)

Moment vs. Field for HTC Loop

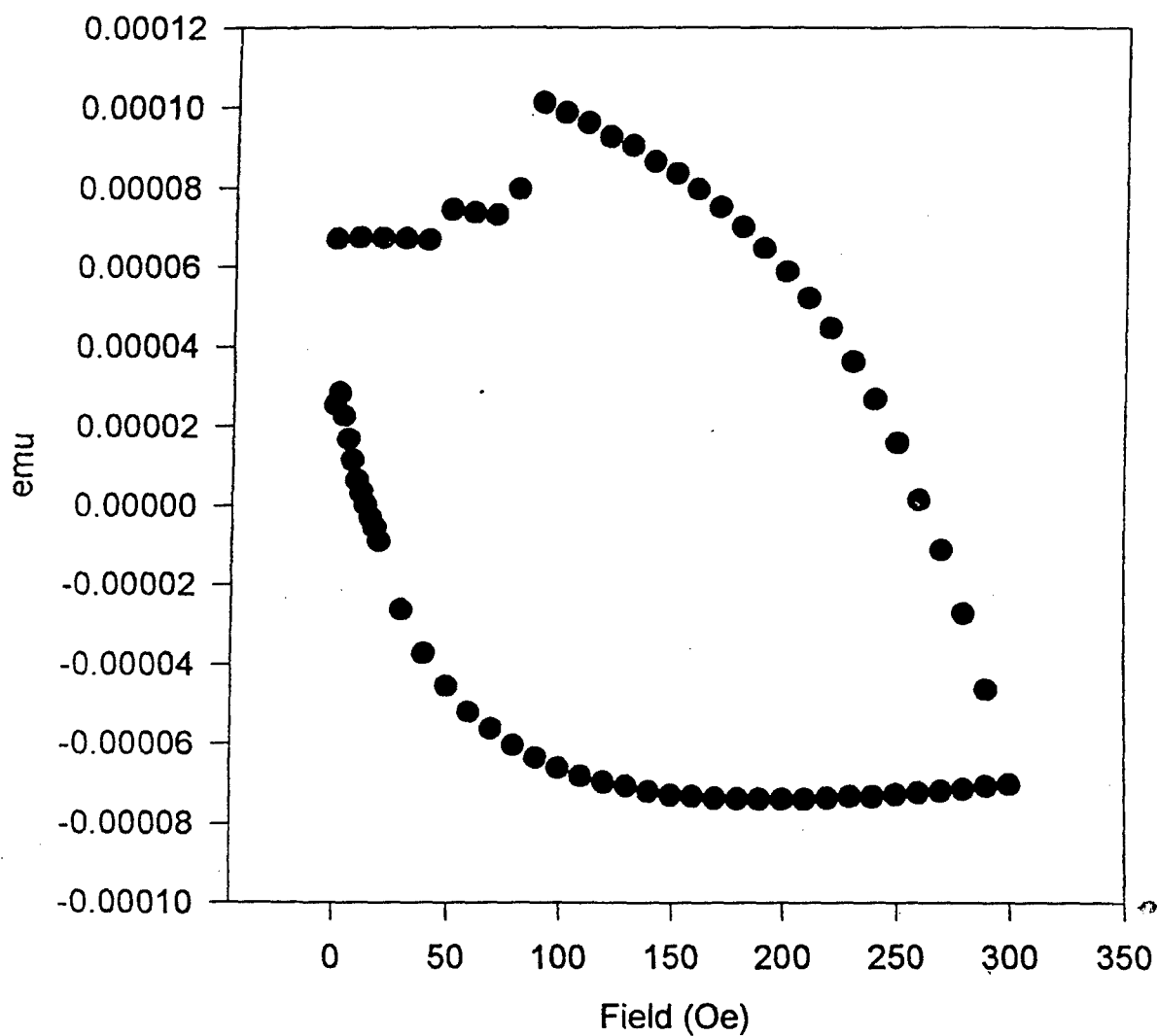


Figure 5. Trapping a magnetic moment within the sample by applying a field and then removing it.

The model used to calculate the mutual inductance M_p between the HTS loop and SQUID is that of a multiturn loop and a coaxial circular filament, where the filament is in a plane perpendicular to the axis of the solenoid [8]:

$$M = n \cdot f \cdot \sqrt{A \cdot a}$$

where the radius a of the high T_c loop is 0.1 cm, the radius A of the NbTi coil is 0.45 cm, n is the number of turns on the coil, f is a function of a , A , and the separation between the pickup coil and the pixel. The resulting mutual inductance of the NbTi coil and the high T_c loop was 0.002 μH .

Using a value of 0.002 μH for M leads to a coupling ratio of $8.9 \times 10^{-4} \phi_0$ for a one flux quantum change in the sample loop. The flux to voltage conversion factor for the SQUID is $1.26 \phi_0 = 1\text{V}$ giving a theoretical voltage step size of 0.7 mV.

4 Task 2: Analyze Array Detection Issues

4.1 Experimental Parameters

To our knowledge there was little experimental work performed by others in the period between writing our Phase I proposal and beginning our experimental investigation. Thus, we had little information to reduce the large range of experimental parameters. The issues of photon coupling into an array and the heat load of the IR signal were measured during this Phase I work on a single pixel element. Measurements on arrays of elements will be performed in Phase II work.

Measurement Bandwidth. One of the major concerns was how much filtering it would be prudent to use. The vortex crossing occurs very rapidly, on the time scale of nanoseconds, so a direct observation of the event in progress using a SQUID readout was impractical. However, it is important to observe distinct individual crossings in order to verify their amplitude. To do so accurately requires as high a measurement bandwidth as possible, which was 48 kHz for our SQUID electronics.

In our probe, the flux coupled into the SQUID for one ϕ_0 change in the high T_c loop was about $10^{-3} \phi_0$. Looking for a $10^{-3} \phi_0$ change in a 48 kHz measurement bandwidth requires a probe noise of about $5 \times 10^{-5} \phi_0 / \sqrt{\text{Hz}}$. This is about the white noise levels of the dc SQUID used when coupled to a coil of similar inductance. However, this is the white noise level for a fully shielded SQUID, for which there is a negligible contribution from the environment. When connected to a coil there is always a contribution from ambient noise and motion in the earth's magnetic field. For the maximum flexibility it was decided not to roll off the pickup coil circuit at all but attempt to do all filtering in the SQUID electronics.

4.2 Experimental Results

4.2.1 Observation of the Photofluxonic Effect

As soon as the SQUID was operational we obtained a clear change in the flux state of the YBCO loops on applying laser light. Figure 6 shows the data from two runs taken with the YBCO film

at 5 K. The field used to trap the circulating current was 15 mT corresponding to a circulating current of order 5×10^6 A/cm². The light from the 1.3 μ m semiconductor diode laser was turned on for 30 seconds, then off for 30 seconds. The data was collected in the computer through an A/D board at a rate of 6 kHz. The data was reduced by averaging in 50-point blocks. Figure 6 clearly indicates the presence of steps in the SQUID response. However, in addition to quantized steps there is a clear drift which occurs only while the light is on and for a short period (1-5 seconds depending on the circulating current) immediately after it is blocked. This same behavior was seen in many other runs at 5 K similar to those shown here. Several runs with light levels about 1% of those shown in Figure 6 showed similar background noise levels, but no drift was observable within the resolution of our measurements. Test runs without the HTS film present produced no increase in the drift signal when the light was present. Furthermore, tests with the film present but with no circulating current within it also gave zero response. Given its clear magnetic nature, the simplest interpretation of the drift is that it is due to flux vortices which become trapped in the film and move in small steps rather than pass across the body of the loop in a single sweep. These steps are too small to be resolved by our apparatus.

The main question is whether the distinct steps correspond to one flux quantum in the regions in which the flux state is changing. We expect the trapping of a single vortex-antivortex pair to produce a dc voltage step of order 0.7 mV. Figure 6a shows a flux jump of about 0.4 mV, and Figure 6b a jump of about 0.7 mV. These numbers are consistent with an interpretation in which the former is a single vortex-antivortex pair being created, and the latter a pair of photofluxonic transitions occurring too close together in time for us to resolve with our data collection limitations. We see a remarkable quantized nature in the amplitude of the steps demonstrating that we are indeed measuring the arrival of quantized units of magnetic flux into the center of our high T_c loop.

Another question which arises in interpreting the data is why the incidence of apparent photofluxonic vortices is so low. The drift rate of the signal in the presence of the laser light indicates that a large number of photons are being absorbed. Studying the efficiency of different materials for producing the photofluxonic effect will be a major Task in Phase II work.

In another set of measurements, we used an electronic circuit to chop the laser light at various frequencies. Typical results are shown in Figure 7. For this data, the light was chopped at a frequency of 10 Hz. In this Figure, we see that the general drift that was present in the unchopped light data is still present, which indicates that the film is responding to an average power input. The large jump occurred when the light was on, and has the same magnitude as the other jumps shown in Figure 6; thus we interpret this as also occurring through the photofluxonic effect.

In yet another set of measurements, we increased the temperature of the pixel to 100 K, applied a field of 12 mT, and cooled the HTS loop in the field to 60 K. The field was then removed and measurements taken with the laser light on for 60 seconds, and off for 60 seconds. The results are shown in Figure 8. During these measurements, the temperature was allowed to drift. We see that there is a large drift in the signal corresponding to the changing temperature. Any jumps due to the photofluxonic effect we unfortunately not distinguishable due to this large drift. In Phase II we will improve the temperature control of our test apparatus to allow for measurements at constant elevated temperature.

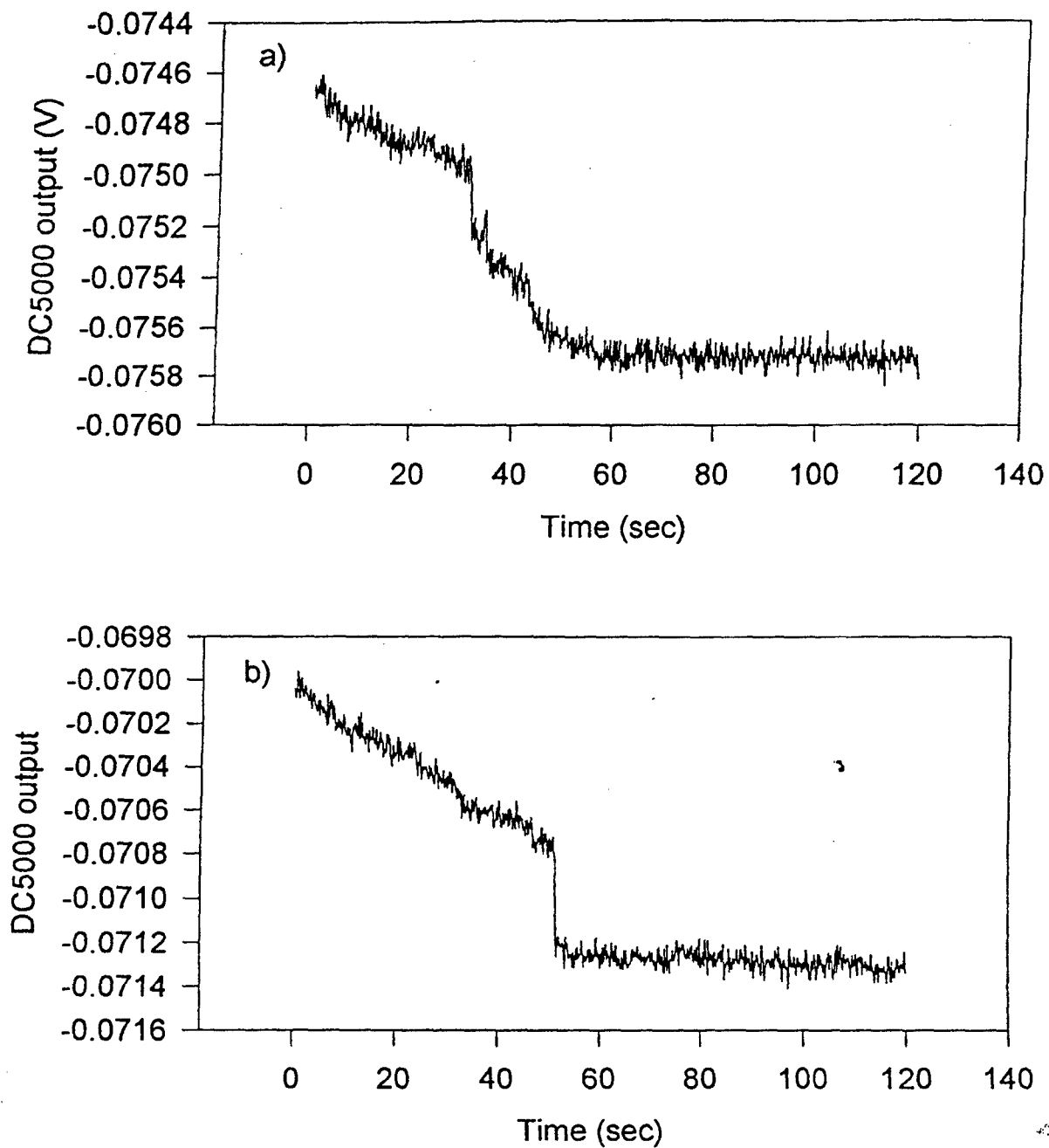


Figure 6. Photoresponse Data for YBCO Loop at 5 K, trapping Field at 12 mT. The laser was on for the first 30 seconds of data collection, then turned off for 30 seconds.

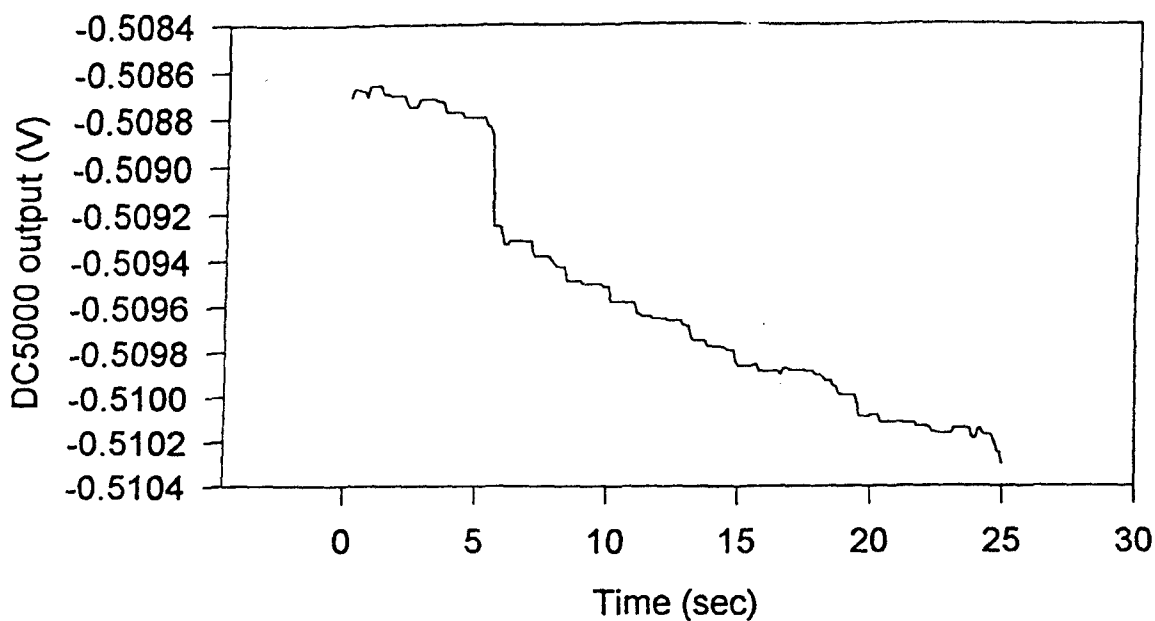


Figure 7. Photoresponse of YBCO Loop at 5 K, with the laser light chopped at a frequency of 10 Hz.

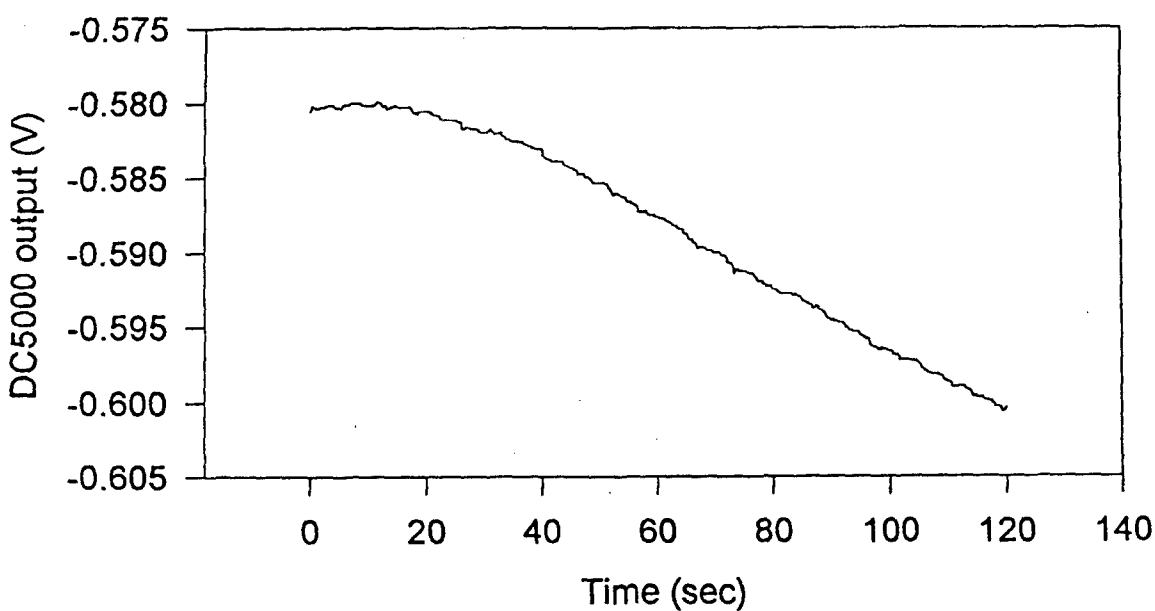


Figure 8. Photoresponse of YBCO Loop at 60 K, with laser light on for 60 seconds, then off for 60 seconds. The large drift is correlated with the changing temperature of the pixel.

4.2.2 Flux Creep

It is important to consider alternative explanations for the behavior observed. The most likely alternative phenomenon, and perhaps the only other possible explanation for the observed photoresponse, is thermally activated flux creep. Essentially, bolometric heating of the film raises its temperature thereby activating fluxons, trapped when the circulating current is set, to jump past their pinning sites. In the flux creep model there is no creation of vortex-antivortex pairs; rather the photons free flux quanta already trapped in the film.

With the laser blocked a large level of flux creep clearly took place each time a new current was set in the HTS loop. Indeed immediately after trapping a higher circulating current the sample response is so dominated by flux creep that the photoresponse is almost unmeasurable; depending on the current level it was necessary to wait between approximately one hour for the non-illuminated jump and drift signal to fall to acceptable levels. The flux creep rate has been quantified in earlier measurements by us by placing a similar sample in a field of 100 G at 5 K in a SQUID magnetometer and measuring its moment every minute for 60 minutes. The field was then dropped to 0 G and again, 60 measurements were made a minute apart. After an initial rapid decrease the creep rate was approximately 10^{-9} emu/s = 10^{-12} Am²/s after an hour. This corresponds to approximately 5000 ϕ_0 which is at least a factor of 500 too large to allow accurate measurements of photofluxonic processes. At 70 K the creep rate was a factor of 3 greater.

The crucial question as far as photofluxonics is concerned is the following: is the flux change signal when the laser is on due to the creation of vortex-antivortex pairs or simply the thermally activated escape of trapped flux? The following general observation can be made: The general drift rate builds up in the first minute after beginning. The photoresponse then proceeds by periods of decreasing drift followed by "flux avalanches" in which groups of trapped vortices appear to move at random intervals in bundles over a period of 1 to 10 seconds.

In discussing flux creep it is important to note that we really do not know the thermal time constant τ_D for this system. There are, however, two possibilities: that the sample reaches thermal equilibrium on a time scale much shorter than our experiments (i.e., τ_D is of order 10^{-6} to 10^{-1} s), or that the sample temperature generally changes during the period of illumination. Even given the uncertainty between these two cases the following arguments may be given against a flux creep interpretation.

A1: if τ_D is short then one expects the film to be raised to a higher temperature with higher light intensity and thus take longer to return to normal.

A2: if τ_D is long then this clearly contradicts a thermal model in which the film temperature increases over the time scale of our experiments (approximately 60 s).

A3: The observation that the drift rate builds up after the light is turned on is more consistent with a phenomenon in which the number of flux quanta increases with time than with one based on the freeing of trapped quanta since in the latter, the number of trapped vortices is actually a maximum at the beginning of the measurement period and should not build up.

In summary, we believe that the jumps in our data are inconsistent with thermally activated motion of flux already trapped in the sample. However this is a question of some subtlety and should be studied further in Phase II (note that an IR sensor based on thermally activated flux creep may be of great practical interest anyway, though not as exciting scientifically).

Effect of Varying the Light Intensity

For scientific reasons it is obvious that the sample photoresponse should in some way depend on the intensity of the illumination. From Figure 6, it is clear we see a clear increase in the photoresponse with increasing illumination. Further measurements demonstrated that the increase is monotonic. The data at low intensities is unreliable owing to variations in the background drift, and the fact that the total flux change is only of order 1 - 5 flux quanta which means that multi-quantum steps have a relatively large effect.

Effect of Varying the Circulating Current

A second major question is how the photoresponse is affected by the circulating current in the film. The variation of the photoresponse with intensity was measured for several values of the trapping field. We see a clear increase in the response with increasing circulating current. There appears to be some saturation of the photoresponse with trapping field at the higher light intensities.

The value of the circulating current can only be inferred from the trapping field and is not precisely known. We see from Figure 5 that the flux trapped in the sample, and hence the circulating current, is not a linear function of the trapping field but tends to a maximum. Thus the lack of increase in the photoresponse with trapping field could simply be due to the circulating current maximizing at the sample critical current.

However the circulating current does not begin to maximize for applied fields below about 10 mT, whereas at the higher intensities, apparent saturation in the photoresponse occurs for fields above 3 mT. It is tempting to suggest that the flattening of the photoresponse is due to an increase in the efficiency of the process. However, at the present time such a claim would be premature. This question will be addressed in much greater detail during Phase II. Similarly the lack of any photoresponse with a trapping field of about 0.3 mT may indicate that for low circulating currents there was insufficient Lorentz force to pull apart a vortex-antivortex pair. This must also be addressed in Phase II.

4.2.3 Comparison with Recent Research by Others

Limited efforts toward demonstrating the photofluxonic effect via resistance measurements have been made by groups at Rochester [10] and TRW. In a resistance measurement, the movement of the vortices under strong current bias results in an induced voltage across the film which can be measured. However it must be borne that all voltage based measurements suffer from the problem that it is very difficult to separate the voltage due to movement of the vortex pair from the myriad other voltages of similar magnitude which are almost certain to be present.

Spurious voltage signals could arise from changes in film resistance due to bolometric heating, the motion of partially pinned fluxons in nearby regions of the superconductor, and insufficient

screening of environmental magnetic noise which changes the local magnetic field at the junction. In fact, the difficulty of an unambiguous subtraction of all possible spurious junction voltages probably accounts for lack of direct observations of the photofluxonic effect in Josephson junctions at the present time.

In the time since our original Phase I proposal, the only notable recent publication regarding photofluxonics has come from Walko and Van Harlingen [11] who proposed an alternative detection scheme. While this scheme is similar to ours in that a SQUID is used to detect the vortex-antivortex pair magnetically, the vortices are measured while moving and no attempt is made to trap the flux created.

There have been several basic experimental investigations into the nonbolometric IR response of superconducting films. Taken as a whole, or in some cases individually, these results are inconclusive regarding the question of vortex-antivortex pair creation by photons. Ghis et al., [12] have observed the now familiar "ultra fast nonbolometric response" followed by a slower bolometric decay in the voltage IR response of YBCO thin films. Chern et al., [13] have found that the microwave response of Tl and Bi based high T_c thin films displays both bolometric and non-bolometric components but is predominantly the latter, while the effect of a cw HeNe laser is mainly bolometric.

Matsuda, et al. have shown that the motion of vortex-antivortex pairs accounts well for the temperature dependence of the Hall number, the diagonal ρ_{xx} resistivity, and Hall ρ_{xy} resistivities in single unit cell thick films of YBCO. It is postulated that a Kosterlitz-Thouless (KT) transition [14] occurs. Below the KT transition temperature vortex-antivortex pairs are bounded by a quasi-long-range order. Above the KT transition the pairs dissociate in the presence of a finite transport current. It is central to the argument that both vortices and antivortices are present. In the model the vortex-antivortex pairs are excited by thermal fluctuations and are extremely numerous; there are about ten times more pairs than vortices induced by application of a 10 T magnetic field. These most recent results will be utilized when planning the research and development to be performed in Phase II.

4.3 Pixel Configuration

The heart of an infrared imaging system is the detector focal plane. The focal plane detector consists of individual detector elements or pixels. The detected signal from each pixel is combined and analyzed to obtain an image of the source using standard mathematical techniques. For actual detectors, it is important that the detector noise dominates the noise of subsequent electronics such as preamplifiers. Also, the detector should be sufficiently fast to accommodate the necessary system bandwidth.

At this very early stage it is difficult to be very specific about the design of the pixels. Our overall concept for the array is shown schematically in Figure 9. The photosensitive detection regions (pixels) are electrically isolated superconducting rings. Given their simplicity there are three basic questions:

- a) What is the optimum high temperature superconductor for this application.

- b) What is the optimum pixel size: what diameter and track width should the loop have and what thickness of film to use.
- c) How can the coupling of light into the detection region be optimized.

Selection of the High T_c Material. Given the quantum nature of the detection process, selection of the optimum high T_c film really requires a detailed assessment of the intrinsic noise mechanisms within the detector material. For example, semiconductor detectors are limited by the presence of a background current due to minority carriers. For photofluxonic detection the dominant noise source is most likely flux creep.

The conventional way to reduce the level of flux creep is to increase the number of flux pinning centers in the material or by lowering its operating temperature. However, making the trapped flux less mobile also increases the probability that a vortex-antivortex pair will become trapped in the film instead of being pulled apart. Thus decreasing flux creep may actually prevent one of the pair being swept into the center and recorded as a detection event.

One strategy would be to use a high T_c film with very little flux pinning. In previous studies we observed a greater ratio of signal to background drift in TBCCO films than in YBCO, although this cannot be seen as a definitive study. However, it is well known that TBCCO films are less effective at pinning flux than YBCO which suggests that reducing pinning may help. Depending on the field trapped, the level of flux creep could initially be high but one could wait or devise flushing procedures to reduce its effect. However, a material with a very low level of pinning would also have a rather low critical current density. Thus the question is then: what is the minimum current necessary to separate a vortex-antivortex pair? At the present time the answer to this is unknown. One of first tasks of Phase II would be to make measurements with several different superconducting materials to determine in a systematic way the current necessary to separate vortex-antivortex pairs. One clear test of the effect of trapped vortices would be to use a type I superconductor, which cannot trap vortices in the same manner as a type II superconductor. Different procedures for depositing the films and annealing them could also be tried, to see the effect on vortex trapping.

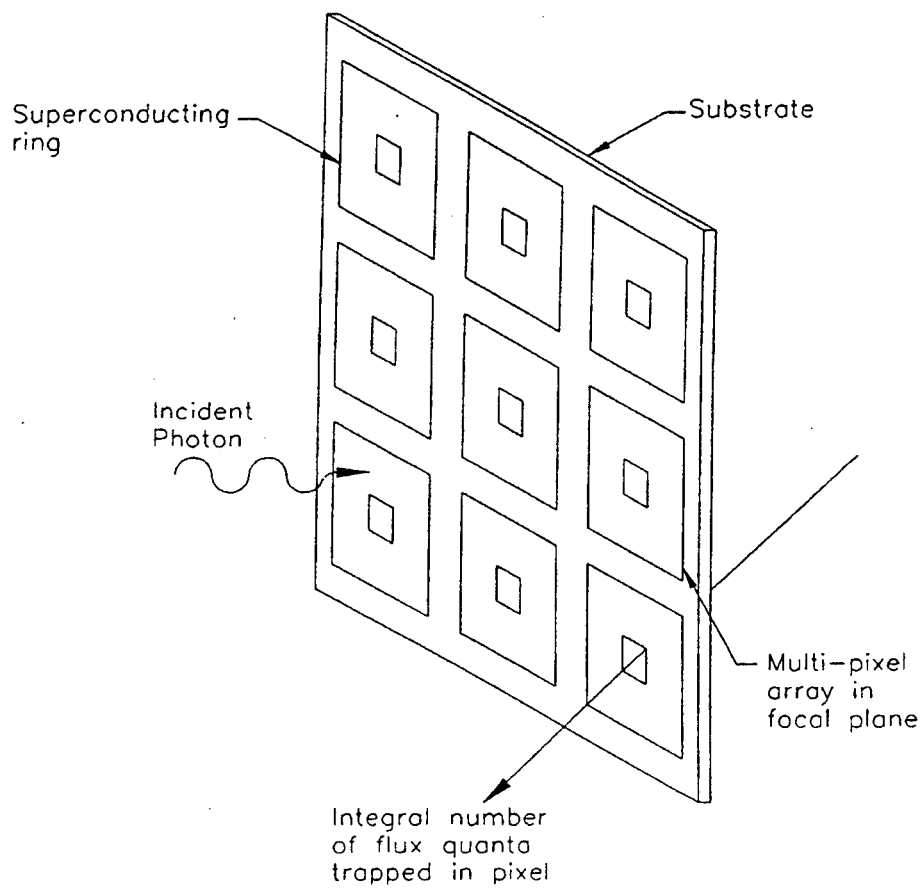


Figure 9. Schematic of Array Concept.

The Optimum Pixel Size. One way to reduce the chance of a vortex pair becoming trapped in the film is to make the width of the loop and/or the thickness of the film as small as possible. The optimum values for the pixel dimensions will depend on a number of factors, including the required resolution, sensitivity and fabrication constraints. In general one would like to make the pixel dimensions as small as possible. The following tradeoffs are apparent.

Pixel Diameter Decreasing individual pixel size will increase the pixel density allowing for more resolution of the image and reducing the cooling power requirements. The trade-offs are that small loops are more difficult to fabricate. In addition, a smaller loop will have a smaller inductance reducing the number of flux quanta that may be trapped in the loop before the loop current goes supercritical. This can, in effect, reduce the available imaging time, before the array has to be recharged by applying a magnetic field to reestablish the circulating current. The inductance of the pixel loop is approximately proportional to its diameter and so 10 μm loops will have an inductance 300 times less than our samples. The circulating current depends on the linewidth and thickness of the loop (see below) so a 3 μm x 1 μm cross section would be approximately 30 times less than used for our experiments. Thus we might expect to trap of order 100 fluxons in such a pixel. Whether such a stored flux is adequate depends on the system application. However it seems unlikely that pixels smaller than this will be feasible.

Pixel Linewidth. As mentioned above, reducing the pixel width reduces the chance that the vortex pair will become trapped within the body of the loop and not reach its center. Of course the loop width cannot be larger than its radius and so for small diameter pixels this is a further reason to make the linewidth small. Advantages of increasing the width include fabrication issues, getting a higher circulating current, and the need to maximize the photon absorption by using as large a film area as possible.

Film Thickness In this case one must trade off the desire for a large circulating current with the issue of unwanted trapping of the vortex pair. One must also consider the absorption depth of the photon within the high T_c material. This is discussed further below.

Coupling Radiation into the Detector. As for many of the above pixel design issues, maximization of the coupling of radiation into the sensor requires a detailed understanding of the physics of the process. At this very early stage we have little experimental data on which to base our discussion. Since we believe the photofluxonic process to be basically caused by local heating it should be possible to increase the efficiency of photon absorption by depositing absorption pads of antireflection coatings on the superconducting loop. Alternatively, one can arrange for the photon to be absorbed in the substrate. For example, detectors have been constructed from superconducting films deposited on GaAs in which the photons are incident on the GaAs substrate. Noise equivalent powers of $3 \times 10^{-13} \text{ W}/\sqrt{\text{Hz}}$ have been achieved on a 200 element series array $10 \times 10 \mu\text{m}^2$ junctions [15]. The choice of absorption material depends strongly on the wavelength of the radiation of interest.

Although we are not able to proceed in detail with the pixel design, from the above discussion and our experimental results we are able to deduce the following overall guidelines:

- The basic pixel configuration will be a simple single turn loop.
- The minimum pixel size will be of order 10 μm .
- Thallium or bismuth based high T_c materials may be better photofluxonic detectors.
- These general observations will be investigated in detail during the research in Phase II.

5 Task 3: Analyze Pixel Bias Issues

5.1 Refreshing the Pixels

A description of the biasing technique used in Phase I work was presented in Section 3.1.3 above. In biasing the pixels one can choose between either having discrete magnetic field coils behind each pixel in order to set them up individually or whether to use a single large coil around the entire array to perform a global refresh. It is not necessary for the coils to be cooled and so there would be no additional heat load on the refrigeration system. However, biasing the pixels individually requires that the magnetic field coils be sufficiently close to the high T_c pixels that one coil affects only the desired array element. Thus using discrete coils will increase the system complexity and may interfere with the readout scheme. Accordingly we will use a global refresh method in Phase II.

6 Task 4: Analyze Array Readout Issues

6.1 The Array Configuration

Present IR focal plane array technology involves the assembly of elements which consist of a high impedance semiconducting detector followed by a semiconducting amplifier [15]. The outputs are mixed together to produce an analog signal. The signal corresponds to the sequential interrogation of the infrared energy falling on each of the individual detector elements. The detectors are usually fabricated in a two-dimensional array on one substrate and the amplifier and mixer circuitry in a corresponding array on a second substrate. The elements are connected together by means such as indium bump bonds sandwiched between the two substrates.

It is a nontrivial task to fabricate large arrays of semiconducting elements on a single substrate having uniform electrical characteristics. It is difficult to achieve high yields because of the highly precise doping, etc. that is required. This limits single array size; larger arrays consist of a group of single arrays connected together. A problem with using large semiconducting arrays is the amount of heat that is generated. Noise considerations require that thermal imaging detectors be operated in the 40 - 100 K range [15]. In addition to this, the cooling system has to absorb the heat generated by the operating device.

Superconducting arrays generate little or no heat; current low T_c systems have to be cooled to lower temperatures than semiconducting arrays, but require less cooling power to be applied because of the reduced heat load. Superconducting arrays can use different types of detection mechanisms. Present superconductor-based device technologies include devices based on bolometric detection and the Josephson effect.

Bolometric detection can be difficult to achieve in an array, because of the need for temperature uniformity (to a millidegree or so) over the array. The sharp resistance transitions of conventional superconductors will make a detector difficult to achieve. High temperature superconductors have a broader transition, and have been used to detect IR radiation [2], but conventional superconducting electronics cannot be used (because of temperature considerations) [15].

The absence of interconnects between the pixel elements of our detector allows us great flexibility in the design of the array. There is no need to attempt to fabricate very large arrays on a single substrate which can lead to difficulties in fabrication. Instead, modest size arrays (10 X 10 or even 5 X 5) can be made and arranged together to make a larger array. Large arrays are needed to maximize the detector area for detecting weak signals. Also, in order to properly image the source, it is advantageous to collect information over as wide an area as possible.

Construction of arrays, per se, will thus be very straightforward. At the present time, almost all IR detector arrays are cooled to cryogenic temperatures and so the need to cool the proposed HTS materials will not increase the system complexity. For the Phase II prototype, we will mount the array directly on the cold finger of a cryocooler as is customary for IR detectors. We will use some form of integrated dewar assembly and so the new system will be functionally equivalent to existing IR arrays. The other issues to consider are how to bias the pixels (see Sections 3.1.3 and 5.1 above), and how to read their state. This issue is discussed below.

6.2 The Pixel Readout Scheme

One of the innovations of the proposed new photodetector is the possibility of using a non-contact inductively coupled readout scheme by detecting the magnetic field present in the high T_c loops. The signal is simply ϕ_0 divided by the loop area, which is approximately 2×10^{-9} T and 2×10^{-5} T for 1 mm and 10 μ m loops respectively. Hall effect sensors and magneto-optic devices are two possible options to use as readout devices. Each of these are magnetic field detectors and should be able to measure the field due to the flux trapped in the superconducting loops at least for smaller loop diameters. They each have their own advantages and disadvantages which will be discussed below.

Hall effect sensors [16] can be thin film and can be integrated into the IR array. A convenient way to fabricate them is to start with a silicon wafer that is suitably doped for low temperature Hall operation. If the doping is on the surface, individual Hall sensors can be made by etching patterns in the silicon wafer. The current and sensing leads can be patterned on the wafer using, say, aluminum thin film deposition and subsequent photolithography. The superconducting focal plane array can then be deposited on the other side of the wafer. If properly aligned, each individual Hall sensor will be positioned on the back of one pixel element.

This technique of using Hall sensors can be inconvenient because of the large number of electrical leads which may be necessary to drive and sense the various Hall elements. In addition to the heat leak through these electrical lines, the operation of the Hall sensors will generate additional heat to be overcome by the refrigerator/cryogen. The main problem is sensitivity. Typical devices can only detect fields down to 10^{-6} T and so will only work for pixels smaller than 50 μ m in diameter.

An alternate approach is to use magneto-optic sensors. A plane-polarized beam of light incident on a magneto-optic material has its plane of polarization rotated upon transmission through it; the amount of rotation is proportional to the thickness of the material and the ambient magnetic field. The constant of proportionality is material dependent and is known as the Verdet constant. This is the Faraday effect [17]. There is a related effect influencing the reflected light called the Kerr magneto-optic effect. For example, a normally incident plane polarized light becomes elliptically polarized on reflection, the degree of the shift in the plane of polarization being dependent on the ambient magnetic field. In one possible detection scheme, the Kerr effect can be exploited to detect the field at the superconducting loops by shining light on a magneto-optic material placed close to the superconducting loops. Field sensors based on the Faraday and Kerr effects have been made and used [18,19].

The advantage of using magneto-optics is that the heat load into the array sensor can be reduced significantly, since fiberoptics can be substituted for the electrical leads that will have to connect up the Hall sensors. There is a strong possibility that a single fiberoptic line can scan the whole array, further reducing the heat load. The pixel readout sensor will likely be simpler; the possibility of using a continuous magnetooptic film on the backside of the pixel array exists. If realized, this will further reduce the fabrication complexity of the array. Lasers to scan the pixel array should be inexpensively available; technology for this exists, for example, in magnetic storage devices and compact disc players.

To estimate the sensitivity we note that the magnetic field of the loop will extend into the magneto-optic to a distance approximately equal to its diameter. For a material with a very high Faraday rotation such as YIG, we expect rotations of 5×10^{-4} and 0.05 degrees for 1 mm and 10 μm loops respectively. These should both be detectable with existing apparatus.

7 References

1. D. Osterman et al., IEEE Trans. Mag., Vol. 27 (1991), p. 2681.
2. B.E. Cole, SPIE Vol. 1394, Progress in High-Temperature Superconducting Transistors and Other Devices (1990), p. 126.
3. A. Davidson and M.R. Beasley, IEEE J. Solid State Circ. SC-14, (1979), p. 748.
4. Y. Enomoto and T. Murakami, J. Appl. Phys., Vol. 59 (1986), p. 3807.
5. N. Fujimaki, Y. Okabe, and S. Okamura, J. Appl. Phys., Vol. 52 (1981), p. 912.
6. A.M. Kadin, Phys Rev Lett 65, (1990), p. 3193.
7. C. P. Bean, Phys. Rev. Lett, 8, 250 (1962).
8. F.W. Grover, "Inductance Calculations," Dover Publications, Inc., New York, NY, 1973.
9. M. Leung et al., Appl. Phys. Lett., Vol 51 (1987), p. 2046.
10. A.M. Kadin, M. Leung, A.D. Smith, and J.M. Murduck, IEEE Trans. on Magnetics, Vol. 27 (1991), p. 1540.
11. Proc. 4th International Superconductive Electronics Conference, Aug 11 - 14, Boulder Colorado (1993), p. 134.
12. A. Ghis et al., IEEE Trans. on Appl. Superconductivity, (1993), p. 2136.
13. J.D. Chern et al., IEEE Trans. on Appl. Superconductivity, (1993), p. 2128.
14. J. M. Kosterlitz and D. J. Thouless, J. Phys. C 6, (1972), p. 1181.
15. F.W. Quelle Jr., "Superconducting Focal Plane Arrays," Naval Research Reviews, Vol. 3 (1989), p. 3.
16. C. Kittel, "Introduction to Solid State Physics", John Wiley & Sons Inc. New York 1976.
17. Jenkins and White, Fundamentals of Optics, McGraw Hill.
18. S. N. Barybin et al., Sensors and Actuators, A25-27 (1991), p. 767.
19. C.D. Wright and N.A.E. Hayes, IEEE Trans. Mag., Vol 27 (1991), p. 5127.

Electronic References

INTERNET LOCATIONS

Note: The following URLs are current as of the date of publication.

Optical Detection Laboratory - http://www.opt-sci.arizona.edu/summaries/Eustace_Dereniak/homepage.html

The primary focus of the laboratory's research is the detection of light, not necessarily in the visible spectrum, and conversion of detected light to electrical signals. Under the umbrella of the Optical Detection Laboratory are five individual laboratories working on different detection technologies.

Infrared Information Analysis Center- IRIA - <http://www.erim.org/IRIA/iria.html>

The Infrared Information Analysis Center (IRIA) was established in 1954 at the Willow Run Laboratories to facilitate the exchange of information within the Department of Defense (DoD) infrared community. The center is now a DoD Information Analysis Center (IAC) sponsored by the Defense Technical Information Center and monitored by the Associate Director for Science and Technology, Army Night Vision and Electronic Sensors Directorate.

IRIA's mission is to collect, analyze, and disseminate information on infrared and electro-optical (IR/EO) technology with an emphasis on military applications.

International Society for Optical Engineering - <http://www.spie.org/>

A non-profit professional society dedicated to advancing research, engineering, and applications in optics, photonics, imaging, and electronics.

National Research Council of Canada-Photonic Systems Group - <http://alpha.ps.iit.nrc.ca/>

Photonics, the synthesis of optics and electronics for data transmission and manipulation, is an area of pivotal importance in information processing and it is a key enabling technology for the information highway.

University of Maryland,

Photonics Switching and Integrated Optoelectronics Lab - <http://www.ee.umd.edu/photonics>

Research in the Photonics Lab spans a wide range of topics in the field of Integrated Optoelectronics. These include semiconductor lasers and amplifiers, integrated receivers, optoelectronic interconnects and packaging, wavelength conversion devices, optical bistability, semiconductor laser reliability studies and laser theory and modeling.

Select "Related Links" to get all the following Laboratories and Research Centers:

NIST

Jet Propulsion Laboratory

David Sarnoff Center

Lawrence Livermore Laboratories

AT&T Bell Laboratories

Sandia National Laboratories

Army Research Laboratories

Rome Labs Surveillance and Photonics Home Page

AT&T Bell Laboratories

Sandia National Laboratories

Optical Sciences Center, University of Arizona

Laboratory for Optics and Quantum Electronics, University of Virginia

Center for Photonics Research, Boston University

Institute of Optics, University of Rochester

Center for Quantized Electronic Structures, University of California, Santa Barbara

Photonic Systems Group, University of Illinois at Urbana Champaign

CREOL, University of Florida

Hyperspectrum News Letter - <http://www.techexpo.com/WWW/opto-knowledge/hyperspectrum/hypersp3.html>

Technology Insertion Engineering:

the Advanced Technology Dilemma - <http://www.mcclellan.af.mil/TI/TIE/homepage.html>

Links to research in specialized areas including:

Advanced Electronics Technology Center AETC

Microelectronics Technology TIEFB

Systems and Technology Integration TIEBD

****Electro-Optics Technology TIEFC - <http://www.mcclellan.af.mil/TI/TIE/laser.html>**

Guide to NASA Online Resources:

Alphabetical List of Resources - <http://naic.nasa.gov/nic/guide/alphabetical.html>

Guide to NASA Online Resources - Alphabetical List of Resources. This page is a simple listing of the resources in this Guide by name. If you are not sure of the name, but know you'd like to find a resource that can be generally classified as scientific try this URL site.

Sample Papers and Documents Available:

Optical and Infrared Interferometric Imaging - http://dopey.caltech.edu/compastro/bispectrum_report.html

Scientific Progress in Optical and Infrared Interferometric Imaging Report prepared July 1990: 1. Overview of Techniques 2. Scientific Objectives 3. Computational Aspects of Bispectral Imaging 4. Results 5. References 6. Publications.

Near-Infrared Spectroscopy - <http://www.scimedia.com/chem-ed/spec/vib/nir.htm>

Near-Infrared Absorption Spectroscopy (NIR) Introduction NIR spectroscopy is the measurement of the wavelength and intensity of the absorption of near-infrared light by a sample. Near-infrared light spans the 800 nm - 2.5 μ m (12,500 - 4000 cm^{-1}) range and is energetic enough to excite overtones and combinations of molecular vibrations to higher energy levels.

Infrared Technology - <http://lancelot.gcs.redstone.army.mil/it.html>

Infrared Technology Functions Perform the common functions with respect to techniques, components, devices, subsystems, and systems which function in the infrared (IR) region of the spectrum such as focal plane arrays, detectors, scanners, radomes, optics.

Additional References

Note: Refer to the order form following the bibliographies for ordering information.

♦AD-A311 078
ARIZONA STATE UNIV TEMPE

(U) Scale-Based Techniques in Secure and Jam-Resistant Communication Systems.

DESCRIPTIVE NOTE: Final rept. Nov 92-Jan 96
JUL 96 29P
PERSONAL AUTHORS: Cochran, Douglas
CONTRACT NO: F49620-93-1-0051

UNCLASSIFIED REPORT

ABSTRACT: (U) This three-year project has focused on theoretical development and preliminary performance analysis for wavelet-based multiple access communication systems. Sets of orthonormal wavelet symbols suitable for asynchronous multiple access spread spectrum communications were developed. Investigation of possible countermeasures to wavelet-based communication systems led to development of a cyclostationary signal detector for which detection thresholds corresponding to desired false-alarm probabilities can be determined analytically. This detector was applied against both traditionally modulated and low probability of detection signals including wavelet modulated signals. Some basic research on wavelet analysis performed in connection with this project led to a class of multidimensional generalizations of the wavelet transform.

DESCRIPTORS: (U) *ANTIJAMMING, *SECURE COMMUNICATIONS, *SPREAD SPECTRUM, *MULTIPLE ACCESS, DETECTION, DETECTORS, PERFORMANCE TESTS, THRESHOLD EFFECTS, SIGNALS, COMMUNICATION AND RADIO SYSTEMS, COUNTERMEASURES.

IDENTIFIERS: (U) *MULTIPLE ACCESS COMMUNICATIONS, *ASYNCHRONOUS COMMUNICATIONS.

AD-A310 906
ROME LAB ROME NY

(U) Anti-Jamming Optical Beam Nuller.

DESCRIPTIVE NOTE: Rept. for Oct 92-Sep 95
MAY 96 56P
PERSONAL AUTHORS: Turbyfill, Michael E.; Lutsko, Jeffrey M.
REPORT NO: RL-TR-96-65

UNCLASSIFIED REPORT

ABSTRACT: (U) The development of an Acousto-optic (AO) based anti-jamming optical beam nuller (AJOB), including laboratory and live radar tests, is presented. The purpose of the AJOB system is the cancellation of multipath jamming interference in advanced surveillance radars. AJOB is a multichannel adaptive optical system which performs cancellation of multiple wideband (10 MBz) interference sources in the presence of multipath. The live radar test consisted of using a downconverted 80 MHz received signal from the main and subarrays of a C-band radar to correlate jamming signals produced by stationary jammers. The correlation parameters fed a tapped delay line filter to form an estimate of the noise, which was subtracted from the main antenna signal. For the scenarios tested, the long integration time for the correlation data provided accurate estimates of the jammer delays, and therefore single-step convergence was achieved.

DESCRIPTORS: (U) *RADAR ANTIJAMMING, *ACOUSTOOPTICS, ALGORITHMS, OPTICAL EQUIPMENT, ACCURACY, TRANSMISSION LINES, OPTICAL CORRELATORS, INTEGRATION, INTERFERENCE, ADAPTIVE SYSTEMS, CONVERGENCE, NULLS(AMPLITUDE), RADAR ANTENNAS, OPTICAL PROCESSING, BEAM STEERING, MULTIPATH TRANSMISSION, PHASED ARRAYS, C BAND, MULTICHANNEL, BRAGG ANGLE, ELECTRIC FILTERS, ACOUSTIC DELAY LINES.

IDENTIFIERS: (U) PHASED ARRAY RADARS, VCSEL (VERTICAL CAVITY SIDE EMITTING LASERS).

AD-A310 484

NATIONAL AIR INTELLIGENCE CENTER
WRIGHT-PATTERSON AFB OH

(U) Developments in Military Infrared and Laser Technology.

JUL 96 12P

PERSONAL AUTHORS: Huifeng, Xiong
REPORT NO: NAIC-ID(RS)T-0313-96

UNCLASSIFIED REPORT

SUPPLEMENTARY NOTE: Trans. of CAMA China
Astronautics and Missilery Abstracts, v3 n1 p173-176 1996.

ABSTRACT: (U) Infrared and laser technology is widely used in aviation and space, in reconnaissance, remote sensing and remote metering, missile warning, aircraft night vision and night navigation, and plays an important role in target detection, identification and tracking, aiming and precision guidance as well as communications. Their application can greatly increase the precision of weapons systems, increase ECM capabilities, counter stealth capabilities, counter surface object interference capabilities, greatly reduce costs, and increase the effectiveness of weapons systems. Therefore, they are recognized as power multipliers for the weapons with which the military is equipped. The military of all countries are playing serious attention to developments in infrared and laser technology, especially the development of elements components and their basic technology. For example, of the 11 different key technologies of the United States Defense Science and Technology, 1.162 billion dollars was invested in optics and electronics (primarily composed of infrared and laser technologies) during the years 1992, 1993 and 1994 (not including SDI). This constituted 13 percent of all investments in key technologies during these three years.

DESCRIPTORS: (U) *INFRARED DETECTION, *LASERS, GUIDED MISSILES, OPTICS, UNITED STATES, AIRCRAFT, DEFENSE SYSTEMS, INVESTMENTS, WEAPON SYSTEMS, TRACKING, COSTS, NAVIGATION, REMOTE DETECTORS, PRECISION, TRANSLATIONS GUIDANCE, NIGHT, NIGHT VISION, TARGET DETECTION, INFRARED RADIATION, ELECTRONIC COUNTERMEASURES, RECONNAISSANCE, CHINA, WARNING SYSTEMS, CHINESE LANGUAGE.

AD-A310 003

NATIONAL AIR INTELLIGENCE CENTER
WRIGHT-PATTERSON AFB OH(U) Applications of GPS in Airborne Electronic
Countermeasure Reconnaissance.

APR 96 10P

PERSONAL AUTHORS: Zhigang, Zhang
REPORT NO: NAIC-ID(RS)T-0082-96

UNCLASSIFIED REPORT

SUPPLEMENTARY NOTE: Trans. of CAMA, China
Astronautics and Missilery Abstracts (China) v2 n3 p39-43
1995.

ABSTRACT: (U) When implementing electronic counter reconnaissance or other electronic countermeasure missions on moving platforms, operating personnel working on the platforms must grasp in real time the exact position of the platform itself. In command posts or control centers, there is a need to understand, in real time, the direction of platform movements. When implementing the positioning of emitting sources, precise platform locations are even more indispensable. In the past, on aircraft, reliance was put on inertial navigation systems and aviation instruments to provide data and, after processing, precise positions. The limitations associated with making use of this type of method are relatively large; precisions are not high. Real time characteristics are relatively bad. Opting for the use of digital transmission navigation display systems based on global satellite navigation systems avoids the shortcomings discussed above. Moreover, it is possible to conveniently generalize application to various types of mobile platforms.

DESCRIPTORS: (U) *AERIAL RECONNAISSANCE, *GLOBAL POSITIONING SYSTEM, *ELECTRONIC COUNTERMEASURES, POSITION(LOCATION), REAL TIME, MOTION, CONTROL CENTERS, AERONAUTICS, PLATFORMS, MOBILE, MISSIONS, PRECISION, NAVIGATION SATELLITES, ARTIFICIAL SATELLITES, INSTRUMENTATION, TRANSLATIONS, CHINA, CHINESE LANGUAGE.

AD-A309 772

NAVAL AIR WARFARE CENTER AIRCRAFT DIV
PATUXENT RIVER MD

(U) F-14 LANTIRN Flight Testing. The Cat is Back!!

DESCRIPTIVE NOTE: Professional paper
APR 96 30P

PERSONAL AUTHORS: Mnich, William

UNCLASSIFIED REPORT

ABSTRACT: (U) The system is currently operational on both the F-15 and F-16. Shown here on the Strike Eagle are the key elements of LANTIRN, which features two independent pod-mounted sensors. On the left side is the navigation pod containing both the Terrain-Following Radar and Navigation FLIR images from which can be presented to the pilot on the Wide FOV raster HUD for lowlevel navigation. The targeting pod is carried on the other side, and incorporates the targeting FLIR and laser rangefinder systems. With the full two-pod system, the F15E can perform the low-altitude strike mission day or night in almost any weather conditions. It's a magnificent weapons system with an outstanding combat record, and was one of the stars of Desert Storm. Unfortunately, the F-15 can't land on an aircraft carrier. So, why did the Navy decide to incorporate the LANTIRN targeting pod on the F-14, and how did we do it?

DESCRIPTORS: (U) *FLIGHT TESTING, *FORWARD LOOKING INFRARED SYSTEMS, *NIGHT FLIGHT, *LOW ALTITUDE, *TERRAIN ANALYSIS RADAR, *NIGHT RECONNAISSANCE, DETECTORS, WEAPON SYSTEMS, LASERS, NAVIGATION, EXTERNAL STORES, LOW LEVEL, DAY, TARGETING, MOUNTS, RANGE FINDING, STRIKE WARFARE, RASTERS, TERRAIN FOLLOWING.

IDENTIFIERS: (U) F-14 AIRCRAFT, LANTIRN(LOW ALTITUDE NAVIGATION TARGETING INFRARED FOR NIGHT).

AD-A309 765

NAVAL AIR WARFARE CENTER AIRCRAFT DIV
PATUXENT RIVER MD

(U) Air Combat Environment Test and Evaluation Facility (ACETEF) Support for Multi-Sensor, Multi-Spectral Sensor Fusion Testing.

MAY 96 22P

PERSONAL AUTHORS: Macone, Dan

UNCLASSIFIED REPORT

ABSTRACT: (U) This paper presents an outline of the following: Description of ACETEF Multi-Sensor/ MultiSpectral Sensor Fusion Testing Issues; Example Applications; Distributed Training and Test Applications; Summary.

DESCRIPTORS: (U) *DATA FUSION, *MULTISENSORS, DETECTORS, TEACHING METHODS, AERIAL WARFARE, MULTISPECTRAL.

IDENTIFIERS: (U) ACETEF(AIR COMBAT ENVIRONMENT TEST AND EVALUATION FACILITY).

★AD-A309 670

ARNOLD ENGINEERING DEVELOPMENT CENTER
ARNOLD AFB TN

(U) Direct Write Scene Generation Development Efforts for
Closed-Loop Evaluation of Focal Plane Arrays.

DESCRIPTIVE NOTE: Final rept. 1 Oct 94-30 Sep 95
MAY 96 48P

PERSONAL AUTHORS: Steely, S. L.; Fugerer, R. H.;
Lowry, H. S., III; Holt, L. L.
REPORT NO: AEDC-TR-95-34

UNCLASSIFIED REPORT

ABSTRACT: (U) Laser based closed loop Direct Write Scene Generation (DWSG) methods are being developed at AEDC to simulate dynamic sensor operations and complex infrared scenes. New photonic image synthesis methods are being developed to employ image to object Whittaker Shannon sampling, anisoplanatic optical convolution by quasiisoplanatic spatial decomposition, and high speed digital electronics for acoustooptic modulation. Because of the large terabyte volume of data to be processed, the increased bandwidth requirements, and the increased simulation fidelity required for DT&E and OT&E of focal plane array sensors, the laser based DWSG methodology is being extended to accommodate optical and computational decomposition methods to better exploit highly and massively parallel real time image processing schemes. Optical and computational decomposition will not only provide high fidelity optical simulation for anisoplanatic optical sensors and complex infrared scenes, but will also facilitate high speed parallel processing schemes for real time closed loop DWSG and sensor operations. A computer simulation has been constructed and is being used to develop and evaluate the high speed computational algorithms required for scene extraction and convolutions. A Proof of Principle demonstration using existing DWSG hardware also illustrated the feasibility of the concept.

DESCRIPTORS: (U) *FOCAL PLANES, *INFRARED HOMING ALGORITHMS, COMPUTERIZED SIMULATION, REQUIREMENTS, FLIGHT TESTING, DIGITAL SYSTEMS, COMPUTATIONS, PARAMETRIC ANALYSIS, COST EFFECTIVENESS, REAL TIME, ARRAYS, LASER APPLICATIONS, INFRARED IMAGES, STATISTICAL PROCESSES, BANDWIDTH, DECOMPOSITION, CLOSED LOOP SYSTEMS, ACOUSTOOPTICS.

IDENTIFIERS: (U) *FOCAL PLANE ARRAYS, DWSG(DIRECT WRITE SCENE GENERATION), WHITTAKER SHANNON SAMPLING.

AD-A309 229

NORTHWESTERN UNIV EVANSTON IL

(U) New Infrared Materials and Detectors.

1995 6P

PERSONAL AUTHORS: Razeghi, M.; Kim, U. D.; Park, S. U.; Choi, Y. H.; Wu, D.

CONTRACT NO: N00014-92-U-1951, \$N00014-94-1-0902

UNCLASSIFIED REPORT

AVAILABILITY: Pub. in Inst. Physics Conference Ser., n145 c8 p1085-1090 1995. Available only to DTIC users. No copies furnished by NTIS.

ABSTRACT: (U) In this paper, we present an overview of the growth of $\text{InAs}(1-x)\text{Sb}_x$, $\text{InAs}(1-x)\text{Sb}(x)$, $\text{In}(1-x)\text{Tl}(x)\text{Sb}$, and $(\text{InP})_x(\text{TlP})_x$ as potential materials for long wavelength (8-12 microns) infrared photodetector applications. Incorporation of thallium into InSb and InP resulted in a bandgap decrease of the alloys. Thallium incorporation has been evidenced by various techniques such as X-ray diffraction, Auger electron spectrometry and photoconductivity measurements. Preliminary photodetectors fabricated from the grown materials are also reported. InAsSb photodetectors showed room temperature photoresponse up to 13 microns.

DESCRIPTORS: (U) *INFRARED DETECTORS, *PHOTODETECTORS, *INFRARED OPTICAL MATERIALS, REPRINTS, HALL EFFECT, X RAY DIFFRACTION, INDIUM ALLOYS, FOCAL PLANES, LONG WAVELENGTHS, AUGER ELECTRON SPECTROSCOPY, PHOTOVOLTAIC EFFECT, CRYSTAL GROWTH, INFRARED SPECTRA PHOTOCONDUCTIVITY, THALLIUM, INDIUM COMPOUNDS, PHOTSENSITIVITY, INFRARED PHOTOCONDUCTORS.

AD-A308 808

WAYNE STATE UNIV DETROIT MI DEPT OF
ELECTRICAL AND COMPUTER ENGINEERING(U) Photoconductive Gain and Generation-Recombination
Noise in Quantum Well Infrared Photodetectors.

FEB 95 6P

PERSONAL AUTHORS: Shadrin, V. D.; Mitin, V. V.;
Kochelap, V. A.; Choi, K. K.
CONTRACT NO: DAAH04-94-G-0097

UNCLASSIFIED REPORT

AVAILABILITY: Pub. in Jnl. of Applied Physics, v77 n4
p1771-1776, 15 Feb 95. Available only to DTIC users. No
copies furnished by NTIS.

ABSTRACT: (U) Photocurrent and excess current noise in a quantum well infrared photodetector are considered using a drift-diffusion model of charge carrier transport. The effect of quantum well recharge under the influence of the nonuniform generated charge carriers is addressed. The recharging effect drastically changes the dependency of both photoconductive gain and excess current noise gain upon detector parameters. We have found that for uniform generation, both gains coincide. For nonuniform generation, noise gain is essentially different from photoconductive gain. This distinction is of the order of 100% for the real device parameters. The existing discrepancy in formulae for photoconductive gain and excess current noise derived in different models, which implicitly assumed drift transport of electrons, is cleared up.

DESCRIPTORS: (U) *INFRARED DETECTORS,
*RECOMBINATION REACTIONS,
*PHOTODETECTORS, REPRINTS, PARAMETERS,
QUANTUM WELLS, CHARGE CARRIERS, TRANSPORT
PROPERTIES, DRIFT CHARGE TRANSFER,
NOISE(ELECTRICAL AND ELECTROMAGNETIC).

IDENTIFIERS: (U) DRIFT DIFFUSION MODEL,
QWIP(QUANTUM WELL INFRARED
PHOTODETECTORS).

AD-A308 323

CORNELL UNIV ITHACA NY LAB OF ATOMIC AND
SOLID STATE PHYSICS(U) Experimental Study of Unusual IR and Far IR
Vibrational Energy Transfer Processes in Solids.DESCRIPTIVE NOTE: Final rept. 1 Aug 92-31 Jan 96
JAN 96 60PPERSONAL AUTHORS: Sievers, A. J.
CONTRACT NO: DAAL03-92-G-0369

UNCLASSIFIED REPORT

ABSTRACT: (U) Seven different experimental studies are described. (a) Hole burning in chalcogenide glasses: The dephasing time is a function of the average coordination number of the glass and is independent of the chemical composition. (b) Vibrational relaxation of diatomic molecules in alkali halide crystals: The matrix isolated CN- molecule obeys an energy gap law while the hydride molecule does not. (c) Vibrational relaxation of diatomic molecules in glass: Our IR pump - probe examination of SH in As₂S₃ glass has shown that this impurity molecule is actually weakly hydrogen bonded in the glassy structure. (d) Pocket vibrational modes in crystals: A systematic study of a point defect in a crystal lattice has demonstrated that there are localized modes with the maximum mode amplitude at sites far removed from the defect itself. (e) Intrinsic localized vibrational modes in perfect crystals: The inclusion of both cubic and quartic terms in the potential has produced not only localized vibrational modes but also a localized dc expansion at the mode site. (f) Extinction sum rules for particles of arbitrary size: We have uncovered a general extinction sum rule which is independent of the size of the particle in relation to the wavelength and independent of the composite nature of the particle. (g) Measurement of a charged particle bunch from the coherent transition radiation mm-wave spectrum: The coherent far infrared radiation induced from relativistic electron bunches submillimeter length provides a new way to characterize the electron bunch shape.

DESCRIPTORS: (U) *INFRARED PHOTOCONDUCTORS,
EXTINCTION, EXPERIMENTAL DATA, HYDRIDES,
MOLECULAR VIBRATION, CRYSTAL LATTICES,
ENERGY GAPS, ENERGY TRANSFER, CHARGED
PARTICLES, GLASS, POINT DEFECTS, IMPURITIES,
FAR INFRARED RADIATION, HALIDES, DIATOMIC
MOLECULES, RELAXATION, SUBMILLIMETER
WAVES, OPTICAL PUMPING, CHALCOGENS, ALKALI
METAL COMPOUNDS.

AD-A307 934

MASSACHUSETTS INST OF TECH LEXINGTON
LINCOLN LAB(U) Spatial-Temporal Detection of Electro-Optic Moving
Targets.

DESCRIPTIVE NOTE: Journal article

APR 95 10P

PERSONAL AUTHORS: Pohlig, Stephen C.

REPORT NO: JA-6920

CONTRACT NO: F19628-90-C-0002

UNCLASSIFIED REPORT

AVAILABILITY: Pub. in IEEE Transactions on Aerospace
and Electronic Systems, v31 n2 p608-616, Apr 95. Available
only to DTIC users. No copies furnished by NTIS.

ABSTRACT: (U) A maximum likelihood algorithm to detect moving targets in space time electrooptic data is derived using a model of temporally stationary and spatially nonstationary clutter statistics. Performance is evaluated in terms of the probabilities of false alarm and detection. This algorithm is applied to a variety of image sequences: visible band and infrared (IR) sensors, with terrestrial and celestial clutter backgrounds. Comparison of theoretically predicted and experimentally derived statistics shows excellent agreement, validating the model and theoretical predictions.

DESCRIPTORS: (U) *ELECTROOPTICS, *INFRARED DETECTORS, ALGORITHMS, REPRINTS, MAXIMUM LIKELIHOOD ESTIMATION, THEORY, CLUTTER, STATISTICS, MOVING TARGETS, FALSE ALARMS, INFRARED IMAGES, BACKGROUND.

AD-A307 923

GENERAL RESEARCH CORP WESTLAKE VILLAGE CA

(U) Advanced Surveillance Testbed (AST) Space Based
Infrared Upgrades.DESCRIPTIVE NOTE: Final technical rept. Mar 94-Feb 95
NOV 95 12P

PERSONAL AUTHORS: Chase, R.; Singkofer, K.

CONTRACT NO: F30602-91-D-0042

UNCLASSIFIED REPORT

ABSTRACT: (U) This report covers upgrades made to the General Research Corporation Advanced Surveillance Testbed (AST). Under this task, major upgrades were made to the AST phenomenological models. These included upgrades to the synthetic background models, development of a statistical persistence model, and development of a target intensity model based on CHARM and SIRRM. In addition, selected AST signal processing and data processing modules were upgraded to accommodate the newly defined phenomenological inputs.

DESCRIPTORS: (U) *RECONNAISSANCE SATELLITES, *INFRARED SURVEILLANCE, SIGNAL PROCESSING, TEST BEDS, MODELS, PROCESSING EQUIPMENT, MODULES(ELECTRONICS), BACKGROUND RADIATION, SPACE BASED.

IDENTIFIERS: (U) AST(ADVANCED SURVEILLANCE TESTBED).

AD-A307 720

MASSACHUSETTS INST OF TECH CAMBRIDGE

(U) Space-Based Space Surveillance with MSX.

1995 12P

PERSONAL AUTHORS: Gaposchkin, E. M.

REPORT NO: MS-10596A

CONTRACT NO: F19628-95-C-0002

UNCLASSIFIED REPORT

AVAILABILITY: Pub. in Spaceflight Mechanics v89 p1681-1690 1995. Available only to DTIC users. No copies furnished by NTIS.

ABSTRACT: (U) Space Surveillance is the task of keeping a current catalogue of information on man made earth bound resident space objects (RSOs) to support military and civilian needs. The mission areas include new launch processing, RSO catalogue maintenance (including debris) and catalogue augmentation, ASAT support, satellite attack warning, RSO mission and payload assessment, and treaty monitoring. Some of the necessary functions to perform these missions are search and detection acquisition, tracking, data processing, tasking and scheduling, and network integration. At present, a mature network of sensors, radar and optical, provide the data to accomplish these missions. Evolving requirements suggest a smart, space based sensor could enhance this system. The Midcourse Space Experiment (MSX) has three sensor systems covering four Infrared bands (Spirit 3), the visible band (SBV), and five UV and Visible bands (UVISI) that will provide space surveillance data to demonstrate concepts for space based space surveillance. For MSX there are 18 space surveillance experiments in four categories. They are incremental. First, there are four sensor technology tests - sensor characterization and calibration - seeking to learn about the performance of this suite of space based sensors in stressing backgrounds for search, target detection, clutter suppression, tracking and metric, photometric, and radiometric accuracy.

DESCRIPTORS: (U) *SPACE SURVEILLANCE, *INFRARED DETECTORS, *WARNING SYSTEMS, DATA PROCESSING, REPRINTS, MILITARY REQUIREMENTS, ULTRAVIOLET RADIATION, MONITORING, NETWORKS, TARGET ACQUISITION, AUGMENTATION, TRACKING, RADAR, FAR INFRARED RADIATION, INTEGRATION, VISIBILITY CALIBRATION, DATA FUSION, TREATIES, RADAR CLUTTER, TARGET DETECTION, CATALOGS, MULTISENSORS, RADIOMETRY, SUPPRESSION, RECONNAISSANCE SATELLITES, SPACE BASED.

IDENTIFIERS: (U) MSX(MIDCOURSE SPACE EXPERIMENT)

*AD-A307 620

NAVAL SURFACE WARFARE CENTER
DAHLGREN DIV VA

(U) Detection Range Performance-Horizon Infrared Surveillance Sensor (HISS). Phase 2.

DESCRIPTIVE NOTE: Rept. for Nov 93-Apr 94

JAN 95 64P

PERSONAL AUTHORS: Dezeew, Patrick A.

REPORT NO: NSWCCD/MP-94/363

UNCLASSIFIED REPORT

SUPPLEMENTARY NOTE: Original contains color plates. All DTIC/NTIS reproductions will be in black and white.

ABSTRACT: (U) The Horizon Infrared Surveillance Sensor (HISS) Phase 2 system was involved in field testing at Wallops Island, Virginia from November 1993 through April 1994. This report discusses the HISS project and presents results from the analysis of system detection range performance. The HISS Phase 2 detection range performance has been used to demonstrate IR contributions to an integrated sensor system and to verify detection range predictions and improve the fidelity of current detection range performance models.

DESCRIPTORS: (U) *INFRARED DETECTORS, INTEGRATED SYSTEMS, FIELD TESTS, GUIDED MISSILE RANGES, INFRARED SURVEILLANCE, HORIZON SCANNERS.

IDENTIFIERS: (U) HISS (HORIZONTAL INFRARED SURVEILLANCE SENSORS).

* Included in *The DTIC Review*, October 1996

AD-A307 617

ELECTROCHEMICAL SOCIETY INC. PENNINGTON NJ

(U) Proceedings of the Third International Symposium on Long Wavelength Infrared Detectors and Arrays: Physics and Applications III Held in Chicago, Illinois on 8-13 October 1995. Volume 95-28.

APR 96 273P

PERSONAL AUTHORS: Calvo, Roque J.

UNCLASSIFIED REPORT

ABSTRACT: (U) The third symposium on Long Wavelength Infrared Detectors and Arrays: Physics and Applications was held at the Fall Meeting of the Electric Chemical Society, October 8-13, 1995 in Chicago. A collection of papers was published in the beginning of the Third International Symposium.

DESCRIPTORS: (U) *SYMPOSIA, *INFRARED DETECTORS, QUANTUM WELLS, ALUMINUM GALLIUM ARSENIDES, SUPERLATTICES, ARRAYS, FAR INFRARED RADIATION, PHOTODETECTORS, FOCAL PLANES, LONG WAVELENGTHS, BOLOMETERS.

IDENTIFIERS: (U) FOCAL PLANE ARRAYS.

AD-A307 392

MASSACHUSETTS INST OF TECH
LEXINGTON LINCOLN LAB

(U) Synthetic-Aperture-Radar Imaging with a Solid-State Laser.

DESCRIPTIVE NOTE: Journal article

OCT 95 10P

PERSONAL AUTHORS: Green, Thomas J., Jr.; Marcus, Stephen; Colella, Barry D.

REPORT NO: MIT-JA-7186

CONTRACT NO: F19628-95-C-0002

UNCLASSIFIED REPORT

AVAILABILITY: Pub. in Applied Optics, v34 n30 p6941-6949, 20 Oct 95. Available only to DTIC users. No copies furnished by NTIS.

ABSTRACT: (U) We report the operation of an imaging Nd:YAG microchip laser synthetic aperture radar, with which we imaged two dimensional (2-D) models of military targets. The images obtained showed spatial resolution significantly better than the diffraction limit of the real aperture in the along-track dimension. The signal processing is described, and the measurement sensitivity is both predicted and verified. In addition, 2-D images with high resolution in both dimensions were generated by using an asymmetric aperture to match the along-track synthetic aperture resolution with the across-track diffraction limited resolution.

DESCRIPTORS: (U) *OPTICAL RADAR, SIGNAL PROCESSING, REPRINTS, SYNTHETIC APERTURE RADAR, SENSITIVITY, HIGH RESOLUTION, DIFFRACTION, LIMITATIONS, MILITARY APPLICATIONS, NEODYMIUM LASERS, LASER TARGETS.

IDENTIFIERS: (U) ND:YAG LASERS.

AD-A306 502

NATIONAL AIR INTELLIGENCE CENTER
WRIGHT-PATTERSON AFB OH(U) Developments in Infrared Detection and Tracking
Technology and Applications to Missiles.

MAR 96 49P

PERSONAL AUTHORS: He, Liping
REPORT NO: NAIC-ID(RS)T-0633-9

UNCLASSIFIED REPORT

SUPPLEMENTARY NOTE: Trans. of unidentified Chinese
language periodical, 45p.

ABSTRACT: (U) The article generally describes the functions, work modes, cooling methods and major performance indicators of infrared detectors. Detailed presentations are given on development of infrared detection tracking technology, in addition to several infrared detectors with development prospects in weapon systems. Moreover, applications of this technology are enumerated in the field of tactical missiles, SDI project, and in the Gulf War. Finally, several proposals are made on future developments.

DESCRIPTORS: (U) *INFRARED DETECTION, *GUIDED MISSILES, * INFRARED TRACKING, METHODOLOGY, WARFARE, GULFS, WEAPON SYSTEMS, TRACKING, COOLING, INFRARED DETECTORS, TRANSLATIONS, INDICATORS, TACTICAL WEAPONS, FIELD EQUIPMENT, CHINA, CHINESE LANGUAGE.

AD-A306 446

NATIONAL AIR INTELLIGENCE CENTER
WRIGHT-PATTERSON AFB OH

(U) Countermeasures of Military Space Systems.

FEB 96 18P

PERSONAL AUTHORS: Bo, Tian
REPORT NO: NAIC-ID(RS)T-0620-95

UNCLASSIFIED REPORT

SUPPLEMENTARY NOTE: Trans. of unknown Chinese
source np nd.

ABSTRACT: (U) Countermeasures can effectively ensure the safety of space systems in coping with space challenges in military space systems. Briefly, the article presents the features and difficulties of space system countermeasures, along with the types and attack principles against hostile threats against satellites, protective techniques of satellite-borne systems, selection of countermeasure platforms, countermeasure types, countermeasure techniques with multiple platforms, space C3 countermeasures, space countermeasure techniques, and integration of space countermeasures.

DESCRIPTORS: (U) *SPACE SYSTEMS, *COUNTERMEASURES, METHODOLOGY, MILITARY REQUIREMENTS, THREATS, ATTACK, PLATFORMS, SAFETY, PROTECTION, TRANSLATIONS, ENEMY, CHINA, CHINESE LANGUAGE.

AD-A306 438

NATIONAL AIR INTELLIGENCE CENTER
WRIGHT-PATTERSON AFB OH(U) The Development of Background Limited Infrared
Detection Systems Outside of China.

FEB 96 28P

PERSONAL AUTHORS: Hui, Li; Zibin, Wang
REPORT NO: NAIC-ID(RS)T-0631-95

UNCLASSIFIED REPORT

SUPPLEMENTARY NOTE: Trans. of Guo Wai Bei Jing
Xian Hong Wai Tan Ce Xi Tong De Fa Zhan (China)
p460-470.ABSTRACT: (U) This article summarizes the development of
background limited infrared detection systems outside China,
describing a number of infrared space detection systems. It
primarily introduces long wave infrared focal plane array
technologies. Finally, it puts forward our proposals.DESCRIPTORS: (U) *INFRARED DETECTORS, FOR-
EIGN TECHNOLOGY, TRANSLATIONS, FOCAL
PLANES, CHINA, CHINESE LANGUAGE.IDENTIFIERS: (U) FOREIGN REPORTS, FOCAL PLANE
ARRAYS, Z PLANE TECHNOLOGY.

AD-A306 425

NATIONAL AIR INTELLIGENCE CENTER
WRIGHT-PATTERSON AFB OH(U) Heat Effect Calculations of PC Type HgCdTe Detectors
when Irradiated by Laser.

FEB 96 10P

PERSONAL AUTHORS: Zhipinq, Jianq; Tianjiao, Lian
REPORT NO: NAIC-ID(RS)T-0610-95

UNCLASSIFIED REPORT

SUPPLEMENTARY NOTE: Trans. of unknown Chinese
source np nd.ABSTRACT: (U) The heat model of laser irradiated PC type
HgCdTe detectors is built with the help of measuring the
resistance temperature relation and the time variation when
laser irradiated. The laser damage thresholds under three
damage mechanisms are calculated.DESCRIPTORS: (U) *INFRARED DETECTORS, *LASER
DAMAGE, COMPUTATIONS, THRESHOLD EFFECTS,
TRANSLATIONS, IRRADIATION, HEAT, MERCURY
CADMIUM TELLURIDES, CHINA, CHINESE LAN-
GUAGE.

IDENTIFIERS: (U) FOREIGN REPORTS.

AD-A306 012

AIR FORCE INST OF TECH
WRIGHT-PATTERSON AFB OH

(U) A Systems Engineering Approach to Aircraft Kinetic Kill Countermeasures Technology: Development of an Active Aircraft Defense System for the C/KC-135 Aircraft. Volume 1.

DESCRIPTIVE NOTE: Master's thesis
DEC 95 243P

PERSONAL AUTHORS: Cherry, Mark C.; Dewitt, Bruce R. Dusseault, Christopher G.; Hagan, Joel U.; Peterson Brian S.
REPORT NO: AFIT/GSE/ENY/95D-01

UNCLASSIFIED REPORT

ABSTRACT: (U) Modern Surface to Air Missiles (SAMs) present a significant threat to today's military and civilian aircraft. Current countermeasure systems such as flares and chaff rely on decoying the missile threat and do not provide adequate protection against advanced computerized missiles (Schaffer, 1993:1). An aircraft defense system that actively seeks out and defeats an incoming missile by placing a physical barrier in the missile's path offers a promising alternative to current countermeasures technology. This thesis reports the preliminary design of an active aircraft defense system for the protection of the C/KC-135 aircraft from SAMs. The developed system utilizes a kinetic kill mechanism to protect the aircraft from shoulder launched missiles while the aircraft is in the takeoff and climbout configurations. Both smart anti-missile expendables and dumb projectile expendables are evaluated. The iterative Systems Engineering approach is used to narrow the solution set to the optimal design. The final outcome is the refined design of two candidate aircraft defense systems employing a kinetic kill mechanism. Both systems utilize a modified ultra-violet tracker and employ one of two types of nets, one made out of Detonation Cord and the other made out of Spectra.

DESCRIPTORS: (U) *TANKER AIRCRAFT, *JET TRANSPORT AIRCRAFT, *COUNTERMEASURES, *AIRCRAFT DEFENSE SYSTEMS, GUIDED MISSILES, OPTIMIZATION, SYSTEMS ENGINEERING, ULTRAVIOLET RADIATION, AIRCRAFT, DEFENSE SYSTEMS, MILITARY AIRCRAFT, ANTIMISSILE DEFENSE SYSTEMS, ACTIVE DEFENSE, THREATS, PHYSICAL PROPERTIES, REPORTS PATHS TRACKING, THESES, SOLUTIONS (GENERAL), BARRIERS, TAKEOFF, DECOYS, COMPUTER APPLICATIONS, CIVIL AVIATION, SYSTEMS APPROACH, SURFACE TO AIR MISSILES, KINETICS, NUMERICAL METHODS AND PROCEDURES, ITERATIONS, KILL MECHANISMS, CHAFF, ADVANCED WEAPONS, EXPENDABLE, DETONATING CORD, SHOULDER LAUNCHED WEAPONS.

IDENTIFIERS: (U) C-135 AIRCRAFT, KC-135 AIRCRAFT.

AD-A305 718

AIR FORCE INST OF TECH
WRIGHT-PATTERSON AFB OH

(U) Non-Imaging Infrared Spectral Target Detection.

DESCRIPTIVE NOTE: Master's thesis
SEP 95 123P

PERSONAL AUTHORS: Whiteley, Matthew R.
REPORT NO: AFIT/GAP/ENP/95S-01

UNCLASSIFIED REPORT

ABSTRACT: (U) Automatic detection of time-critical mobile targets using spectral-only infrared radiance data is explored. A quantification of the probability of detection, false alarm rate, and total error rate associated with this detection process is provided. A set of classification features is developed for the spectral data, and these features are utilized in a Bayesian classifier singly and in combination to provide target detection. The results of this processing are presented and sensitivity of the class separability to target set, target configuration, diurnal variations, mean contrast, and ambient temperature estimation errors is explored. This work introduces the concept of atmospheric normalization of classification features, in which feature values are normalized using an estimate of the ambient temperature surrounding the target being observed and applying the Planck radiation law with those estimates. This technique is demonstrated to reduce the total error rate associated with classification processing to less than one-fourth of that observed using non-normalized features. Classification testing of spectral field measurements made on an array of U.S. and foreign military assets reveals a total error rate near 5% with a 95% probability of detection and a concurrent false alarm rate of 4% when a single classification feature is employed. Multiple feature classification on the same data yields detection probabilities near 97% with a concurrent false alarm rate of 2.5%. Sensitivity analysis indicates that the probability of detection is reduced to 70-75% in the hours preceding daylight, and that for the total error rate to be less than 10%, the target-to-background mean contrast must be greater than 0.

DESCRIPTORS: (U) *INFRARED DETECTION, *INFRARED SPECTRA PROBABILITY DISTRIBUTION FUNCTIONS, TARGET RECOGNITION, PROBABILITY, MOVING TARGETS, THESES, FALSE ALARMS, ERROR ANALYSIS, BAYES THEOREM, BLACKBODY RADIATION, SPECTRUM ANALYSIS, RADIOMETRY, ATMOSPHERIC ATTENUATION, DIURNAL VARIATIONS, RADIANT INTENSITY.

AD-A304 832

NAVAL POSTGRADUATE SCHOOL MONTEREY CA

(U) Existing and Emerging Maritime Surveillance Technologies.

DESCRIPTIVE NOTE: Master's thesis

SEP 95 135P

PERSONAL AUTHORS: Burkholder, Gary A.

UNCLASSIFIED REPORT

ABSTRACT: (U) This paper presents an assessment of present and near-future maritime surveillance technologies. Radar, optical and infrared sensor systems are each discussed. Thirty-two major domestic and foreign manufacturers' market position, current products and their applications are reviewed. State-of-the-art research is presented and analyzed to see in what direction the future of maritime surveillance is headed. In examining current systems and those being researched, rapid signal processing, data fusion, interpretation and dissemination constitute the major challenges and provide the most opportunities for improvement.

DESCRIPTORS: (U) *AERIAL RECONNAISSANCE, *RADAR, *INFRARED DETECTORS, *OPTICAL DETECTORS, *OCEAN SURVEILLANCE, SIGNAL PROCESSING, COASTAL REGIONS, MANUFACTURING, MARKETING, REAL TIME, STATE OF THE ART, ACOUSTIC WAVES, SIGNAL TO NOISE RATIO, DOPPLER RADAR, THESES, INTEGRATED CIRCUITS, SYNTHETIC APERTURE RADAR, SEMICONDUCTORS, AIR TRAFFIC CONTROL SYSTEMS, FIBER OPTICS TRANSMISSION LINES, CAMERAS, PHOTOGRAPHY, ELECTROMAGNETIC INTERFERENCE, TRAVELING WAVE TUBES, DATA FUSION, RADAR CLUTTER, RADAR ANTENNAS, ANALOG TO DIGITAL CONVERTERS, LAW ENFORCEMENT, TRANSMITTER RECEIVERS, INFRARED TRACKING, EARLY WARNING SYSTEMS, KLYSTRONS, MAGNETRONS.

IDENTIFIERS: (U) INVERSE SYNTHETIC APERTURE RADAR, SPACE TIME, MONOLITHIC MICROWAVE INTEGRATED CIRCUITS.

AD-A304 506

NATIONAL AIR INTELLIGENCE CENTER
WRIGHT-PATTERSON AFB OH

(U) Electronic Warfare in China's Past, Present, and Future.

NOV 95 12P

PERSONAL AUTHORS: Xu, Shaoxing

REPORT NO: NAIC-ID(RS)T-0273-95

UNCLASSIFIED REPORT

SUPPLEMENTARY NOTE: Trans. of unidentified Chinese language document, n.d.

ABSTRACT: (U) Chinese electronic warfare has a recorded beginning in February of 1931. Before that war, personnel on our side maintained intercept of enemy stations for more than twenty days, grasping the enemy points of departure, times, routes, and causing our forces to achieve a very brilliant victory. Praise and commendation were received from Committee Member Mao and Commander in Chief Zhu. During the more than thirty years of history from 1931 to 1965, this is the breeding period of Chinese electronic warfare. During the entire phase, it is possible to make use of the six characters' analysis, renovation, system (illegible) in order to summarize the development of the specialty in question. There were no electronic countermeasures personnel in the early period. With study and analysis on the one hand and renovation of captured Japanese and U.S. intercept, reconnaissance, and jamming equipment on the other--eager to meet the needs of war--this equipment was put to new uses in battle. In application, there was familiarization, mastery, and study. In particular, during the ten or so years after liberation, stress was placed on the analysis of electronic countermeasures equipment on the U.S. P2V7 (illegible) low altitude reconnaissance aircraft and the U-2 high altitude reconnaissance aircraft as well as the Soviet built cp6-1 radar reconnaissance machine and cp6-5 radar jammer, communications reconnaissance, jamming devices, pulse analyzers, and so on. At the same time as this, a number of pieces of airborne, ground, and submarine borne reconnaissance and jamming equipment were manufactured in imitation.

DESCRIPTORS: (U) *ELECTRONIC WARFARE, *HISTORY, *TECHNOLOGY FORECASTING, *CHINA, STATIONS, INTERCEPTION ELECTRONIC EQUIPMENT, FREQUENCY BANDS, JAMMING, COMMUNICATION AND RADIO SYSTEMS, TRANSLATIONS, ENEMY, MILITARY TRAINING, ELECTRONIC COUNTERMEASURES, COMBAT FORCES, NARROWBAND, LOW ALTITUDE, RECONNAISSANCE AIRCRAFT, DIRECTIONAL, CHINESE LANGUAGE, PULSE ANALYZERS.

IDENTIFIERS: (U) FOREIGN REPORTS.

AD-A303 802

MITRE CORP BEDFORD MA

(U) Enhanced Capabilities of Advanced Airborne Radar Simulation.

DESCRIPTIVE NOTE: Final technical rept. Oct 93-Sep 94
JAN 96 117P

PERSONAL AUTHORS: Babu, V. N.; Tortes, J. A.
CONTRACT NO: F19628-94-C-0001

UNCLASSIFIED REPORT

ABSTRACT: (U) MITRE has enhanced the capabilities of the Advanced Airborne Radar Simulation, a flexible end-to-end steady-state simulation that can be used to evaluate the critical issues affecting the performance of advanced airborne radars that use adaptive antenna techniques, i.e., space-time processing (STP), for both jamming and clutter suppression. For a large phased-array antenna, the limitations of a practical implementation of optimal STP will generally require suboptimal adaptive array architectures, such as element space, beam space, and subarrays. The simulation was modified to augment these suboptimal architectures with spatial degrees of freedom in elevation. The received signal models, i.e., target jamming and clutter, were modified to include the effects of near-field scattering using a multiple point scatterer model.

DESCRIPTORS: (U) *SIMULATION, *RADAR, STEADY STATE, SPATIAL DISTRIBUTION, SCATTERING, MODELS, AIRBORNE, ARRAYS, DEGREES OF FREEDOM, SIGNALS, ANTENNAS, ADAPTIVE SYSTEMS, JAMMING, RADAR CLUTTER, ELEVATION, ARCHITECTURE, NEAR FIELD, SUPPRESSION, PHASED ARRAYS.

AD-A303 476

ENVIRONMENTAL RESEARCH INST OF MICHIGAN
ANN ARBOR

(U) Utility Analysis of High Resolution.

DESCRIPTIVE NOTE: Final rept. 26 Jan-1 Oct 94
APR 95 47P

PERSONAL AUTHORS: Gerber, Garth L.; Reiley, Michael F.; Eismann, Michael T.; Jacobs, James M.
REPORT NO: ERIM-253885-2-F-VOL-1
CONTRACT NO: DLA900-88-D-0392

UNCLASSIFIED REPORT

SUPPLEMENTARY NOTE: ADA303475 ADB206544

ABSTRACT: (U) This report summarizes the results of two studies conducted to address specific issues related to the utility of a specific high resolution multispectral sensor, designated the F sensor. The first study assessed the validity of a sensor model, entitled the Performance Prediction Model (PPM), which was provided by the sensor contractor. This was performed by cross checking results with an independent sensor model. In most cases, good agreement was achieved. The second study assessed the expected performance of a vital component of the F sensor a magnetic bearing system (MBS) for line of sight control and stabilization.

DESCRIPTORS: (U) *INFRARED IMAGES, *INFRARED DETECTORS, LINE OF SIGHT, MAGNETIC FIELDS, TRANSFER FUNCTIONS, SIGNAL TO NOISE RATIO, HIGH RESOLUTION, MATHEMATICAL PREDICTION, MULTISPECTRAL.

IDENTIFIERS: (U) PPM(PERFORMANCE PREDICTION MODEL), MBS(MAGNETIC BEARING SYSTEM), MTF(MODULATION TRANSFER FUNCTIONS), NYQUIST DIAGRAMS.

AD-A303 475

ENVIRONMENTAL RESEARCH INST OF MICHIGAN
ANN ARBOR(U) Utility Analysis of High Resolution Multispectral
Imagery. Volume 3. Image Based Sensor Model (IBSM)
Users Manual.DESCRIPTIVE NOTE: Final rept. 26 Jan 94-31 May 95
MAY 95 82PPERSONAL AUTHORS: Eismann, Michael T.; Ingle,
Stephen D.

REPORT NO: ERIM-253885-2-F-VOL-3

CONTRACT NO: DLA900-88-D-0392

UNCLASSIFIED REPORT

SUPPLEMENTARY NOTE: ADB 206544, ADA 303476

ABSTRACT: (U) The Image Based Sensor Model (IBSM) is a modular set of numerical tools for designing, evaluating, and modeling electrooptical and infrared (EOJIR) imaging sensors. The primary motivation which led to the development of IBSM was the need for a model which (a) could produce simulated sensor imagery (based on high fidelity input imagery) in addition to sensor performance metrics to better characterize the imaging performance of a sensor system, and (b) provides the flexibility to evaluate and compare sensors and imaging configurations with differing characteristics without rewriting computer code. The model operates within the Khoros Cantata environment, and can perform realistic simulation of image degradations and parametric modeling with a wide range of atmospheric, sensor, and processing effects. This report provides a comprehensive overview of the model.

DESCRIPTORS: (U) *IMAGE PROCESSING,
*INFRARED IMAGES, *INFRARED DETECTORS,
COMPUTER PROGRAMS, MATHEMATICAL MODELS,
USER MANUALS, PARAMETRIC ANALYSIS,
DEGRADATION, ELECTROOPTICS,
PERFORMANCE(ENGINEERING), NUMERICAL
ANALYSIS, HIGH RESOLUTION, CONFIGURATIONS,
MOTIVATION MULTISPECTRAL.

IDENTIFIERS: (U) IBSM (IMAGE BASED SENSOR
MODEL).

AD-A303 219

LAWRENCE LIVERMORE NATIONAL LAB CA

(U) Dispersive-Infrared Gas Sensor System Design and
Operation Manual.DESCRIPTIVE NOTE: Final rept. Sep 86-Oct 89
AUG 95 135PPERSONAL AUTHORS: Kulp, T. U.; McRae, T. G.;
Kennedy, R.; Garvis, D.

UNCLASSIFIED REPORT

ABSTRACT: (U) This technical report describes the methodology to build and operate a remotely operated, radio controlled, battery powered infrared detector for measuring hydrogen chloride (HCL) emissions from Space Launch operations.

DESCRIPTORS: (U) *INFRARED DETECTORS,
*LAUNCH VEHICLES, COMPUTER PROGRAMS,
MICROPROCESSORS, SPACE SHUTTLES, DATA
ACQUISITION, CALIBRATION, ABSORPTION,
INFRARED RADIATION, BANDPASS FILTERS, SOLID
PROPELLANT ROCKET ENGINES, HUMIDITY, GAS
DETECTORS, OPTICAL FILTERS, EXHAUST GASES,
HYDROGEN CHLORIDE.

IDENTIFIERS: (U) RELATIVE HUMIDITY.

AD-A303 071

MISSISSIPPI STATE UNIV MISSISSIPPI STATE

(U) Target Discrimination/Classification Radar.

DESCRIPTIVE NOTE: Final rept. 1 Aug 92-31 Jul 95
AUG 95 153PPERSONAL AUTHORS: Skinner, B. J.; Ingels, Frank;
Donohoe, P.

CONTRACT NO: DAAL03-92-G-0355

UNCLASSIFIED REPORT

ABSTRACT: (U) Adaptive FSK/PSK is a spectrally agile pulse compression radar signaling scheme that learns target-specific information over time and integrates that information into the design of its radar signal processor in real-time. This use of target-specific information into the real-time transmitter signal design process enhances the return from the target, thus improving the performance of the radar system in both additive noise environments (jamming) and ground clutter limited environments (low altitude targets). Since FSK/PSK signaling is a pseudorandom pulse compression scheme with a large time-bandwidth product, it has inherent low probability of intercept characteristics. Additionally, adaptive FSK/PSK signaling is able to earn target specific information which can be used to identify the target using existing target identification techniques. In this study, the cross-ambiguity function of a general FSK/PSK waveform is derived and analyzed in a probabilistic manner. The results of this probabilistic analysis are used to develop a design methodology that allows the signal to be matched to an arbitrary target. It is shown that both the signal to clutter ratio and signal to noise ratio of a matched FSK/PSK radar are superior to those of a conventional signaling radar that utilizes no target-specific information.

DESCRIPTORS: (U) *TARGET DISCRIMINATION, *RADAR SIGNALS, *RADAR TARGETS, DATABASES, ALGORITHMS, SIGNAL PROCESSING, COMPUTERIZED SIMULATION, OPTIMIZATION, TARGET SIGNATURES, REAL TIME, TARGET RECOGNITION, RESOLUTION, SIGNAL TO NOISE RATIO, RADAR TRACKING, DOPPLER RADAR, LEARNING MACHINES, RAYLEIGH SCATTERING, BROADBAND, ADAPTIVE SYSTEMS, RADAR RECEIVERS, PATTERN RECOGNITION, RADAR JAMMING, MATCHED FILTERS, TARGET CLASSIFICATION, INTERCEPTION PROBABILITIES, PHASE SHIFT KEYERS, PULSE COMPRESSION, GROUND CLUTTER, NOISE(RADAR), PHASE MODULATION, PSEUDO RANDOM SYSTEMS, FREQUENCY SHIFT KEYERS.

AD-A302 749

NATIONAL AIR INTELLIGENCE CENTER
WRIGHT-PATTERSON AFB OH

(U) Preliminary Exploration of Early Warning Aircraft Countermeasures.

NOV 95 10P

PERSONAL AUTHORS: Chen, Pengjyu

REPORT NO: NAIC-ID(RS)T-0380-95

UNCLASSIFIED REPORT

SUPPLEMENTARY NOTE: Trans. of Yu Jing Ji Dui Kang
Chu Jan (China) p33-35, n.d.

ABSTRACT: (U) This article makes a simple introduction and explanation with regard to the roles of early warning aircraft in modern warfare as well as their electronic equipment. It points out that countermeasures concerning early warning aircraft will be combined countermeasures. They include destruction of the fuselage of early warning aircraft as well as the use of electronic countermeasure equipment to carry out jamming. In order to achieve effective countermeasures against early warning aircraft, the author puts forward research work associated with 8 areas which should be developed, such as, active/passive combined detection systems.

DESCRIPTORS: (U) *AIRCRAFT EQUIPMENT, *ELECTRONIC AIRCRAFT, *EARLY WARNING SYSTEMS, WARFARE, FORWARD AREAS, DETECTORS, ELECTRONIC EQUIPMENT, FUSELAGES, JAMMING, TRANSLATIONS, ELECTRONIC COUNTERMEASURES, CHINA, CHINESE LANGUAGE.

IDENTIFIERS: (U) *EARLY WARNING AIRCRAFT.

AD-A302 748

NATIONAL AIR INTELLIGENCE CENTER
WRIGHT-PATTERSON AFB OH

(U) An Overview of Technology for Jamming Early Warning Aircraft in the National Air Defense System. Part 1.

DEC 95 24P

PERSONAL AUTHORS: Baichuan, Liang
REPORT NO: NAIC-ID(RS)T-0384-95

UNCLASSIFIED REPORT

SUPPLEMENTARY NOTE: Trans. of unknown Chinese source.

ABSTRACT: (U) Based on his research of the characteristics of different electronic systems of early warning aircraft, the author proposes methods of countering early warning aircraft, and studies techniques of jamming their radar, communications systems, and Identification Friend or Foe IFF systems.

DESCRIPTORS: (U) *JAMMING, *AIRCRAFT EQUIPMENT, *EARLY WARNING SYSTEMS, AIR DEFENSE, ELECTRONIC EQUIPMENT, RADAR, COMMUNICATION AND RADIO SYSTEMS, TRANSLATIONS, ELECTRONIC COUNTERMEASURES, NATIONAL DEFENSES CHINA, IFF SYSTEMS, CHINESE LANGUAGE.

AD-A302 747

NATIONAL AIR INTELLIGENCE CENTER
WRIGHT-PATTERSON AFB OH

(U) One Type of Self-Adapting Airborne Passive-Photoelectric Countermeasure System.

NOV 95 29P

REPORT NO: NAIC-ID(RS)T-0382-95

UNCLASSIFIED REPORT

SUPPLEMENTARY NOTE: Trans. of Yi Zhong Zi Shi De Ji Zai Wu Yuan Guang Dlan Dui Kang Xi Tong (China) P15-26.

ABSTRACT: (U) Passive jamming and infrared jamming are among important component parts making up combined electronic countermeasures systems at the present time. In modern warfare, following along with the widespread application of precision guided weapons--in particular, photoelectric-infrared guidance weapons--they constitute a threat to the survival of combat aircraft which grows more severe by the day. Modern limited wars--in particular, the practical realization of the Gulf war--clearly show that most damaged or lost aircraft were all due to being attacked by infrared homing missiles. At the present time, approximately 80% of missiles opt for the use of infrared guidance. Moreover, the U.S. has already taken passive photoelectric detection equipment to act as the principal military sensors of the future. It has also been used to supply target acquisition, tracking, and positioning capabilities for stealth aircraft in order to strengthen covering capabilities. As a result, the militaries of various nations pay serious attention to passive-photoelectric countermeasure system technology equipment, which has already become one type of effective means for modern combat aircraft to carry out defense penetrations and to increase effective guarantees of airborne security.

DESCRIPTORS: (U) *ELECTRONIC COUNTERMEASURES, *PHOTOELECTRICITY *INFRARED JAMMING, GUIDED MISSILES, POSITION(LOCATION), WARFARE, DETECTORS, AIRCRAFT, DEFENSE SYSTEMS, MILITARY AIRCRAFT, TARGET ACQUISITION, AIRBORNE, SECURITY, TRACKING, PASSIVE SYSTEMS, SURVIVAL(GENERAL), PENETRATION, GUARANTEES, POSITION FINDING, SALARIES, TRANSLATIONS, HOMING DEVICES, SUPPLIES, COMBAT FORCES, INFRARED HOMING, CHINA, CHINESE LANGUAGE.

IDENTIFIERS: (U) *PASSIVE JAMMING.

AD-A302 656

COAST GUARD RESEARCH AND DEVELOPMENT
CENTER GROTON CT(U) Evaluation of Infrared Sensors for Oil Spill Response
Operations.DESCRIPTIVE NOTE: Final rept. Oct 94-Jun 95
JUN 95 75P

PERSONAL AUTHORS: Hover, G. L.; Plourde, J. V.

REPORT NO: CGR/DC-33/95

CONTRACT NO: DTCG39-94-D-E56616

UNCLASSIFIED REPORT

ABSTRACT: (U) During November 1994, the USCO conducted a field evaluation of several commercially available portable infrared (IR) sensors for their ability to detect oil on water at night. The evaluation was conducted over the natural oil seeps off the coast of Santa Barbara, CA. The portable sensors were operated from the open door of a Coast Guard HH-60J helicopter. Sensors evaluated included the Agema Thermovision 1000 and Texas Instruments LOCUSP operating in the long wave IR (LWIR) and the Cincinnati Electronics IRC-160ST and IRRIS-256ST operating in the medium wave IR (MWIR). The installed FLIR 2000 LWIR system provided a baseline reference of current CG IR capabilities. The LOCUSP was the only uncooled sensor evaluated.

DESCRIPTORS: (U) *INFRARED DETECTORS, *OIL SPILLS, TEST AND EVALUATION, IMAGE PROCESSING, PORTABLE EQUIPMENT, COASTAL REGIONS, DETECTORS, WATER, FIELD TESTS, BASE LINES, RESPONSE, NIGHT, INFRARED RADIATION, LONG WAVELENGTHS, OILS, COAST GUARD.

IDENTIFIERS: (U) SURFACE TRUTH DATA, NIGHTTIME IMAGING S-VHS TAPE, LONG WAVE INFRARED, MEDIUM WAVE INFRARED, OIL SLICK DETECTION, LOCUSP(LOW COST UNCOOLED SENSOR PROTOTYPE), LOW COST UNCOOLED SENSOR PROTOTYPE, HH-60d AIRCRAFT, AGEMA THERMOVISION 1000, IRC-160ST, IRRIS-256ST.

AD-A302 289

MASSACHUSETTS INST OF TECH LEXINGTON
LINCOLN LAB(U) A Metric Analysis of IRAS Resident Space Object
Detections.DESCRIPTIVE NOTE: Technical rept.
NOV 95 56PPERSONAL AUTHORS: Lane, Mark T.; Baldassini, Joseph
F.; Gaposchkin, E. M.

REPORT NO: TR-1022

CONTRACT NO: F19628-95-C-0002

UNCLASSIFIED REPORT

ABSTRACT: (U) The Infrared Astronomy Satellite (IRAS) was launched and operated during a 10-month period in 1983. The orbit was close to the MSX orbit design, but the science data were collected in a mode where the focal plane was pointing directly away from the Earth. The Space Research Institute at Groningen, Netherlands, collected approximately 139,000 tracks of data that had focal plane motion different than astronomical sources, and the IRAS Processing and Analysis Center (IPAC) determined the boresite pointing of IRAS to within 20 arcsec. This report will focus on the nonastronomical detections from IRAS, many of which are Resident Space Objects (RSOs). In particular, the focus of the study is on how many are correlated to the known RSO catalogue for 1983 and the calibration and characterization of the metric accuracy for the correlated data. This study was undertaken to prepare for analysis of RSO detections from the MSX satellite, and in particular, so that automatic analysis tools designed for analysis of surveillance experiment data could be tested. The supporting analysis tools, required corollary data, and metric calibration procedure will be described, and the results of the accuracy of the IRAS ephemeris and metric RSO detections will be presented.

DESCRIPTORS: (U) *INFRARED DETECTION, *ASTRONOMY, *SCIENTIFIC SATELLITES, DATA BASES, DATA MANAGEMENT, EARTH ORBITS, SPACE SURVEILLANCE, ACCURACY, CORRELATION, ERROR ANALYSIS, CALIBRATION, DATA COMPRESSION, INFRARED RADIATION, FOCAL PLANES, PIXELS, AUTOMATIC, SPACE OBJECTS INFRARED TRACKING, INFRARED SCANNING, SYNCHRONOUS SATELLITES, EPHEMERIDES.

IDENTIFIERS: (U) IRAS(INFRARED ASTRONOMY SATELLITE), RSO(RESIDENT SPACE OBJECTS).

AD-A300 899

MASSACHUSETTS UNIV AMHERST DEPT OF
COMPUTER SCIENCE

(U) High-Level Adaptive Signal Processing Architecture with Applications to Radar Non-Gaussian Clutter. Volume 4. The Problem of Weak Signal Detection.

DESCRIPTIVE NOTE: Final rept. Apr 91-Jun 94
SEP 95 160P

PERSONAL AUTHORS: Chakravarthi, Prakash R.
CONTRACT NO: F30602-91-C-0038

UNCLASSIFIED REPORT

SUPPLEMENTARY NOTE: Prepared in cooperation with Syracuse Univ., NY. ADA300898 ADA300900 ADA300901 ADA300902

ABSTRACT: (U) This thesis addresses the performance of Locally Optimum Detectors in radar weak signal detection for finite sample sizes where the radar disturbance is modeled as a correlated non-Gaussian random process. The theory of Spherically Invariant Random Process is used for statistical characterization of non-Gaussian radar clutter. In particular, the K-distribution and the Student-T distributions have been considered as models for radar clutter. A canonical form is established for the Locally Optimum Detector that is a product of the Gaussian linear receiver and a zero memory nonlinearity. The functional form of the zero memory nonlinearity depends on the approximation used for the underlying radar clutter probability density function. Since the weak signal detector is nonlinear, thresholds for specified false alarm probability cannot be established in closed form. Given a specified false alarm probability a new method for threshold estimation based on extreme value theory is derived that reduces by orders of magnitude the computation and sample size required to set the threshold. Once the threshold is set the performance of the Locally Optimum Detector is carried out for finite sample sizes through computer simulations.

DESCRIPTORS: (U) *SIGNAL PROCESSING, *RADAR SIGNALS, COMPUTERIZED SIMULATION, OPTIMIZATION, DETECTION, THEORY, COMPUTER ARCHITECTURE, FALSE ALARMS, RADAR, PROBABILITY DENSITY FUNCTIONS, ESTIMATES, SAMPLING, ADAPTIVE SYSTEMS, BACKGROUND, RADAR CLUTTER, INVARIANCE, BACKGROUND RADIATION, LOW STRENGTH.

IDENTIFIERS: (U) SIRV(SPHERICALLY INVARIANT RANDOM VECTORS).

AD-A300 413

NATIONAL AIR INTELLIGENCE CENTER
WRIGHT-PATTERSON AFB OH

(U) Medium Wave Band Infrared Imaging Systems and Their Applications.

SEP 95 31p
REPORT NO: NAIC-ID(RS)T-0256-95

UNCLASSIFIED REPORT

SUPPLEMENTARY NOTE: Trans. of Zhong Bo Duan Hong Wai Cheng Xiang Xi Tong Ji Qi (China) p1-9, 11 Sep 95.

ABSTRACT: (U) This article makes only a simple introduction of the status of developments and applications associated with 3 - 5 micron wave band infrared imaging technology outside China. Concise analysis and comparisons are carried out on its performance, discussing the situations and causes giving precedence to an option for the use of 3 - 5 micron infrared imagery.

DESCRIPTORS: (U) *INFRARED DETECTION, *ANTIMISSILE DEFENSE SYSTEMS, *INFRARED IMAGES, *INFRARED COUNTERMEASURES, FOREIGN TECHNOLOGY, TRANSLATIONS, INFRARED RADIATION, INFRARED HOMING, ATMOSPHERIC ATTENUATION, INFRARED TRACKING, CHINA, WARNING SYSTEMS, CHINESE LANGUAGE.

IDENTIFIERS: (U) FOREIGN REPORTS.

AD-A300 409

NATIONAL AIR INTELLIGENCE CENTER
WRIGHT-PATTERSON AFB OH

(U) Infrared Imagery Recognition Processing.

SEP 95 22P

PERSONAL AUTHORS: Jinrong, Huang K.

REPORT NO: NAIC-ID(RS)T-0257-95

UNCLASSIFIED REPORT

SUPPLEMENTARY NOTE: Trans. of Hong Wai Tu Xiang
Shi Bie Chu Li, (China) n1 p50-54 1994.

ABSTRACT: (U) This document addresses in simple terms the flow of information in infrared imagery recognition and processing, and proposes using knowledge-based expert systems and advanced neural networks to bring about a development direction for automated, intelligent imagery recognition and processing. This document also presents a kind of effective missile-borne infrared imagery detection, tracking, and extrapolation method.

DESCRIPTORS: (U) *INFRARED DETECTION, *IMAGE PROCESSING, *INFRARED IMAGES, NEURAL NETS, TARGET RECOGNITION, EXPERT SYSTEMS, TRANSLATIONS, INFRARED RADIATION, INFRARED TRACKING, CHINA, CHINESE LANGUAGE, EXTRAPOLATION.

IDENTIFIERS: (U) FOREIGN REPORTS.

AD-A300 240

NAVAL COMMAND CONTROL AND OCEAN
SURVEILLANCE CENTER RDT & E DIV
SAN DIEGO CA

(U) Summary of the Marine Aerosol Properties and Thermal Imager Performance Trial (MAPTIP).

DESCRIPTIVE NOTE: Professional paper

AUG 95 12P

PERSONAL AUTHORS: De Leeuw, G.; van Eijik, A. M.

UNCLASSIFIED REPORT

AVAILABILITY: Pub. in Sensor and Propagation Panel Symposium on Propagation Assessment in Coastal Environments, p18-1 - 18-10, 19-22 Sep 94. Available only to DTIC users. No copies furnished by NTIS.

ABSTRACT: (U) This paper describes a 1993 field experiment entitled Marine Aerosol Properties and Thermal Imager Performance Trial (MAPTIP) conducted by NATO AC/ 243 Panel 04/RSG.8 and 04/RSG.5 in the Dutch coastal waters. Objectives were: to improve and validate vertical marine aerosol models by providing an extensive set of aerosol and meteorological measurements, within a coastal environment at different altitudes and for a range of meteorological conditions; make aerosol and meteorological observations in the first 10 m of the ocean surface with a view to extending existing aerosol models to incorporate near-surface effects; and to assess marine boundary layer effects on thermal Imaging systems.

DESCRIPTORS: (U) *AEROSOLS, *INFRARED SIGNATURES, *SHIP SIGNATURES, *METEOROLOGICAL DATA, *THERMAL IMAGES, DATA BASES, SPATIAL DISTRIBUTION, PARTICLE SIZE, DEGRADATION, OCEAN SURFACE, BOUNDARY LAYER, TURBULENCE, ATMOSPHERIC MOTION, MARINE ATMOSPHERES, INFRARED IMAGES, CALIBRATION METEOROLOGICAL INSTRUMENTS, REFRACTION, SHIP MODELS RADIOFREQUENCY, EARTH ATMOSPHERE, SURFACE TRUTH, INFRARED IMAGE TUBES.

IDENTIFIERS: (U) MAPTIP(MARINE AEROSOL PROPERTIES AND THERMAL IMAGER PERFORMANCE).

AD-A300 185

NATIONAL AIR INTELLIGENCE CENTER
WRIGHT-PATTERSON AFB OH

(U) Computer Assisted Laser Range Finding and Detection Systems.

AUG 95 13P
REPORT NO: NAIC-ID(RS)T-0258-95

UNCLASSIFIED REPORT

SUPPLEMENTARY NOTE: Trans. of unknown source (China), p45-47, n.d.

ABSTRACT: (U) Up to the present time, the majority of laser radars which have been reported were very expensive, had large volumes, and were very complicated in terms of utilization and maintenance. As far as this type of low cost laser range finding and detection system reported in this paper is concerned, use is made of a type of semiconductor laser diode emission device and a small model computer to do control. With regard to making use of semiconductor laser diodes to replace Nd: YAG lasers, the results were to improve optical emission efficiencies, electronic control compatibility, and reduce system dimensions. One type of high sensitivity PIN diode receiver is capable of receiving radar pulses reflected back from targets, and, in conjunction with that, directly supplying digital output. Electronic methods are used to measure laser pulse travel time of flight. In conjunction with that, an IBM-AT compatible minicomputer is used, and it is possible to realize the needed calculations as well as displaying target distance, speed, and position. Systems are capable of tracking horizon range targets more than 50m away from emitters.

DESCRIPTORS: (U) *RADAR, *LASER APPLICATIONS, *RANGE FINDING, *LASER TRACKING, YAG LASERS, OUTPUT, CONTROL, DIGITAL SYSTEMS, ELECTRONICS, EMISSION, OPTICAL PROPERTIES, DETECTORS, MODELS, COMPUTERS, ELECTRONIC EQUIPMENT, EFFICIENCY, COMPATIBILITY, SEMICONDUCTOR LASERS, SEMICONDUCTOR DIODES, REFLECTION, TARGETS, LASERS COMPUTER APPLICATIONS, TRANSLATIONS, RANGE(DISTANCE), UTILIZATION, RADAR PULSES, CHINA, MINICOMPUTERS, HORIZON.

IDENTIFIERS: (U) *LASER RADAR.

AD-A300 028

NATIONAL AIR INTELLIGENCE CENTER
WRIGHT-PATTERSON AFB OH

(U) Jamming Performance of Infrared Bait/Chaff.

AUG 95 13p
PERSONAL AUTHORS: Pan, Gongpei
REPORT NO: NAIC-ID(RS)T-0383-95

UNCLASSIFIED REPORT

SUPPLEMENTARY NOTE: Trans. of Bulletin of Nanjing University of Science and Engineering (China) n7(77), 1994.

ABSTRACT: (U) The effectiveness of infrared guidance and radar guidance jamming with infrared bait and chaff has been proven in modern high-tech warfare. Their jamming regime relies on infrared radiation of the infrared bait and radar reflective waves from chaff to simulate the target (such as aircraft, warships, tanks, and point targets) performance to confuse, disturb, and jam the infrared guidance and radar guidance, as well as their probing and aiming systems. In tactical applications, these are divided into centroid mode, dump mode, dilution mode, and confusion mode. Study of the jamming performance of infrared bait and chaff is required in developing the smoke, flame, light, and electric/sourceless jamming technologies. It is very important and practical to enhance the jamming performance of infrared bait and chaff, as well as to extend the jamming frequency spectrum.

DESCRIPTORS: (U) JAMMING, *INFRARED HOMING, *CHAFF, FREQUENCY, CENTER OF GRAVITY, AIRCRAFT, PERFORMANCE(ENGINEERING), RADAR, TARGETS SPECTRA, SMOKE, RADAR REFLECTIONS, TRANSLATIONS, GUIDANCE, AIMING, RADAR SIGNALS, RADAR JAMMING, INFRARED RADIATION, TACTICAL WARFARE, DILUTION, NAVAL VESSELS(COMBATANT), CHINA, CHINESE LANGUAGE.

AD-A299 797

TEMPLE UNIV PHILADELPHIA PA

(U) Laser Interactions in STM and STM-Like Devices:
Applications to Infrared and Optical Detection.

DESCRIPTIVE NOTE: Final rept. 15 Apr 92-14 Apr 95
APR 95 115P

PERSONAL AUTHORS: Sullivan, T. E.; Cutler, P. H.
CONTRACT NO: F49620-92-U-0209

UNCLASSIFIED REPORT

DESCRIPTORS: (U) *SCANNING ELECTRON
MICROSCOPES, TUNNELING (ELECTRONICS), LASER
APPLICATIONS, INFRARED DETECTORS, OPTICAL
DETECTORS.

AD-A299 514

RUTGERS - THE STATE UNIV PISCATAWAY NJ DEPT
OF MECHANICAL AND AEROSPACE ENGINEERING

(U) High-Speed Four-Color Infrared Digital Imaging for
Studying In-Cylinder Processes in a DI Diesel Engine.

DESCRIPTIVE NOTE: Final rept.

JUL 95 101P

PERSONAL AUTHORS: Rhee, K. T.

UNCLASSIFIED REPORT

ABSTRACT: (U) The study was to investigate in-cylinder events of a direct injection-type diesel engine by using a new high-speed infrared (IR) digital imaging system for obtaining information that was difficult to achieve by the conventional devices. For this, a new highspeed dual-spectra infrared digital imaging system was developed to simultaneously capture two geometrically identical (in respective spectral) sets of IR images having discrete digital information in a (64x64) matrix at rates as high as over 1,800 frames/sec each with exposure period as short as 20 micron sec. At the same time, a new advanced four-color W imaging system was constructed. The first two sets of spectral data were the radiation from water vapor emission bands to compute the distributions of temperature and specie in the gaseous mixture and the remaining two sets of data were to find the instantaneous temperature distribution over the cylinder surface. More than eight reviewed publications have been produced to report many new findings including: Distributions of Water Vapor and Temperature in a Flame; End Gas Images Prior to Onset of Knock; Effect of MTBE on Diesel Combustion; Impact of Oxygen Enrichment on In-cylinder Reactions; Spectral IR Images of Spray Plume; Residual Gas Distribution; Pre flame Reactions in Diesel Combustion; Pre flame Reactions in the End Gas of an SI Engine; Post flame Oxidation; and Liquid Fuel Layers during Combustion in an SI Engine. In addition, some computational analysis of diesel combustion was performed using KIVA-II program in order to compare results from the prediction and the measurements made using the new IR imaging diagnostic tool.

DESCRIPTORS: (U) *DIESEL ENGINES, *INFRARED
IMAGES, DIGITAL SYSTEMS, TEMPERATURE,
COMPUTATIONS, DISTRIBUTION, LAYERS, LIQUIDS,
EMISSION SPECTRA, GASES, MIXTURES, SURFACES,
OXYGEN, COMBUSTION, FUELS, SPECTRA,
OXIDATION, CYLINDRICAL BODIES, RESIDUALS,
IMAGES, DIAGNOSTIC EQUIPMENT, PLUMES,
INFRARED RADIATION, DIESEL FUELS, SPRAYS,
ENRICHMENT, WATER VAPOR, FUEL INJECTION.

AD-A298 763

NAVAL COMMAND CONTROL AND OCEAN
SURVEILLANCE CENTER RDT & E DIV
SAN DIEGO CA

(U) A FLIR Case Study Using the Electro-Optical Tactical
Decision Aid (EOTDA) Mark III.

DESCRIPTIVE NOTE: Professional paper
AUG 95 11P
PERSONAL AUTHORS: McGrath, Charles P.

UNCLASSIFIED REPORT

AVAILABILITY: Pub. in Propagation Assessment in Coastal
Environments, AGARD-CP-567, p38-1 - 38-8, Feb 95.
Available only to DTIC users. No copies furnished by NTIS.

ABSTRACT: (U) This report compares measured forward-
looking infrared (FLIR) system detection ranges of a target
ship, the Research Vessel Point Sur, with predictions from the
Electro-Optical Tactical Decision Aid (EOTDA) version 3.0.
The EOTDA was primarily developed by the Air Force, with
only minimal attention applied to the complexities of the
marine environment. The objective of this case study was to
evaluate the EOTDA performance for a target in an open
ocean background.

DESCRIPTORS: (U) *INFRARED DETECTION,
*FORWARD LOOKING INFRARED SYSTEMS,
*ELECTROOPTICS, *DECISION AIDS, *TACTICAL
DATA SYSTEMS, AIR FORCE, SHIPS, DECISION
MAKING, TARGETS, CASE STUDIES, OCEANS,
RANGE(DISTANCE), OCEAN ENVIRONMENTS,
ANTISHIP WARFARE, OPEN WATER, RESEARCH
SHIPS.

IDENTIFIERS: (U) *SHIP TARGETS, EOTDA(ELECTRO
OPTICAL TACTICAL DECISION AID).

AD-A297 635

NATIONAL AIR INTELLIGENCE CENTER
WRIGHT-PATTERSON AFB OH

(U) Infrared Thermal Imaging Technique: Advances and
Prospects.

JUL 95 19P
PERSONAL AUTHORS: Yu, Xin
REPORT NO: NAIC-ID(RS)T-0402-95

UNCLASSIFIED REPORT

SUPPLEMENTARY NOTE: Trans. of Guangxue Jishu
(China) n6 p1-3, 20, 1994, by Edward A. Suter.

ABSTRACT: (U) Rapid advances have been made recently in
the development and applications of infrared thermal imaging
technology used primarily for military purposes. In this
article, advances in infrared thermal imaging are introduced
in brief, and discussion is focused on technical progress in the
field of infrared focal plane arrays (IRFPA). Also, the trend
for infrared thermal imaging technique to expand rapidly
from purely military use to civil applications is demonstrated.

DESCRIPTORS: (U) *INFRARED IMAGES, *INFRARED
DETECTORS *THERMAL IMAGES, ARRAYS,
MILITARY APPLICATIONS, TRANSLATIONS, FOCAL
PLANES, CIVIL AFFAIRS, CHINA.

IDENTIFIERS: (U) IFFPA(INFRARED FOCAL PLANE
ARRAYS), FOREIGN REPORTS.

AD-A296 638

NAVAL COMMAND CONTROL AND OCEAN
SURVEILLANCE CENTER RDT & E DIV
SAN DIEGO CA

(U) Focal Plane Characterization Capabilities at NCCOSC
RDT&E Division.

DESCRIPTIVE NOTE: Professional paper
JUN 95 9P
PERSONAL AUTHORS: Frisbie, S. A.

UNCLASSIFIED REPORT

AVAILABILITY: Pub. in Smart Focal Plane Arrays and Focal
Plane Array Testing, v2474, p187-192, Apr 95. Available only
to DTIC users. No copies furnished by NTIS.

ABSTRACT: (U) The infrared measurement facility at the
NRaD (formerly NOSC) division of NCCOSC has been
involved in infrared radiometric testing for over forty years.
This versatile facility provides complete radiometric testing
of single element detectors, detector arrays and hybrid focal
plane arrays (FPAs). Measurement capabilities include
spectral response flood illumination, spot illumination and
ionizing radiation testing in low to medium background
photon flux environments.

DESCRIPTORS: (U) *INFRARED DETECTORS, *FOCAL
PLANES TEST AND EVALUATION, INFRARED
DETECTION, MEASUREMENT FACILITIES, ARRAYS,
HYBRID SYSTEMS, RADIOMETRY, IONIZING
RADIATION.

AD-A296 005

AKADEMIYA NAUK SSSR MOSCOW INST OF PHYSICS

(U) Fullerenes Film IR Detectors.

MAR 95 81P
PERSONAL AUTHORS: Dityatyev, A. A.; Gurey, A. E.;
Mazaev, A. A.; Semenov, O. G.; Tikhomirov, A. A.
REPORT NO: SLPI-1/95

UNCLASSIFIED REPORT

ABSTRACT: (U) On the base of analysis of experimental
results and theoretic researches the phenomenological model
of a charge carrier generation under the action of irradiation is
presented, and the carrier transport in thin film photoadvices
is discussed. A possibility of IR sensible devices realization
on the base of high fullerenes or doped fullerenes is
considered. It is proposed to study Shottky transition and
hetero Junction with polymers for realization of all
photosensitive properties of fullerenes. On the base of
extended Huckel model the numeric calculations of electron
structure of high fullerenes and the search of isomers with
defined band gap value are made. Experimental researches of
absorption spectra for UV-, optic and IR bands are made.

DESCRIPTORS: (U) *FULLERENES, *INFRARED
DETECTORS OPTICAL PROPERTIES, INFRARED
SPECTROSCOPY, POLYMERS, HETERO JUNCTIONS,
THIN FILMS, CHARGE CARRIERS, ISOMERS,
TRANSPORT PROPERTIES, DOPING, IRRADIATION,
ABSORPTION SPECTRA, PHOTODETECTORS,
SCHOTTKY BARRIER DEVICES, INFRARED SPECTRA,
PHOTOCONDUCTIVITY, ULTRAVIOLET SPECTRA,
PHOTOSENSITIVITY, PHOTON BEAMS.

IDENTIFIERS: (U) HUCKEL THEORY.

AD-A295 816

SURFACE OPTICS CORP SAN DIEGO CA

(U) Giant Enhanced Backscattering in Laser Radar Signatures.

1995 13P

PERSONAL AUTHORS: Gu, Zu-Han; Dummer, Richard S.; McKenna, Paul; Maradudin, Alexei A.; Estep, Jeff A.
CONTRACT NO: DAAH04-93-G-0014

UNCLASSIFIED REPORT

AVAILABILITY: Pub. in SPIE, v2271, p97-108, 1995.
Available only to DTIC users. No copies furnished by NTIS.

ABSTRACT: (U) Due to underestimation of rough surface scattering at retro-reflection direction, consideration of enhanced backscattering (i.e., opposition effect) can be critically important in developing laser radar signatures. This is illustrated by the comparison of two signature models of the same airplane - one developed using bidirectional reflectance measurement data at one degree from the retro-direction, and the other developed from monostatic measurement data at true retro-direction. The unique instrument used to obtain the laser reflectance data, the reflectance data itself, and the software ensemble used to develop the signature are described and discussed.

DESCRIPTORS: (U) *OPTICAL RADAR, *RADAR COUNTERMEASURES, *OPTICAL SIGNATURES, *RADAR SIGNATURES, LIGHT SCATTERING ROLL, YAW, SURFACE ROUGHNESS, BACKSCATTERING LASERS, RADIANCE, RADAR CROSS SECTIONS, AERODYNAMIC CHARACTERISTICS, REFLECTANCE, RANGE FINDING, STEALTH TECHNOLOGY, BISTATIC RADAR.

AD-A295 138

BROWN UNIV PROVIDENCE RI LAB FOR
ENGINEERING MAN/MACHINE SYSTEMS

(U) Multicovariance Matched Filter for Target Detection in Images.

DESCRIPTIVE NOTE: Final rept. Jul-Dec 94
MAR 95 9p

PERSONAL AUTHORS: Scheffe, Molly M.; Cooper, David B.; Silverman, Harvey F.; Blane, Michael M.
REPORT NO: LEMS-TR-126
CONTRACT NO: F49620-93-1-0501

UNCLASSIFIED REPORT

ABSTRACT: (U) Our original research on the multicovariance matched filter deals with optimum low resolution target detection in a single-frame multicolor image, such as a multispectral infrared or polarimetric synthetic aperture radar picture. The multicovariance method completely uses all the joint variability of the problem, in both space and frequency, in a way that generalizes both the traditional spatial matched filter and also techniques involving scalar ratios between frequency bands. The main new focus of our work, directed toward achieving the best target detection performance that is possible, is to develop a preprocessing step involving optimal adaptive estimation of the local clutter background. This involves segmenting the image into regions, which correspond to different background/clutter statistical models. Statistics of real data are being studied and used in new state-of-the-art hierarchical segmentation algorithms based on Markov Random Field, polynomial and autoregressive models for vector-valued random processes. The major algorithmic challenges here are in estimating the best possible background/clutter models and in accurately estimating the boundaries between different model regions. We are in the process of developing extremely efficient and robust algorithms to estimate these clutter models. These are similar to familiar algorithms from mainstream signal processing, but solve the interpolation problem for Markov Random Fields, which is different than the usual linear prediction problem.

DESCRIPTORS: (U) *IMAGE PROCESSING, *COVARIANCE, *TARGET DETECTION, *MATCHED FILTERS, ALGORITHMS, SIGNAL PROCESSING, CLUTTER, SIGNAL TO NOISE RATIO, SYNTHETIC APERTURE RADAR, TERRAIN, INFRARED IMAGES, PATTERN RECOGNITION, LOW RESOLUTION, INFRARED SPECTRA, MULTISPECTRAL, AERIAL PHOTOGRAPHY.

IDENTIFIERS: (U) COVARIANCE.

AD-A293 811

NAVAL RESEARCH LAB WASHINGTON DC

(U) Millimeter Wave Radiometer Utility Study.

DESCRIPTIVE NOTE: Final rept. May 93-Oct 94
MAR 95 105PPERSONAL AUTHORS: Gaiser, Peter W.; Hollinger, James P.; Highley, Steven R.; Sandlin, Glenn D.
REPORT NO: NRL/MR/7220--95-7652

UNCLASSIFIED REPORT

SUPPLEMENTARY NOTE: Original contains color plates.
All DTIC/NTIS reproductions will be in black and white.

ABSTRACT: (U) Many military and environmental applications require wide area surveillance on a timely and global basis. Passive microwave and millimeter wave imaging has the advantage over visual and infrared systems of being a near all-weather surveillance system with the ability to see through clouds and most adverse weather conditions with equal day and night sensitivity. The major disadvantage of microwave and millimeter wave radiometric systems is that the relatively long wavelengths require aperture several orders of magnitude larger than at infrared to obtain comparable spatial resolution. However, even low resolution microwave and millimeter wave radiometers can contribute significantly to intelligence gathering and environmental remote sensing. This document presents a study of the capabilities of microwave and millimeter wave imaging from space with systems which provide resolutions of 100-400 m at observation frequencies of 1.4-140 GHz. Possible radiometer architectures and their space development are examined. The surveillance and environmental remote sensing benefits of multifrequency high resolution microwave and millimeter wave radiometry are discussed in depth.

DESCRIPTORS: (U) *MILLIMETER WAVES, *RADIOMETRY, *INFRARED SURVEILLANCE, FREQUENCY, SPATIAL DISTRIBUTION, OCEAN SURFACE, RESOLUTION, SIGNAL TO NOISE RATIO, PASSIVE SYSTEMS, MICROWAVE EQUIPMENT, SENSITIVITY, BRIGHTNESS, IMAGES, REMOTE DETECTORS, ADVERSE CONDITIONS, MILITARY APPLICATIONS, INFRARED DETECTORS, RADIOMETERS, GEOPHYSICS, LONG WAVELENGTHS, BENEFITS, AREA COVERAGE, BACKGROUND NOISE, ALL WEATHER, SEA ICE.

IDENTIFIERS: (U) REMOTE SENSING.

AD-A293 464

ARMY ENGINEER WATERWAYS EXPERIMENT
STATION VICKSBURG MS ENVIRONMENTAL LAB

(U) Physics-Based Infrared Terrain Radiance Texture Model.

DESCRIPTIVE NOTE: Final rept.
FEB 95 123PPERSONAL AUTHORS: Weiss, Richard A.; Sabol, Bruce M.; Smith, James A.; Bales, John W.
REPORT NO: WES/TR/EL-95-5

UNCLASSIFIED REPORT

SUPPLEMENTARY NOTE: Prepared in collaboration with
Tuskegee Univ., AL.

ABSTRACT: (U) This report develops a physics-based semiempirical model for predicting the texture of an infrared (IR) image of terrain areas including soil, grass, and forest canopies. The model is based on an empirical determination of the relationship between the standard deviation and correlation length of the terrain radiance variations in an IR image and the average value of the radiance in the image. The average value of the terrain radiance is then theoretically predicted by the WESTHERM terrain radiance prediction model in terms of local terrain and weather conditions and in terms of the time of day. In this way, the diurnal variation of the standard deviation and correlation length of the radiance or brightness temperature can be predicted for specified terrain and weather conditions.

DESCRIPTORS: (U) *INFRARED IMAGES, *TERRAIN INTELLIGENCE, THERMAL PROPERTIES, WEATHER, PREDICTIONS, BRIGHTNESS, CORRELATION, RADIANCE, LENGTH, STANDARD DEVIATION, DIURNAL VARIATIONS, TREE CANOPY, GRASSES, TERRAIN MODELS.

IDENTIFIERS: (U) WESTHERM MODEL.

AD-A293 057

OFFICE OF NAVAL RESEARCH ARLINGTON VA

(U) Data Collection at the Lockheed Santa Cruz Facility Using Midwave Hyperspectral Imagers.

FEB 95 16P

PERSONAL AUTHORS: Shaffer, William A.; Schaum, Alan P.; Hinnrichs, Michelle; Massie, Mark A.; Fields, David
REPORT NO: NRL/MR/5620--95-7648

UNCLASSIFIED REPORT

SUPPLEMENTARY NOTE: Prepared in collaboration with Pacific Advanced Technology, Solvang, CA and Lawrence Livermore National Lab., CA.

ABSTRACT: (U) From September 12-15, 1994, two midwave hyperspectral imagers (the Infrared Multi-spectral Sensor (IMSS) of Pacific Advanced Technology and the Livermore Imaging Fourier Transform Infrared Spectrometer (LIFTIRS) of Lawrence Livermore National Laboratory) made measurements of particular patches of forest background and a Lockheed Santa Cruz Facility test stand at various times of day and observed the firing of the rocket engine from a sensitive piece of hardware mounted in the Lockheed test stand. The hyperspectral image cubes of the same patch of background observed at various times will be used to investigate the temporal nature of the constituent-temperature interaction. The data of the rocket firing was collected as part of a classified program of the U.S. Army Missile Command. Two sets of data cubes taken of the same background region by IMSS and LIFTIRS simultaneously will be used both to compare the two instruments and to aid in instrument characterization. This paper describes the instruments used in this data collection, the types of backgrounds observed and the experiments performed, and the data collected.

DESCRIPTORS: (U) *INFRARED DETECTORS, FOURIER TRANSFORMATION, TERRAIN, INFRARED IMAGES, DATA ACQUISITION, BACKGROUND RADIATION, ROCKET ENGINES MULTISPECTRAL, INFRARED SPECTROMETERS, FORESTS.

IDENTIFIERS: (U) HYPERSPECTRAL IMAGERY, IMSS(INFRARED MULTISPECTRAL SENSOR)

*AD-A292 784

QUANTUM MAGNETICS INC SAN DIEGO CA

(U) Inductively Coupled IR Staring Array Based on Photofluxonic Pixels.

DESCRIPTIVE NOTE: Final rept. 15 Jul 94-14 Jan 95
MAR 95 29P

PERSONAL AUTHORS: Hibbs, Andrew D.; Singsaas, Alan L.; Taussig, Douglas A.
REPORT NO: CM1198F
CONTRACT NO: F49620-94-C-0058

UNCLASSIFIED REPORT

ABSTRACT: (U) The goal of this study was to investigate the feasibility of fabricating a new type of monolithic focal plane multipixel staring array for infrared (IR) radiation detection. This sensor works by the recently postulated process of photofluxonic conversion in which an infrared photon creates a vortex-antivortex pair in a superconducting material. The novelty of the new sensor lies in the detection mechanism itself, and in the way the vortex (or antivortex) is trapped in the device allowing individual sensing pixels to be read out without direct electrical connections. The overall objective of Phase I was to determine the feasibility of building an inductively coupled, non-contact staring array based on the new photofluxonic detection elements. To this end, we have performed a series of experiments on a single array element, a 2 mm diameter loop of YBa2Cu3O7, and considered pixel requirements for constructing an array. The new system offers tremendous potential for improvement over current infrared detection devices via both the enhanced detection sensitivity and the greatly reduced system complexity.

DESCRIPTORS: (U) *INFRARED DETECTORS, INFRARED DETECTION, ARRAYS, SENSITIVITY, FEASIBILITY STUDIES, PHOTONS, MONOLITHIC STRUCTURES (ELECTRONICS), INFRARED RADIATION, FOCAL PLANES, HIGH TEMPERATURE SUPERCONDUCTORS, PIXELS.

IDENTIFIERS: (U) PHOTOFUXONIC EFFECT, FOCAL POINT ARRAYS, STARING ARRAYS.

AD-A291 218

SRI INTERNATIONAL MENLO PARK CA

(U) LNTISb as a Long-Wave Infrared (LWIR) Material:
Defects and Transport Properties.

DESCRIPTIVE NOTE: Final rept. 19 Apr 93-14 Jan 95
FEB 95 67P

PERSONAL AUTHORS: Krishnamurthy, S.; Van
Schilfgaarde, M.; Bending, M. A.; Sher, A.
CONTRACT NO: N00014-93-C-0091

UNCLASSIFIED REPORT

ABSTRACT: (U) We have evaluated three III-V semiconductor alloys as possible candidates for future long-wave infrared (LWIR) detector materials. The cohesive energies, elastic constants, band structures, electron mobilities, and phase diagrams are calculated and are compared to those of Hg sub 1-xCd sub xTe (MCT) alloys. All three of these III-V alloys have their band gap change from negative to positive values as the alloy composition x decreases from 1 to 0. The x values for the 0.1-eV gap are estimated to be 0.67, 0.15, and 0.08, respectively, for ITP, ITA, and ITS. While ITP and ITA form stable zincblende solid solutions for all alloy compositions, zincblende ITS is stable only for a range of x less than 0.15. ITP and ITA have considerably larger cohesive energies and elastic constants than does MCT, indicating that they are structurally robust. At a 0.1 eV gap, the band structures near the gap and the electron mobilities in ITP, ITA, and ITS are also found to be comparable to those of MCT. Because the lattice constants of ITP and ITA are less than 2X larger than the respective values in InP and InAs, the latter should provide natural substrates for the growth of active LWIR alloys.

DESCRIPTORS: (U) *OPTICAL MATERIALS,
*SEMICONDUCTORS, *INFRARED DETECTORS,
* ELECTRON MOBILITY, ELASTIC PROPERTIES,
EPITAXIAL GROWTH, SUBSTRATES, ALLOYS,
TRANSPORT PROPERTIES, DEFECTS(MATERIALS),
TITANIUM, LONG WAVELENGTHS, INDIUM,
ANTIMONY, MELTING POINT, INFRARED SPECTRA,
GROUP III METALS.

<http://www.dtic.mil/dtic/docorderform.html>

E = Express- Mailed Next Business Day (Guaranteed Delivery in 2 Business Days) (\$20.00 surcharge/document)

[illegible]

The DTIC Review is now available as a subscription product to DTIC registered users!

Only \$85/year for quarterly updates...

For more **information** call:

Phone: (703) 767-8266/DSN 427-8266

Fax: (703) 767-9070/DSN 427-9070

Email: bibs@dtic.mil

To **order** a single copy for \$25, contact DTIC's Reference and Retrieval Branch at:

1-800-225-3842 (menu selection 1, option 1)

Phone: (703) 767-8274/DSN 427-8274

Fax: (703) 767-9070/DSN 427-9070

Email: msorders@dtic.mil or rp-orders@dtic.mil

To **subscribe** call:

1-800-225-3842 (menu selection 2, option 2)

Phone: (703) 767-8272/DSN 427-8272

Fax: (703) 767-8228/DSN 427-8228

Email: reghelp@dtic.mil